PARTICLE-SCALE STUDY OF HEAT TRANSFER IN GRANULAR GEOMATERIALS

Wenbin Fei
ORCID: 0000-0002-9275-8403

Submitted in fulfilment of the requirements for the degree of
Doctor of Philosophy

Department of Infrastructure Engineering
The University of Melbourne
2020

Page intentionally left blank

Abstract

The effective thermal conductivity of granular geomaterials is the one of the most important parameters in some geotechnical and reservoir engineering applications. Various effective thermal conductivity models have been developed over the years, aiming to predict effective thermal conductivity accurately. However, these models usually predict effective thermal conductivity that are different from the experimental measurements. This may be due to the limited access to the material microstructure and thus limited understanding of its effects on the macroscopic or 'engineering' effective thermal conductivity. With the advent of computed tomography and complex network theory, digital samples can be reconstructed based on high-resolution computed tomography images and then microstructure of the samples can be quantified at multiple length scales. At the microscale, three-dimensional sphericity and roundness are selected in this work to describe particle shape based on a critical examination of the literature. They are calculated for each particle in different sands using an in-house developed code. Mesoscale parameters, perhaps with the exception of 'coordination number', are still scarcely used in engineering. This issue is addressed by representing the granular materials as either *contact* networks or *thermal* networks and applying complex network theory to obtain new mesoscale parameters that characterise the granular assemblies. A network consists of nodes and edges. Specifically, in the *contact* network, a node represents a particle and an edge means an interparticle contact. Since heat transfers through not only interparticle contacts but also the 'small' gaps between adjacent particles, the *contact* network can be extended to a *thermal* network by considering the 'small' gaps as new edges. The complex network features extracted from these networks can capture the information of particle connectivity or/and contact quality which are essential to heat transfer. Results show that granular geomaterials with higher average sphericity or roundness can render a higher effective thermal conductivity because the two particle shape descriptors have a positive correlation with average coordination number and interparticle contact radius ratio (i.e., the ratio of the equivalent radius of interparticle contact area to the particle radius). Different types of *network features* can characterise the microstructure from diverse aspects. For examples, the *degree* is related to contact number, *closeness centrality* is about the average distance between

particles, and *betweenness centrality* describes the role of a node or edge acting as a 'bridge'. Many network features can be used as predictors of effective thermal conductivity, especially the features weighted by contact area in the *contact* network or by thermal conductance in the *thermal* network. In this work, a single weighted network feature that considers both particle connectivity and contact quality have shown a strong correlation with effective thermal conductivity of different granular materials either generated by discrete element method or digital sands. Some examples of these single features include *weighted degree* and *weighted closeness centrality.* The implementation of various advanced tools makes access to microstructure becoming readily and promote a data-driven approach to build effective thermal conductivity models automatically without subjective bias. The multiple characterisations and correlations determined through the thesis allow to rigorously select the input parameter(s) for an artificial neural network model with the capability of predicting the effective thermal conductivity with high accuracy and computational efficiency. The proved feasible data-driven framework from this thesis offers a new paradigm for effective thermal conductivity prediction.

Table of Contents

List of Figures

Chapter 1

Figures in the included journal papers:

Section 3.2 Impact of three-dimensional sphericity and roundness on heat transfer in granular materials

Page intentionally left blank

List of Tables

Tables in the included journal papers:

Page intentionally left blank

Declaration

This is to certify that

1. the thesis comprises only my original work towards the PhD,

2. due acknowledgement has been made in the text to all other material used,

3. the thesis is less than 100,000 words in length, exclusive of tables, figures, references and appendices.

Wenbin Fei, March 2020

Page intentionally left blank

Preface and Publications

This thesis consists of several published or submitted (under review) research papers. Publications 1 and 2 comprise Chapter 3 while Chapter 4 is made up by Publication 3. Publications 4 and 5 from Chapter 5, followed by Chapter 6 which is related to Publication 6.

1. Fei, W., Narsilio, G. A. & Disfani, M. M. (2019) Impact of three-dimensional sphericity and roundness on heat transfer in granular materials. *Powder Technology* **355**:770-781.
2. Fei, W. & Narsilio, G. A. (2020) Impact of three-dimensional sphericity and roundness on coordination number. In *Journal of Geotechnical and Geoenvironmental Engineering - Technical Note*. (conditionally accepted 17 March 2020, accepted).
3. Fei, W., Narsilio, G. A., Van Der Linden, J. H. & Disfani, M. M. (2019) Quantifying the impact of rigid interparticle structures on heat transfer in granular materials using networks. *International Journal of Heat and Mass Transfer* **143**:118514.
4. Fei, W., Narsilio, G. A., Van Der Linden, J. H. & Disfani, M. M. (2020) Network analysis of heat transfer in sphere packings. *Powder Technology* **362**:790-804.
5. Fei, W. & Narsilio, G. A. (2020) Network analysis of heat transfer in sands. In *Computers and Geotechnics*. (conditionally accepted).
6. Fei, W., Narsilio, G. A. & Disfani, M. M. (2020) Predicting effective thermal conductivities of sands by artificial neural network with multiscale microstructural parameters. *Journal of Geotechnical and Geoenvironmental Engineering*. (Advanced draft, getting ready for submission).

Page intentionally left blank

Acknowledgements

This PhD journey is with tears and joys. It challenges my critical thinking, learning ability, time management and communication skills but also completes me as a person with more knowledge, more resilience and a global perspective and social responsibility. I thank The University of Melbourne for offering me the Melbourne Research Scholarship and the kindness people around me to fulfil this journey.

First and foremost, I acknowledge my principal supervisor, A/Prof. Guillermo Narsilio, for his intellectual contributions to this PhD project, supports to my professional development and advice for my life. He is so approachable and trustable that I have enough freedom to fly in the academic sky without the worry of losing the main direction. I also express my gratitude to my co-supervisor, Dr. Mahdi Disfani who is also easy to work with and offer wonderful suggestions to my PhD and professional career. Additionally, I am delighted to have Nelson Lam as the chair of my advisory committee. I thank his concern for my needs in each year's progress review and his reminder of the change of University's policy.

My PhD could not be finished without the supports from my colleagues and friends. I wound like to thank Dr Joost van der Linden for the fruitful discussions about the methods used in this project. I acknowledge Min Zhang from the University of Nottingham Nighbo China for sharing the experience in PFC. I thank Yu Zhou for taking pictures of the sands used in this paper. The CT images were collected with the support of Australian Synchrotron. I acknowledge the efforts that Dr Joost van der Linden, Dr Tabassom Afshar, Dr Miao Xiuxiu, Dr Anton Maksimenko and other beam scientists at Australian Synchrotron made for the collection. I also thanks Bamford Rock Testing Services (BRTS) for offering me the opportunity to have an insight into the Australian industry. I would also to appreciate all excellent colleagues from BRTS and The University of Melbourne and all friends to spend a pleasant time together.

I would like to thank my parents for the understanding that I pursue a PhD degree overseas and their support and family education I benefited early on. I am grateful to my wife, Qifang, for her love, accompany, patience, raising and teaching the next generation in a different culture with me. I would also like to thank my kid, Hanghang, for bringing happiness and the family integrity to me.

Page intentionally left blank

Chapter 1: Introduction

This chapter introduces the research context in section 1.1, followed by the objectives of the research and approaches to reach them in section 1.2. The significance and scope of this research are described in section 1.3 which also presents definitions of terms used. Finally, section 1.4 outlines the structure of the remaining thesis.

1.1 RESEARCH CONTEXT

Heat transfer is one of the dominant processes in energy systems studied in geothermal engineering (Yun and Evans 2010), pebble bed reactor (Moscardini et al. 2018) and thermal energy storage (Cole et al. 2012) comprising granular materials, to name a few examples. The effective thermal conductivity (λ_{eff}) is a critical variable used to describe how easily heat travels within (granular) materials. Therefore, a thorough understanding of heat transfer processes and predicting λ_{eff} accurately and efficiently is of great importance.

The λ_{eff} characterises heat transfer of a granular material at macroscale similar to what porosity does when characterising the number of voids within the granular assembly. Hence, λ_{eff} models based on porosity alone miss the information of the particle geometry at the microscale and particle arrangement at mesoscale. Bypassing these microstructural parameters may be the cause of the differences between the λ_{eff} from models and experimental measurements (Abdulagatova et al. 2009; Abyzov et al. 2013; Van Antwerpen et al. 2010). The lack of microstructural characterisations for granular materials is due to the limited access to the microstructure, especially for natural sands comprising particles with irregular shapes. Even though some λ_{eff} models (Fricke 1924; Keller et al. 2001; Zehner and Schlunder 1970) attempted to involve the effect of particle/pore shape, the shape was described by *aspect ratio* which only works well for regular particles such as spheres and ellipsoids (Fei et al. 2019).

With the advent of X-ray computed tomography (CT), it is possible to generate sequential cross-sectional images of soil and rock samples. The sequential images include the interior structural information in the samples and can be stacked together to digitally reconstruct the sample microstructure in three-dimensions (3D). Based on

the digital sample, it is feasible to extract geometrical parameters such as particle shape descriptors using image post-processing algorithms. Although a number of parameters (Cho et al. 2006; Hryciw et al. 2016; Legland et al. 2016; Rorato et al. 2019; Sneed and Folk 1958; Wadell 1932) have been attempted in quantifying particle shape, most of them are two-dimensional and even different equations were employed to calculate the *same* parameter. For instance, the sphericity in (Legland et al. 2016) and (Wadell 1932) depends on particle surface area and volume, while the sphericity in (Cho et al. 2006) is computed using the radii of the maximum-inscribed sphere and minimum circumscribed sphere. Some other studies (Hryciw et al. 2016; Sneed and Folk 1958) considers aspect ratio identical to sphericity, and its value is related to different combinations of axial length. Consequently, the selection of particle shape descriptors and their defining equations should be compared and selected carefully.

In gas/fluid stagnant granular materials, the heat transfer paths can be classified into (1) particle conduction; (2) interparticle conduction; (3) particle-gas/fluid-particle conduction and (4) heat radiation from solid surface to other media. The last three heat transfer mechanisms indicate the importance of structural arrangement to λ_{eff} prediction. The coordination number (CN) describes the connection of a target particle with its surrounding particles and is well related to mechanical stability (Fonseca et al. 2013). However, for granular materials under loads, the average coordination number (CN_{ave}) cannot fully characterise the spatial change of the microstructure, and the variation of interparticle contact area which is vital to heat transfer (Abyzov et al. 2013; Askari et al. 2017). According to rigidity theory, interparticle triangle structures can resist more deformation compared with the quadrilateral structure. Nevertheless, their impact on λ_{eff} has not been studied yet.

Characteristics about particle connectivity (except for CN) are still scarce. An order characteristic (Dai et al. 2019) or Voronoi tessellation (Cheng et al. 1999) can measure the particle connectivity but for sphere packings rather than natural sands. Complex network theory has gained significant success in presenting social networks (Smailovic et al. 2018) and infrastructure systems (Fu et al. 2016). By presenting a granular material as a network consisting of nodes and edges, complex network theory has also been applied to granular materials to study the impact of microstructure on mechanical behaviour (Tordesillas et al. 2011) and fluid flow (van der Linden et al. 2016). The physical meanings of nodes and edges vary according to the application.

Contact networks are usually used to investigate the mechanical behaviour of granular materials by presenting a particle as a node and an interparticle contact as an edge. Network features from the *contact* network also have the ability to detect the shear band in an early stage (Tordesillas et al. 2010). The aforementioned interparticle triangle structure corresponds to the concept of *3-cycle* in complex network theory. However, complex network theory has not been introduced to investigate the impact of microstructure on heat transfer. It is also noticeable that heat transfer through gaps (near-contact) between adjacent particles cannot be quantified by features from the contact network which only considers the interparticle contacts. Only a few pioneering simulation tools called *thermal* network models involved near-contacts, but they focus on λ_{eff} calculation (Desu et al. 2019; Yun and Evans 2010) rather than extracting mesoscale parameters.

Even though granular materials are complex systems and the complex network-based approach offers an opportunity to enrich particle connectivity features (e.g., degree, centrality measures, cycles and clustering coefficients) (Papadopoulos et al. 2018), considering many of them together with traditional parameters such as particle size and porosity may increase the redundancy of λ_{eff} models. Hence, the most important network features related to λ_{eff} are required to be screened to quantify the particle arrangement succinctly at multiple scales. The screening processes are implemented objectively using machine learning (ML) techniques in this PhD project (i.e., feature selection). In addition to the feature selection, ML also shows great potential for predicting material properties in a more efficient, objective and autonomous process (Ju and Shiomi 2019). λ_{eff} prediction using ML methods have been studied in (Desu et al. 2019; Kautz et al. 2019; Wei et al. 2018). However, particle connectivity parameters were absent and the studies used artificial materials. This project will address the issue by employing both virtual and real samples.

1.2 OBJECTIVES AND APPROACHES

The PhD project aims to predict λ_{eff} accurately and efficiently based on a thorough understanding of how microstructure in granular assemblies affects heat transfer. In order to reach the aim, it is necessary to achieve the following objectives:

1. Samples are the basis of both exploring microstructural parameters and evaluating λ_{eff}, so granular geomaterials should be prepared and digitalised to enable their microstructure to be accessible;

2. Based on the digital samples, the complex microstructure in granular geomaterials should be quantified accurately at multiple scales, especially the mesoscale parameters to compensate for the deficiency of variables related to particle arrangement.

3. Since multiple microstructural parameters could be achieved from objective no.2, the most relevant and least redundant material parameters that affect λ_{eff} should be identified.

4. Since λ_{eff} is not only related to the microstructure in granular geomaterials but also the boundary conditions such as the loadings that the materials bear, this project also intends to investigate the change of microstructure in deforming materials and its impact on λ_{eff}.

5. With the access to multiple microstructure parameters from previous objectives, this project attempts to predict λ_{eff} in a data-driven approach to make the prediction automatically without human bias.

Detailed *approaches* of how to fulfil the objectives are summarised below.

1. In order to obtain microstructural data, this PhD project uses two approaches
    - to apply the discrete element method (DEM) to create sphere packings;
    - to digitally reconstruct sand from CT images and extract representative samples from the digital sands.
2. In order to quantify the complex microstructure in granular geomaterials at multiple scales, this project intends
    - to develop codes to compute microscale 3D particle shape descriptors from digital sands;
    - to establish networks from which mesoscale network structure features can be extracted.
3. In order to identify the effects of material parameters on λ_{eff} in granular geomaterials, this project intends

- to introduce a strategy to mitigate the overestimation of λ_{eff} using finite element method (FEM).
- to collect network features from Objective no. 2 and traditional geotechnical parameter to characterise microstructure at multiple scales.

4. Inspired by the rigidity theory, network structure features such as the cycles are used to characterise the change of microstructure . They are compared with porosity, a traditional geotechnical parameter, to investigate their effects on λ_{eff}.
5. In order to implement data-driven approaches, λ_{eff} models are built using a deep ML method, i.e., Artificial neuron network (ANN) model. The project will not treat ANN as a black-box by feeding the model any achievable parameters and perform agnostic to the physics (heat transfer). The input parameters will be selected according to the existing λ_{eff} models and heat transfer mechanisms.

1.3 SIGNIFICANCE AND SCOPE

1.3.1 Significance

This project will improve the fundamental understanding of the thermo-mechanical responses of granular geomaterials subjected to microstructural changes (either due to deformation or original particle arrangement) and lead to the development of a better predictive tool.

The advanced CT techniques, complex network theory, new numerical simulation method and ML approaches used in this project are integrated into a platform for predicting properties of granular geomaterials and unveiling the patterns in the materials (see Figure 1.1). The platform is not only suitable for research on heat transfer but also has the potential to study the mechanical, hydraulic and electric response of various geo-materials. The platform is made of ten blocks. Microstructural data are required to be collected either from real sand after scanning in the CT machine (block 1) or artificial data using DEM (block 2). CT data can be post-processed to reconstruct digital samples which alongside DEM samples are used for three purposes: (1) to calculate traditional features such as particle size, shape, porosity in block 3; (2) to build networks and calculate network features with complex network theory (block

4); (3) to compute λ_{eff} either using FEM or thermal conductance network model (TCNM) in block 5, which will be specified in chapter 4. The traditional and network features are collected as input parameters while the λ_{eff} as an output parameter in a feature set in block 6. Each pair of features is imported to different models in block 7 to calculate the correlation coefficient (R^2). The model having the largest R^2 is the 'best fit' model, and the R^2 is used to find λ_{eff} predictors by evaluating the importance of the features to λ_{eff} and their interplay in block 8. Next, the pattern of how the λ_{eff} predictors affect λ_{eff} can be unveiled in block 9 and λ_{eff} model can be established in block 10.

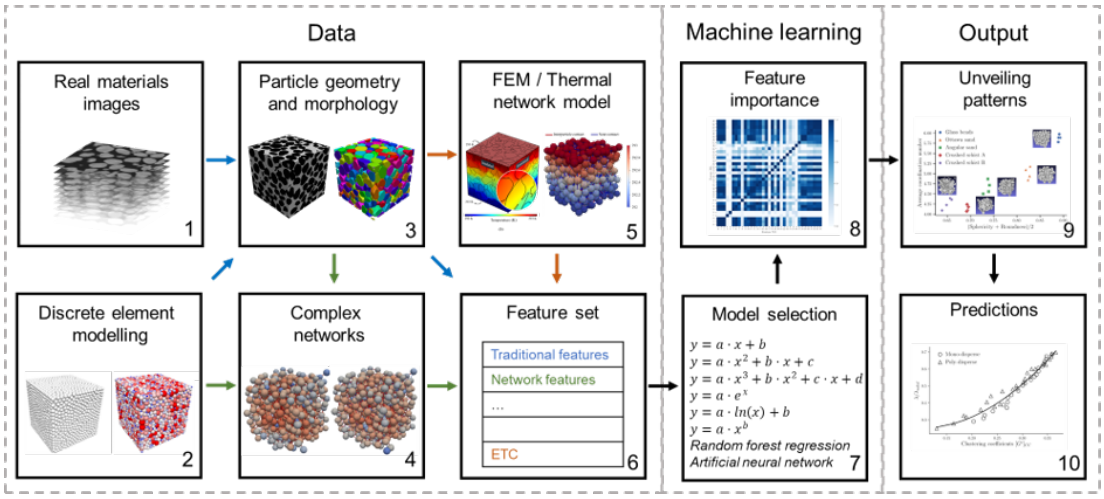

Figure 1.1 Platform can be used to predict properties of granular geomaterials and unveil the patterns in the materials.

This thesis involves the development of the key blocks in the platform that can provide automatic processes, thus minimising or eliminating concern about time-consuming and inconsistency when predicting λ_{eff} from microstructural data. The development of these blocks also allows for gaining physical insights in heat transfers in granular geomaterials. Compared with a typical twenty-four hours that are required to saturate a sample to test porosity in the laboratory, calculating porosity based on CT images can be completed in a shorter timeframe since saturation is unnecessary. Furthermore, a smaller specimen is enough to achieve obtaining microstructural parameters with unnecessity of the saturation process. Moreover, the same CT images can be used to extract more microstructural information and to simulate other physics.

The PhD work is also contributing to geothermal engineering. For horizontal shallow geothermal systems, ground improvement simply by compaction can enhance thermal conductivity. The developed knowledge of how microstructures affect transport properties under deformation may further help in the ground improvement not only for bearing capacity but also heat transfer.

1.3.2 Scope

Although the platform is suitable to study a number of transport phenomena, this thesis focuses on heat transfer of granular materials. Granular materials are assemblies of discrete connected particles/grains whose size is larger than 100 μm (Richard et al. 2005). Packings consist of smaller particles is defined as powders (Brown and Richards). The granular materials with only air in the void are considered as dry while referred to saturated if the voids are fully occupied by water. The air and water do not move in the granular materials, so they are in a stagnant situation. Different physics (thermal, mechanical, hydraulic) have interactions, but their coupled response is out of the scope of this thesis. The λ_{eff} measured in the laboratory is used to validate the results from FEM and TCNM. The TCNM at the current stage is only used to compute the λ_{eff} for dry sands.

The microstructure of granular materials is characterised at multiple *length scales*. In this thesis, the *microscale* is defined as the average size of solid or void. In contrast, the *macroscale* is defined as the characteristic size of a sample (Torquato 2013), i.e., *representative element volume (REV)*. The *mesoscale* is at the length scale of conglomerates and layers, which is between *microscale* and *macroscale.*

1.4 THESIS OUTLINE

This thesis presents a combination of standalone but interdependent published or being published journal papers following a brief 'overarching' literature review (chapter 2) and overall conclusion and recommendations for future works (chapter 7). The papers have different themes but are interrelated. Some of them may share samples and methods.

In chapter 3, a combination of 3D sphericity and roundness was determined as good particle shape descriptors to cover the shape of a range of irregular shapes after analysis of various existing definitions. An in-house program was developed to calculate them automatically for each particle in different sands imaged using micro-

CT. The effects of particle shape on heat transfer and traditional microstructural parameters such as coordination number were studied in this chapter.

Chapter 4 reveals the variation of the rigid interparticle structure in deforming granular geomaterials. The rigid interparticle structure is quantified by the number of triangular structures (i.e., *3-cycles* in complex network theory) and its density. Then the rigid interparticle structures indicating the particle connectivity, together with particle shape descriptors indicating contact quality is employed to quantify how the change of microstructure affects λ_{eff} in granular materials under loadings. In this chapter, the λ_{eff} is calculated using TCNM which can mitigate the overestimation of λ_{eff} using FEM because of the partial volume effect (Wiebicke et al. 2017).

Chapter 5 aims to find single parameters that can characterise both the particle connectivity and particle contact quality in granular geomaterials and their potential links to λ_{eff}. Parameters arising by applying complex network theory to both *contact* networks and *thermal* networks were explored. Correlations between these parameters (features) on λ_{eff} were studied. Furthermore, the *contact* network features and *thermal* network features were compared, and the limitations of each approach were identified.

λ_{eff} models can be established by selecting a known form to fit empirical equations using sparse experimental data, but obtaining experimental results is expensive and can be time-consuming. The numerical simulation of the tests is an alternative option (e.g. FEM). However, these approaches are computationally expensive. The availability of multiscale microstructural parameters promotes to predict λ_{eff} in a data-driven manner. An ANN model is able to bring about new λ_{eff} models in a more automatic way without human bias. Traditional parameters and network features were extracted from more sands varying in size, shape and under different loadings in Chapter 6. Some of them were selected as the input parameters for the ANN model to investigate the feasibility of the data-driven approach for λ_{eff} prediction.

The thesis concludes with a summary of the main lessons learned and follow up ideas for future work (chapter 7).

Chapter 2: Literature review

This chapter begins with the available methods to acquire λ_{eff} and the factors affecting λ_{eff} in section 2.1. Then, the literature on microstructural characterisation is reviewed (section 2.2) followed by machine learning (section 2.3) which is an option to predict λ_{eff} based on microstructural parameters. Section 2.4 highlights the implications based on the literature review. Each paper included in this thesis also contains a specific literature review.

2.1 EFFECTIVE THERMAL CONDUCTIVITY ACQUISITION

λ_{eff} indicates the ease with which heat transfers through materials. It can be measured in the laboratory or estimated (computed) (section 2.1.1) on a proper REV (section 2.1.2). The factors affecting λ_{eff} are reviewed in section 2.1.3, which can benefit the development of new λ_{eff} models.

2.1.1 Effective thermal conductivity measurement and computation

Several methods to estimate λ_{eff} are summarised in Table 2.1. Methods of testing thermal conductivity (Donazzi et al. 1977) can be classified into two main categories: (1) steady methods (typically time-consuming and inapplicable in some cases) and (2) transient methods (typically faster, only needing a small temperature change). A needle probe test (ASTM D5334-14 2014) is a widely used transient method to estimate λ_{eff}; it comprises a thermocouple and a looped heating wire inserted in a seamless thin-walled stainless steel tube. Compared with other methods such as the plane source method (Gustafsson 1991) and the 3ω method (Cahill 1990), the transient needle probe method attains a wide application because of its easy design and usage. The main concern of physical experiments is the inconsistency between various measurements which are necessary to build an empirical equation.

A number of theoretical and empirical equations are also available, but they seldomly involve microstructural parameters. FEM and network models are two available methods to compute transport properties based on large and high-resolution images which contain microstructural information. FEM has a wide application for natural sands in the dry, saturated and unsaturated situation but it may overestimate

λ_{eff}. In contrast, network models are novel and computationally cost-effective, but most of them are only available to sphere packings.

Table 2.1 Overview of methods to estimate effective thermal conductivity

Methods	Descriptions	Comments
Physical tests	Steady methods: Guarded heater methods (ASTM E1225-13 2013) and hot wire methods (Kraemer and Chen 2014). Transient methods: needle test (ASTM D5334-14 2014), plane source method (Gustafsson 1991) and 3ω method (Cahill 1990).	Tend to be reliable as far as the samples reflect the real conditions; The sample size is limited; Undisturbed samples are hard to obtain, e.g. sandy materials; Samples may be aggravated during transport; Results from different tests may be inconsistent.
	Is-situ methods include active drill hole methods and passive indirect methods (Kukkonen and Suppala 1999).	Soil is undisturbed; The environment is hard to be controlled.
Theoretical and (semi) empirical equations	refer to Table 2.2 and (Abdulagatova et al. 2009; Abyzov et al. 2013; Mo and Ban 2017; van Antwerpen et al. 2010).	Closed-form equations were developed based on idealised geometries; Large uncertainties increase when considering the heterogeneity and complex pore geometries; Rarely consider microstructure parameters such as particle shape and connectivity.
FEM	Heat flux is first solved with constitutive equation and continuity equation. Then Fourier's law is used to calculate the thermal conductivity (Narsilio et al. 2010).	Solve the governing equations at the microscale; Calculations are conducted on real geometry; Thermal conductivity was overestimated because of the improper representation of surface roughness at the particle contacts (Narsilio et al. 2010); Computation is costly.
Network models	In thermal conductance network models, nodes are assigned to the particle centroids and edges resemble the inter-particle contacts. The heat flow in the network is simulated related to the conductance of every sole contact or near contact. After calculating the heat flow, the λ_{eff} can be achieved with Fourier's law (Kanuparthi et al. 2008).	Network models have a high computational efficiency (Kanuparthi et al. 2008); Thermal conductance network models are now mostly focusing on the packing of spheres (Kanuparthi et al. 2008; Yun and Evans 2010) rather than the assemblies of irregular particles that are ubiquitous in nature.
Lattice Boltzmann Method (LBM).	Employ evolution rules that follow the same conservation laws used in FEM at a mesoscopic scale (Kandhai et al. 1999; Wang et al. 2007).	No need to solve the transportation equation and is mesh-free; Can acquire detailed local information (Guo and Zhao 2002);

Methods	Descriptions	Comments
		Handle interparticle contacts and interfaces between fluids; Direct application on large and high-resolution 3D images has significant challenges (Fredrich et al. 2006).

Table 2.2 Empirical and theoretical equations of computing effective thermal conductivity

Researchers	Equations	Type	Comments
Johansen (1975)	$\lambda = (\lambda_{sat} - \lambda_{dry})K_e + \lambda_{dry}$ $\lambda_{dry} = \frac{0.137\rho_{dry} + 64.7}{\rho_{soild} - 0.947 \cdot \rho_{dry}} \pm 20\%$ $\lambda_{dry} = 0.039n^{-2.2} \pm 25\%$ for crushed rock	E	Consider particle size, saturation and particle conductivity.
Becker et al. (1992)	$S = c_1[sinh(c_2\lambda + c_3) - sinh(c_4)]$	E	Consider saturation
Gavriliev (2004)	$\lambda = 0.025 + 0.238\rho_{dry} - 0.193\rho_{dry}^2 + 0.114\rho_{dry}^3$	E	Available for mineral/organic soil. ρ_{dry}< 2g cm^{-3}
Tong et al. (2009)	$\lambda^L = \eta_1(1-n)\lambda_s + [1-\eta_1(1-n)]^2 \times [\frac{(1-n)(1-\eta_1)}{\lambda_s} + \frac{nS_r}{\lambda_w} + \frac{n(1-S_r)}{\lambda_g}]^{-1}$ $\lambda^U = \eta_1(1-n)\lambda_s + [(1-n)(1-\eta_1)\lambda_s + nS_r\lambda_w + n(1-S_r)\lambda_g]$ $\lambda_{eff} = (1-\eta_2)\lambda^L + \eta_2\lambda^U$	E	Consider the combined effects of mineral composition, temperature, liquid saturation degree, porosity and pressure.
DeVera Jr and Strieder (1977)	$\lambda_{eff} = (\sum_{i=1}^{N} \frac{\omega_i}{\lambda_i})^{-1}$	T	Series
	$\lambda_{eff} = \sum_{i=1}^{N} \omega_i \cdot \lambda_i$	T	Parallel
Sass et al. (1971)	$\lambda_{eff} = \lambda_i^{\omega_i}$	T	Geometric mean
Hashin and Shtrikman (1962)	$\lambda_{eff} = \lambda_1[1 + \frac{3f_2(\lambda_2 - \lambda_1)}{3\lambda_1 + f_1(\lambda_2 - \lambda_1)}]$	T	Hashin and Shtrikaman Boundary
Hill (1965); Tarnawski et al. (2002)	$\lambda_{eff} = \frac{1}{3}[\frac{1-n}{2\lambda_{eff} + \lambda_m} + \frac{n}{2\lambda_{eff} + \lambda_m}]^{-1}$	T	Self-consistent method
Gori and Corasaniti (2004)	$\frac{1}{\lambda_{eff}} = \frac{\beta - 1}{\lambda_a \cdot \beta} + \frac{\beta}{\lambda_a \cdot (\beta^2 - 1) + \beta_m}$ $\beta = [\frac{1}{1-n}]^{1/3}$ dry soil	T	Cubic cell
Zehner and Schlunder (1970)	$\frac{\lambda_{eff}}{\lambda_f} = 1 - \sqrt{1-\phi} + \frac{2\sqrt{1-\phi}}{1-\xi B}[\frac{(1-\xi)B}{(1-\xi B)^2}\ln(\frac{1}{\xi B}) - \frac{B+1}{2} - \frac{B-1}{1-\xi B}]$, $r^2 + \frac{z^2}{[B-(B-1)z]^2} = 1$, $\xi = \frac{\lambda_f}{\lambda_s}$	T	r and z are the radii of the particle in two principal axes. B is the shape factor, The particle approach to z-axis with no solid volume when $B \to 0$, a sphere when $B \to 1$ and a cylinder when $B \to \infty$.
Fricke (1924)	$\frac{\lambda_{eff}}{\lambda_s} = \frac{(1-\phi)(1-\xi)+\xi\beta\phi}{(1-\phi)(1-\xi)+\beta\phi}$, $\xi = \frac{\lambda_f}{\lambda_s}$,	T	β is related to γ and aspect ratio.

Researchers	Equations	Type	Comments
Keller et al. (2001)	$\lambda_{eff} = \lambda_s \left[1 + \frac{\alpha_p}{\alpha_s}\left(\frac{b}{a}\right)^2 \left(2 - \frac{b/a}{(1-b/a)^2}\right)\right]^{-1}$, $\phi = \frac{\alpha_p}{\alpha_s}\left(\frac{b}{a}\right)^2 \left(2 - \frac{b}{a}\right)$,	T	α_p is the aspect ratio of the pore while α_s is the aspect ratio of solid (grain), b is the pore radius while a is the grain radius.

K_e is Kersten number, which depends on the saturation and temperature in soil (Andersland and Ladanyi 2004). λ_{sat} and λ_{dry} (W/(m K)) are thermal conductivity of saturated and dry soil, λ_{eff} (W/(m K)) is the effective thermal conductivity, ω_i is the volume fraction. λ_1 and λ_2 (W/(m K)) are thermal conductivities of two different phases with volume fractions f_1 and f_2. $\lambda_m$and λ_a (W/(m K)) are thermal conductivities of mineral and air, λ_s, $\lambda_w$and λ_g (W/(m K)) are thermal conductivities of solid, water and gas. λ^L and λ^U (W/(m K)) are lower and upper limit of thermal conductivity, ρ_{soild} (kg/m^3) is the specific weight, ρ_{dry} (kg/m^3) is dry density, c_i (i=1,2,3 and 4) are model parameters, n is porosity, E stands for empirical equation and T stands for theoretical equation, η_1 is a coefficient related to porosity and η_2 is a coefficient related to both porosity and saturation.

2.1.2 Representative element volume (REV)

REV is defined as the smallest volume of a heterogeneous material that is sufficient to represent the mean macroscopic constitutive response. A REV is required to be determined before estimating transport properties with numerical simulations. Table 2.3 summarises researches regarding REV for calculating λ_{eff}. Samples six or seven times larger than D_{50} are required for the calculation.

Table 2.3 Overview of REV and mesh size to calculate effective thermal conductivity

Researchers	REV/D_{50}	Mesh number	Comments
Narsilio et al. (2009)	5.8×5.8×3	308955	Spherical glass beads. Seventeen meshes across the particle diameter.
Azadi et al. (2010)	7.1×7.1×3.6		Materials have three phases sample
Łydżba and Różański (2014)	$\sqrt[n]{\left(\frac{\eta(\Theta)-1}{f+(1-f)\eta(\Theta)}\right)^2 \frac{D_{50}^n f(1-f)}{\varepsilon}}$, $\eta(\Theta) = min\left\{\Theta, \frac{1}{\Theta}\right\}$		n=2 for two-dimensional and 3 for 3D.

Θ is the contrast in phase properties, f is the maximum volume fraction of phases, ε is the error tolerance, and is usually prescribed as 3%.

2.1.3 Effective thermal conductivity dependencies

Researchers conducted numerous studies to determine the effects of various factors on λ_{eff} (Table 2.4). Among these factors, particle size and particle shape determine the particle geometry, but the effect of particle shape on λ_{eff} is seldomly quantified for natural sands. Mesoscale parameters can characterise particle connectivity which dominates the heat transfer via interparticle contacts. However, the

particle connectivity parameters are scarce and few studies about its influence on λ_{eff} have been published.

Table 2.4 Overview of factors related to effective thermal conductivity

Factors	Relation to λ_{eff}	Comments
Porosity	Negative	Low porosity indicates high density.
Particle size	Positive	Dry sand (Chari et al. 2013); Fine sands whose water content was lower may have a higher λ_{eff} than coarse sands (Zhang et al. 2015).
Gradation	Positive	Well-graded sands has lower porosity; λ_{eff} increases when decreasing porosity.
Shape	λ_{eff} increases when aspect ratio deviates from 1.0 (Gan et al. 2017)	Ellipsoids packings generated in DEM.
Fine contents	Positive	A critical fine content exists, and it increases along with the decrease of the ratio of average fine particle size to average coarse particle size (Zhang et al. 2015).
Fluid	Positive to the thermal conductivity of the fluid.	(Yun and Santamarina 2008)
Moisture content	Positive when dry soil is added to a small amount of water.	
Mineralogy	Positive to the thermal conductivity of minerals.	
Mixture	λ_{eff} is larger in mixtures with large isolating materials (e.g. rubber) than those with small ones (Lee et al. 2015).	Sphere packings.
Load	Positive (Weidenfeld et al. 2004)	The particle irregularity renders λ more dependent on the stress state (Yun and Santamarina 2008).
Diagenesis	Positive to precipitation (Yun and Evans 2010).	The contact area is increased.

2.2 MICROSTRUCTURAL CHARACTERISATION

In DEM, artificial samples can be generated by placing particles in a 'box', following certain criteria such as porosity and grain size distribution. The DEM software can offer the radius and coordinates of each particle, so microstructural parameters can be computed using the information. In contrast, non-destructive techniques are required to achieve the geometry and topology of particles in real sands. Section 2.2.1 introduces the available imaging techniques followed by image processing algorithms in section 2.2.2. Section 2.2.3 summarises the particle shape descriptors and section 2.2.4 describes complex network theory which is a powerful tool for probing the insights into granular materials and characterise the microstructure at multiple length scales.

2.2.1 Imaging techniques

Geometries of granular materials can be digitalised as images using imaging techniques. Then, the samples can be virtually reconstructed to compute particle size, shape and other microstructural variables. Some imaging techniques are summarised in Table 2.5. Among them, CT has become the most prevalent one to achieve 3D morphological information of granular materials (Lai and Chen 2019). It currently acts as a mean to characterise specimen heterogeneity (Aste et al. 2005), to visualise multiphase flow (Wong and Wibowo 2000), and to track shear deformation and fracture characteristics (Alshibli and Alramahi 2006). However, only a few studies have used this 3D information to 'mine' or extract and fundamentally understand other key geomaterial properties.

Table 2.5 Overview of image techniques

Techniques	Theory	Comments
Optical Microscope (OM) (Thomas et al. 2014)	Visible light and a series of lenses are used to magnify images of small objects.	Cannot scan the interior structure of granular assemblies; Low accurate reconstruction of grain with an irregular shape.
Scanning Electron Microscopy (SEM) (Cox and Budhu 2008)	A focused beam of electrons interacting with atoms in the samples is employed to produce various signals.	Samples are required to be sliced; Can apply X-Ray to classify the constituents (mineralogy) of the particles.
Optical Tomography (OT) (Thomas et al. 2014)	Light transfers and scatters through an object rotated at regular angular intervals.	Samples over mm and cm scales; Lower accuracy but relatively cheap; It works well on soft tissue in the medical field.
X-Ray Computed Tomography (X-Ray CT)) (Cnudde et al. 2006; Fredrich et al. 2006; Santamarina and Fratta 2005)	A sample is placed between an X-ray source and an X-ray detector; then the detector rotates systematically to record 2D radiographs at different angles from 0° to 360°.	Ideal to objects with distinguished X-ray absorption coefficient (dense materials); Performs badly for a mixture of objects with low and high density together; CT images can be identified by simple threshold-based tools.
Magnetic Resonance Imaging (MRI) (Johns and Gladden 1999; Pohlmeier 2011)	A magnetic field is created by a cylindrical magnet that acts on protons in water and generates echo because of the MRI scan's radio waves. Then these echoes can be captured and organised into images by a computer.	Water 'X-ray'; Can obtain information on flow pathways, water content (Amin et al. 1994) and liquid flow velocity (Deurer et al. 2002). Ideal for distinguishing between different soft tissues in the medical field; Can take cross-sectional images of an object from almost any angle; Manual segmentations are necessary.

2.2.2 X-ray computed tomography image processing

Images are required to remove artefacts and be processed with multiple algorithms for different purposes such as achieving different phases or individual particles.

CT artefacts

CT images directly achieved in the field may have artefacts including ring artefact, noise, beam hardening, scatter, metal artefact, pseudo-enhancement, cone beam and motion etc. (Boas and Fleischmann 2012). Ring artefact and noise are two common artefacts in the CT images from granular materials in this study.

The ring artefacts in CT images may be induced by miscalibration and defective detector, or impurities on scintillator screens. Recalibrate or replace the detector in the filed can avoid the artefact in a new scanning. Alternatively, since the ring artefacts are strips in sinogram, it can be removed by applying Fourier filter with a Gaussian filter to the achieved images in the polar system (Münch et al. 2009).

Poisson noise may exist when a sample is exposed to a low dose of CT. It can be smoothed out using model-based iterative reconstruction (MBIR) (Thibault et al. 2007) while keeping the edges of solids sharp. 'Salt and pepper' noise (Ahmed and Lebedev 2019) may exist in good quality CT images. They can be removed using the median filter resulting in non-Gaussian noises and sharp edges. Non-local means filter (Buades et al. 2005) is another option and has a better performance for small particles but is not as effective as the median filter (Ahmed and Lebedev 2019).

Threshold segmentation

As different phases have different densities which render the corresponding voxels in contrasting grayscale. Based on the intensity levels of the grayscale, threshold segmentation can be implemented to binarize the images and separate the phases. Various thresholding algorithms were reviewed in (Iassonov et al. 2009; Sezgin and Sankur 2004; Wiebicke et al. 2017) and classified into: global and local thresholding, level sets, region growing methods, probabilistic clustering and Bayesian methods. Local thresholding methods can generate satisfactory results, but they are sensitive to initial inputs. Otsu (Otsu 1979) and Rilder (Hughey 2020) are two global thresholding algorithms that are adequate to segment different phases. The connectivity or neighbourhood between voxels also needs to be specified when

applying a threshold segmentation. In 3D, 6-, 18- or 26-connectivity of a voxel is related to common face, edge or vertex. 6-connectivity can reduce the overestimation of particle surface area or contact area (Taylor et al. 2015) while 26-connectivity benefits the identification of particle boundaries (Fonseca et al. 2012).

Segmentation of Aggregates

After identifying solid phases, aggregates in non-destructive samples need to be segmented to obtain discrete particles to calculate particle size and shape. The watershed algorithm is a popular choice to complete this task. It uses a topographic analogy on greyscale images or distance map (Soille and Vincent 1990; Vincent and Soille 1991). A distance map is generated from a binary image which can be achieved after threshold segmentation. Then each pixel in the solid is assigned with a new grayscale whose value is equal to the distance from the pixel to the nearest background pixel. The greyscales are considered as altitudes such that an image can be converted to topographic surface. From each minimum region (i.e. local minima on greyscale images or distance maps), water is flooded, and dams are created at where the water from different valleys meet to find different catchment basin. The watersheds are the zones dividing neighbouring catchment basins.

The classic watershed algorithm works best for smooth convex objects without large overlap (Schindelin et al. 2012). It may lead to overestimation if too many local minima are found due to noise in the images. Filters such as Gaussian and median filter are recommended to remove the noise. A plugin named MorphoLibJ (Legland et al. 2016) also offers the option to merge over-segmented regions. Other minima such as extended minima can also be generated using other algorithms or selected manually to replace the local minima in classic watershed segmentation. Additionally, Canny edges created based on the gradients of CT images can represent particle boundaries and be used to check the validity of watersheds (Kim et al. 2003).

As an alternative to the watershed algorithm, a machine learning tool named *Trainable Weka Segmentation* (Arganda-Carreras et al. 2017) was developed. It is a voxel-based algorithm and generates possibility maps indicating which class each voxel belongs to. Hence, if the classes are trained for only solid and void phase, it can binarize the images as threshold segmentation does. It can also segment different objects if voxels are marked into different classes during training.

2.2.3 Particle shape

Particle shape is known to affect the macro properties of granular materials. For instance, angular sands tend to possess a higher void ratio, a larger compressibility potential, a higher friction angle, greater anisotropy and non-coaxially (Yang et al. 2015), and higher hydraulic conductivity (Cabalar and Akbulut 2016) than the rounded counterpart. However, limited research has attempted to quantify these effects with appropriate true particle shape descriptors. Elongation, roundness and roughness are three important aspects in particle shape (Cho et al. 2004). Some approaches that can be used to characterise the particle shape from different aspects are summarised in Table 2.6.

Despite a large number of 2D shape parameters that have been developed, as shown in Table 2.6, they may be inaccurate because of the random projection, especially for platy grains such as mica shown in Figure 2.1. 3D shape parameters (Taylor 2002; Zhou et al. 2017) are available, but the number is limited. Furthermore, academics attempted to unify the shape parameters. Specifically, Wadell (1932) adopted the ratio of roundness and sphericity to express the image of a solid. Cho et al. (2004) developed regularity, which is the average of sphericity and roundness. A total shape index was also introduced by Parylak (2000), which considers sphericity, angularity and roughness; further details can also be found in the work of Zięba (2017). However, the same shape parameter may be calculated using different equations. Furthermore, limited research was conducted to apply the shape parameters to empirical equations for solving transport properties.

Table 2.6 Overview of shape descriptors

Scale	Shape descriptors	Definition	Comment
Sphericity (Elongation)	Sphericity (Wadell 1932)	The ratio of sphere surface that has the same volume as the particle to the real surface of the particle. MinR/MaxR in Particles8_Plus. MinR and MaxR are the radius of the inscribed and enclosing circles at the centre of mass, respectively.	The proximity of a particle to a sphere; Can be an ambiguous indicator unless coupling with 'shape factor' (Zingg 1935) because disc-like bodies may have the same sphericity as rod-like or bladed bodies. Different definitions in computer programs;
	Circularity	$(4*\pi*\text{Area})/(\text{Perimeter}^2)$	2D sphericity
	Aspect Ratio	Feret / Breadth	Feret = Major axis; Breadth = Minor axis

Scale	Shape descriptors	Definition	Comment
	ModRatio	(2*MinR)/ Feret	MinR: Radius of the inscribed circle centred at the centre of mass,
Roundness (Angularity)	Roundness (Wadell 1932)	The ratio of average curvature at particle corner to overall particle curvature; 4*Area/(π*Feret^2) in Particles8_Plus, where Feret is the Major axis.	The extent to which the corners and edges have been rounded; Not always appropriate to quantify the finer detail of particle contour, for crushed particles in particular (Lees 1964). Different definitions in computer programs; Imply angularity and texture; Together with sphericity are easy to use with a 2D chart (Figure 2.3).
	Compactness	(SQRT[(4*Area)/ π])/ Feret	
Smoothness (Roughness)	Solidity	Area/ConvexArea	ConvexArea: Area of the Convex Hull polygon.
	Convexity	ConvexHull/Perimeter	
	RFactor	ConvexHull/(Feret*π)	
	Fourier series (Ehrlich and Weinberg 1970)	Shape (wave of the profile) is obtained by measuring the relationship between radii and the angle between the measurements using Fourier series.	
	Fourier descriptors (Luerkens 1991)	Calculation from the Fourier series coefficients.	Independents of the size of grain and the relative position in the input image; Lower frequency descriptors indicate the integral particle shape while the higher frequency descriptors relate to textural qualities (Kunttu et al. 2003)
	Fractal dimension (Mandelbrot 1975)	Describe the capability of a rough boundary approaching the particle. Fractal dimension (D) is derived from the relation between the approximate profile length L, the number of segments N and the segment length r.	Characterises shape which cannot be described by other traditional Euclidean geometry; Highly depends on the segment lengths.

Figure 2.1. 2D particle shape is subject to the projection, especially for platy grains such as mica (Teachers 2012).

2.2.4 Complex network theory

From the 1990s onwards, network models and image analysis technologies were introduced to characterise the microgeometry and connectivity (Bultreys et al. 2016). Newman (2010) reviewed the theory, development and applications of 'complex network' theory which has the advantage of capturing succinct, inherent multi-scale properties to present the structure, topology, dynamics and functionality of the network (Newman 2003). Papadopoulos et al. (2018) summarised the measures for characterising granular networks (degree, walks, paths, cycles, clustering coefficients, centralities, etc.). However, the previous work focused on micromechanics, rather than other key geomaterial behaviours. Even though van der Linden et al. (2016) pioneered a pore network and a particle contact network to quantify the connectivity of the pores and particles and its effects on fluid flow, the 'complex network' theory has still not been used to study the heat transfer in granular media.

2.3 MACHINE LEARNING

Machine learning refers to that computers have the ability to learn a task without being explicitly programmed (Samuel 1959). Machine learning trains models based on examples of input variables (features) and output variables (labels). After learning a number of examples, supervised machine learning predicts new examples without a label. Unsupervised machine learning has no labels, aiming to find the structure in the data.

Determining the relationships between multiple microstructural parameters and macro-properties, and then proposing an accurate empirical equation is a challenge. While modelling or experiments can be used to investigate these relationships, such processes are generally time-consuming. Machine learning can solve complex

classification and regression problems. Hence, the statistical techniques regarding regression provide alternative approaches to generate data-driven predictive models which identify the 'empirical' relations with uncertainties and errors rigorously addressed. Machine learning also conducts a holistic investigation and is efficient at selecting features consisting of only the most relevant and non-redundant variables. Additionally, machine learning is capable of analysing all variables at the same time, rather than studying a single property. Different techniques of varying complexity and degree of interpretability can be applied to machine learning.

Machine learning techniques highlight a wide application in geotechnical engineering, such as load capacities, liquefaction and slope stability (Shahin 2013). However, the implementation of machine learning on predicting the λ_{eff} of granular geomaterials is limited. Khandelwal (2012) predicted thermal conductivity by using machine learning that was dependent on the following features: density, porosity, uniaxial compressive strength and P-wave velocity. More advanced deep machine learning techniques were used to predict the λ_{eff} of sphere packing (Desu et al. 2019; Kautz et al. 2019) and irregular virtual materials (Wei et al. 2018) considering porosity and particle size. However, microscale particle shape and mesoscale particle connectivity have not been involved in the predictive models. Microstructural parameters from the samples constructed using CT images or DEM with network properties can enrich the input variables.

2.4 SUMMARY AND IMPLICATIONS

From the section of effective thermal conductivity dependences (section 2.1.3), it is known that λ_{eff} is governed by the microstructure in granular materials and the boundary conditions applied to the materials. However, the theoretical and empirical equations seldomly consider the microstructural parameters, perhaps except for including porosity. Hence, it is necessary to quantify the microstructure of granular materials and study its effect on λ_{eff}.

Particle shape descriptors are microscale parameters which are considered in some λ_{eff} models using aspect ratio after simplifying granular materials as idealised geometries such as sphere packings or ellipsoid packing. However, the aspect ratio is not suitable to quantify the shape of irregular particles in natural sands. Therefore, the first research question arises as:

Question A (Chapter 3): What are the particle shape descriptors suitable for all-natural geomaterials, and their impacts on λ_{eff} and traditional microstructural parameters?

Geomaterials are usually prone to deformation (due to changes in effective stresses). The changes in boundary conditions and the interior structure of geomaterials will increase the complexity of predicting conduction phenomena. Hence, a research question is posted as:

Question B (Chapter 4): How to quantify the effect of the interior microstructure change on the variation of λ_{eff} in geomaterials during deformation?

Mesoscale parameters to characterise the particle connectivity for natural sands are scarce. CT techniques and complex network theory provide the opportunity to 'mine' this information. However, the network features have not been used to study heat transfer. This research gap leads to the following research question:

Question C (Chapter 5): How can particle connectivity be characterised for the purpose of predicting λ_{eff} ?

Normally, an empirical equation for predicting transport properties can be developed by conducting a large number of physical experiments. However, this process is time-consuming and costly. The algorithms in machine learning to solve regression problems can train the relationship between microstructural parameters and transport properties. However, machine learning is usually be considered as a 'magic' tool: *train your data, solve your problems*. As for the application of machine learning to study heat transfer in granular geomaterials. On the one hand, limited works have been conducted. On the other hand, the selection of input parameters in existing studies is not based on the understanding of heat transfer mechanism so that particle connectivity parameters are missing. With the inspiration of these limitations, the next research question is:

Question D (Chapter 6): What microstructural parameters should be involved in machine learning models to predict the λ_{eff} of natural sand accurately and efficiently?

Page intentionally left blank

Chapter 3: Impact of particle shape on heat flow and microstructure

3.1 OVERVIEW AND STRUCTURE

Particle shape is vital to understand the behaviour of natural geomaterials. However, the commonly-used two-dimensional descriptors (e.g., circularity, convexity, compactness and solidity.) may be inaccurate because they depend on the projection direction, and thus unable to truly represent the three-dimensional particle shape in generalised cases. In this chapter, an algorithm is developed to calculate three-dimensional particle shape descriptors automatically from a large assembly of particles imaged using micro-computed tomography. The code is then used to study the effects of particle shape on heat flow and coordination number. Some results indicate (1) irregular particles have lower sphericity and roundness than round particles; (2) packings assembled by irregular particles have a wider range of sphericity and roundness and (3) a higher thermal conductivity could be achieved by increasing the average of sphericity and roundness. (4) well-sorted (poorly graded) and more spherical particle packings may have higher average coordination number.

This chapter consists of two manuscripts: (1) a journal paper entitled ‘Impact of three-dimensional sphericity and roundness on heat transfer in granular materials’ published in Powder Technology; and (2) a technical note entitled ‘Impact of three-dimensional sphericity and roundness on coordination number’, which has been conditionally accepted by Journal of Geotechnical and Geoenvironmental Engineering. The papers have different themes but are interrelated. Some of them may share samples and methods.

3.2 IMPACT OF PARTICLE SHAPE ON HEAT TRANSFER

Powder Technology 355 (2019) 770–781

Contents lists available at ScienceDirect

Powder Technology

journal homepage: www.elsevier.com/locate/powtec

Impact of three-dimensional sphericity and roundness on heat transfer in granular materials

Wenbin Fei, Guillermo A. Narsilio *, Mahdi M. Disfani

Engineering Block B 208, Department of Infrastructure Engineering, The University of Melbourne, Parkville, VIC 3010, Australia

ARTICLE INFO

Article history:
Received 25 April 2019
Received in revised form 22 July 2019
Accepted 25 July 2019
Available online 26 July 2019

Keywords:
Heat transfer
Particle shape
Granular material
Particle reconstruction

ABSTRACT

Knowledge of particle morphology is vital to understand the behaviour of natural geomaterials including heat transfer. The effects of particle shape on heat transfer have been mostly quantified with two-dimensional (2D) particle descriptors or at most with a single three-dimensional (3D) descriptor. However, these particle shape descriptors may fail to capture the shape of all irregular particles. To redress this issue, we developed a method to reconstruct particles from micro-computed tomographic (μCT) images and to extract 3D sphericity and roundness of individual particles in the assembly. Sphericity and roundness of five real sand packings are calculated using the new proposed method. Furthermore, the effective thermal conductivity (ETC) of each sample is estimated using finite element modelling. Our results show that packings with higher sphericity or roundness tend to render higher ETC. A further examination of the microstructure in the assemblies indicates that sphericity or roundness corresponds to inter-particle contacts.

1. Introduction

Knowledge of effective thermal conductivity (λ_{eff}) of granular systems, for example, is required in design, prediction and control of processes in many engineering applications such as radioactive waste disposal [1], geological carbon dioxide storage [2], hydrocarbon energy [3] and geothermal engineering [4]. As the λ_{eff} is affected by the microstructure [5,6] in the granular materials, to quantify the impact of microstructural features on λ_{eff} enhances the fundamental understanding of heat transfer processes. Particle shape is a fundamental feature in characterising the microstructure of natural soils and rocks. Hence, it is vital to fundamentally understand how particle shape affects the λ_{eff} of these geomaterials and of other granular materials.

Many experiments and simulations show that particle shape contributes significantly to the mechanical [7–10], hydraulic [11–14] and thermal [15–17] behaviour of geomaterials. Even though the correlation between particle shape and λ_{eff} has been quantified by introducing two-dimensional (2D) particle descriptors [15,18], the easily measured 2D particle shape descriptors [10,19–21] (e.g., circularity, sphericity, roundness, aspect ratio, convexity, compactness and solidity) can be random and inaccurate as they may depend on the projection direction. This is particularly the case for irregular and platy particles. The relationship between particle shape and thermal conductivity were also studied by using three-dimensional (3D) sphericity to characterise the particle shape [22,23]. However, (synthetic) particles with only a certain shape such as sphere and cylinder were selected for those studies. Moreover, the 3D sphericity defined [24] as the ratio of the surface area of the equivalent sphere of a particle to the real surface area of the particle can be used to represent the particle shape. However, this sphericity definition cannot distinguish, for example, between particles with a disc-shape and particles with a rod-shape. Discrete element method (DEM) has also been used to generate ellipsoids varying in aspect ratio to study the effect of particle shape on λ_{eff} [17]. However, the artificial ellipsoid or supper-ellipsoid [25] from DEM are different from many real natural sands. As other definitions of sphericity [24,26–29] and other 3D particle shape descriptors such as roundness [24] are available, these 3D particle shape descriptors (and definitions) should be identified and chosen carefully to ensure they can properly describe *all* possible irregular particles in a packing or assembly.

Particle shape and particle arrangement (i.e., microstructure) influence the behaviour of the assemblies. To rigorously study their impact on the thermal (and other) response of geomaterials, one would prefer to derive shape descriptors from the same sample (and of the particle assembly) for testing thermal parameters. Since particle shape descriptors are calculated based on the particle geometry, individual particles should be extracted from the particle assembly without disturbing the structure of the sample rather than selecting a few representative particles from the sample. Techniques such as resin impregnation, followed by sequential 2D physical slicing and polishing of surfaces throughout the sample, together with the use of common microscopic facilities are effective but time and labour intensive, and destroy the samples [20,30,31]. Alternatively, X-ray computed tomography (CT) is one of the non-destructive image techniques able to visualize 3D particles in

* Corresponding author.
E-mail address: narsilio@unimelb.edu.au (G.A. Narsilio).

https://doi.org/10.1016/j.powtec.2019.07.094
0032-5910/

https://doi.org/10.1016/j.powtec.2019.07.094 0032-5910/© 2019 Elsevier B.V. All rights reserved.

the samples [32–34]. Even though CT techniques have been used in the study of mechanical response [35,36] and fluid flow [37] in granular materials, they have rarely been applied to the study of heat transfer. CT techniques can generate sequential cross-sectional images of the geomaterial at a certain interval (image resolution) and the solid phase can be detected based on the greyscale of each image. From the stacking of the solid phase in all images, one can construct a "voxelated" geometry. However, the particles in the geometry may overestimate [38] the inter-particle contact area or even look cemented to each other. As the contact area is related to the thermal conductance [39], post-processing image techniques are required to identify "true" individual particles.

Based on the collection of individual particles extracted from voxel-constructed geometry, the particle surface area can be measured using the boundary voxels, and the particle volume can be computed based on the number of voxels inside each particle [38,40]. However, the voxelated particle surface has a saw-tooth pattern and overlapping voxels, leading to an overestimation [38] which may further affect the accuracy of measuring sphericity and roundness. Moreover, since 3D roundness are widely accepted [24,27,41] as the ratio of the average radius of the particle corners and the radius of the maximum inscribed circle, the voxel-constructed particle surface cannot be used to calculate the correct curvature for identifying the corners. Consequently, smoothing the voxel-constructed particles before calculating the 3D sphericity and roundness is required. These issues will be addressed in the present study.

The study aims to investigate the effect of particle shape on the effective thermal conductivity of granular materials. To achieve this, various particle shape descriptors are compared to determine a combination of shape descriptors that can actually cover particle with a wide range of different shapes. Moreover, the theories used to compute the selected particle shape descriptors are explained. A framework is introduced to generate individual smooth particles based on CT images and the methodology is exemplified using five real sand packings. The experimental and numerical methods used to measure the effective thermal conductivity are explained in detail, followed by quantitative analysis on how and why particle shape and microstructure affect heat transfer in granular materials.

2. Particle shape descriptors

Particle shape can be generally described at three different length scales [7] (Fig. 1): Sphericity/Elongation, Roundness/Angularity and Smoothness/Roughness. At the scale of the equivalent particle diameter, sphericity indicates the global form of the particle and describes the proximity of a particle to a sphere while elongation describes the opposite trend. At approximately one tenth of the scale of the equivalent particle diameter, roundness characterises the particle shape at a smaller scale than the scale of sphericity. Roundness is a local feature and represents the extent to which the corners and edges of the particle have been rounded, its counterparty is known as angularity. Smoothness or roughness describes the smallest scale and indicates the platenenss of the particle surface. Since images with resolution higher than 1 μm [42] are typically required to calculate the roughness, the present work focuses on the implementation of sphericity and roundness because the resolution of CT scans is typically lower. The CT scanned images used in this work, for example, have a resolution of approximately 13 μm.

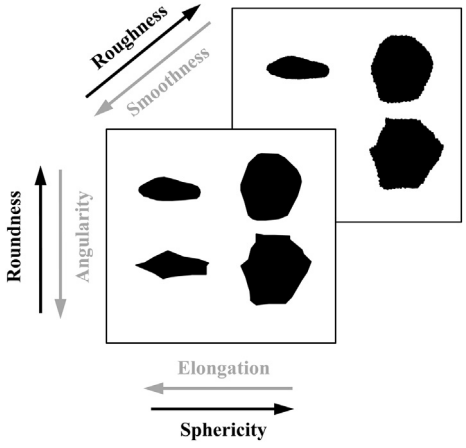

Fig. 1. Particle shape descriptors at three different scales: Sphericity, Roundness and Smoothness.

2.1. Three-dimensional sphericity and roundness

A number of definitions (and corresponding equations) have been proposed in the literature to calculate three-dimensional (3D) sphericity and roundness. Table 1 summarises some of these definitions and formulae to compute 3D sphericity (S1 – S5) employing different parameters. While particle volume V and surface area SA are used in S1 and S2, the radius of maximum inscribed and minimum circumscribed sphere ($r_{max\text{-}in}$ and $r_{min\text{-}cir}$, respectively) are adopted in S3. The length of principal axes of the particle d_i is employed in S4 and S5. However, none of these descriptors can distinguish all particles with different shapes. For example, S1 and S2 cannot distinguish between disc-shape particles and rod-shape particles because they may have the same surface area and volume, as depicted in Fig. 2(a). In Fig. 2(b) and (c) S3 cannot recognise the difference between particle 1 and particle 2 because they have the same maximum inscribed circle and the minimum circum-scribed circle. Moreover, S4 and S5 cannot distinguish particle 1 and particle 2 in Fig. 2(c) since they have the same principle axes if considering the two particles have the same thickness in 3D.

In contrast to the various definitions of sphericity, only few equations have been proposed to compute 3D roundness. Eq. (1) below is used to calculate 3D roundness (R) as the ratio of the average radius of the particle corners to the radius of the maximum inscribed sphere (see Fig. 2(b)):

$$R = \frac{\sum r_i / N}{r_{max-in}} \tag{1}$$

where r_i is the radii of corners in a particle as shown in Fig. 2(b), N is the total number of corners and r_{max-in} is the radius of the maximum inscribed circle of a particle. However, the roundness of the particles in Fig. 2(c) cannot be distinguished if neglecting the local feature on particle surface where the radius of curvature is larger than the maximum inscribed circle.

Table 1
A summary of various definitions of sphericity.

Notation	Equation	Description	Reference
S1	$\frac{\sqrt[3]{36\pi V^2}}{SA}$	The ratio of the surface area of the equivalent sphere of a particle to the real surface area of the particle. V is particle volume and SA is particle surface area.	[24]
S2	$\frac{36\pi V^2}{SA^3}$	The cubic order of S1.	[26]
S3	$\frac{r_{max-in}}{r_{min-cir}}$	The ratio of the radius r_{max-in} of the maximum inscribed circle (sphere in 3D) to the radius ($r_{min-cir}$) of the minimum circum-scribed circle of a particle shown in Fig. 2(b).	[27]
S4	$\frac{d_S}{d_L}$	The ratio of the maximum axial length (d_S) to the minimum axial length (d_L) of a particle.	[28]
S5	$\sqrt[3]{\frac{d_S^2}{d_L d_I}}$	Fitting a particle to an ellipsoid, d_S, d_I and d_L are the shortest, intermediate and the longest axial length of the fitted ellipsoid.	[29]

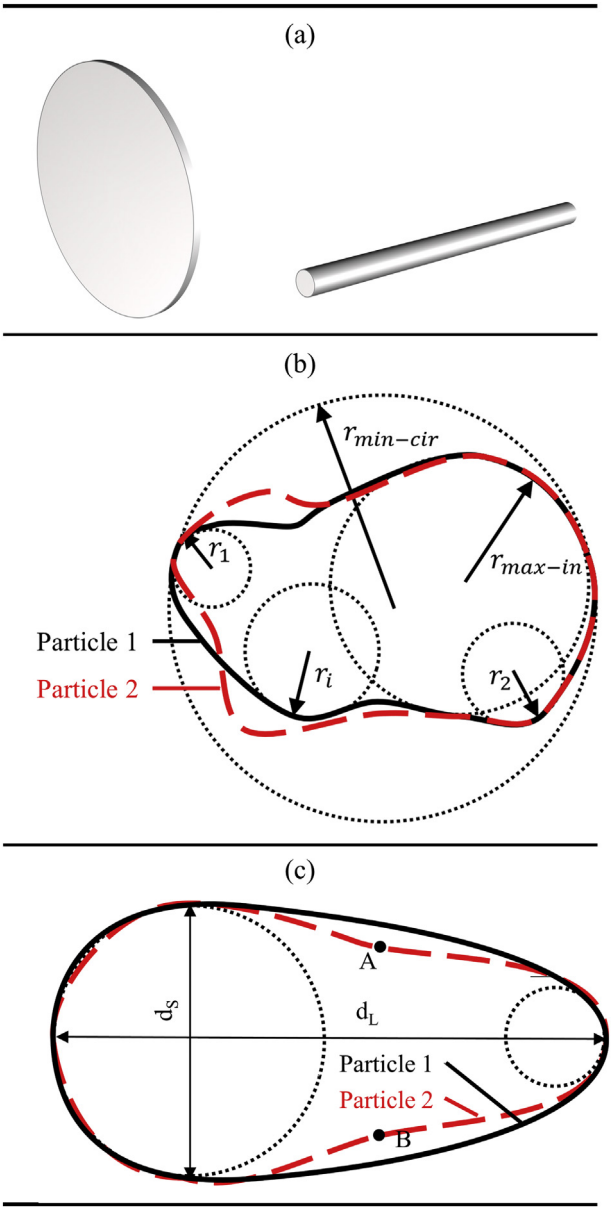

Fig. 2. Examples of potential shortcomings of the various definitions of sphericity and roundness: (a) Example of two particles of different shape but same sphericity (S1 and S2 in Table 1); (b) Example of two particles of different shape but same sphericity (S3 in Table 1) and roundness. (c) Example of two particles of different shape but same sphericity (S4 and S5 in Table 1) and roundness.

Since neither sphericity nor roundness alone can distinguish *all* particles with different shapes, combinations of sphericity and roundness have been used to ensure that all particles with various shapes can be identified [41]. From the previous explanation, particles shown in Fig. 2(c) still cannot be distinguished even if roundness is combined with sphericities S4 or S5. Furthermore, S3 cannot distinguish the two particles in Fig. 2(c), hence using roundness with S3 still fails to recognise the two different particles. Consequently, the remaining S1 and S2 definitions are good candidates which together with roundness could characterise particle shape unambiguously.

To analyse the performance of S1 and S2, a hexahedron with dimensions $L_1 \times L_2 \times L_3$ is adopted but keeping L_1 equal to L_2 and then changing the ratio of L_3 to L_1. According to the results in Fig. 3, a hexahedron with L_3/L_1 varying between 1 and 7, shows a sphericity that shifts from 0.81 to 0.59 when using definition S1,

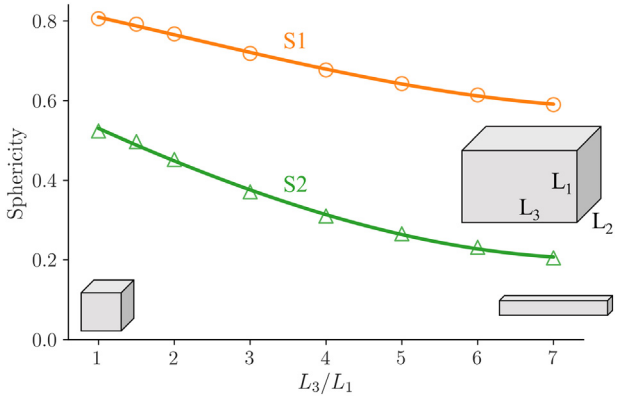

Fig. 3. Comparison of sphericity S1 and S2 defined in Table 1 of a hexahedron with varying dimensions ($L_1 = L_2$, $1 \le L_3/L_1 \le 7$).

while it changes from 0.52 to 0.21 when using definition S2. Since sphericity is conceptually defined as the proximity of a particle shape to a sphere (sphericity is 1) and a hexahedron with $L_3/L_1 = 7$ is far from a sphere, assigning 0.59 to the sphericity of such an elongated particle may be intrinsically unacceptable, as one would expect a much lower value.

As a consequent of the above discussions, in this work sphericity as defined in S2 in Table 1 and roundness as defined in Eq. (1) (revisited later in Eq. (5)) are selected as the combination of descriptors to better characterise the shape of particles in natural granular materials like sands.

2.2. Calculation of sphericity and roundness

From the last section, it is known that the particle surface area and volume are required to compute sphericity whereas curvature is required for calculating roundness. While Fiji [43] is available to compute the particle surface area and volume, the computations are based on voxel-constructed particles which have saw-tooth boundary patterns. The saw-tooth boundary patterns may lead to overestimation of real particle surface area and an incorrect calculation of curvature, the computation of sphericity and roundness should be based on smooth particles. However, no commercial software or open-source code is available to achieve smooth particle geometry and calculate 3D sphericity and roundness using the equations we selected. In this work, we first identify each individual particle and then the smoothing particle surface is made up of triangle surface meshes similar to [41] as shown in Fig. 4(a). Therefore, the surface area of each facet on the particle surface is easily computed, and the summation of all the triangular facet areas is the surface area of the particle (Fig. 4(b)). To compute the individual particle volume, the following procedure is followed. A point inside the particle together with the three points of a single triangular facet form a tetrahedron, so the total volume of the tetrahedrons related to all facets is the particle volume (Fig. 4(b)). Thus, to calculate the particle surface area and volume, Eqs. (2) and (3) are used. Given particle volume and surface area, then S2 can be calculated as the sphericity of each particle.

$$SA = \sum_{i=1}^{n} \frac{1}{2} \left| \overrightarrow{A_iB_i} \times \overrightarrow{B_iC_i} \right| \tag{2}$$

$$V = \sum_{i=1}^{n} \frac{1}{6} \left| \overrightarrow{OA_i} \cdot \left(\overrightarrow{OB_i} \times \overrightarrow{OC_i} \right) \right| \tag{3}$$

where O is the particle centre calculated as the average coordinates of all vertices in the particle, A_i, B_i and C_i are three vertices of the

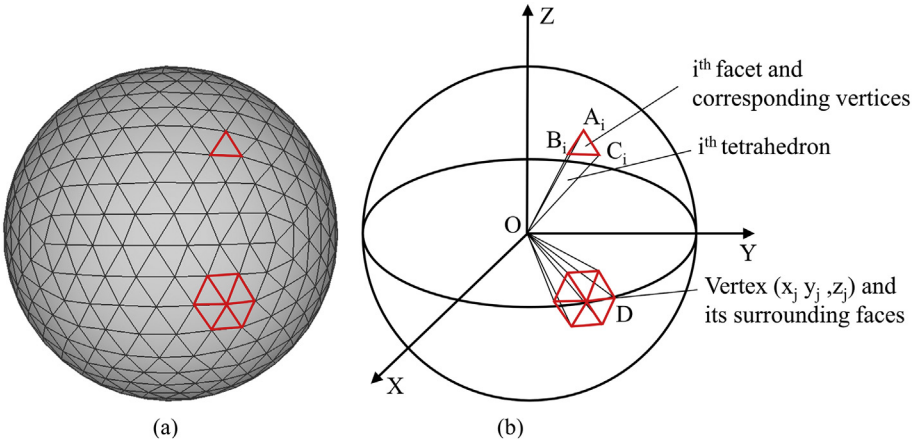

Fig. 4. A particle surface is made up of triangular meshes. (a) Triangular meshes of a sphere, (b) A diagram to illustrate the principles of computing particle surface area, volume and curvature at vertices (after [41]).

i^{th} triangular facet and n is the total number of the facets on the particle surface.

To calculate the roundness of a particle, the first step is to identify corners of the particle. An available criterion is that considering a vertex as a corner when its radius of curvature is smaller than the maximum inscribed sphere. The principal curvatures (the maximum curvature κ_{max} and minimum curvature κ_{min}) are two common measurements [44], and quadratic fitting in MeshLab [45] can be used to compute them at all vertices. The key of this method is to use rings of a vertex (e.g., the first ring of vertex D in Fig. 4(b) is composed of the six vertices around it) to fit a micro-surface by generating a quadratic polynomial equation. Based on the equation, a Hessian matrix [44] can be established and the eigenvalues of the matrix are the principal curvatures. Subsequently, the principal curvature radii are computed as $r_{min} = 1/\kappa_{max}$ and $r_{max} = 1/\kappa_{min}$. Between the two radii, r_{min} is more reasonable to be used for identifying corners because more local features on the particle surface are considered. Then, the corners in a particle can be found using Eq. (4).

$$g(k) = \begin{cases} 1 \; if \; r_{min} < r_{max-in} \\ 0 \; if \; r_{min} \geq r_{max-in} \end{cases} \tag{4}$$

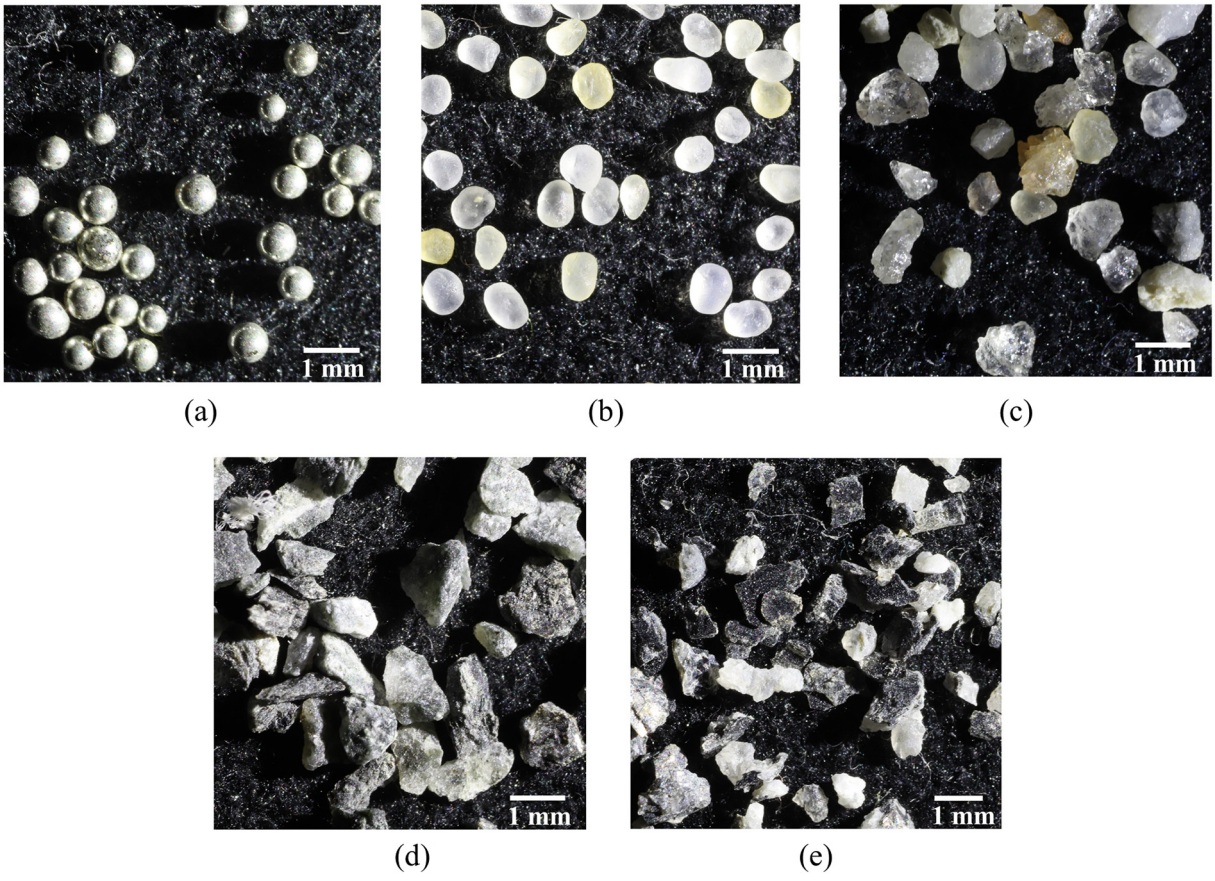

Fig. 5. Micro-pictures of five granular materials with particles of different shape. (a) Glass beads, (b) Ottawa sand, (c) Angular sand, (d) Crushed schist rock A and (e) Crushed schist rock B.

Table 2
Particle size of studied granular materials.

Sample	d_{50} (mm)[a]	d_{50} (mm)[b]	Particle size range (mm)[a]	Particle size range (mm)[b]
Glass beads	0.60	0.60	0.50–0.70	0.40–0.80
Ottawa sand	0.73	0.76	0.60–0.85	0.58–0.94
Angular sand	0.89	0.68	0.60–1.18	0.39–0.99
Crushed schist rock A	0.84	0.58	0.50–1.18	0.23–0.95
Crushed schist rock B	0.84	0.61	0.50–1.18	0.16–1.10

[a] Diameter from sieve analysis.
[b] Equivalent diameter calculated from particle volume using CT reconstruction.

where 1 indicates that the vertex is a corner while 0 is not. r_{max-in} is the radius of the maximum inscribed sphere of the particle. By introducing $g(k)$ into Eq. (1), the 3D roundness is computed as:

$$R = \frac{\sum g(k) r_{\min} / N}{r_{max-in}} \tag{5}$$

3. Particle reconstruction

3.1. Granular material samples

To test the framework and to analyse the impact of particle shape on effective thermal conductivity, five sands with increasing irregularity of particles are selected (Fig. 5): (a)glass beads are near-spherical particles made from silica; (b) Ottawa sand is sieved to pass No.20 (850 μm) mesh and be retained on No.30 (600 μm), the achieved 20–30 standard sands are in line with ASTM standard C778 [46]. These particles consist of quartz [47] and are rounded during long-term erosion. (c) an Angular sand also containing a high proportion of quartz with more irregularly shaped particles when compared to the Ottawa sand. (d) Crushed schist sand A is even more irregular than the Angular sand and the particles in Crushed schist A are made of chlorites. (e) Crushed schist B have particles with the most complex shape and more than half of the particles are platy and elongated [48] because they consist of quartz and biotite [49]. The Crushed schist rock B is made from a particular metamorphic rock collected from the Delamarian Fold Belt in western Victoria, Australia. The particle size of each sample is shown in Table 2. Crushed schist rock A and schist rock B are prepared to have the same mean particle size and range in the laboratory.

These five materials were used to prepare samples in a 25 mm diameter and 25 mm height cylindrical containers made of aluminium using the air-pluviation technique to ensure the homogeneity of the samples and density similarity. The samples are scanned using x-ray computed tomography (CT) to generate sequential grey-scale images with a resolution of 0.013 mm. This resolution lies between the recommendations by Wiebicke, Andò, Herle and Viggiani [50]. Their work suggested that 10–15 μm per voxel and >10 pixels across each grain diameter are required to capture the interparticle contact with improved image processing techniques. The greyscale in each voxel represents the image intensity which relates to the density of the scanned materials. Typical cross-sectional image of each sample is shown in Fig. 6. Particles in Glass beads, Ottawa sand and Angular sand samples have similar greyscale even though some defects exist on the boundary of glass beads because of their coating. In contrast, particles in crushed

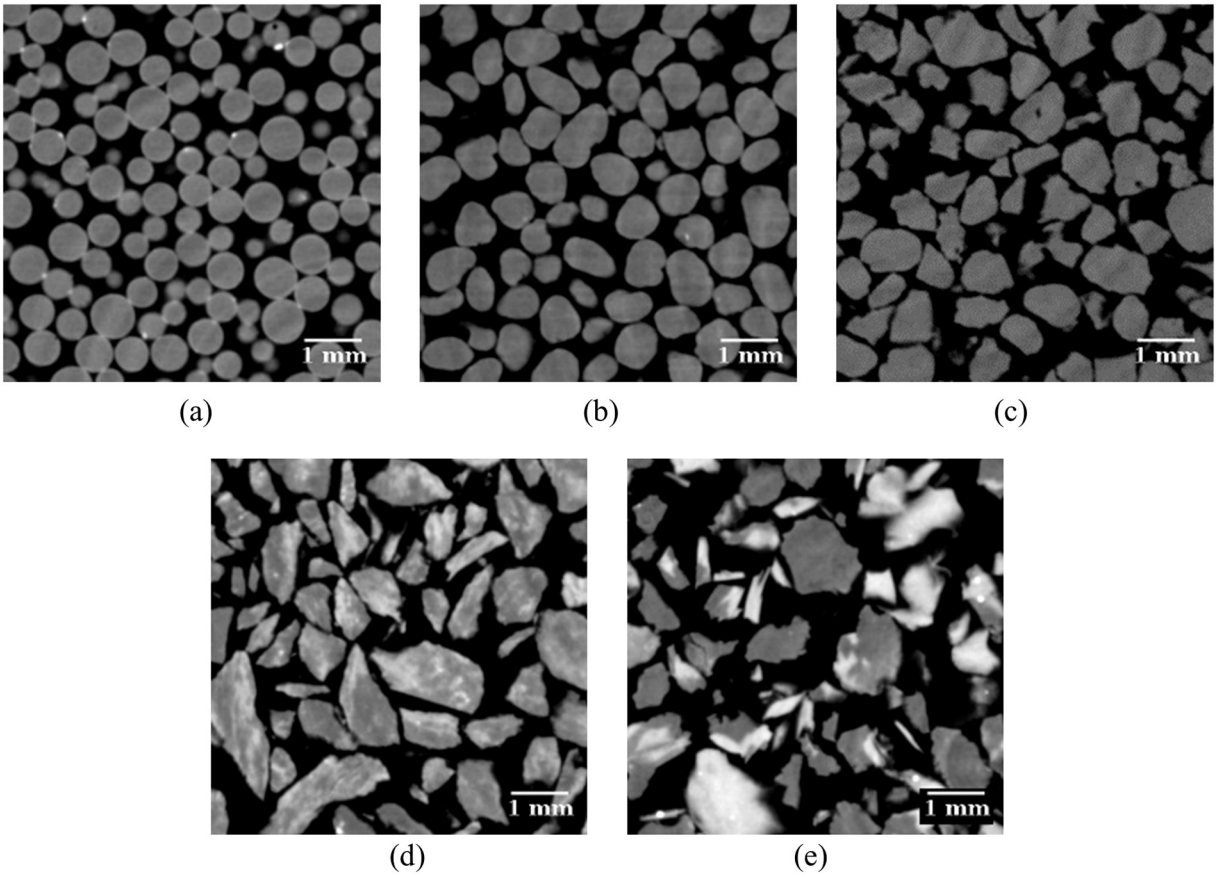

Fig. 6. CT scanned images of the five granular material packings. (a) Glass beads, (b) Ottawa sand, (c) Angular sand, (d) Crushed schist rock A and (e) Crushed schist rock B.

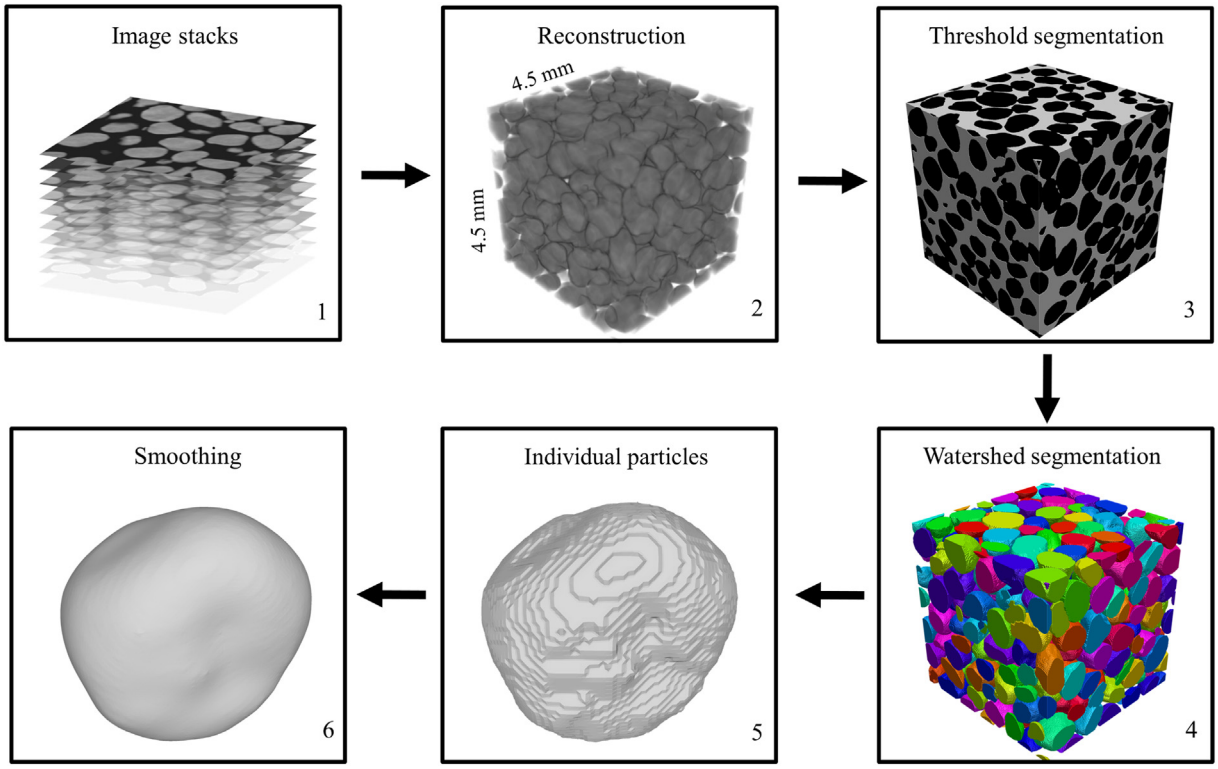

Fig. 7. A framework is used to reconstruct induvial smoothing particles.

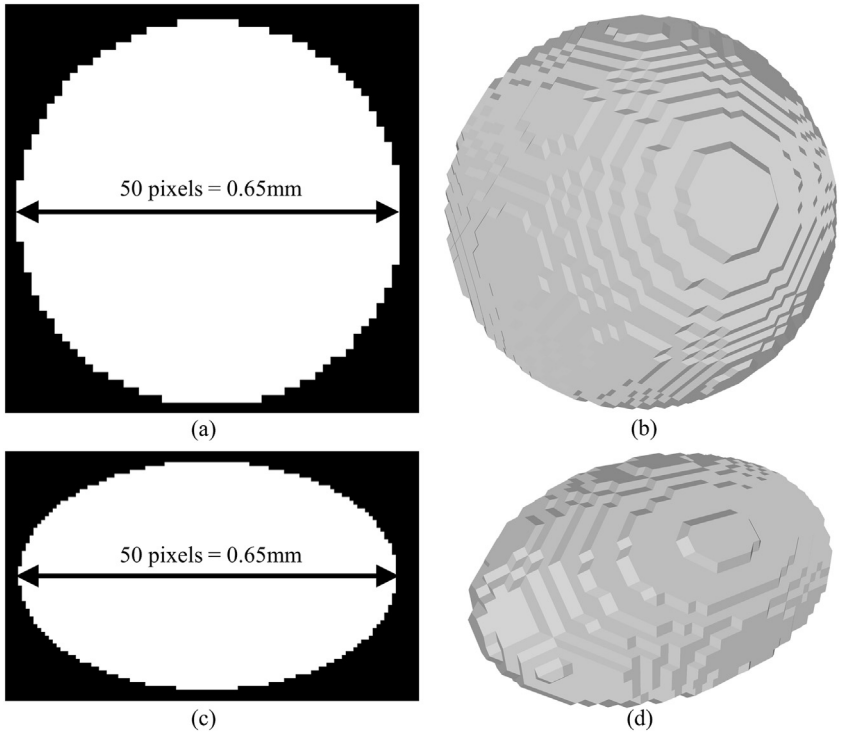

Fig. 8. Voxelated sphere and ellipsoid are constructed from images stacks generated from Fiji: (a) 2D image slice of a sphere, (b) and the resulting voxelated sphere; (c) 2D image slice of an ellipsoid and (d) the resulting voxelated ellipsoid. The resolution of images is 0.013 mm, same as the resolution of CT scanned images later used int his work.

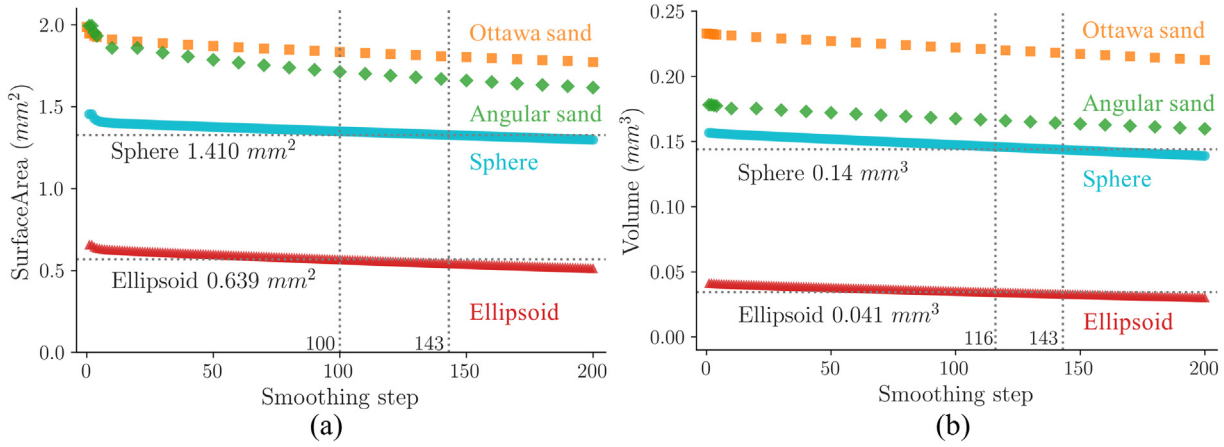

Fig. 9. The surface area (a) and volume (b) decrease gradually with the increase in the number of smoothing steps for $\lambda > -\mu$ in the Taubin smoothing method.

schist rock samples have significant different greyscale because of their complex mineral components.

3.2. Framework

The geometries of *individual* particles can be acquired using the X-ray CT scans of separate particles placed in a container filled with a (low density) silicon filler [41]. However, identifying individual particles in the samples (i.e., assembly of particles) is not always straightforward. Hence, segmentation is required to identify and extract information of individual particles from the specimen. To accurately calculate 3D sphericity and roundness, a smooth digital particle geometry with the "same" surface area and volume as the real particle is required. Here we combined different techniques and propose a series of steps to reach this goal. This section introduces a framework (Fig. 7) to reconstruct individual smooth particles from a stack of cropped X-ray CT scanned images (Step 1). An open source image processing software Fiji [43] is used to reconstruct the sample micro-geometry (Step 2) and to execute threshold segmentation to identify the solid phase of the particle assemblies (Step 3). Iassonov, Gebrenegus and Tuller [51] applied various threshold segmentation techniques (e.g. local thresholding, global thresholding, region growing methods, deformable surface, probabilistic clustering and Bayesian methods) to porous media. In their work, they found that *local* thresholding can generate satisfactory results but are sensitive to the initial input, while the two *global* threshold segmentation methods (Otsu and the Rilder's [50,52–54]) produced satisfactory results without this limitation [38,50]. Therefore, in our work, the multilevel Otsu threshold segmentation method is applied to the greyscale images. Then a watershed segmentation with 6-connectivity [38,55] in MorphoLibJ library [26] is adopted to split ("artificially") connected particles based on the threshold segmentation geometry (Step 3). The 6-connectivity is selected herein because it shows to reduce the overestimation of particle surface area and volume [38]. Boundary particles are discarded because they are part of integral particles resulting from generating the cubic subsamples in Step 1. The individual voxel-constructed particles are thus obtained (Step 5) and then the Taubin smoothing algorithm [56] is used to smooth each particle (Step 6).

3.3. Smoothing method

In Step 6 of the aforementioned framework, a smoothing algorithm is required to polish the saw-tooth surface of voxelated particles and preserve the general particle morphology. Common iterative mesh smoothing algorithms utilise "processing mesh normals" scheme [57–59]. Most of these traditional smoothing algorithms, including Gaussian smooth and Laplacian smooth, have a general shrinkage problem which means a particle may collapse to a point when smoothing is implemented for a large number of iterations. Alternatively, the Taubin λ/μ method [56] consists of two Gaussian smoothing algorithms in each step: λ is positive and relates to the shrinkage whereas μ is negative and controls the infatuation.

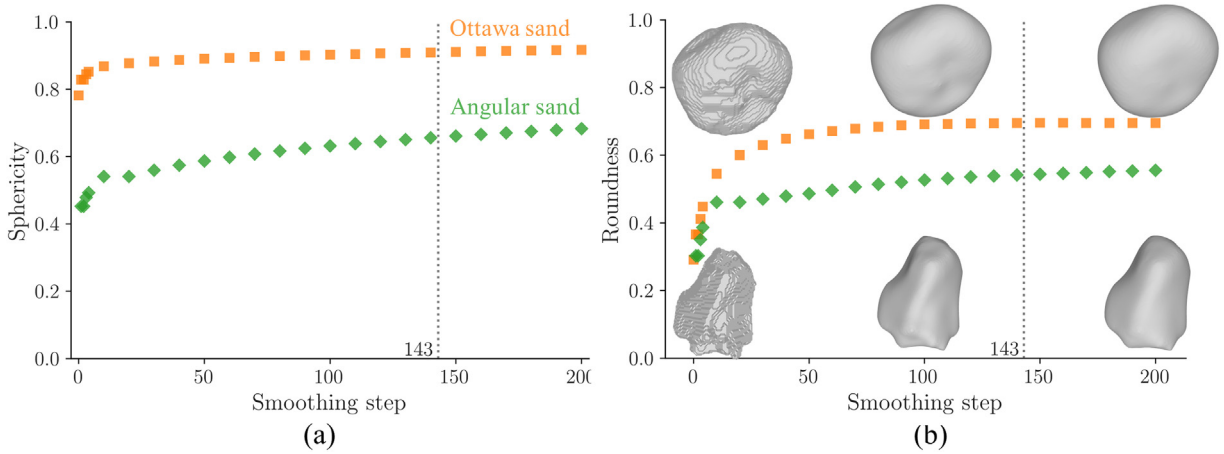

Fig. 10. The sphericity and roundness of two particles from the Ottawa sand and the Angular sand samples as a function of smoothing steps: (a) Sphericity and (b) Roundness. One can also visualize the Ottawa and Angular sand particles at 0, 100 and 200 smoothing steps for comparison.

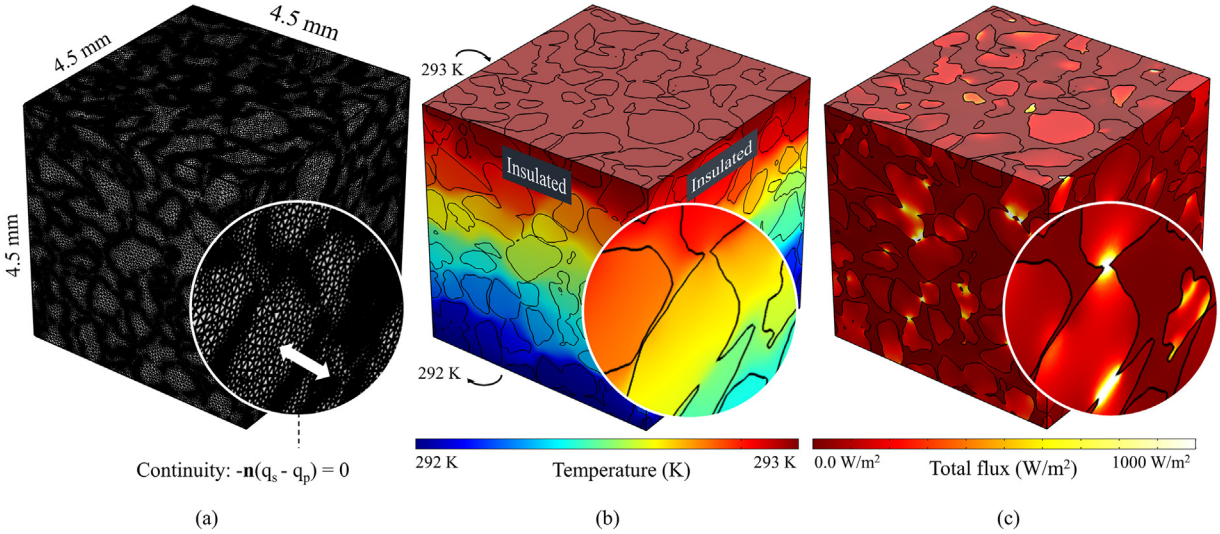

Fig. 11. Finite element mesh and heat transfer simulation results of the Angular sand packing (a) Mesh (b) Temperature distribution and (c) Total heat flux distribution.

To identify the proper range of values of input parameters in the Taubin method for our samples, synthetic pixelated image stacks of a sphere and an ellipsoid are generated using the image analysis software Fiji [43], the resolution of these images is set at 0.013 mm, which is the same as the resolution used in the CT of the tested samples. The diameter of the sphere is set as 0.65 mm (50 voxels), and the three-principal axial lengths of the ellipsoid are set at 0.65 mm (50 voxels), 0.39 mm (30 voxels) and 0.26 mm (20 voxels). The resulting cross-section images and 3D voxelated particles are shown in Fig. 8.

The Taubin smoothing method effectively generates a *low pass filter effect* that is controlled by λ and μ, and the amount of attenuation is then determined by the number of smoothing steps set in the algorithms. The Taubin smoothing method can preserve the geometry of the reconstructed particles from CT images when $\lambda < -\mu$ [56]. Hence, the shrinkage problem in Gaussian smooth and Laplacian smooth is addressed in the Tuabin smoothing method. However, if the surface area and volume from the voxelated particles in the initial step are overestimated to begin with (typical of microCT images), these overestimations are also preserved [38]. To mitigate the initial overestimation of surface area and volume of a particle, $\lambda > -\mu$ is adopted in this work by setting λ as 0.6 and μ as −0.3, which also happen to preserve the geometry of the particles. Together with the synthetic sphere and ellipsoid generated above, two microCT imaged particles, one from the Ottawa sand and one from the Angular sand samples, are also used to investigate the variation of surface area and volume with the number of smoothing steps. Fig. 9 shows that the surface area gradually decreases with smoothing steps, and that the surface area of the voxelated sphere reaches the theoretical value (1.410 mm^2) at the 143rd smoothing step while that of the ellipsoid is reached earlier at the 100th step. As for the reduction of volume, the four particles share a similar trend but at a slower rate of change than that of surface area, the volume of the voxelated sphere reaches the theoretical value (0.41 mm^3) at the 143rd step, which is the same as that of surface area, while the ellipsoid, at the 116th step. In addition to the above analysis to define the range of smoothing steps values that may be appropriate for our studies, sphericity and roundness of Ottawa sand and Angular sand particles are computed and shown in Fig. 10 together with their images at 0, 100 and 200 smoothing steps. It can be seen that the local features of the surface are preserved during the process of Taubin smoothing. Fig. 10 shows that sphericity and roundness converge at early smoothing steps, which is far earlier than the 143rd step found in the previous analysis. To be conservative and to allow a good balance between computational time and accuracy of results, 143 steps (together with λ as 0.6 and μ as −0.3) are selected as input parameters in the smoothing method used herein in the following calculations for all individual particles in natural sands scanned in the micro-CT.

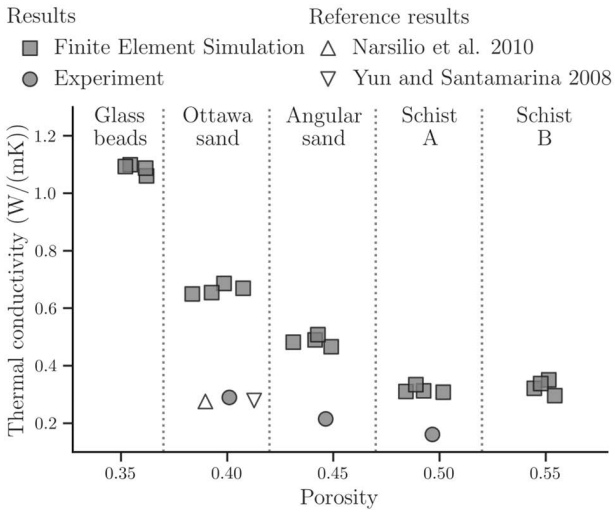

Fig. 12. The effective thermal conductivity of five natural sands from finite element simulations are larger than the experimental measurements, which may because numerical simulation does not capture particle surface roughness and particle geometry irregularity [51].

4. Finite element simulation and measurements

The mineral component of a sand can affect its effective thermal conductivity, especially the content of quartz in dry samples [60]. To eliminate this effect, finite element simulation is used in this paper by assigning the same thermal conductivity to the solids of all samples. Experimental measurements, however, are used to validate the numerical results.

4.1. Finite element simulation

The geometry of a sand sample can be reconstructed from scanned CT images and used to simulate heat transfer in a similar fashion as in [61,62] by numerically solving an elliptic partial differential equation (Eq. (6)), Fourier's law (Eq. (7)) and a continuity equation (Eq. (8)), using COMSOL Multiphysics [63]. The thermal conductivity of the packing are obtained by integrating the heat flux at the top and bottom

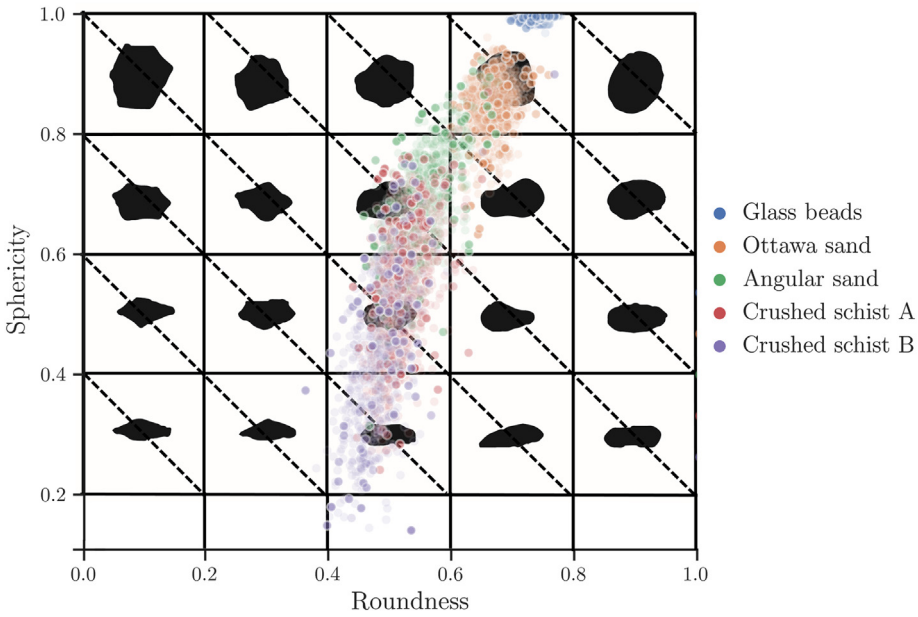

Fig. 13. Irregular particles have lower sphericity and roundness than round particles. Packings assembled by irregular particles have a wider range of sphericity and roundness. The background refers to [61].

boundaries using Eq. (9), and their average is taken as the effective thermal conductivity of the entire sample.

$$\rho C\frac{\partial T}{\partial t}+\rho Cu\cdot\nabla T=\nabla\cdot(\lambda\nabla T) \tag{6}$$

where, for each phase involved in the simulation, ρ is the density (kg/m), C is the heat capacity (J/(kg K)), T is the temperature (K), t is the time (s), u is the velocity vector (m/s), λ is the thermal conductivity (W/(m K)).

$$q=\lambda\nabla T \tag{7}$$

$$-n\left(q_s-q_p\right)=0 \tag{8}$$

where n is the unit normal vector of the solid-pore interface, q_s and q_p are the heat fluxes in the particle and pore, respectively.

The effective thermal conductivity λ_{eff} (W $m^{-1}K^{-1}$) of a sample of horizontal cross-section area A (m^2) is found as:

$$\lambda_{eff}=\frac{\frac{1}{A}\int_A Q_z\,dA}{\frac{T_a-T_b}{L}} \tag{9}$$

where T_a and T_b are the prescribed temperatures at the inlet and outlet boundaries, L (m) is the height of the sample and Q_z (W/m^2) is the vertical heat flux of nodes at the inlet or outlet.

The mesh of the Angular sand is shown in Fig. 11(a) and it was generated in Simpleware ScanIP [64] by setting coarseness as −40 after a mesh size sensitivity analysis showed convergence to an asymptotic value of computed thermal conductivity (analysis not included here). The thermal conductivity of minerals has been suggested to be set between 1 and 8 W/(m K) in the literature [61]. Since the aim of this study is on the effect of particle shape on effective thermal conductivity, 3 W/(m K) [39,65,66] is assigned to solid particles in all samples to mitigate the potential effects of different mineralogy on the effective thermal conductivity. Thermal conductivity of 0.025 W/(m K) [67] and 0.591 W/(m K) [67] is assigned to the void space within the packings for simulating heat transfer in dry and water-saturated granular materials, respectively.[1] The boundary temperature on the top surface is prescribed at 293 K, while at 292 K on the bottom surface to generate a small thermal gradient, other boundaries are considered as insulation as shown in Fig. 11(b). With this material and boundary conditions, the system is numerically solved for temperature distribution and heat fluxes are estimated to then derive an effective thermal conductivity as described in detail in [61].

4.2. Experimental measurements

In order to validate finite element simulating results, the effective thermal conductivity of Ottawa sand, Angular sand and Crushed schist A are measured in the laboratory. Samples are also air-pluviated into a PVC cylindrical container with a diameter of 50 mm and a height of 120 mm to achieve similar homogeneity as shown in the CT images (Fig. 6). The measurements use a 100 mm thermal needle probe (KD2 Pro thermal properties analyser from Decagon Devices, Inc) following ASTM standard D5334–14 [68]. The thermal needle has a diameter of 2.4 mm which is larger than the largest particle diameter, which results in a good accuracy of the measurement at ±10% for 0.2–0.4 W/(mK) [69].

5. Results

5.1. Finite element simulating validation

Four subsamples from each scanned natural sand are extracted to calculate the effective thermal conductivity using the finite element simulation. Fig. 12 shows that the thermal conductivity decreases with porosity, and this trend agrees with the results presented previously by Yun and Santamarina [39] [65] and Narsilio et al. [61]. Fig. 12 also reveals that the numerical values are higher than that from experimental measurements but in an acceptable range [61]. The overestimation may result from the contact condition in both physical testing and numerical

[1] Thermal conductivity of bound water may differ from that of free water, while this effect is negligible in coarse grained packings, it may need to be considered in fine grain packings (e.g., clays).

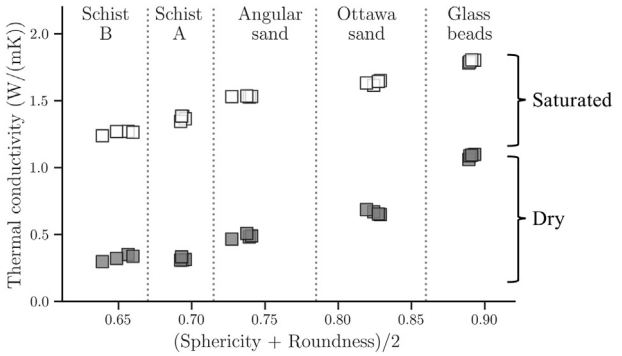

Fig. 14. Effective thermal conductivity increases when the average of sphericity and roundness increases in both dry (grey) and water saturated sands (white).

simulation. The needle probe testing has an accuracy of ±10% [69] and the error of finite element simulation come from its limitation in capturing particle surface roughness and particle geometry irregularity [61].

5.2. Effect of particle shape on thermal conductivity

A sub-sample X-ray CT image stack from each natural sand is selected to extract smooth individual particles using the framework summarised in Fig. 7. The average number of particles in each sub-sample is 150. This number of particles considered sufficiently representative for studies of uniform sands [20]. Within each sub-sample, for each smooth particle in it, its sphericity and roundness are calculated using S2 in Table 1 and Eq. (5). Readers must recall that sphericity (S) and roundness (R) characterise particle shape at two different length scales: the overall form of the particle (S) and local features (i.e., the shape of "edges or corner" in the particle, R) as it can be seen in Fig. 1. Each coloured point in Fig. 13 corresponds to the calculated sphericity and roundness of each particle in the sub-sample assembly of particles. A particle shape chart [70] is also included as a background in Fig. 13 to provide a rough visualisation of the particle geometry. From Fig. 5, we already qualitatively know that the ascending ordering of angularity of the five sands is: Glass beads, Ottawa sand, Angular sand, Crushed schist A and Crushed schist B. In Fig. 13, we can also observe this trend: irregular particles have lower sphericity and roundness than more regular (and round) particles. Moreover, the range of sphericity and roundness in irregular sands have a wider distribution.

After determining sphericity and roundness, their average can be used as a uniformed character of particle shape for the assembly of particles in each sub-sample [27]. The effect of particle shape on effective thermal conductivity can now be analysed with the quantitative particle shape descriptors. In this work, both the thermal conductivity of the five sands in dry and static water saturated conditions are computed as shown in Fig. 14 for five sub-samples of each sand. According to Fig. 14, the effective thermal conductivity increases when the average of sphericity and roundness increases. Furthermore, the trend in dry samples and water saturated samples are similar; however, the rate of increase in dry samples is slightly higher. The difference of the increasing rate may arise from the change in the main heat transfer pathways in the granular materials. As shown in Fig. 11(c), the heat flux in *dry* granular materials is high at the particle contacts which is the main particle scale path for heat transfer in dry granular materials. However, the main heat transfer path in saturated sand is particle-fluid-particle whose contribution to the λ_{eff} is between 39.6% (in saturated Glass beads) and 74.1% (in saturated Crushed schist B). Since the pore space now is filled with water, the λ_{eff} of saturated Crushed shist B is around four times larger than the λ_{eff} of dry Crushed Schist B and larger than the λ_{eff} of dry Glass beads.

5.3. Effect of particle shape on microstructure

Since the inter-particle contact is the main heat transfer pathway in dry granular materials, coordination number and the inter-particle contact area are two microstructure properties believed to have a significant influence on the overall thermal conductivity. Accordingly, we further study the relationship between these two microstructure parameters and particle shape descriptors. After watershed segmentation (step 4 in Fig. 7), coordination number and contact area are calculated, and then the average coordination number and the average contact radius ratio for each microCT-ed sub-samples are calculated as well. The contact radius ratio is defined as the ratio between the radius of contact area and the radius of particles. Fig. 15 shows that both coordination number and contact radius ratio increase with the increase of the average value of sphericity and roundness, except for the Crushed schist B. Particles in the Crushed schist A and the Crushed schist B samples have similar average coordination number but Crushed schist B shows a higher average contact radius ratio, which may be because almost half of the particles in the Crushed schist B sample are platy and elongated (Fig. 13) particles resulting in larger interparticle contact areas. The increase of coordination number in the samples having more regular (round) particle coincide with the increment of λ_{eff} shown in Fig. 14. In general, the increase of contact ratio in more regular particle packings also coincide with the increment of λ_{eff} except for the packings containing very irregular and platy particles. These observations indicate the impact of particle shape represented by the three-dimensional sphericity and roundness on heat transfer in dry granular materials is more

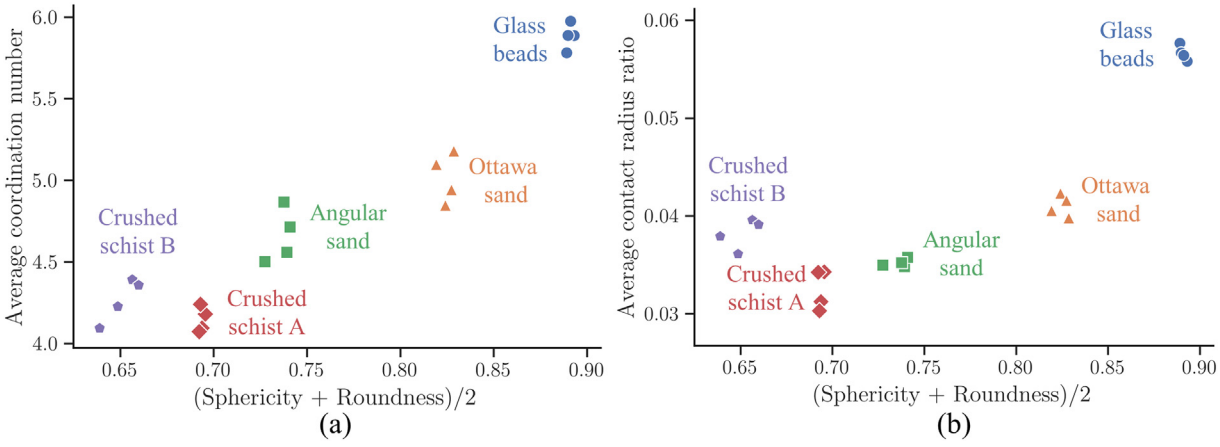

Fig. 15. Average contact radius ratio and average coordination number increase with the increment of the mean value of sphericity and roundness. (a) Average contact radius ratio and (b) Average coordination number.

originated from its influence on the inter-particle contact number than on contact ratio (contact area).

6. Conclusion

This study develops a method to calculate three-dimensional (3D) sphericity and roundness of individual particles in a specimen while preserving its internal structure. By comparing the existing definitions of 3D sphericity, a combination of sphericity and roundness is used to characterise particle shape. Sphericity and roundness are required to be calculated on a smooth particle surface which is achieved using a proposed framework including CT techniques, imaging techniques and the Tabuin smoothing method. The reliability of the smoothing framework is presented by its application to voxel-constructed sphere, ellipsoid, Ottawa sand particle and Angular sand particle.

By calculating the sphericity and roundness of individual particles in five natural sands, we found that irregular particles tend to show lower sphericity and roundness than more regular (and round) particles, and granular packings formed by irregular particles show a wider range of sphericity and roundness. Moreover, after estimating the thermal conductivity of the natural sands, we observed that granular materials with a higher average value of sphericity and roundness show a tendency to boost higher thermal conductivity. This is because we also found that lower average value of sphericity and roundness may lead to lower average coordination number and contact radius ratio, important parameters governing heat transfer at the particle scale. Granular assemblies containing more platy particles may exhibit higher average contact radius ratio compared to other assemblies with the same average coordination number. The five materials in this paper have different friction coefficients, the effect of the friction coefficient on the coordination number and contact ratio requires to be quantified in future work.

Acknowledgements

The authors acknowledge Yu Zhou for taking micro-photos of the sands. The CT images were obtained using the Imaging and Medical Beam Line (IMBL) at the Australian Synchrotron, Victoria, Australia. We acknowledge Dr. Anton Maksimenko and the other beam scientists at Australian Synchrotron for their support during our experiments. This work is supported by the Melbourne Research Scholarship from The University of Melbourne.

References

[1] A.E. Bergles, J. Collier, J.M. Delhaye, G. Hewitt, F. Mayinger, Two-Phase Flow and Heat Transfer in the Power and Process Industries, Hemisphere, New York, 1981.
[2] W.B. Fei, Q. Li, X.C. Wei, R.R. Song, M. Jing, X.C. Li, Interaction analysis for CO2 geological storage and underground coal mining in Ordos Basin, China, Eng. Geol. 196 (2015) 194–209.
[3] D.M. Scott, D.K. Das, V. Subbaihaannadurai, V.A. Kamath, A computational scheme for fluid flow and heat transfer analysis in porous media for recovery of oil and gas, Pet. Sci. Technol. 23 (2005) 843–862.
[4] W.M. Rohsenow, J.P. Hartnett, E.N. Ganic, Handbook of Heat Transfer Applications, McGraw-hill book co., New York, 1985 973 No Individual Items Are Abstracted in this Volume., (1985).
[5] U. El Shamy, O. De Leon, R. Wells, Discrete element method study on effect of shear-induced anisotropy on thermal conductivity of granular soils, Int. J. Geomech. 13 (2013) 57–64.
[6] Y. Hu, J. Wang, J. Yang, I. Mudawar, Q. Wang, Experimental study of forced convective heat transfer in grille-particle composite packed beds, Int. J. Heat Mass Transf. 129 (2019) 103–112.
[7] J. Santamarina, G.-C. Cho, Soil Behaviour: the role of particle shape, Advances in Geotechnical Engineering: The Skempton Conference, Citeseer 2004, pp. 604–617.
[8] I. Cavarretta, M. Coop, C. O'Sullivan, The Influence of Particle Characteristics on the Behaviour of Coarse Grained Soils, 2010.
[9] H. Shin, J. Santamarina, Role of particle angularity on the mechanical behavior of granular mixtures, J. Geotech. Geoenviron. 139 (2012) 353–355.
[10] T. Afshar, M.M. Disfani, A. Arulrajah, G.A. Narsilio, S. Emam, Impact of particle shape on breakage of recycled construction and demolition aggregates, Powder Technol. 308 (2017) 1–12.
[11] A.B. Göktepe, A. Sezer, Effect of particle shape on density and permeability of sands, Proc. Inst. Civ. Eng. Geotech. Eng. 163 (2010) 307–320.
[12] X. Garcia, L.T. Akanji, M.J. Blunt, S.K. Matthai, J.P. Latham, Numerical study of the effects of particle shape and polydispersity on permeability, Phys. Rev. E 80 (2009), 021304.
[13] A.F. Cabalar, N. Akbulut, Evaluation of actual and estimated hydraulic conductivity of sands with different gradation and shape, SpringerPlus 5 (2016) 820.
[14] A. Banala, H. Ma, A. Kumar, Influence of particulate geometry on permeability of porous materials, Powder Technol. 345 (2019) 704–716.
[15] C. Lee, H.S. Suh, B. Yoon, T.S. Yun, Particle shape effect on thermal conductivity and shear wave velocity in sands, Acta Geotech. 12 (2017) 615–625.
[16] Y.F. Chen, M. Wang, S. Zhou, R. Hu, C.B. Zhou, An effective thermal conductivity model for unsaturated compacted bentonites with consideration of bimodal shape of pore size distribution, Sci. China Technol. Sci. 58 (2015) 369–380.
[17] J. Gan, Z. Zhou, A. Yu, Effect of particle shape and size on effective thermal conductivity of packed beds, Powder Technol. 311 (2017) 157–166.
[18] A.S. Cherkasova, J.W. Shan, Particle aspect-ratio effects on the thermal conductivity of micro-and nanoparticle suspensions, J. Heat Transf. 130 (2008), 082406.
[19] G. Landini, Advanced shape analysis with ImageJ, Proceedings of the Second ImageJ User and Developer Conference, Luxembourg 2008, pp. 6–7.
[20] M.R. Cox, M. Budhu, A practical approach to grain shape quantification, Eng. Geol. 96 (2008) 1–16.
[21] H. Gerhardter, R. Prieler, C. Schluckner, M. Knoll, C. Hochenauer, M. Mühlböck, P. Tomazic, H. Schroettner, Modelling convective heat transfer to non-spherical particles, Powder Technol. 343 (2019) 245–254.
[22] R.L. Hamilton, O. Crosser, Thermal conductivity of heterogeneous two-component systems, Ind. Eng. Chem. Fundam. 1 (1962) 187–191.
[23] L. Verma, A. Shrotriya, R. Singh, D. Chaudhary, Thermal conduction in two-phase materials with spherical and non-spherical inclusions, J. Phys. D 24 (1991) 1729.
[24] H. Wadell, Volume, shape, and roundness of rock particles, J. Geol. 40 (1932) 443–451.
[25] S. Zhao, N. Zhang, X. Zhou, L. Zhang, Particle shape effects on fabric of granular random packing, Powder Technol. 310 (2017) 175–186.
[26] D. Legland, I. Arganda-Carreras, P. Andrey, MorphoLibJ: integrated library and plugins for mathematical morphology with ImageJ, Bioinformatics 32 (2016) 3532–3534.
[27] G. Cho, J. Dodds, J. Santamarina, Particle Shape Effects on Packing Density, Stiffness and Strength of Natural and Crushed Sands-Internal Report, Georgia Institute of Technology, 2006 (33pp).
[28] R.D. Hryciw, J. Zheng, K. Shetler, Particle roundness and sphericity from images of assemblies by chart estimates and computer methods, J. Geotech. Geoenviron. 142 (2016), 04016038.
[29] E.D. Sneed, R.L. Folk, Pebbles in the lower Colorado River, Texas a study in particle morphogenesis, J. Geol. 66 (1958) 114–150.
[30] J.D. Frost, C.-T. Yang, Effect of end platens on microstructure evolution in dilatant specimens, Soils Found. 43 (2003) 1–11.
[31] L. Wang, J. Frost, J. Lai, Three-dimensional digital representation of granular material microstructure from X-ray tomography imaging, J. Comput. Civ. Eng. 18 (2004) 28–35.
[32] V. Cnudde, B. Masschaele, M. Dierick, J. Vlassenbroeck, L. Van Hoorebeke, P. Jacobs, Recent progress in X-ray CT as a geosciences tool, Appl. Geochem. 21 (2006) 826–832.
[33] J. Neumann, J.-W. Simon, S. Reese, Digital sieving of irregular 3D particles—a study using XRCT and statistically similar synthetic data, Powder Technol. 338 (2018) 1001–1015.
[34] F. Cernuschi, C. Rothleitner, S. Clausen, U. Neuschaefer-Rube, J. Illemann, L. Lorenzoni, C. Guardamagna, H.E. Larsen, Accurate particle speed prediction by improved particle speed measurement and 3-dimensional particle size and shape characterization technique, Powder Technol. 318 (2017) 95–109.
[35] Y. Lu, S. Xiao, Z. Ge, Z. Zhou, Y. Ling, L. Wang, Experimental study on rock-breaking performance of water jets generated by self-rotatory bit and rock failure mechanism, Powder Technol. 346 (2019) 203–216.
[36] G. Bagheri, C. Bonadonna, On the drag of freely falling non-spherical particles, Powder Technol. 301 (2016) 526–544.
[37] M. Aboufoul, A. Chiarelli, I. Triguero, A. Garcia, Virtual porous materials to predict the air void topology and hydraulic conductivity of asphalt roads, Powder Technol. 352 (2019) 294–304.
[38] J. Fonseca, C. O'Sullivan, M.R. Coop, P. Lee, Non-invasive characterization of particle morphology of natural sands, Soils Found. 52 (2012) 712–722.
[39] T.S. Yun, J.C. Santamarina, Fundamental study of thermal conduction in dry soils, Granul. Matter 10 (2008) 197.
[40] B. Zhao, J. Wang, M. Coop, G. Viggiani, M. Jiang, An investigation of single sand particle fracture using X-ray micro-tomography, Géotechnique 65 (2015) 625–641.
[41] B. Zhou, J. Wang, H. Wang, Three-dimensional sphericity, roundness and fractal dimension of sand particles, Géotechnique 68 (2017) 18–30.
[42] G. Kerckhofs, G. Pyka, M. Moesen, J. Schrooten, M. Wevers, High-Resolution Micro-CT as a Tool for 3D Surface Roughness Measurement of 3D Additive Manufactured Porous Structures, iCT Conf, 2012 77–83.
[43] J. Schindelin, I. Arganda-Carreras, E. Frise, V. Kaynig, M. Longair, T. Pietzsch, S. Preibisch, C. Rueden, S. Saalfeld, B. Schmid, Fiji: an open-source platform for biological-image analysis, Nat. Methods 9 (2012) 676.
[44] M.d. Carmo, Differential geometry of curves and surfaces, in: F. Rehsteiner, H.J. Rewker (Eds.), Collision Free Five Axis Milling of Twisted Ruled Surface, vol. 42, Prentice-Hall, Englewood Cliffs, New Jersey 1976, pp. 457–461 , Ann. CIRP. (1993).

[45] P. Cignoni, M. Callieri, M. Corsini, M. Dellepiane, F. Ganovelli, G. Ranzuglia, Meshlab: an open-source mesh processing tool, Eurographics Italian Chapter Conference 2008, pp. 129–136.
[46] ASTM, C778–17 Standard Specification for Standard Sand, ASTM International, West Conshohocken, PA, 2017.
[47] N. Zhang, X. Yu, A. Pradhan, A.J. Puppala, Thermal conductivity of quartz sands by thermo-time domain reflectometry probe and model prediction, J. Mater. Civ. Eng. 27 (2015), 04015059.
[48] K.K. Neuendorf, J.P. Mehl Jr., J.A. Jackson, Glossary of Geology, American Geological Institute, Alexandria, Virginia, 2005.
[49] A. VandenBerg, The Tasman Fold Belt System in Victoria: Geology and Mineralisation of Proterozoic to Carboniferous Rocks, Geological Survey of Victoria, 2000.
[50] M. Wiebicke, E. Andò, I. Herle, G. Viggiani, On the metrology of interparticle contacts in sand from x-ray tomography images, Meas. Sci. Technol. 28 (2017), 124007.
[51] P. Iassonov, T. Gebrenegus, M. Tuller, Segmentation of X-ray computed tomography images of porous materials: a crucial step for characterization and quantitative analysis of pore structures, Water Resour. Res. 45 (2009).
[52] N. Otsu, A threshold selection method from gray-level histograms, IEEE Trans. Syst., Man, Cybern. 9 (1979) 62–66.
[53] S. Schlüter, A. Sheppard, K. Brown, D. Wildenschild, Image processing of multiphase images obtained via X-ray microtomography: a review, Water Resour. Res. 50 (2014) 3615–3639.
[54] Z. Karatza, E. Andò, S. Papanicolopulos, J. Ooi, G. Viggiani, Evolution of deformation and breakage in sand studied using X-ray tomography, Géotechnique (1) (2018) 1–11.
[55] H. Taylor, C. O'Sullivan, W. Sim, A new method to identify void constrictions in micro-CT images of sand, Comput. Geotech. 69 (2015) 279–290.
[56] G. Taubin, Curve and surface smoothing without shrinkage, computer vision, Proceedings., Fifth International Conference on, IEEE, 1995 1995, pp. 852–857.
[57] A.G. Belyaev, Y. Ohtake, K. Abe, Detection of Ridges and Ravines on Range Images and Triangular Meshes, Vision Geometry IX, International Society for Optics and Photonics, 2000 146–155.
[58] Y. Ohtake, A. Belyaev, I. Bogaevski, Mesh regularization and adaptive smoothing, Comput. Aided Des. 33 (2001) 789–800.
[59] Y. Belyaev, H. Seidel, Mesh Smoothing by Adaptive and Anisotropic Gaussian Filter Applied to Mesh Normals, Vision, Modeling, and Visualization, 2002 203–210.
[60] V. Tarnawski, T. Momose, W. Leong, Assessing the impact of quartz content on the prediction of soil thermal conductivity, Geotechnique 59 (2009) 331–338.
[61] G.A. Narsilio, J. Kress, T.S. Yun, Characterisation of conduction phenomena in soils at the particle-scale: finite element analyses in conjunction with synthetic 3D imaging, Comput. Geotech. 37 (2010) 828–836.
[62] G.A. Narsilio, O. Buzzi, S. Fityus, T.S. Yun, D.W. Smith, Upscaling of Navier–Stokes equations in porous media: theoretical, numerical and experimental approach, Comput. Geotech. 36 (2009) 1200–1206.
[63] C. AB, COMSOL Multiphysics v5.0, http://www.comsol.com 2015.
[64] S. Ltd., Simpleware ScanIP, http://www.simpleware.com/software/scanip , date of access, 15 2015 12.
[65] T.S. Yun, T.M. Evans, Three-dimensional random network model for thermal conductivity in particulate materials, Comput. Geotech. 37 (2010) 991–998.
[66] J. Sundberg, P.-E. Back, L.O. Ericsson, J. Wrafter, Estimation of thermal conductivity and its spatial variability in igneous rocks from in situ density logging, Int. J. Rock Mech. Min. Sci. 46 (2009) 1023–1028.
[67] H.D. Young, R.A. Freedman, T. Sandin, A.L. Ford, University Physics, Addison-Wesley, Reading, MA, 1996.
[68] ASTM D5334–14, Standard Test Method for Determination of Thermal Conductivity of Soil and Soft Rock by Thermal Needle Probe Procedure, ASTM International, West Conshohocken, PA, 2014.
[69] T. Brandon, J. Mitchell, Factors influencing thermal resistivity of sands, J. Geotech. Eng. 115 (1990) 1683–1698.
[70] W.C. Krumbein, L.L. Sloss, Stratigraphy and Sedimentation, 1963.

3.3 IMPACT OF PARTICLE SHAPE ON COORDINATION NUMBER

Type of paper: letter (Journal of Geotechnical and Geoenvironmental Engineering – Technical Note)
Date text written: January 2020
Date text revised: April 2020
Number of words in main text and tables = 2712
Number of figures = 6
Number of tables = 1

Impact of three-dimensional sphericity and roundness on coordination number

Author 1
Wenbin Fei, PhD student, ME, BE
Department of Infrastructure Engineering, The University of Melbourne, Parkville, Australia
ORCID: 0000-0002-9275-8403

Author 2
Guillermo A. Narsilio□, PhD, MSc (Math), MSc (CE), CEng
Department of Infrastructure Engineering, The University of Melbourne, Parkville, Australia
ORCID: 0000-0003-1219-5661

Full contact details of corresponding author
Guillermo A. Narsilio, Associate Professor in Geotechnical Engineering
Engineering Block B 208, Department of Infrastructure Engineering, The University of Melbourne, Parkville, VIC 3010, Australia
Email: narsilio@unimelb.edu.au, Phone: +61 (3) 8344 4659, Fax: +61 (3) 8344 4616

ABSTRACT

Coordination number (CN) is a fundamental micro-scale variable in soils affecting the macroscale parameters of the material such as porosity, stiffness under loading and stability under hydraulic gradients. However, most studies on CN have focused on sphere or ellipsoid packings using discrete element method (DEM). By means of computed tomography (CT) and image processing techniques, this work rigorously computes the three-dimensional sphericity and roundness of each grain in five sands and investigates the impact of particle shape on CN. The results show that the average coordination number (CN_{ave}) of *different* sands and the CN of grains *within a given* sand may be impacted differently by particle shape. For a given equivalent diameter of a given sand, more irregular grain packings show a subtle higher CN, this change in CN increases with increasing grain size. However, air-pluviated irregular particle packings with poor gradation may exhibit lower average CN_{ave} because of particle orientational alignment, particle interlocking and surface roughness.

KEYWORDS: particle-scale behaviour; fabric/structure of soils; sands

INTRODUCTION

Coordination number (CN) quantifies how many neighbouring particles surround a given particle in a granular material. The *average* coordination number (CN_{ave}) of a soil affects the macroscale behaviour and characterising parameters of the assembly. Shear-wave velocity in sandstones can be estimated using CN_{ave} (Wang et al. 2019). The internal stability of a material under compaction or seepage force can also be indicated by CN_{ave}. Triaxial compression tests revealed that higher shear stiffness was attributed to higher CN_{ave} in sands (Fonseca et al. 2013). Hence, materials with high CN_{ave} can be used to minimise particle breakage in pavements (Minh and Cheng 2013). The stability of an embankment filter may decrease as CN_{ave} reduces monotonically in both sphere packings (Shire and O'Sullivan 2013) and real sands (Fonseca et al. 2014). As CN_{ave} shows great importance, a study of how it is affected by particle geometry (e.g. shape, gradation, friction, cohesiveness) is necessary because these geometrical attributes may guide the material selection in engineering applications.

CN_{ave} generally increases with the particle size in non-uniform sphere packings (Minh and Cheng 2013). A better gradation can also increase the CN_{ave} in sphere packings (Minh and Cheng 2013). In the discrete element method (DEM) study of packings of super-ellipsoids that can be represented by Equation 1 (i.e., oblate and prolate spheroids), the correlation between CN_{ave} and aspect ratio (aspect ratio is 'c' in Equation 1 after setting 'a' = 'b' = 1) shows an 'M' shape (Delaney and Cleary 2010; Donev et al. 2004; Gan et al. 2017; Zhou et al. 2011) with the lowest CN_{ave} found at an aspect ratio of 1 (a sphere packing always has the lowest CN_{ave}). Additionally, the CN_{ave} reduces when ` shape parameter 'm' changes from 3 to 5 (in Equation 1, increasing 'm' from 2 make a sphere more cubic-like in shape) (Delaney and Cleary 2010) because of high particle orientational alignment:

$$\left(\frac{x}{a}\right)^m + \left(\frac{y}{b}\right)^m + \left(\frac{z}{c}\right)^m = 1 \quad (1)$$

where m is a shape parameter. a, b and c are principal axis lengths.

Similar results were found by Zhao et al. (2017) who used blockiness (defined as '$1/m$') to create virtual particle assemblies in DEM. They also found that a high packing density does

not necessarily correspond to high CN_{ave}, cubic-like particle packings with high particle orientational alignment may have high packing density but low CN_{ave}.

Even though DEM enables studying the effects of particle shape on CN_{ave}, the particle shape indicators (aspect ratio) cannot cover the whole range of particle shapes encountered in natural sands as discussed by Fei et al. (2019).

X-ray computed tomography (CT) sheds lights onto the analysis of microstructure (Druckrey et al. 2017; Fei et al. 2019; Nadimi et al.) in irregular natural sands and makes calculating three-dimensional (3D) sphericity and roundness of each grain in the sands possible. The present work selected five sands and rigorously quantified the particle size, 3D sphericity and roundness, CN of each grain in the sand and the CN_{ave} of each sand from CT images. This work aims to bridge the gap between the particle shape, CN of each grain and CN_{ave} in the real sands.

Materials

As shown in Fig. 1, five natural sands with distinct grain shape but similar diameter (D_{50}) were selected. 'Glass beads' are nearly spheres made of silica with silver coats. 'Ottawa sand' (ASTM 2017) particles are more irregular than that of glass beads but still have relatively round corners. Similar to Ottawa sand, grains in 'angular sand' are made of quartz but with sharp corners. 'Crushed schist A' has even more irregular particles which are made of chlorites. Grains in 'crushed schist B' consist of both quartz and biotite, have the most irregular shape and more than half of them are elongated and platy. The D_{50}, the particle size range and the sorting index SI (the ratio of standard deviation to the equivalent mean particle size, as defined by Ahmed and Lebedev (2019)) of these sands are summarised in Table 1. A soil with lower SI means that it is well sorted but poorly graded. Please note that these parameters were calculated using four representative element volumes (REVs) with dimensions of 4.5×4.5×4.5 mm and were chosen from top-left, top-right, bottom-left and bottom-right regions of each sample. The number of particles in a single REV excluding the particles on the border is also shown in Table 1.

<Fig. 1 around here>

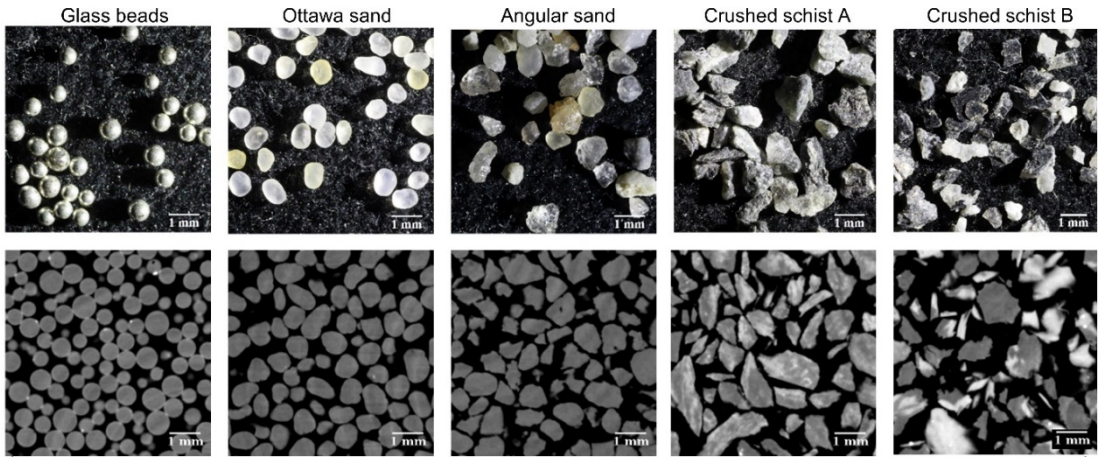

Fig. 1. Five sands with distinct particle shape. The pictures in the top row were photographed while the images in bottom row were CT scanned with a pixel size of 13 µm.

<Table 1 around here>

Table 1 Particle size and sorting index (SI) of the studied granular materials

Sample	D_{50} (mm) *	D_{50} (mm)^	Particle size range (mm) *	Particle size range (mm) ^	*SI*	Number of particles in a REV^
Glass beads	0.60	0.60	0.50 – 0.70	0.40 - 0.80	0.14	270
Ottawa sand	0.73	0.76	0.60 – 0.85	0.58 - 0.94	0.22	118
Angular sand	0.89	0.68	0.60 – 1.18	0.39 – 0.99	0.22	100
Crushed schist rock A	0.84	0.58	0.50 – 1.18	0.23 – 0.95	0.36	119
Crushed schist rock B	0.84	0.61	0.50 – 1.18	0.16 - 1.10	0.28	94

* Diameter from sieve analysis.
^ Equivalent ball diameter calculated from particle volume after CT reconstruction.

Methods

The five sands are air-pluviated into relatively small PVC containers and scanned at the Australian Synchrotron to then extract particle shape and CN.

To date, various particle shape descriptors using different definitions have been proposed to characterise particles (Cho et al. 2006; Hryciw et al. 2016; Legland et al. 2016; Sneed and Folk 1958; Wadell 1932). Some two-dimensional (2D) descriptors were compared against 3D (true) descriptors in (Rorato et al. 2019). Upon a critical assessment and comparison of the existing definitions of particle shape descriptors, Fei et al. (2019) suggested that the

combination of 3D sphericity (S in Equation 2) and roundness (R in Equation 3) can capture the shape of most irregular particles reasonably well:

$$S = \frac{36\pi V^2}{\mathrm{SA}^3} \tag{2}$$

$$R = \frac{\sum r_i/N}{r_{max-in}} \tag{3}$$

where V is the particle volume, SA is the particle surface area, r_i is the radius of each one out of N corners in a particle and r_{max-in} is the radius of the maximum inscribed sphere of a particle. These variables and the CN of each grain in the packings are obtained following the procedures detailed in (Fei et al. 2019) with some corrections as outlined next.

The isolation of individual grains from CT images is required to calculate their geometrical features. This is a non-trivial task given that grains in natural sands are in contact each other, thus the framework shown in Fig. 2 was proposed to reconstruct individual particles. Particle surface area SA and volume V are required to calculate sphericity S in Equation 2, whereas curvature $1/r_i$ in Equation 3 needs to be computed for roundness R. Pixel-counting with the saw-tooth particle surface (Fig. 2(e)) may result in overestimation of particle surface area and volume as well as incorrect roundness. Hence, the framework used here also includes a step to generate a smooth particle surface for more accurate estimations of sphericity and roundness from CT images.

Each sand was air-pluviated into a PVC cylinder (d = 50 mm, h = 120 mm) and scanned at the Australian Synchrotron to achieve sequential CT images with a pixel size of 13 μm (related to image resolution). The selection of sample size and pixel size is a trade-off, noting that images with a small pixel size (i.e., higher image resolution) can be used to identify more accurate interparticle contact area (Persson et al. 2004; Wiebicke et al. 2017) but does not significantly affect CN. CT images (Fig. 2(a)) with a REV of 4.5×4.5×4.5 mm (Fig. 2(b)) were firstly denoised by applying a median filter and a non-local mean filter in Fiji (Schindelin et al. 2012). These filters do not blur the images and keep the particle edge/boundary sharp. Applying the filters may comparatively smooth the particle surface but cause subtle loss of contacts formed by angular edges (Ahmed and Lebedev, 2019). The post-processed results

were shown in Fig. 1. Next, the widely used Otsu threshold segmentation (Otsu 1979) was applied to binarize the solid and void phases (Fig. 2(c)). A plugin named MorphoLibJ (Legland et al. 2016) in Fiji (Schindelin et al. 2012) was employed to execute watershed segmentation on solids (Fig. 2(d)) and obtain individual voxelated particles (Fig. 2(e)). Six-voxel neighbourhood was selected in the watershed segmentation to reduce the overestimation of particle surface area and volume (Fonseca et al. 2012). At last, the saw-tooth surface of the voxelated particles was smoothed by using the Taubin smoothing method (Taubin 1995). Taubin smoothing method includes two parameters λ and μ to control shrinkage and inflation, respectively. Here λ = 0.6 and μ = -0.3 were determined after calibrating the particle surface area and volume of CT reconstructed sphere and ellipsoid against theoretical values, following (Fei et al. 2019).

An in-house program (Fei et al. 2019) was used to identify the interparticle contact by searching the shared boundary voxels between particles. The number of interparticle contacts was then used to calculate the CN of each grain and the CN_{ave} of each sample of the sands.

<Fig. 2 around here>

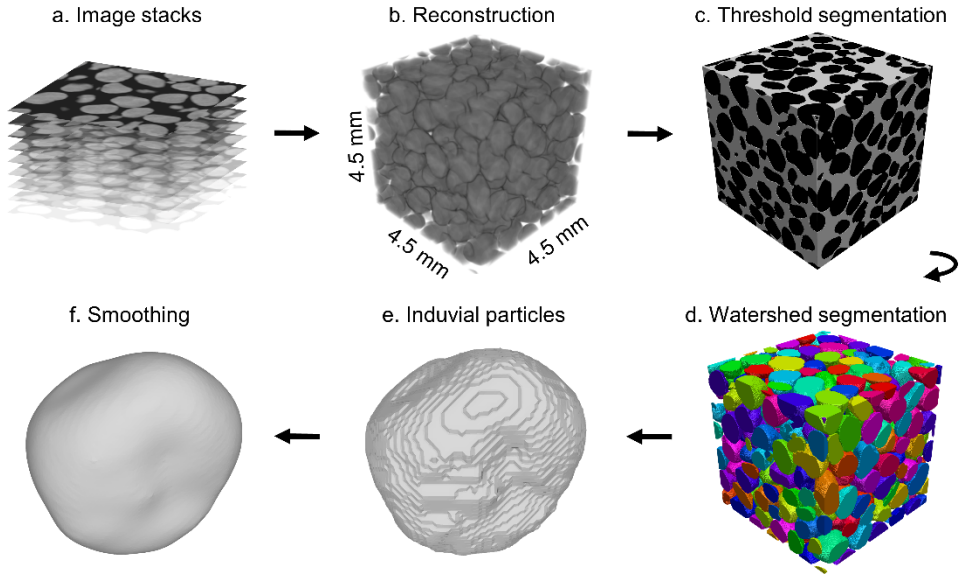

Fig. 2. Procedures to achieve individual particles of Ottawa sand from CT images

RESULTS AND DISCUSSION

For each sand, four subsamples from top-left, top-right, bottom-left and bottom-right regions of each sample were selected to calculate the CN and particle shape characteristics of every sand grain. The distributions of CN for the four subsamples from each material are shown in Fig. 3. It is clear from the fitted normal distribution curves that the CN_{ave} in the round glass beads is about 7. As glass bead size is not uniform, the maximum CN of a glass bead is 13 (slightly higher than in mono-dispersed Face Centred Cubic (FCC) sphere packings). The CN_{ave} then decreases to 5.3 and 5.7 in crushed schist A and B. The maximum CN in the very irregular crushed schist B is above 14 which is possible even for ellipsoids having strong friction (Donev et al. 2004). Besides particle shape, gradation also varies in all five sands according to the SI shown in Table 1. Hence, well-graded but more irregular particle packings may have lower CN_{ave} in real sands in contrast with the findings that better gradation can increase the CN_{ave} in sphere packings (Minh and Cheng 2013). Fig. 3 shows that an irregular particle (e.g., crushed schist) may have higher CN than a round particle (e.g., Ottawa sand), this is true when one focuses on single grains. The effect of particle shape on average value of coordination number of a grain packing may be different from its effect on the coordination number of a single grain.

<Fig. 3 around here>

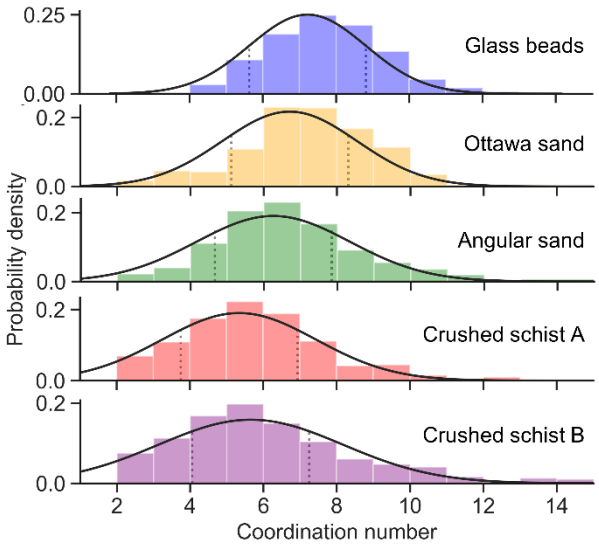

Fig. 3. Distribution of coordination number and fitted normal distribution curve. The coordination number at the crest of the normal distribution curve is CN_{ave}. The vertical dotted lines show the limits of two standard deviations around CN_{ave}.

To further quantify the impact of particle shape on coordination number, Fig. 4 shows the computed 3D sphericity and roundness of each grain in the five sands and their probability distributions. Note that DEM studies typically use aspect ratio, a more straightforward parameter for ellipsoids than sphericity and roundness. Both sphericity and roundness range between 0 and 1. It is noticeable that the glass beads are not perfect spheres and the bright dots in the CT images of glass beads (Fig. 1) resulting from their silver coats could lead to the defects in reconstructed surface mesh and artifical low roundness in some particles. The average sphericity and roundness decrease from round glass beads to irregular crushed schist B, which indicates that these descriptors capture well their particle shape. Excluding the glass beads, sphericity shows a larger range than roundness and the range of sphericity expands gradually from glass beads to crushed schist B.

<Fig. 4 around here>

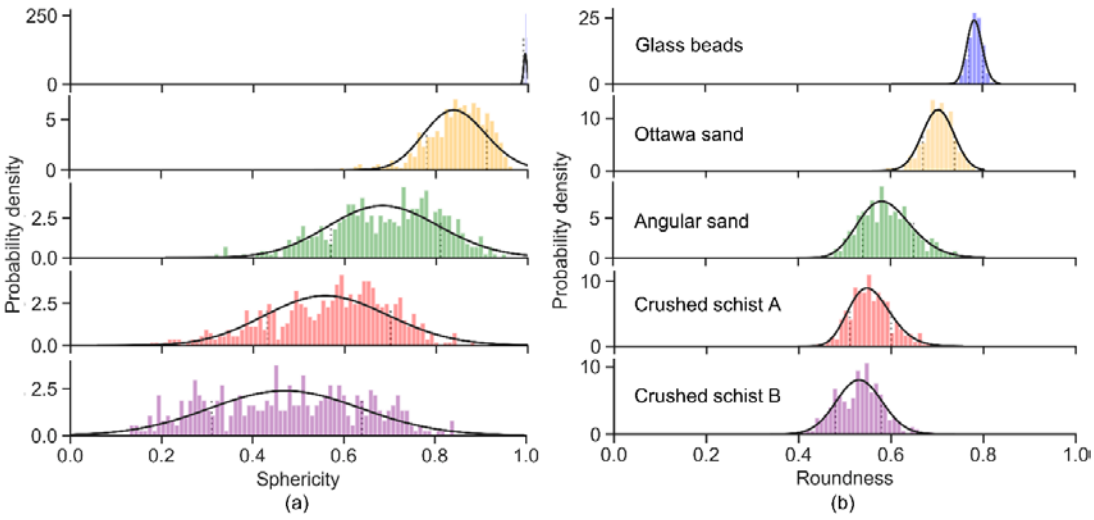

Fig. 4. Distribution of sphericity (a) and roundness (b) with fitted normal distribution curves. The vertical dot lines show the limits of two standard deviations around the average.

Since DEM studies set the ellipsoids having the same equivalent diameter, we also computed the equivalent diameter from the particle volume V in Equation 2. For a clearer visualisation, particles from only one of four REVs of each specimen were used to show the relationship between equivalent diameter, the average of 3D sphericity and roundness, and CN of each grain in Fig. 5. The averaging of sphericity and roundness was proposed by Cho et al. (2006) based on the commonly used particle shape chart (Krumbein and Sloss 1963), and selected here since sphericity and roundness show similar trends to each other in Fig. 4. The red data points at the right of Fig. 5(a) shows larger CN because the grains have a larger equivalent diameter (Fonseca et al. 2014). This trend can also be clearly observed in each material from Fig. 5(b) – (f). Within a certain soil such as angular sand (Fig. 5(d)), the increasing trend is not only observed from left to right but also from top to bottom. This trend indicates that a more irregular large grain may exhibit higher CN in a given sand. For a given equivalent diameter, a subtle increase in the CN of more irregular grains can also be seen along the dashed line in each sand, which is the same as the trend reported in DEM based papers (Delaney and Cleary 2010; Donev et al. 2004; Gan et al. 2017; Zhou et al. 2011) but different from the decreasing trend of CN_{ave} in more irregular sand packings as shown in Fig. 3.

<Fig. 5 around here>

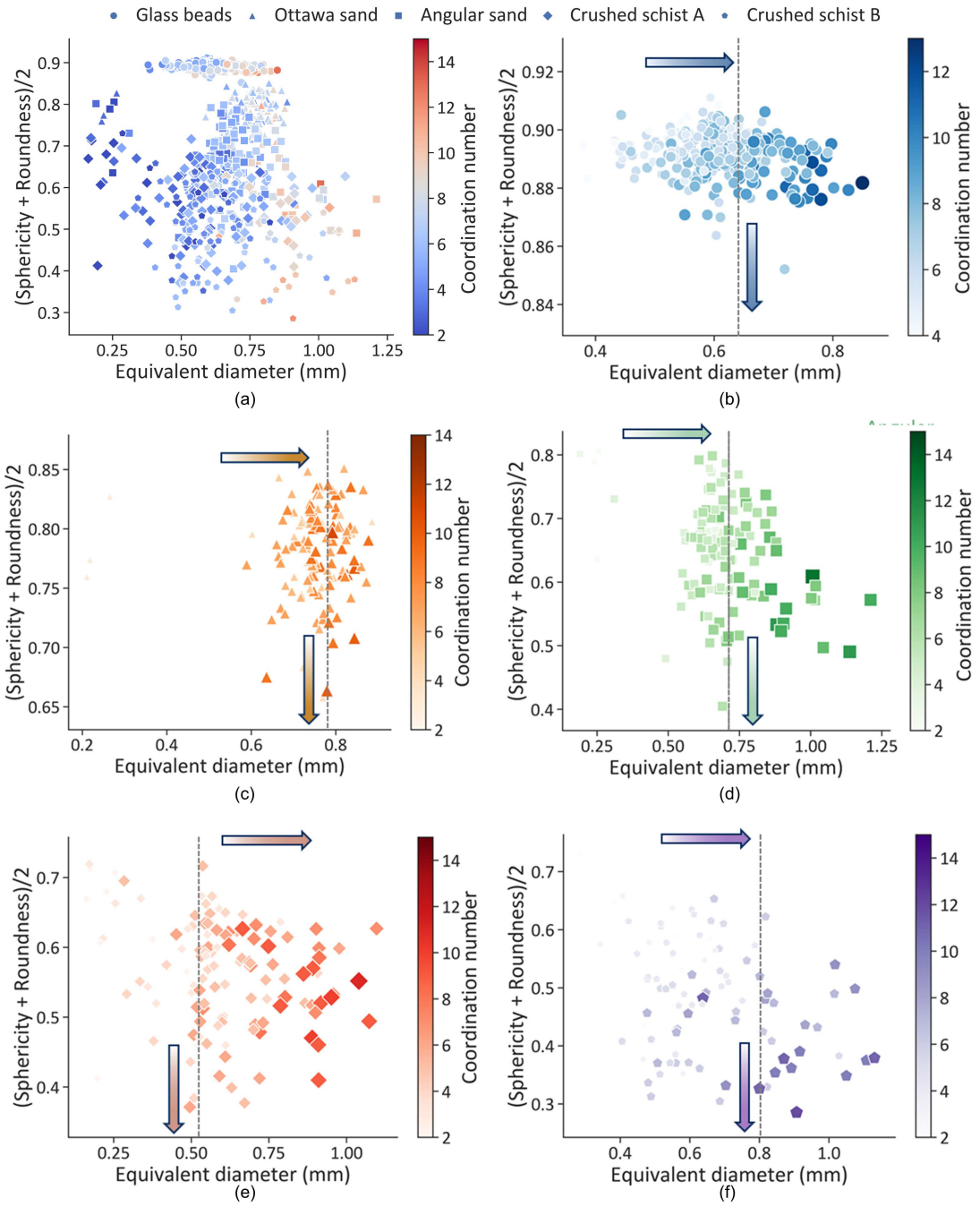

Fig. 5. A subsample from each material are selected. For each grain, its particle shape is plotted against equivalent diameter and rendered by coordination number. Grains from (a) combined five sands, (b) glass beads, (c) Ottawa sand, (d) angular sand, (e) crushed schist A, (f) crushed schist B.

A qualitative explanation for these observations can be rooted in the micro-structural arrangement of particles in a packing and the inherent (reasonable) assumptions used in DEM modelling. CN is known to be related to the particle rolling and sliding when packing particles together under gravity (Delaney and Cleary 2010; Donev et al. 2004). DEM studies show that ellipsoid packings have higher CN_{ave} than that in sphere packings because an ellipsoid has more rotational degrees of freedom to be restricted than a sphere in sphere packings (Delaney and Cleary 2010; Donev et al. 2004; Gan et al. 2017; Zhou et al. 2011) as shown in Fig. 6 (a) and (b). Let us illustrate this by focusing on the degree of freedom on the two-dimensional planes in Fig. 6 (a) and (b): the central 'spherical' particle cannot move when it is in contact with other three spherical particles. In contrast, an 'ellipsoidal' particle restricted by three other ellipsoids can still rotate and have more neighbours to contact, resulting in a higher CN for itself. 3D CT reconstructed geometry of each sand is also visualised in Fig. 6 (c) – (g) to compare the particle arrangement. In the angular sand (Fig. 6 (e)), particle No.0 is jammed by only two particles. In the more irregular crushed schist B (Fig. 6 (g)), the platy particle No. 0 can be supported stably by a single particle No. 1. Hence, the orientational alignment of the irregular particles results in a low CN_{ave} even though the single irregular particle has the possibility of high individual CN. Additionally, the concave surface on irregular particles may induce interlocking so that a particle cannot move even when touching fewer particles (Fig. 6 (f)). In addition, the irregular particle may also exhibit higher roughness (another particle shape descriptor at a smaller scale than sphericity and roundness). Higher roughness is related to a higher coefficient of friction which resists the rotation and sliding of particles during gravity deposition and shear loading. However, DEM simulations usually set sliding and rolling friction coefficient the same for all the particles in the assembly and also generally assumes that particles with different particle shape have the same Young's modulus (which may be different in reality). Furthermore, the detection of CN in DEM is sensitive in the selection of a critical separation distance (Zhou et al. 2011) which is also assumed as the same for all the particles. These limitations may be the cause of the contrasting observations made in this paper.

<Fig. 6 around here>

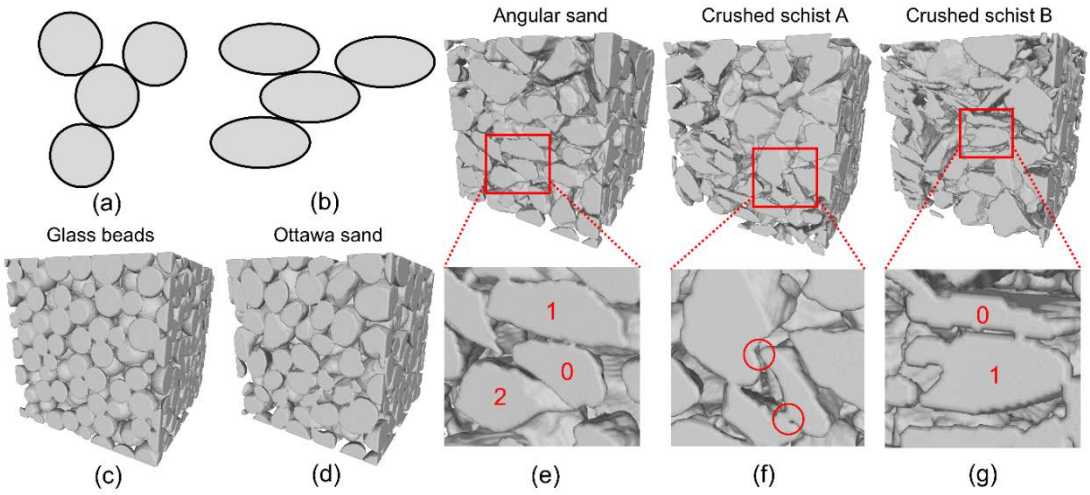

Fig. 6. Schematic sphere packings (a) and ellipsoid assembly (b), and CT reconstructed glass beads (c), Ottawa sand (d), angular sand (e), crushed schist A (f) and crushed schist B (g).

CONCLUSIONS

This study investigates the impact of particle shape on coordination number in real sands with the help of computed tomography (CT) and image processing techniques. In a given sand, a more irregular grain has subtle higher *individual* coordination number (CN) and the CN of the grain increases with increasing particle size. However, the trend may be different when comparing the *average* coordination number (CN_{ave}) in different sands. An air-pluviated more irregular particle packing with poor gradation may result in lower CN_{ave} due to particle orientational alignment, particle interlocking and surface roughness.

The trend of the CN_{ave} in this paper is different from that reported from DEM studies since this work is based on real sands and uses different particle shape descriptors. The reasons of this apparent discrepancy are a key finding in this work. It is hard to ensure that the different sands have the same average equivalent diameter as well as gradation compared with the flexible setting in DEM. However, DEM studies include simplifications such as setting a certain critical separation distance to detect all particle contacts and usually assume that particles with different particle shape have the same Young's modulus, sliding and rolling

friction coefficients (they may be different in reality); all of which may impact on the characterization of actual soils at the microscale, even in the absence of external load but when using DEM to generate samples by gravity deposition.

The particle surface roughness and interlocking have not been quantified in this article and are interesting topics for future research.

DATA AVAILABILITY

Some or all data, models, or code that support the findings of this study are available from the corresponding author upon request.

ACKNOWLEDGEMENTS

The Imaging and Medical Beam Line (IMBL) at the Australian Synchrotron, Dr A Maksimenko and other beam scientists are acknowledged for their support. The first author thanks The University of Melbourne for offering the Melbourne Research Scholarship.

- REFERENCES

Ahmed, Z., and Lebedev, M. (2019). "Elastic properties of sands, Part 1: Micro computed tomography image analysis of grain shapes and their relationship with microstructure." *Geophysical Prospecting*, 67(4), 723-744.

ASTM (2017). "C778-17 standard specification for standard sand." *ASTM International, West Conshohocken, PA*.

Cho, G., Dodds, J., and Santamarina, J. (2006). "Particle Shape Effects on Packing Density." *Stiffness and Strength of Natural and Crushed Sands-Internal Report, Georgia Institute of Technology, 33pp*.

Delaney, G. W., and Cleary, P. W. (2010). "The packing properties of superellipsoids." *EPL (Europhysics Letters)*, 89(3), 34002.

Donev, A., Cisse, I., Sachs, D., Variano, E. A., Stillinger, F. H., Connelly, R., Torquato, S., and Chaikin, P. M. (2004). "Improving the density of jammed disordered packings using ellipsoids." *Science*, 303(5660), 990-993.

Druckrey, A., Alshibli, K., and Al-Raoush, R. (2017). "Discrete particle translation gradient concept to expose strain localisation in sheared granular materials using 3D experimental kinematic measurements." *Géotechnique*, 68(2), 162-170.

Fei, W., Narsilio, G. A., and Disfani, M. M. (2019). "Impact of three-dimensional sphericity and roundness on heat transfer in granular materials." *Powder Technology*, 355, 770-781.

Fei, W., Narsilio, G. A., van der Linden, J. H., and Disfani, M. M. (2019). "Quantifying the impact of rigid interparticle structures on heat transfer in granular materials using networks." *International Journal of Heat and Mass Transfer*, 143, 118514.

Fonseca, J., O'Sullivan, C., Coop, M. R., and Lee, P. (2013). "Quantifying the evolution of soil fabric during shearing using directional parameters." *Géotechnique*, 63(6), 487-499.
Fonseca, J., O'Sullivan, C., Coop, M. R., and Lee, P. (2012). "Non-invasive characterization of particle morphology of natural sands." *Soils and Foundations*, 52(4), 712-722.
Fonseca, J., Sim, W., Shire, T., and O'sullivan, C. (2014). "Microstructural analysis of sands with varying degrees of internal stability." *Géotechnique*, 64(5), 405-411.
Gan, J., Zhou, Z., and Yu, A. (2017). "Effect of particle shape and size on effective thermal conductivity of packed beds." *Powder Technology*, 311, 157-166.
Hryciw, R. D., Zheng, J., and Shetler, K. (2016). "Particle roundness and sphericity from images of assemblies by chart estimates and computer methods." *Journal of Geotechnical and Geoenvironmental Engineering*, 142(9), 04016038.
Krumbein, W. C., and Sloss, L. L. (1963). "Stratigraphy and sedimentation."
Legland, D., Arganda-Carreras, I., and Andrey, P. (2016). "MorphoLibJ: integrated library and plugins for mathematical morphology with ImageJ." *Bioinformatics*, 32(22), 3532-3534.
Minh, N., and Cheng, Y. (2013). "A DEM investigation of the effect of particle-size distribution on one-dimensional compression." *Géotechnique*, 63(1), 44.
Nadimi, S., Fonseca, J., Andò, E., and Viggiani, G. (2019). "A micro finite-element model for soil behaviour: experimental evaluation for sand under triaxial compression." *Géotechnique*, 0(0), 1-6.
Otsu, N. (1979). "A threshold selection method from gray-level histograms." *IEEE transactions on systems, man, and cybernetics*, 9(1), 62-66.
Persson, B., Albohr, O., Tartaglino, U., Volokitin, A., and Tosatti, E. (2004). "On the nature of surface roughness with application to contact mechanics, sealing, rubber friction and adhesion." *Journal of physics: Condensed matter*, 17(1), R1.
Rorato, R., Arroyo, M., Andò, E., and Gens, A. (2019). "Sphericity measures of sand grains." *Engineering Geology*, 254, 43-53.
Schindelin, J., Arganda-Carreras, I., Frise, E., Kaynig, V., Longair, M., Pietzsch, T., Preibisch, S., Rueden, C., Saalfeld, S., and Schmid, B. (2012). "Fiji: an open-source platform for biological-image analysis." *Nature methods*, 9(7), 676.
Shire, T., and O'Sullivan, C. (2013). "Micromechanical assessment of an internal stability criterion." *Acta Geotechnica*, 8(1), 81-90.
Sneed, E. D., and Folk, R. L. (1958). "Pebbles in the lower Colorado River, Texas a study in particle morphogenesis." *The Journal of Geology*, 66(2), 114-150.
Taubin, G. "Curve and surface smoothing without shrinkage." *Proc., Computer Vision, 1995. Proceedings., Fifth International Conference on*, IEEE, 852-857.
Wadell, H. (1932). "Volume, shape, and roundness of rock particles." *The Journal of Geology*, 40(5), 443-451.
Wang, J., Wu, S., Zhao, L., Wang, W., Wei, J., and Sun, J. (2019). "An effective method for shear-wave velocity prediction in sandstones." *Marine Geophysical Research*, 40(4), 655-664.
Wiebicke, M., Andò, E., Herle, I., and Viggiani, G. (2017). "On the metrology of interparticle contacts in sand from x-ray tomography images." *Measurement Science and Technology*, 28(12), 124007.
Zhao, S., Zhang, N., Zhou, X., and Zhang, L. (2017). "Particle shape effects on fabric of granular random packing." *Powder technology*, 310, 175-186.
Zhou, Z.-Y., Zou, R.-P., Pinson, D., and Yu, A.-B. (2011). "Dynamic simulation of the packing of ellipsoidal particles." *Industrial & Engineering Chemistry Research*, 50(16), 9787-9798.

3.4 CONCLUSIONS

Three-dimensional sphericity and roundness are selected to characterize particle shape in sands after a critical assessment of the literature and an in-house program was developed to compute them based on CT images of real sands. After calculating the sphericity and roundness of particles, effective thermal conductivity and coordination number in different sands, it is found that (1) irregular particles have lower sphericity and roundness than round particles; (2) the range in an irregular particle assembly is wider than that in regular (round) particle assembly; (3) higher average of sphericity and roundness show a tendency to boost higher effective thermal conductivity; (4) an air-pulvinated more spherical particle packings with poor gradation may have higher average coordination number.

Page intentionally left blank

Chapter 4: Quantifying the impact of rigid interparticle structures on heat transfer in granular materials using networks

4.1 OVERVIEW AND STRUCTURE

Coordination number is widely used to quantify the deformability of granular material. However, the use of average coordination number is not able to fully characterise the variation of the microstructure of all variations of granular materials. Triangular structures formed by particles within granular materials tend to be more rigid than particulate rectangular structures during deformation. This chapter aims to apply contact network features to characterise the rigidity of materials by counting the triangular structures and their particle shape as an indicator of the contact quality in granular materials. Their effects on thermal conductivity in deforming geomaterials are then quantified.

This chapter has been published as a journal paper entitled ‘Quantifying the impact of rigid interparticle structures on heat transfer in granular materials using networks’ in *International Journal of Heat and Mass Transfer*. The paper has a different theme but is interrelated with the papers in the previous chapter. They may share some samples and methods.

4.2 QUANTIFYING THE IMPACT OF RIGID INTERPARTICLE STRUCTURES ON HEAT TRANSFER IN GRANULAR MATERIALS USING NETWORKS

International Journal of Heat and Mass Transfer 143 (2019) 118514

Contents lists available at ScienceDirect

International Journal of Heat and Mass Transfer

journal homepage: www.elsevier.com/locate/ijhmt

Quantifying the impact of rigid interparticle structures on heat transfer in granular materials using networks

Wenbin Fei, Guillermo A. Narsilio *, Joost H. van der Linden, Mahdi M. Disfani

Department of Infrastructure Engineering, The University of Melbourne, Parkville, Australia

ARTICLE INFO

Article history:
Received 16 May 2019
Received in revised form 25 July 2019
Accepted 26 July 2019
Available online 16 August 2019

Keywords:
Heat transfer
Rigidity
Thermal network model
Microstructure
Deformation

ABSTRACT

Coordination number can be used to quantify the particle connectivity and deformability of a granular material. However, it is a local feature of particles at the microscale, and the use of an average coordination number does not allow for full characterization of the microstructural variation in the granular material. Mesoscale structures can be used to overcome this limitation: triangular-like structures at the mesoscale tend to be rigid, whereas square-like structures tend to be deformable. However, the effect of these structures on heat transfer has not been studied in deforming granular materials. A better understating of how microstructure variation affects effective thermal conductivity is necessary. This work constructs contact networks representing the granular materials with particles as nodes and linking neighbouring nodes with edges that represent particle contacts. Then, '3-cycles' (i.e., a triangular structure) and 'clustering coefficients' are extracted from the contact network. As contact thermal conductance is vital to heat transfer and affected by particle shape, microscale three-dimensional particle shape descriptors are also calculated. To compute the effective thermal conductivity of the granular assembly, a thermal network model is established by adding 'near-contact' edges to the contact network and assigning a thermal conductance to each edge. The results show that mesoscale local clustering coefficients can indicate the rigidity of granular materials and, together with particle shape descriptors, can be used to predict well the effective thermal conductivity of granular materials under deformation.

1. Introduction

Compaction is one of the simplest ways to improve the ground bearing capacity. It also has the potential to enhance the heat transfer of the ground in shallow geothermal energy systems because the interparticle contact areas and the number of interparticle contacts may increase while pore spaces shrink during compaction. Heat transfer in any materials occurs because of conduction, convection and radiation. Since convection is important due to fluid currents [1] and radiation becomes significant when the temperature is greater than 1000 K [2,3], conduction usually contributes the most strongly to heat transfer in dry granular materials [1,4]. The heat conduction depends on the thermal conductivity of solid particles [1], the interparticle contact conductance [1,5-9] and the structure of particle packings [2,10]. As the rigidity/deformability of granular materials is related to their microstructures [11], a better understating of how the microstructure variation affects the effective thermal conductivity (λ_{eff}) is necessary.

The coordination number has a strong relationship with mechanical stability [12] and the jamming transition [13,14] in granular materials. However, the coordination number is a microscale variable describing the connection of an individual particle to others. The often-used average coordination number cannot fully capture the spatial variation of the microstructure of granular materials. An order characteristic can also indicate the packing structure by measuring the rotational symmetry of particles [15]. However, it required complex calculation and was applied to sphere packings in the study. According to rigidity theory, a triangular structure tends to resist more deformation than a quadrilateral structure under an external loading (Fig. 1). However, the effect of interparticle triangular structures on λ_{eff} has not been studied in deforming granular materials.

Complex network theory can quantify the structure of a complex system and it has been successfully applied to represent civil infrastructure systems [16-18]. As granular materials are also complex systems [19], complex network theory has also been used to investigate the mechanical behaviour [11,20] and pore connectivity [21] in the granular materials. However, it has not been used

* Corresponding author at: Engineering Block B 208, Department of Infrastructure Engineering, The University of Melbourne, Parkville, VIC 3010, Australia.
E-mail address: narsilio@unimelb.edu.au (G.A. Narsilio).

https://doi.org/10.1016/j.ijheatmasstransfer.2019.118514
0017-9310/

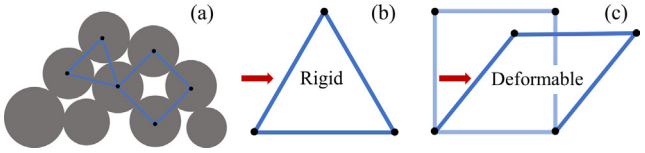

Fig. 1. In representing the structure of a granular material in the network, a triangular structure (a '3-cycle' in complex network theory) is rigid whereas a quadrilateral structure is deformable.

to study heat transfer in granular materials. A granular material could be simplified as a contact network in which a node is assigned to each particle and an edge is created when two neighbouring particles are in contact. Various mesoscale structural features can be obtained by calculating the number of *n*-cycles using complex network theory [20]. A 'cycle' is a loop that begins and ends at the same node, so 3-cylce is a triangle, 4-cycle is quadrangle and 5-cycle is pentagon. A 3-cycle is the smallest arrangement of particles formed by 3 neighbouring particles in contact [22]. These 3-cycle structures are more persistent and stable than n-cycle of higher orders ($n > 3$) during deformation of granular materials [11]. 3-cycles have a crucial role in rigidity because they can frustrate rotation and provide lateral support to surrounding particles even in three-dimensional (3D) analyses [23,24]. Rivier (2006) showed that odd circuits (3-cycle is an odd circuit) are sufficient to ensure stability in 3D [23]. Mesoscale clustering coefficients can also be extracted from the contact network to measure the density of 3-cycles (triangles). Compared with the coordination number, which only provides information on a single node, the mesoscale 3-cycle and clustering coefficients have the advantage of containing information about more than one node without comprising the entire network. Hence, investigating the relationship between mesoscale rigidity features and λ_{eff} can potentially improve our knowledge of heat transfer in deforming granular materials.

In addition to the microstructure (rigidity) of the packings that can be characterized by the 3-cycle or cluster coefficients, particle contact thermal conductance is also important in the overall heat conduction [25]. In dry materials, the contact conductance is believed to be affected by particle shape [26,27], as particle shape affects both the contact number and contact area [1,28]. Therefore, three-dimensional particle shape descriptors are employed here to study the variation in λ_{eff}.

To extract the '3-cycle' and particle shape descriptors of granular materials, their internal microstructural information should be acquired. High-resolution X-ray computed tomography (CT) techniques applied to granular materials can generate sequential CT images at a certain interval (resolution) [29-31]. Based on the images, the particle geometrical information and connectivity can be extracted using imaging postprocessing techniques. The geometry of the granular materials can also be reconstructed and numerical simulations can be undertaken to estimate their λ_{eff}. Finite element simulation (FEM) is an available method to compute the λ_{eff} but it is time-consuming because fine meshes are required to discretize the interparticle contacts and the interface between solid and pore phases. It usually overestimates λ_{eff} due to oversmoothing the interparticle contact areas [32,33] and the lack of consideration of particle surface roughness [32]. Alternatively, network models [34-36] can discretely represent particle packings and calculate the heat transfer through interparticle contacts (real contacts) and small gaps between particles (near-contacts). However, very few thermal network models are available for nonsphere packings. The thermal conductance network model (TCNM) [37] developed by our team extended the application to packings of irregular (i.e., nonspherical) particles.

This article aims to find the relationship between the deformability of granular materials or rigidity and the λ_{eff} of granular materials using network techniques. Five granular materials with different particle shapes were scanned using CT techniques under different loadings. For each material at each level of compaction, four smaller subsamples were selected to (i) construct contact networks to calculate the number of mesoscale 3-cycle and clustering coefficients to characterize the rigidity of granular materials, (ii) construct thermal conductance network models (TCNMs) to calculate λ_{eff}, and (iii) compute the shape descriptors of individual particles. The λ_{eff} calculated from TCNMs were compared to those from FEM and experiments. Then, multiscale parameters were used to analyze the reasons underlying the λ_{eff} variation in deforming materials.

2. Materials

Five granular materials were used in this work. The pictures in the upper row of Fig. 2 show that the selected materials have different particle shapes. The round glass beads were made of silica and have a silver coating. The Ottawa sand was sieved following ASTM standard C778 [38] to achieve particles retained between sieve No. 20 (0.60 mm) and No. 30 (0.85 mm). Particles in both Ottawa sand and Angular sand are mainly made of quartz, but the former are more rounded. Crushed schist A is made of chlorites and the particles in the packings are more irregular than the Angular sand. Crushed schist B has the most irregular particles, which consist of quartz and biotite [39]. Each material was air-pluviated into a cylindrical container with a diameter of 25 mm and a height of 25 mm. This container was equipped with a loading module designed by Afshar et al. [40]. The five materials were scanned under different axial loads corresponding to 0, 2, 6.1 and 10.2 MPa stress levels. The images shown in the bottom row of Fig. 2 are typical cross-section images of the five materials without loading (0 MPa). The voxels with a resolution of 13 μm in them present different grayscale that indicates the density of the mineral. The distinct grayscale in the voxels of the crushed schist CT image results from the corresponding different mineral components. Selecting the resolution of CT images is a trade-off between obtainning fewer grains with higher resolution and more grains with lower resolution. CT images with high resolution could better identify the partial contacts which may be wrongly recognized as a "complete or full contact" between particles [41] otherwise (at lower resolutions) and result in an overestimate [42] of interparticle contact area between irregular grains. The particle size of the five materials is summarized in Table 1.

3. Methods

3.1. Network construction

Two types of networks are constructed in this work. *Contact* networks are constructed to acquire the 3-cycles and cluster coefficients using complex network theory. *Thermal* networks are extensions of the contact networks that also consider near-contacts as edges (Fig. 3) and it can be used to calculate the λ_{eff} by adding thermal conductance at the edges.

As summarized in Fig. 3, a sequence of CT images with a representative element volume is cropped from the scanned sample and the image noise is decreased by using 3D Median filter in Step 1. These images are used to reconstruct the (3D) geometry in which the two phases (solid in black and pore in grey) are segmented with a common multilevel Otsu segmentation method [42-45] implemented in Fiji with automatic parameters selection [46] in Step 2. They do differ for each tested sample. To determine the

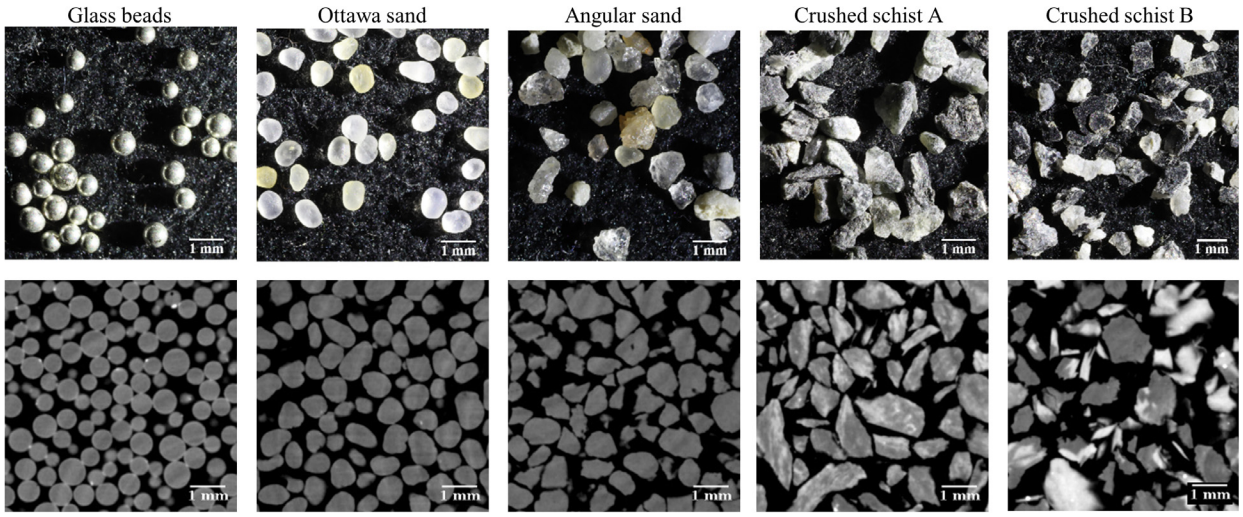

Fig. 2. Five natural sands with different particle shapes. The pictures in the first row were photographed and the images in the second row were scanned with computed tomography.

Table 1
Particle size characteristics of the selected granular materials.

Sample	d_{50} (mm)	Particle size range (mm)
Glass beads	0.60	0.50–0.70
Ottawa sand	0.73	0.60–0.85
Angular sand	0.89	0.60–1.18
Crushed schist rock A	0.84	0.50–1.18
Crushed schist rock B	0.84	0.50–1.18

location of each particle for constructing the networks, the watershed segmentation from MorphoLibJ [47] in Fiji is employed to split connected particles [48] in Step 3. Although Taylor et al. [49] found that the watershed segmentation with a 26 voxel neighbourhood can better capture the boundary of irregular particles, the results usually overestimate the surface (contact) area [50]. Therefore, a 6-voxel neighbourhood was used in this work because it has been shown to render satisfactory results [50].

After the watershed segmentation, each particle is assigned a unique identifier (ID) and its centroid is calculated as the average coordinates of the voxels in the particle. To identify the real interparticle contact and near-contacts, the voxels in each particle are grouped as boundary voxels if they are adjacent to anything other than the voxels in the same particle. A subset of these boundary voxels is identified as interparticle contact voxels if they also border on another particle (and its corresponding boundary voxels).

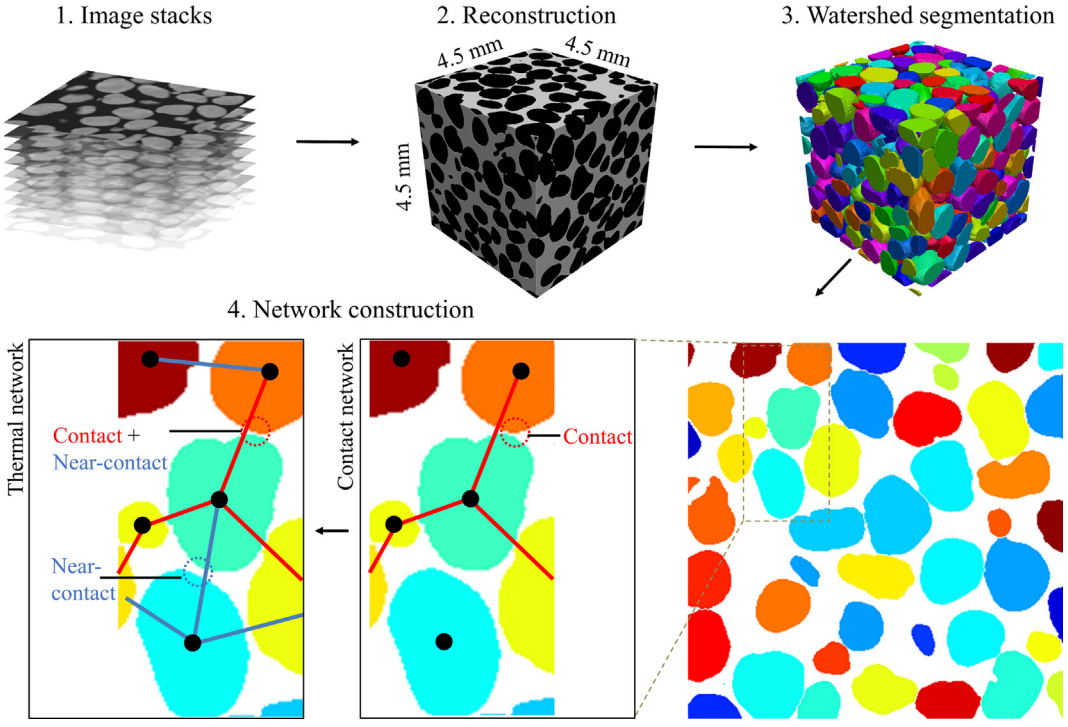

Fig. 3. Procedures to construct a contact network and a thermal network. Contact edges are in red, near-contact edges are in blue. (For interpretation of the references to colour in this figure legend, the reader is referred to the web version of this article.)

To efficiently identify the near-contacts, watershed segmentation is also applied to the void space (grayscale colours in Fig. 4 left) by first inverting the colour of phases and then following the same steps as with the solid phase watershed segmentation. The particle-pore connection (orange arrows) can be detected if the boundary voxels border on pore space. Then, the particle-pore-particle connections are identified as the location of potential near-contacts. Next, to determine the voxels that form a near-contact, cylinders representing gaps between particles or 'gap' cylinders are created for boundary voxels on a particle, as shown in Fig. 4 right, and their lengths L_l^g are computed as the minimum distance to the boundary voxels on the neighbouring particle. Finally, the gap cylinder(s) will be considered to be in a near-contact if their respective lengths are shorter than a threshold ϵ. The threshold ϵ is selected as half of the mean particle radius after a calibration [37].

3.2. Contact network features

After constructing contact networks, three contact network features (3-cycle, local clustering coefficient and global clustering coefficient) are extracted as rigidity features to indicate the mesoscale structure of granular materials. N_3-cycles is calculated as the number of triangles in the contact network. Local clustering coefficients [51] and global clustering coefficients [20] measure the density of triangles and can be computed using Eqs. (1) and (2), respectively. The local clustering coefficient, in particular, can quantify the fraction of possible triangles through each node. Clustering coefficients also indicate how fractured or integrated the contact network is. For instance, Fig. 5(a) is a relatively fractured network that has a higher clustering coefficient than the network in Fig. 5(b).

$$\left[G^{C}\right]_{LC}(\mathrm{i}) = \frac{2T(i)}{N(i)(\mathrm{N}(i)-1)} \tag{1}$$

where T(i) is the number of triangles that pass node i, and N(i) is the degree of node i.

$$G^{C}{}_{GC} = 3 \cdot \frac{number\ \ of\ \ triangles}{number\ \ of\ \ connected\ \ triples} \tag{2}$$

where a triple is a group of three nodes that can contain either three edges (in a 3-cycle) or two edges.

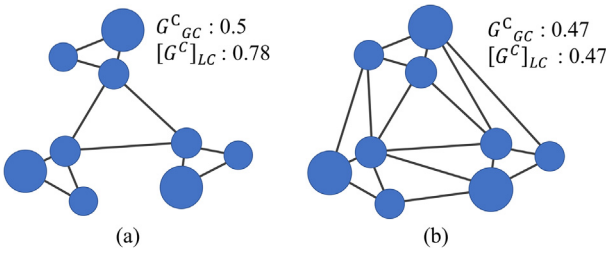

Fig. 5. (a) A fractured network with a local clustering coefficient of 0.78 and global clustering coefficient of 0.5 (b) An integrated network with a local clustering coefficient of 0.47 and global clustering coefficient of 0.47.

3.3. Thermal conductance network model

3.3.1. Thermal conductance calculation

The thermal conductance at the thermal network edges is required to calculate the effective thermal conductivity of granular materials [34]. For a cylinder with cross-sectional area A, length L and thermal conductivity λ, its heat conductance C can be calculated as $C = \lambda A/L$. Hence, equivalent cylinders are used to represent the heat conductance in network edges. These representations were proposed by Batchelor and O'brien [52] for randomly arranged sphere packings and then developed for more general assemblies, as validated by Yun and Evans [34] for spheres and Shapiro et al. [53] for powder packed beds. As heat conducts through solids, real interparticle contacts and near-contacts, three types of equivalent cylinders [37] are considered in this work and summarized in Fig. 6: (i) a particle cylinder with conductance C^p, (ii) a real interparticle contact cylinder $C^{contact}$ and (iii) a near-contact cylinder C^{gap}. The conductances through a 'particle' cylinder and interparticle contact cylinder can be computed using Eqs. (3) and (4), respectively,

$$\mathrm{C}^{\mathrm{p}} = \lambda_s \frac{A^p}{L^p} = \lambda_s \frac{\chi V^P/L^P}{L^P} \tag{3}$$

where λ_s represents the thermal conductivity of the solid and the void phase. $L^P$is the distance between the centroid of a particle and its corresponding contact. $L^P$is equal to the particle radius for a spherical particle. The particle cylinder area A^P is derived as $\chi V^P/L^P$. Here, V^P is the particle volume and χ is a model coefficient that can be computed as $1/N(i)$where $N(i)$ is the coordination number of particle i (i.e., the degree of node i in contact network).

$$\mathrm{C}^{contact} = \lambda_s \frac{\kappa A^C}{L^C} = \lambda_s \frac{\kappa \sum_{i,j,k} A^v_{i,j,k}}{3L^v} \tag{4}$$

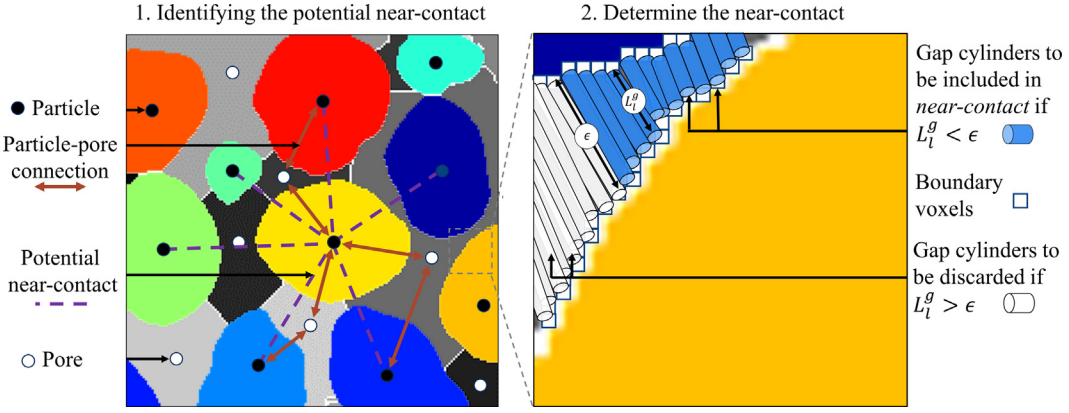

Fig. 4. Identification of near-contacts. ϵ is the threshold length ($D_{50}/4$ in this case) for near-contacts.

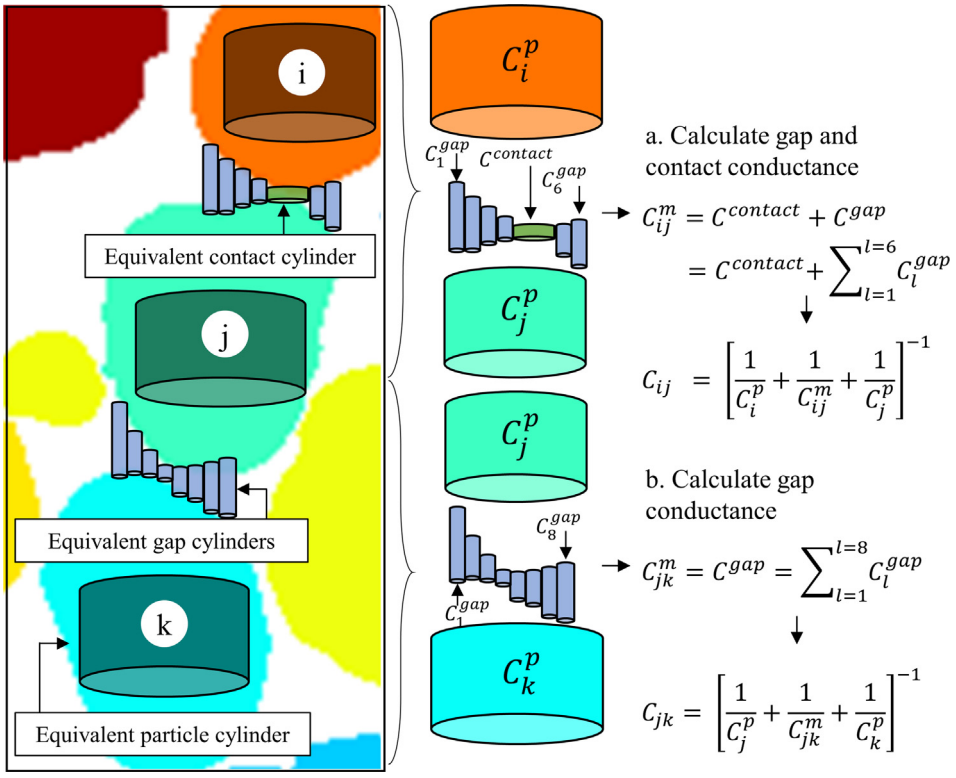

Fig. 6. Computation of thermal conductance in the thermal conductance network (TCNM).

where A^C is the interparticle contact area computed as the sum of the area of contact voxel $\sum_{i,j,k} A^v_{(i,j,k)}$ and L^v is the length of a voxel However, interparticle contact is essentially a combination of contact points because of the particle surface roughness [54]. The results of Askari et al. [54] show that a 25% overestimation of λ_{eff} may occur due to neglecting the roughness. Thus, κ is set as 0.75 in our work. L^C is the length of the interparticle contact cylinder, assumed to be $3 \cdot L^v$ [37] refer to the work of Bauer and Schlunder [55] that was validated by Shapiro et al. [53].

Interparticle contact is usually over-smoothed during the threshold segmentation, as illustrated in Fig. 7, where the voxels partially filled with solid and void are incorrectly identified as a contact. The over-smoothing of the contact area results in a higher λ_{eff} in simulation [32,33]. Since the partially filled voxels have specific grayscales, a penalty coefficient τ [37] is introduced to correct the area of partially filled voxels as:

$$A^v_{(i,j,k)} = \left(\frac{g_{(i,j,k)}}{g^{contact}_{max}}\right)^{\tau} L^2_v \tag{5}$$

where $g_{(i,j,k)} \in (0, 255)$ is the gray value of each voxel (i, j, k) at the interparticle contact and the $g^{contact}_{max}$ is the largest value among them. The power of τ is used to vary the severity of the penalty and is set as 10 [37] after calibrating the λ_{eff} of sphere packings using the results of an existing thermal network for sphere packings [34].

Near-contact cylinders are generated based on the near-contacts identified in Fig. 4. Then, the conductance at near-contact cylinders C^{gap} can be calculated as:

$$C^{gap} = \sum_l C^g_l = \lambda_v (L^v)^2 \sum_l \frac{1}{L^g_l} \tag{6}$$

where λ_v represents the thermal conductivity of the void phase and L^g_l is the length of the near-contact cylinder.

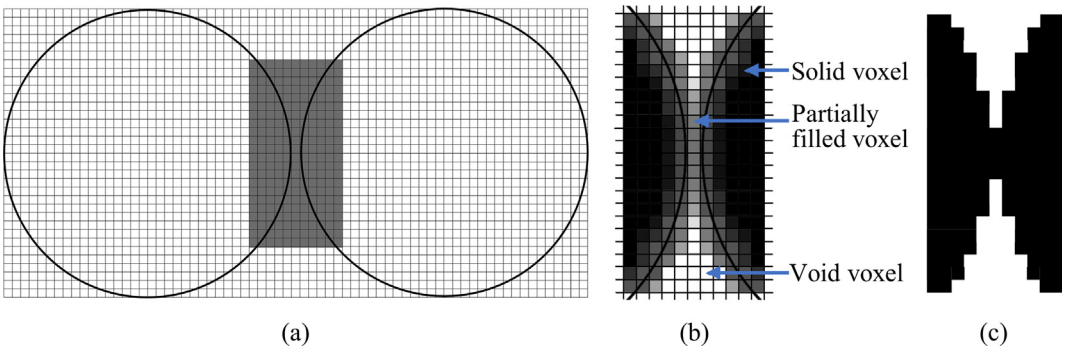

Fig. 7. Over-smoothing of CT images after threshold segmentation: (a) Two discs with a 1-pixel gap; (b) a small gap in grayscale; (c) over-smoothing in the contact after threshold segmentation (after [42]).

3.3.2. Effective thermal conductivity calculation

To calculate the λ_{eff} of dry granular materials by solely considering heat conduction, the heat flux Q_{ij} of an edge connecting nodes i and j is solved by importing the computed thermal conductances to Fourier's law (Eq. (7)) as part of the open-source Python library OpenPNM [56]. As this study focuses on the structure variation beyond the mineralogy, the thermal conductivity of the solid was fixed at 3 W/(mK) [1,34,57] and the thermal conductivity of the air filled in the void space is 0.025 W/(mK). The boundary temperatures at the top and bottom nodes are 293 K and 292 K, respectively. The heat flux is calculated as:

$$\sum_{i\to j} Q_{ij} = \sum_{i\to j} C_{ij}(T_i - T_j) \tag{7}$$

where C_{ij} is the conductance of the interparticle contact of the near-contact conductance and T_i and T_j are the temperatures at nodes i and j.

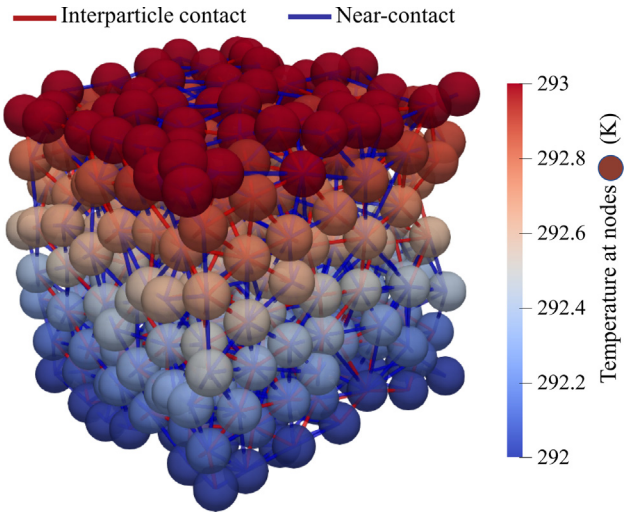

Fig. 8. TCNM simulation results showing the temperature of each node. From this network system, it is easy to see paths of heat transfer: interparticle contacts are shown in red and the near-contacts are blue. (For interpretation of the references to colour in this figure legend, the reader is referred to the web version of this article.)

After calculating the local heat flux Q_{ij} at each edge, the total heat flux in a typical cross-sectional plane perpendicular to the heat transfer direction can be used in Eq. (8) to compute the λ_{eff} of the sample. A simulation result by TCNM is shown in Fig. 8.

$$\lambda_{\text{eff}} = \frac{\frac{1}{A}\int_A Q_z dA}{(T_a - T_b)/L} = \frac{\frac{1}{A}\sum Q_{ij}}{(T_a - T_b)/L} \tag{8}$$

3.4. Finite element simulation and laboratory measurement

To validate the heat transfer simulation by TCNM, finite element simulation and thermal needle testing were also used to measure the λ_{eff} of the granular materials.

3.4.1. Finite element simulation

We follow the framework introduced by Narsilio et al. [58] for fluid flow and its adaption for heat transfer at the particle scale [32,37,59]. For each sample, CT image stacks were imported to Simpleware ScanIP [60] to reconstruct the 3d microgeometry, segment the solid and void (Step 2 in Fig. 3), and generate meshes that were transferred to the finite element software COMSOL Multiphysics [61] for heat transfer simulation. Fig. 9 shows the mesh of Ottawa sand, the mesh size and sample size were decided after a sensitivity analysis. The input thermal conductivity of air and solid grains are same as that in TCNM (solids at 3 W/(mK), air at 0.025 W/(mK)). Similar to the simulation process in TCNM, the local temperature is first calculated by solving the governing balance energy equations for a system with thermal insulation on all sides and a small temperature cdifferential between the top and bottom boundaries (Fig. 9). The local heat flux density Q_z is estimated from the local temperature field using Fourier's law. Finally, the integrated format $\frac{1}{A}\int_A Q_z dA$ in Eq. (8) is used to determine the effective thermal conductivity of the sample. Additional details on this procedure can be found in papers [32,37,58].

3.4.2. Laboratory measurement

A 100-mm long thermal needle probe with a diameter of 2.4 mm was used to measure the λ_{eff} in the laboratory. The diameter of the needle was selected to be larger than the particle diameter to maximize the contacts between particles and the thermal needle probe. The granular materials were air-pluviated into a PVC cylinder with a diameter of 50 mm and a height of 120 mm.

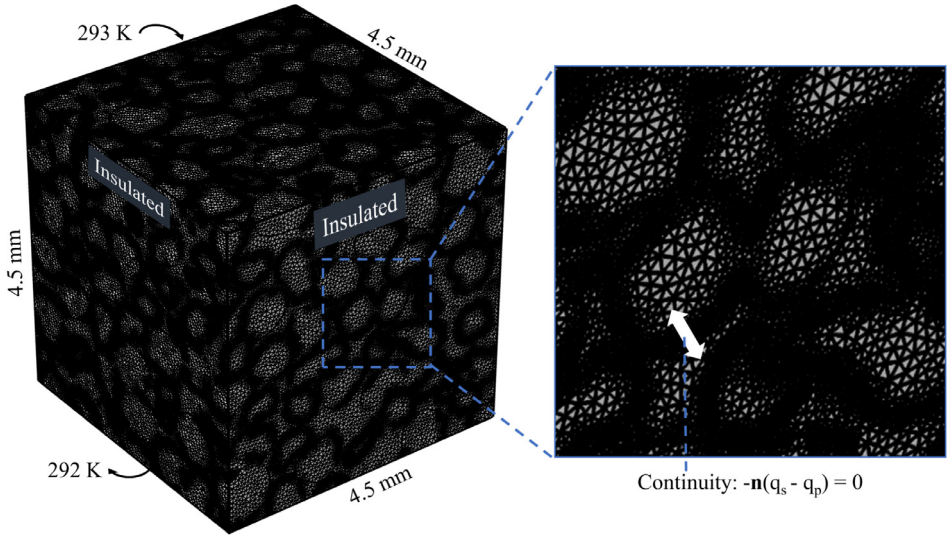

Fig. 9. The finite elements and boundary condition used for simulating the heat transfer in Ottawa sand without loading.

We followed ASTM standard D5334-14 [62] to measure the thermal conductivity of the air-pluviated materials, achieving good accuracy at ±10% for 0.2 – 4W/(mK) [63].

3.5. Particle shape descriptors

Sphericity (S) and roundness (R) are two indicators that describe particle shape and can be calculated using Eqs. (9) [47] and 10 [64], respectively.

$$S = \frac{36\pi V^2}{SA^3} \tag{9}$$

where V is the particle volume and SA is the particle surface area.

$$R = \frac{\sum r_i / N}{r_{max-in}} \tag{10}$$

where r_i is the radius of a particle corner, N is the total number of corners and r_{max-in} is the radius of the maximum inscribed sphere in the particle.

To calculate the sphericity and roundness of each particle automatically based on CT images, an in-house program has been developed [28]. Since the connected particles were separated in Step 3 (Fig. 3), the individual particles can be extracted from the samples. The surface mesh of the extracted particles from CT images have tooth-saw patterns (Fig. 10), which may overestimate the particle volume and particle surface area, so the Taubin smoothing algorithm [65] is applied to achieve a smooth particle surface (Fig. 10). Since the smooth particle surface is composed of triangles, the sum of each triangle surface area is the particle surface area. Similarly, a tetrahedron is constructed for each triangle by considering the centre of the particle, and the sum of the volume of all the tetrahedrons is the particle volume.

Identifying the corners in each particle is required and their radii are used to calculate the roundness using Eq. (10). The maximum curvature of each vertex is first computed by quadratically fitting a microsurface using its ring adjacent vertices. Next, a quadratic polynomial equation can be obtained and the principal curvatures can be calculated by solving Hassian matrix [66] which created with coefficients in the equation. Then, corners are identified if the absolute value of the reciprocal of the curvature is smaller than r_{max-in}, the radius of the maximum inscribed sphere in the particle, and the reciprocal is selected as the radius of the corner r_i.

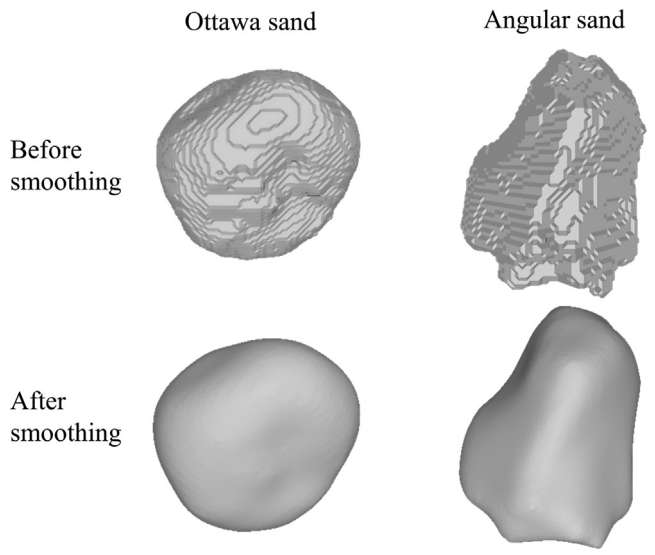

Fig. 10. The Taubin smoothing algorithm is used to transform the particles with a tooth-saw surface to a smooth surface.

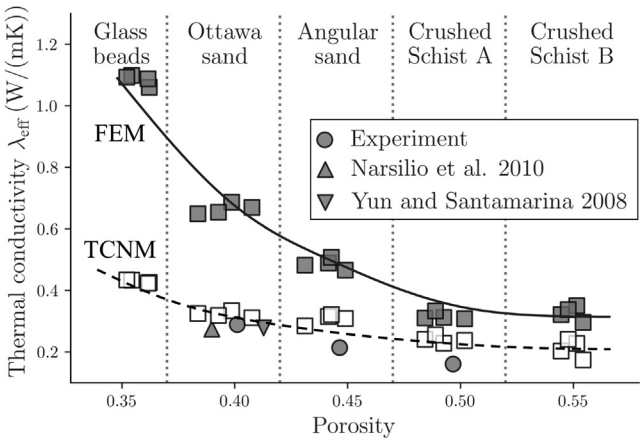

Fig. 11. The effective thermal conductivity calculated from TCNM compared with the finite element numerical and experimental results.

4. Results and discussion

4.1. Effective thermal conductivity comparisons

For each material shown in Fig. 2 under no pressure, four subsamples with a dimension of 4.5 by 4.5 by 4.5 mm from random locations within the sample were selected to check the homogeneity of the sample. Their λ_{eff} were calculated by both FEM and TCNM, as shown in Fig. 11. Experimental measurements from the literature [32,34] and our laboratory are also included. The porosity of the experimental results is the mean value of the four subsamples in FEM and TCNM.

Fig. 11 illustrates that the λ_{eff} from TCNM shows good agreement with the experimental results, despite a slight overestimation of λ_{eff} for high-porosity samples. Woodside and Messmer [67] indicate that an underestimation may occur in the thermal needle test because of the imperfect contact between the needle and particles. Moreover, the mineralogy in the real materials is not considered in simulations. The effective thermal conductivity from TCNM shows a moderate decreasing rate with porosity. This observation is consistent with the results from papers [32,34] that reported small decreases in effective thermal conductivity when porosity is increased without loading. In contrast, the λ_{eff} from FEM shows a much larger overestimation, which can be attributed to the oversmoothing of the interparticle contact area as shown in Fig. 7 since interparticle contact dominates the heat transfer in dry granular materials [1]. The FEM simulation also has limited ability to capture inter-particle contact surface roughness so that the actual point-to-point contacts in real imperfect particle-contacts are overestimated as flat face-to-face contacts [54,59]. The overestimation of FEM is most obvious for samples with low porosity. For glass beads, the FEM value is almost three times the TCNM value. A higher porosity in granular materials usually means fewer interparticle contacts (coordination number in Fig. 12(d)), resulting in the lower overestimation in FEM. Thus, FEM predicts the effective thermal conductivity more accurately in dense granular materials whereas TCNM may render accurate predictions for a wider range of materials.

4.2. Variation in λ_{eff} under loading: a particle-scale analysis

Another advantage of using TCNM to calculate λ_{eff}^{TCNM} is that the thermal conductances (Equations (4) and (6)) between two particles can be readily computed at the microscale. Hence, the contribution of near-contact conductance (at the blue edges in Fig. 8) to

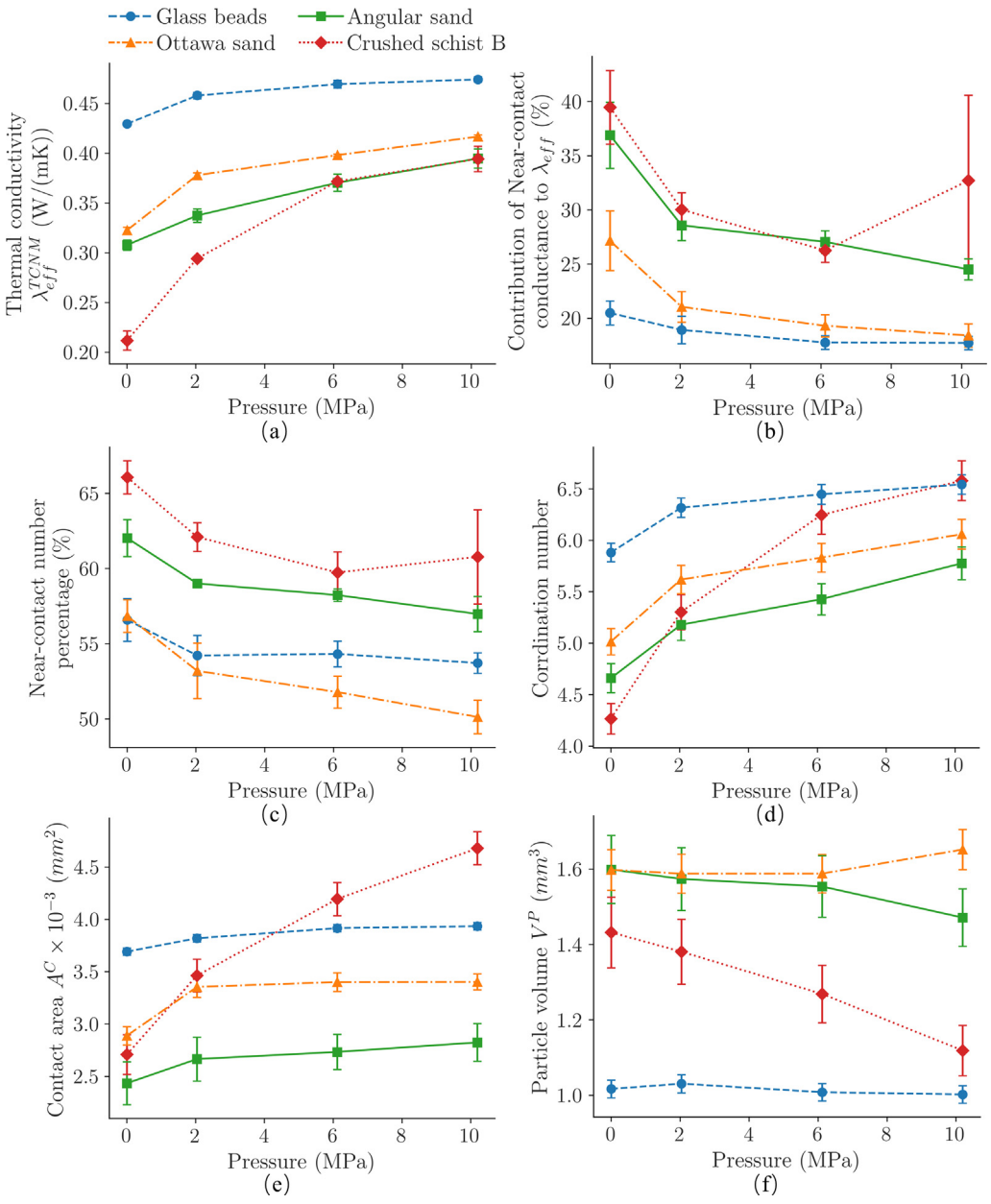

Fig. 12. Contribution of the near-contact conductance to λ_{eff}^{TCNM} and microstructural analysis of the near-contact percentage, coordination number, contact area and particle volume. For the thermal conductivity, contribution of near-contact and near-contact percentage, the error bar shows the 95% confidence interval of the average from four subsamples for each material. For others, the error bar shows the 95% confidence interval calculated on network nodes or edges of the combined set of the four subsamples.

the λ_{eff}^{TCNM} of a sample can be distinguished in the overall calculations by computing the difference of λ_{eff}^{TCNM} with and without near-contact conductance. Fig. 12(a) shows the evolution of the average λ_{eff}^{TCNM} of the four subsamples of different materials under increasing loading. Round glass beads show the largest λ_{eff}^{TCNM} compared with the λ_{eff}^{TCNM} of the most irregular crushed schist B, which consistently showed the lowest conductivity among the four materials. Fig. 12(b) shows that the contribution of the near-contact conductance to the λ_{eff}^{TCNM} is the lowest in round glass beads and highest in the schist B. Surprisingly, the contribution of the near-contact conductance is approximately 40% in crushed schist B with no compression. Even for the dense irregular sand (rounder than crushed schist B) under 10 MPa, the contribution still accounts for 25%. The contribution will be higher with the increase of gas pressure in dry granular materials with low porosity due to Smoluchowski effect (gas thermal conductivity reduces with the decreasing pressure) [68,69]. The high contribution of the near-contact conductance is related to the number of near-contacts. As show in Fig. 3, two kinds of edges are created in a thermal network; one type of edge in blue only considers the pure near-contact and the other in red involves both interparticle contact and near-contact. Indeed, Fig. 12(c) shows that the percentage of the pure near-contact in the materials under any loading is larger than 50%. A higher number of near-contacts may indicate loose interparticle contacts. For instance, Angular sand has higher near-contact count than Ottawa sand, in Fig. 12(c), but less interparticle contacts (as shown by coordination number in Fig. 12(d)). Notably, the Ottawa sand has fewer near-contacts and real interparticle contacts than glass beads.

For the sensitivity of λ_{eff}^{TCNM} to the loading, the λ_{eff}^{TCNM} of the four materials increase substantially up to 2 MPa. During this loading period, the role of the near-contacts weakens in contrast with the higher contribution of interparticle contact number (coordination number) in Fig. 12(d) and the interparticle contact quality (contact area) in Fig. 12(e). When the load is increased, the λ_{eff}^{TCNM} remains steady for glass beads and slowly increases for Ottawa sand and angular sand. These trends are also observed in the variation of the coordination number but not in the change in the contact area. Hence, the interparticle contact number may be more important to heat transfer in granular materials than the near-contact and contact areas. Furthermore, the ordering of the materials in Fig. 11, Fig. 12(a), (b) and (d) indicates that packings with more irregular particles could have higher porosity, lower interparticle contact [1,70] and a resulting lower λ_{eff}^{TCNM}. The λ_{eff}^{TCNM} of crushed schist B reaches the same value as angular sand when the pressure is 6 MPa. The large increment of λ_{eff}^{TCNM} for crushed schist B is due to the particle breakage (Fig. 13), which is indicated by the distinct decrease in its particle volume, shown in Fig. 12(f). The earlier particle breakage in crushed schist B is because it contains a large proportion of biotite in the schist (Fig. 2) with lower Mohs hardness (2.5–3) than that of quartz (Mohs hardness is 7) composing Ottawa sand [71]. Particles in crushed schist B with more irregular shape than the particles in Ottawa sand are more prone to breakage [72].

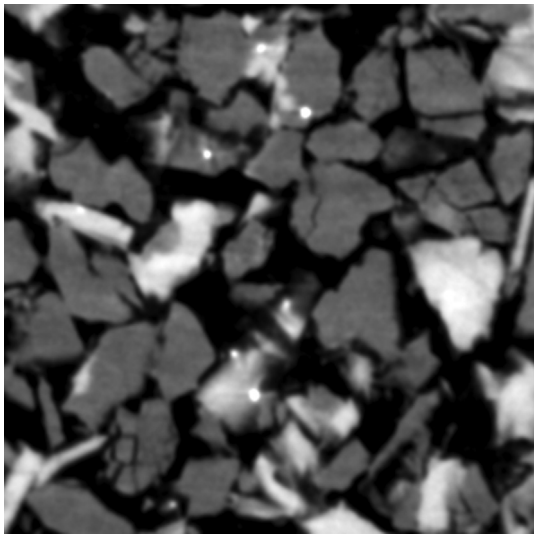

Fig. 13. Particle breakage in crushed schist B under 6 MPa.

4.3. Variation in λ_{eff} under loading: Rigidity and a multi-scale analysis

Although the variation in the coordination number in Fig. 12(d) indicates the sensitivity of particle connectivity to compaction, the coordination number only describes the particle-scale rather than the mesoscale structure. Since particle connectivity changes due to the particle sedimentation and rotation during compression [40], N_3-cycles and clustering coefficients can make up for the disadvantage of using the coordination number to determine the change in the mesoscale structure and show the rigidity of the granular materials. We remind the readers that a 3-cycle is the smallest arrangement of particles formed by 3 neighbouring particles in contact, and that a higher count of 3-cycles structures than n-cycles (n > 3) indicate higher rigidity of the overall assembly, i.e., a low count of 3-cycles indicates that the granular material is more deformable. Fig. 14(a) shows that higher pressure results in a higher N_3-cycle number. The round glass beads have the most N_3-cycles among all materials at almost all levels of loading, which indicates that the regular particle packings are more rigid to the level of loading [73]. The continuously increasing number of N_3-cycles in crushed schist B is due to the decreasing particle volume, which means that the N_3-cycles reflect the particle breakage in Fig. 14(b). The ordering of the global clustering coefficient for all materials at different levels is similar to that of N_3-cycles and its relationship with pressure in different materials become closer. Moreover, the local clustering coefficient in Fig. 14(c) can almost unify the mesoscale structure change in the four granular materials under loading. Hence, it was used to further analyze the relationship between the rigidity and λ_{eff}^{TCNM} in dry granular materials.

Fig. 15(a) shows that samples with a higher local clustering coefficient have a high normalized λ_{eff}^{TCNM}. Among the four materials, the range of the local clustering coefficient of round glass beads is narrow while that of the very irregular crushed schist sand is wide. As the local clustering coefficient quantifies the percentage of possible triangles through a node, the different range of the local clustering coefficient may because of the different particle shape. The decreasing range of the local clustering coefficient from irregular crushed schist B to round granular materials also reveals that samples with a regular particle shape are more rigid to loading. A linear regression was also conducted to fit the relationship for each material. The fitted lines for the four materials have a similar slope,

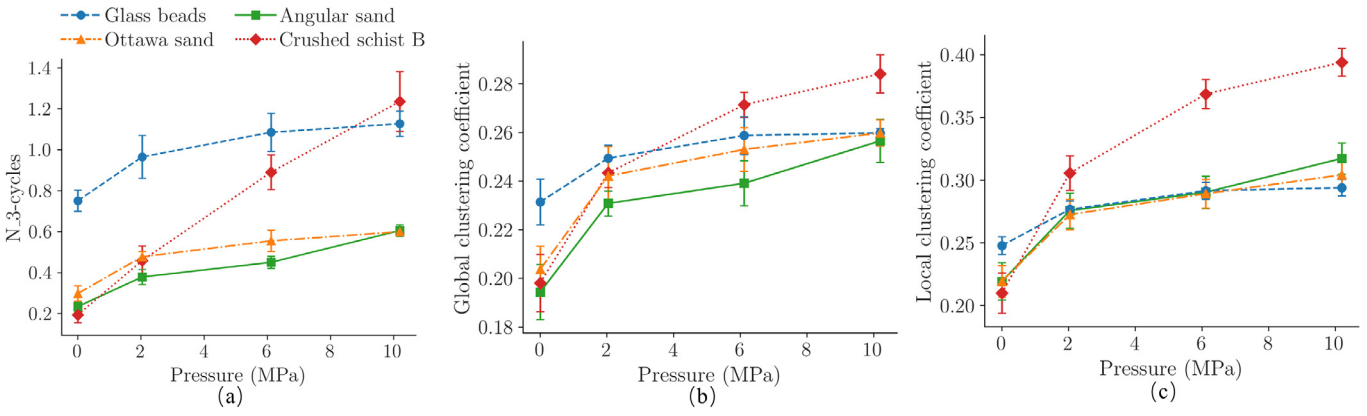

Fig. 14. Variation of mesoscale structural features under pressure. For N_3-cycles and global clustering coefficient, the error bar shows the 95% confidence interval of the average from four subsamples for each material. For local clustering coefficient, the error bar shows the 95% confidence interval calculated on network nodes or edges of the combined set of the four subsamples.

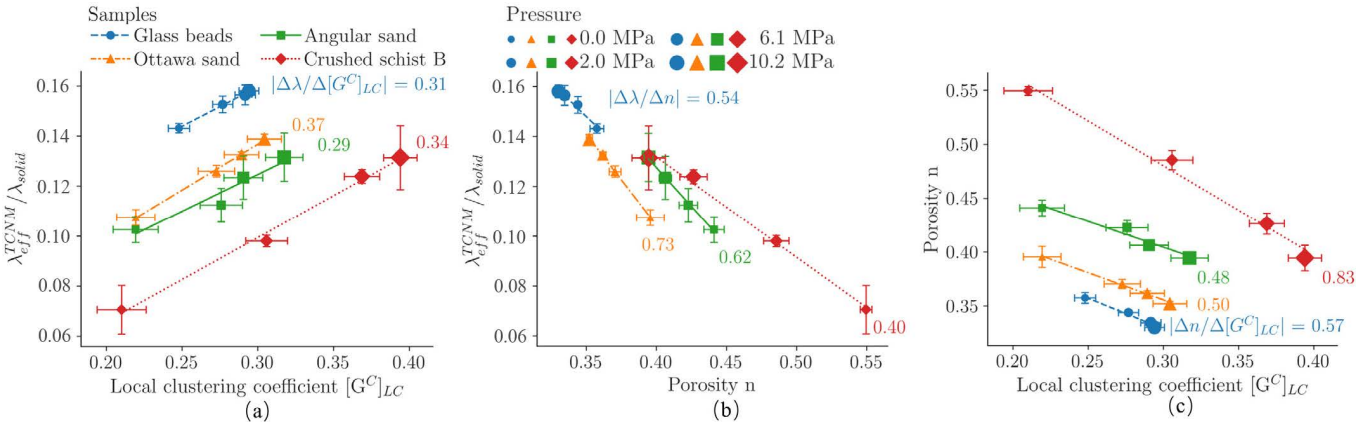

Fig. 15. The relationship between mesoscale local clustering coefficient, macroscale porosity and dimensionless λ_{eff}^{TCNM} calculated from TCNM. For thermal conductivity and porosity, the error bar shows the 95% confidence interval of the average from four subsamples for each material. For local clustering coefficient, the error bar shows the 95% confidence interval calculated on network nodes or edges of the combined set of the four subsamples.

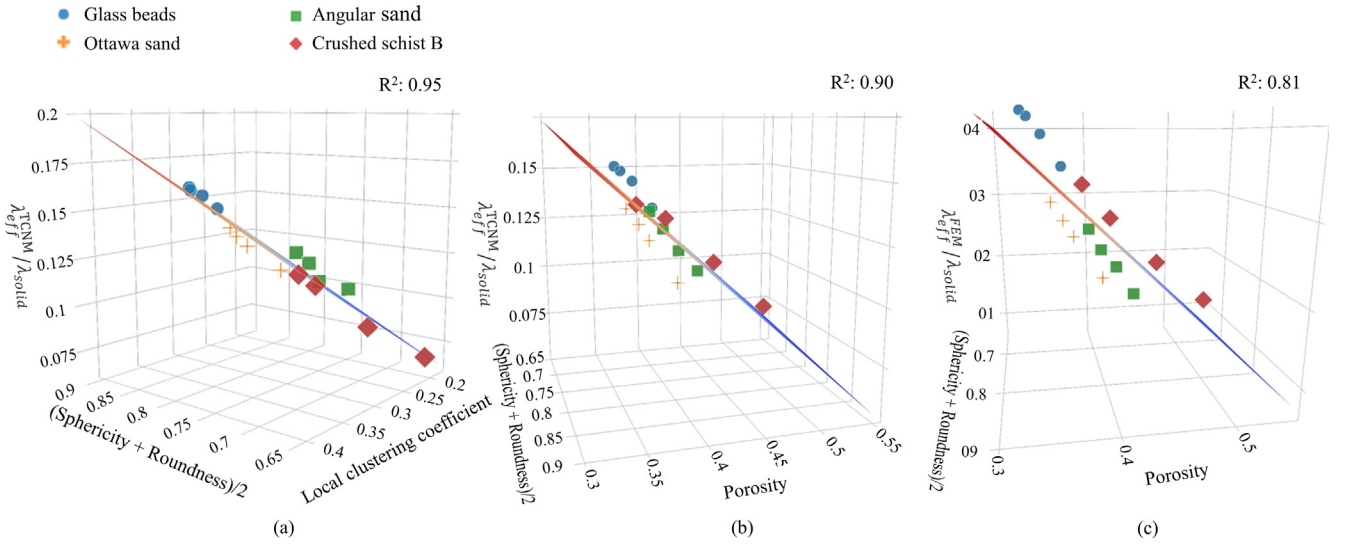

Fig. 16. The dimensionless λ_{eff}^{TCNM} shows a better relationship with particle shape and local clustering coefficient than with particle shape and porosity. (https://wenbinfei.github.io/research_demos/4-rigidity/).

from 0.29 in angular sand to 0.37 in Ottawa sand, which indicates that local clustering coefficient as a rigidity feature can capture the similar impacts of deformation on heat transfer in different materials. The relationship between the traditional porosity and normalized thermal conductivity is shown in Fig. 15(b). The λ_{eff}^{TCNM} decreases linearly for each sample. However, the decreasing rates exhibit differences of 0.40 in crushed schist B and 0.73 in Ottawa sand. As local clustering coefficient measures the density of triangles, a material with a larger local clustering coefficient means that it has more "triangles" and is denser. Hence the porosity reduces with the increase of local clustering coefficient as shown in Fig. 15(c).

Since particle shape affects the contact conductance and the observed importance in Fig. 15(a), the average sphericity and roundness were employed to extend Fig. 15(a) in three dimensions (Fig. 16(a)). A plane also fits the relationship between the rigidity variable (local clustering coefficient), particle shape and λ_{eff}^{TCNM}. The results show that the correlation coefficient is high at 0.95, which indicates that a rigid structure variable with particle shape descritpors can be used to predict well the effective thermal conductivity of granular materials under deformation Although still high, the correlation coefficient decreases to 0.90 if the traditional porosity is considered as the controlling variable instead of the local clustering coefficient (Fig. 16(b)). To show the robustness of TCNM and derived nonconventional features, the relationship between the two microstructural parameters and the λ_{eff}^{FEM} calculated using FEM is depicted in Fig. 16(c). After the linear regression, the correlation between them is lower, 0.81. The higher correlation coefficient in Fig. 16(b) is because TCNM values are closer to the experimental results as shown in Fig. 11.

5. Conclusions

This work investigated the impact of microstructure variation on effective thermal conductivity. A thermal conductance network model (TCNM) was used to calculate the effective thermal conductivity λ_{eff} of granular materials based on CT images. By comparing the results with those from FEM and experimental measurements, the TCNM was found to be robust and without as much overestimation as FEM when calculating λ_{eff}. Since TCNM is derived from the thermal network by adding thermal conductance at network edges, it has another advantage over FEM in that the contribution

of heat transfer from gaps and 'near-contacts' between particles can be identified. This work shows that this particular contribution is larger in irregular granular particles than in more rounded and regular particles at approximately 40% in crushed schist sand without loading. Additionally, three variables (3-cycle, global clustering coefficient and local clustering coefficient) from the contact network indicate the variation of the mesoscale structures of the granular packings under compaction. Comparing their variation in all samples with the increasing loading indicates that the local clustering coefficient may be best suited to quantify the 'rigidity' of granular materials. To make up for the shortcoming of the mesoscale rigidity parameter, which does not have a direct relation with the contact conductance, a microscale particle shape descriptor was calculated for each particle in the granular materials. The local clustering and particle shape show higher correlations with λ_{eff} (with a coefficient of correlation as high as 0.95) than the traditional porosities of the materials. Hence, a mesoscale rigidity variable with microsalce particle shape descriptors can capture the underlying mechanisms. They can also describe and be used to predict well λ_{eff} in granular materials at a variety of confinements.

Declaration of Competing Interest

The authors declared that there is no conflict of interest.

Acknowledgements

This research was undertaken in the Imaging and Medical Beam Line (IMBL) at the Australian Synchrotron, Victoria, Australia. The authors would like to acknowledge Dr Anton Maksimenko and the other beam scientists at Australian Synchrotron for their support during our experiments. The authors also thank Dr Tabassm Afshar and Dr Xiuxiu Miao for their support in collecting the CT images. The first author thanks The University of Melbourne for offering the Melbourne Research Scholarship.

References

[1] T.S. Yun, J.C. Santamarina, Fundamental study of thermal conduction in dry soils, Granular Matter 10 (3) (2008) 197.
[2] U. El Shamy, O. De Leon, R. Wells, Discrete element method study on effect of shear-induced anisotropy on thermal conductivity of granular soils, Int. J. Geomech. 13 (1) (2013) 57–64.
[3] Y. Asakuma, Y. Kanazawa, T. Yamamoto, Thermal radiation analysis of packed bed by a homogenization method, Int. J. Heat Mass Transf. 73 (2014) 97–102.
[4] C. Argento, D. Bouvard, Thermal conductivity of granular media, Powders & grains (1993) 129–134.
[5] R. Askari, S.H. Hejazi, M. Sahimi, Thermal conduction in deforming isotropic and anisotropic granular porous media with rough grain surface, Transp. Porous Media 124 (2018) 221–236.
[6] B. Aduda, Effective thermal conductivity of loose particulate systems, J. Mater. Sci. 31 (24) (1996) 6441–6448.
[7] M. Gangadhara Rao, D. Singh, A generalized relationship to estimate thermal resistivity of soils, Can. Geotech. J. 36 (4) (1999) 767–773.
[8] J. Côté, J.-M. Konrad, Thermal conductivity of base-course materials, Can. Geotech. J. 42 (1) (2005) 61–78.
[9] L. Fletcher, Recent developments in contact conductance heat transfer, J. Heat Transfer 110 (4b) (1988) 1059–1070.
[10] Y. Hu, J. Wang, J. Yang, I. Mudawar, Q. Wang, Experimental study of forced convective heat transfer in grille-particle composite packed beds, Int. J. Heat Mass Transf. 129 (2019) 103–112.
[11] A. Tordesillas, Q. Lin, J. Zhang, R. Behringer, J. Shi, Structural stability and jamming of self-organized cluster conformations in dense granular materials, J. Mech. Phys. Solids 59 (2) (2011) 265–296.
[12] L. Papadopoulos, M.A. Porter, K.E. Daniels, D.S. Bassett, Network analysis of particles and grains, J. Complex Networks 6 (4) (2018) 485–565.
[13] J. Scott, Social network analysis, Sociology 22 (1) (1988) 109–127.
[14] A.J. Liu, S.R. Nagel, W. Van Saarloos, M. Wyart, The jamming scenario—an introduction and outlook, in: L. Berthier, G. Biroli, J.-P. Bouchaud, L. Cipelletti, W. van Saarloos (Eds.), Dynamical Heterogeneities in Glasses, Colloids, and Granular Media, Oxford University Press, 2011, pp. 298–340, https://doi.org/10.1093/acprof:oso/9780199691470.003.0009.
[15] W. Dai, D. Hanaor, Y. Gan, The effects of packing structure on the effective thermal conductivity of granular media: a grain scale investigation, Int. J. Therm. Sci. 142 (2019) 266–279.
[16] G. Fu, S. Wilkinson, R.J. Dawson, A spatial network model for civil infrastructure system development, Comput.-Aided Civ. Infrastruct. Eng. 31 (9) (2016) 661–680.
[17] S. Argyroudis, J. Selva, P. Gehl, K. Pitilakis, Systemic seismic risk assessment of road networks considering interactions with the built environment, Comput.-Aided Civ. Infrastruct. Eng. 30 (7) (2015) 524–540.
[18] A. Bozza, D. Asprone, F. Parisi, G. Manfredi, Alternative resilience indices for city ecosystems subjected to natural hazards, Comput.-Aided Civ. Infrastruct. Eng. 32 (7) (2017) 527–545.
[19] H.M. Jaeger, T. Shinbrot, P.B. Umbanhowar, Does the granular matter?, Proc Natl. Acad. Sci. 97 (24) (2000) 12959–12960.
[20] M.E. Newman, The structure and function of complex networks, SIAM Rev. 45 (2) (2003) 167–256.
[21] J.H. van der Linden, G.A. Narsilio, A. Tordesillas, Machine learning framework for analysis of transport through complex networks in porous, granular media: a focus on permeability, Phys. Rev. E 94 (2) (2016) 022904.
[22] A.G. Smart, J.M. Ottino, Evolving loop structure in gradually tilted two-dimensional granular packings, Phys. Rev. E 77 (4) (2008) 041307.
[23] N. Rivier, Extended constraints, arches and soft modes in granular materials, J. Non-Cryst. Solids 352 (42–49) (2006) 4505–4508.
[24] R.M. Baram, H. Herrmann, N. Rivier, Space-filling bearings in three dimensions, Phys. Rev. Lett. 92 (4) (2004) 044301.
[25] J. Kim, Y.-R. Goo, I. Choi, S. Kim, D. Lee, Toward high-accuracy and high-applicability of a practical model to predict effective thermal conductivity of particle-reinforced composites, Int. J. Heat Mass Transf. 131 (2019) 863–872.
[26] A.M. Abyzov, A.V. Goryunov, F.M. Shakhov, Effective thermal conductivity of disperse materials. I. Compliance of common models with experimental data, Int. J. Heat Mass Transf. 67 (2013) 752–767.
[27] F. Liu, Y. Cai, L. Wang, J. Zhao, Effects of nanoparticle shapes on laminar forced convective heat transfer in curved ducts using two-phase model, Int. J. Heat Mass Transf. 116 (2018) 292–305.
[28] W. Fei, G.A. Narsilio, M.M. Disfani, Impact of three-dimensional sphericity and roundness on heat transfer in granular materials, Powder Technol. 355 (2019) 770–781.
[29] A. Abbas, M.E. Kutay, H. Azari, R. Rasmussen, Three-dimensional surface texture characterization of Portland cement concrete pavements, Comput.-Aided Civ. Infrastruct. Eng. 22 (3) (2007) 197–209.
[30] M.E. Kutay, A.H. Aydilek, Pore pressure and viscous shear stress distribution due to water flow within asphalt pore structure, Comput.-Aided Civ. Infrastruct. Eng. 24 (3) (2009) 212–224.
[31] M.R. Khelifa, S. Guessasma, New computational model based on finite element method to quantify damage evolution due to external sulfate attack on self-compacting concretes, Comput.-Aided Civ. Infrastruct. Eng. 28 (4) (2013) 260–272.
[32] G.A. Narsilio, J. Kress, T.S. Yun, Characterisation of conduction phenomena in soils at the particle-scale: Finite element analyses in conjunction with synthetic 3D imaging, Comput. Geotech. 37 (7) (2010) 828–836.
[33] L. Miettinen, P. Kekäläinen, T. Turpeinen, J. Hyväluoma, J. Merikoski, J. Timonen, Dependence of thermal conductivity on structural parameters in porous samples, AIP Adv. 2 (1) (2012) 012101.
[34] T.S. Yun, T.M. Evans, Three-dimensional random network model for thermal conductivity in particulate materials, Comput. Geotech. 37 (7–8) (2010) 991–998.
[35] R.K. Desu, A.R. Peeketi, R.K. Annabattula, Artificial neural network-based prediction of effective thermal conductivity of a granular bed in a gaseous environment, Comput. Particle Mech. 6 (3) (2019) 503–514.
[36] O. Birkholz, Y. Gan, M. Kamlah, Modeling the effective conductivity of the solid and the pore phase in granular materials using resistor networks, Powder Technol. 351 (2019) 54–65.
[37] J.H. van der Linden, G. Narsilio, A. Tordesillas, Thermal conductance network model for computerised tomography images of real geomaterials (Under review), Comput. Geotech. (2019).
[38] ASTM, C778-17 standard specification for standard sand, ASTM International, West Conshohocken, PA, 2017.
[39] A. VandenBerg, The Tasman Fold Belt system in Victoria: geology and mineralisation of Proterozoic to Carboniferous rocks, Geological Survey of Victoria, 2000.
[40] T. Afshar, M. Disfani, G. Narsilio, A. Arulrajah, Changes to Grain Properties due to Breakage in a Sand Assembly using Synchrotron Tomography, in: EPJ Web of Conferences, EDP Sciences, 2017, pp. 07004.
[41] B. Persson, O. Albohr, U. Tartaglino, A. Volokitin, E. Tosatti, On the nature of surface roughness with application to contact mechanics, sealing, rubber friction and adhesion, J. Phys.: Condens. Matter 17 (1) (2004) R1.
[42] M. Wiebicke, E. Andò, I. Herle, G. Viggiani, On the metrology of interparticle contacts in sand from x-ray tomography images, Meas. Sci. Technol. 28 (12) (2017) 124007.
[43] N. Otsu, A threshold selection method from gray-level histograms, IEEE transactions on systems, man, and cybernetics 9 (1) (1979) 62–66.
[44] S. Schlüter, A. Sheppard, K. Brown, D. Wildenschild, Image processing of multiphase images obtained via X-ray microtomography: a review, Water Resour. Res. 50 (4) (2014) 3615–3639.
[45] Z. Karatza, E. Andò, S. Papanicolopulos, J. Ooi, G. Viggiani, Evolution of deformation and breakage in sand studied using X-ray tomography, Géotechnique 1 (2018) 1–11.

[46] J. Schindelin, I. Arganda-Carreras, E. Frise, V. Kaynig, M. Longair, T. Pietzsch, S. Preibisch, C. Rueden, S. Saalfeld, B. Schmid, Fiji: an open-source platform for biological-image analysis, Nat. Methods 9 (7) (2012) 676.
[47] D. Legland, I. Arganda-Carreras, P. Andrey, MorphoLibJ: integrated library and plugins for mathematical morphology with ImageJ, Bioinformatics 32 (22) (2016) 3532–3534.
[48] H. Kim, C.T. Haas, A.F. Rauch, C. Browne, 3D image segmentation of aggregates from laser profiling, Comput.-Aided Civ. Infrastruct. Eng. 18 (4) (2003) 254–263.
[49] H. Taylor, C. O'Sullivan, W. Sim, A new method to identify void constrictions in micro-CT images of sand, Comput. Geotech. 69 (2015) 279–290.
[50] J. Fonseca, C. O'Sullivan, M.R. Coop, P. Lee, Non-invasive characterization of particle morphology of natural sands, Soils Found. 52 (4) (2012) 712–722.
[51] D.J. Watts, S.H. Strogatz, Collective dynamics of 'small-world'networks, Nature 393 (6684) (1998) 440.
[52] G.K. Batchelor, R. O'brien, Thermal or electrical conduction through a granular material, Proc. R. Soc. Lond. A 355 (1682) (1977) 313–333.
[53] M. Shapiro, V. Dudko, V. Royzen, Y. Krichevets, S. Lekhtmakher, V. Grozubinsky, M. Shapira, M. Brill, Characterization of powder beds by thermal conductivity: effect of gas pressure on the thermal resistance of particle contact points, Part. Part. Syst. Char. 21 (4) (2004) 268–275.
[54] R. Askari, S. Taheri, S.H. Hejazi, Thermal conductivity of granular porous media: a pore scale modeling approach, AIP Adv. 5 (9) (2015).
[55] R. Bauer, E. Schlunder, Effective radial thermal-conductivity of packings in gas flow, Part -ii: Thermal conductivity of packing fraction without gas flow, Int. Chem. Eng. 18 (2) (1978) 189–204.
[56] J.T. Gostick, Versatile and efficient pore network extraction method using marker-based watershed segmentation, Phys. Rev. E 96 (2) (2017) 023307.
[57] J. Sundberg, P.-E. Back, L.O. Ericsson, J. Wrafter, Estimation of thermal conductivity and its spatial variability in igneous rocks from in situ density logging, Int. J. Rock Mech. Min. Sci. 46 (6) (2009) 1023–1028.
[58] G.A. Narsilio, O. Buzzi, S. Fityus, T.S. Yun, D.W. Smith, Upscaling of Navier-Stokes equations in porous media: theoretical, numerical and experimental approach, Comput. Geotech. 36 (7) (2009) 1200–1206.
[59] G. Narsilio, T. Yun, J. Kress, T. Evans, Hydraulic and thermal conduction phenomena in soils at the particle-scale: towards realistic FEM simulations, in: IOP Conference Series: Materials Science and Engineering, IOP Publishing, 2010, p. 012086.
[60] Simpleware Ltd., Simpleware ScanIP, http://www.simpleware.com/software/scanip, Date of access, 15, (2015) 12.
[61] COMSOL AB, COMSOL multiphysics v5.0, http://www.comsol.com, 2015.
[62] ASTM D5334-14, Standard Test Method for Determination of Thermal Conductivity of Soil and Soft Rock by Thermal Needle Probe Procedure, in, ASTM International, West Conshohocken, PA, 2014
[63] T. Brandon, J. Mitchell, Factors influencing thermal resistivity of sands, J. Geotech. Eng. 115 (12) (1990) 1683–1698.
[64] H. Wadell, Volume, shape, and roundness of rock particles, J. Geol. 40 (5) (1932) 443–451.
[65] G. Taubin, Curve and surface smoothing without shrinkage, in: Computer Vision, 1995. Proceedings., Fifth International Conference on, IEEE, 1995, pp. 852–857.
[66] B. Zhou, J. Wang, H. Wang, Three-dimensional sphericity, roundness and fractal dimension of sand particles, Géotechnique 68 (1) (2017) 18–30.
[67] W. Woodside, J. Messmer, Thermal conductivity of porous media. I. Unconsolidated sands, J. Appl. Phys. 32 (9) (1961) 1688–1699.
[68] M. Moscardini, Y. Gan, S. Pupeschi, M. Kamlah, Discrete element method for effective thermal conductivity of packed pebbles accounting for the Smoluchowski effect, Fusion Eng. Des. 127 (2018) 192–201.
[69] W. Dai, S. Pupeschi, D. Hanaor, Y. Gan, Influence of gas pressure on the effective thermal conductivity of ceramic breeder pebble beds, Fusion Eng. Des. 118 (2017) 45–51.
[70] J. Choo, Y.J. Kim, J.H. Lee, T.S. Yun, J. Lee, Y.S. Kim, Stress-induced evolution of anisotropic thermal conductivity of dry granular materials, Acta Geotech. 8 (1) (2013) 91–106.
[71] J.W. Anthony, R.A. Bideaux, K.W. Bladh, M.C. Nichols, Handbook of Mineralogy, Mineral Data Publ., Tucson, 1990.
[72] D. Wei, B. Zhao, D. Dias-da-Costa, Y. Gan, An FDEM study of particle breakage under rotational point loading, Eng. Fract. Mech. (2019).
[73] G.-C. Cho, J. Dodds, J.C. Santamarina, Particle shape effects on packing density, stiffness, and strength: natural and crushed sands, J. Geotech. Geoenviron. Eng. 132 (5) (2006) 591–602.

Page intentionally left blank

Chapter 5: Application of complex network theory to heat transfer

5.1 OVERVIEW AND STRUCTURE

Chapter 4 shows that contact network features can quantify interparticle rigidity structures. The contact network feature together with particle shape which is related to the interparticle contact area can be used to predict λ_{eff}. However, *3-cycle* and *clustering coefficient* in chapter 4 are only one type of network features based on a contact network. A contact network does not directly account for heat transfer via the small gaps between adjacent particles. This limitation can be overcome by building and using a thermal network (Desu et al. 2019; Yun and Evans 2010).

In this chapter, granular materials are represented by both contact networks and thermal networks. From the networks, additional network features are explored using complex network theory to characterise the particle arrangement and evaluate their importance to λ_{eff}. Since some weights can be added to each edge in a network, this chapter also aims to find single parameters that can characterise both the particle connectivity and particle contact quality by considering contact area or thermal conductance as the weight. Furthermore, the contact network features and thermal network features are compared, and the limitations of each approach are identified.

This chapter includes the application of complex network theory to heat transfer in sphere packings and sands, respectively. The studies are summarised in two manuscripts entitled: (1) 'Network analysis of heat transfer in sphere packings' published *in Powder Technology*; and (2) 'Network analysis of heat transfer in sands' which has been submitted to *Computers and Geotechnics.* The papers have different focuses, but they are interrelated and use lessons from papers in previous chapters and thus use some shared samples and methods.

5.2 NETWORK ANALYSIS OF HEAT TRANSFER IN SPHERE PACKINGS

Powder Technology 362 (2020) 790–804

Contents lists available at ScienceDirect

Powder Technology

journal homepage: www.elsevier.com/locate/powtec

Network analysis of heat transfer in sphere packings

Wenbin Fei, Guillermo A. Narsilio *, Joost H. van der Linden, Mahdi M. Disfani

Department of Infrastructure Engineering, The University of Melbourne, Parkville, Australia

ARTICLE INFO

Article history:
Received 13 September 2019
Received in revised form 8 November 2019
Accepted 29 November 2019
Available online 30 November 2019

Keywords:
Complex network theory
Graph theory
Heat transfer
Machine learning
Microstructure

ABSTRACT

Porosity-dependent models can be used to predict the effective thermal conductivity (ETC) of particulate materials. However, they cannot directly account for microstructural features such as particle connectivity and interparticle contact area. Complex network theory can be used to extract network features as microstructural characteristics. However, these features have not been used to study heat transfer. In this work, both contact network and thermal networks are constructed for mono-disperse and poly-disperse sphere packings. Network features are extracted using complex network theory and machine learning techniques are applied to investigate the correlation between these features and the ETC. The most relevant thermal and contact network features for predicting thermal conductivity are identified. The network features capturing both interparticle connectivity and contact quality, such as "weighted degree", show high correlation with ETC. Furthermore, random forest regression results show that involving multi-network features in a model enhances the accuracy in predicting ETC.

1. Introduction

Heat transfer in geomaterials is a dominant process in the design and construction of various engineering applications including geothermal engineering [1], petroleum engineering [2], carbon dioxide geology storage [3] and radioactive waste disposal [4]. The thermal conductivity λ is a key parameter used to describe and quantify heat transfer processes commonly encountered in many of the above applications. Hence, understanding and being able to accurately estimate the effective thermal conductivity (ETC) of geomaterials are of great importance.

Models [5–13] used to predict the ETC of static granular materials can be roughly classified into two types: mixing-law models and packing structure models. *Mixing-law models* combine the thermal conductivity of the different phases found in the materials based on solid volume fraction or porosity to estimate an overall ETC. Examples of models related to the volume fractions of the solid are series models [14], parallel models [14] and geometric mean models [15]. Porosity-dependent models are summarised by Abdulagatova et al. [11]. However, solid volume fraction and porosity are characteristics at the sample scale, leading mixing-law models to potentially neglecting the effect of microstructure [5,16–19]. Most of these models can be used only within certain limited ranges of porosity. They are rarely valid for the entire (wide) porosity range encountered in materials, especially for materials with large solid-fluid thermal conductivity ratio ($\lambda_s/\lambda_f \to \infty$) [11]. For instance, Maxwell's model [20] is proposed to predict the ETC of randomly distributed and non-interacting spheres packings with large porosity. Modifications are required, though, for the model to be valid for medium porosity [21] and low porosity materials [22].

As an alternative, *packing structure models* are employed to predict ETC by replacing porosity with certain structural characteristics. A better understanding of the microstructure in granular materials can also assist in designing artificial (granular) materials [23–25]. Batchelor and O'Brien [26] found that heat flux was related to the minimum gap between particles and the mean of the particles' local curvature. Finney [27] introduced a method to measure particle connectivity using Voronoi tessellation and Cheng et al. [28] proposed two models based on the connectivity of particles. These models are valid in a wide range of solid-fluid thermal conductivity ratios. However, these works were performed based on mono-sized sphere packings. Later, Siu and Lee [29] investigated dry simple cubic (SC), body-centered cubic (BCC) and face-centered cubic (FCC) packings and found that the ETC of a disperse sphere packing bed was related to one of these structures and had a linear relationship with contact radius ratio (the ratio of contact radius to particle radius) under the chosen structure. However, to use these models for other granular materials, one must first match their porosity and microstructure to the closest one of SC, BCC or FCC and estimate the contact radius ratio of these materials before using the proposed relationship. Therefore, parameters are required to characterise the microstructure of granular materials and their correlations with ETC need to be investigated.

Complex network theory is available to characterise the microstructure and connectivity based on the network built according to the topology of a material [30,31]. A network is a collection of nodes that are linked by edges. Different networks can be constructed and the

* Corresponding author at: Engineering Block B 208, Department of Infrastructure Engineering, The University of Melbourne, Parkville, VIC 3010, Australia.
E-mail address: narsilio@unimelb.edu.au (G.A. Narsilio).

https://doi.org/10.1016/j.powtec.2019.11.123
0032-5910/

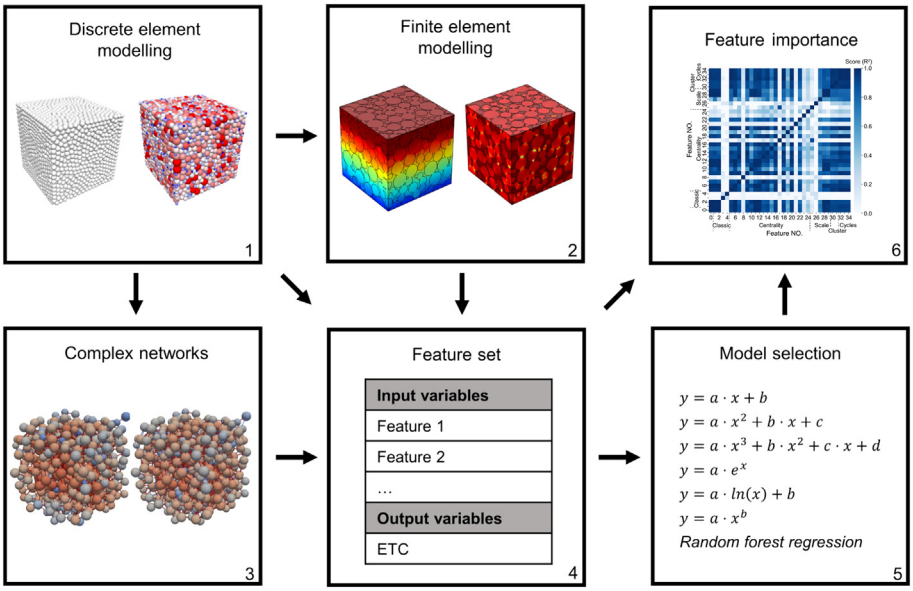

Fig. 1. Mono-disperse and poly-disperse sphere packings are generated in step 1. Heat transfer is simulated using the finite element method to calculate the effective thermal conductivity (ETC) in step 2. In step 3, a contact network and a thermal network are constructed for each packing; then complex network theory is used to extract network features. In step 4, classic physical parameters, network features and ETC are collected. Machine learning techniques are used to select the proper model for each feature to find its correlation coefficient with ETC in step 5. Finally, the relative importance of each feature is computed and compared.

meanings of nodes and edges change along with the type of the network. For example, in a pore network, a node is created to represent a pore and an edge represents a pore throat connecting them [32]. In a contact network, each node indicates a particle and an edge connects two nodes when two particles are in contact [31]. Newman [33] reviewed the theory, development and applications of complex network theory. Tools arising from complex network theory have the advantage of capturing succinct, inherent multi-scale properties to present the structure, topology, dynamics and functionality of the network [34].

In geotechnical engineering, complex network theory has been applied to investigate the behaviours of granular materials such as mechanical stability and fluid flow. Russell et al. [35] proved that contact networks and pore networks contained important information about the jamming-unjamming dynamics and preferential paths in a deforming granular material, respectively. Van der Linden et al. [31] quantified the connectivity of the pores and particles using a pore network and a particle contact network, respectively, and then applied machine learning techniques to study their correlations to fluid flow. The network features extracted from a contact network may be correlated well to heat transfer because heat conducts primarily through the contact area between particles. However, heat also conducts through small gaps [13] between particles and this gap is not considered in a classical contact network. A *thermal* network that considers these small gaps or 'near contacts' was built [36,37] to compute the ETC of sphere packings. Although contact networks and thermal networks have been built for spherical granular materials, complex network theory has not been employed to extract microstructure and connectivity features and to characterise heat transfer in granular materials.

Table 1
Simulation parameters used in PFC.

Grain shape	Spherical
Density [kg/m^3]	2550
Local damp coefficient	0.7
Friction coefficient	0
Grain radius [mm]	0.3 for mono-disperse packings 0.1–0.5 for poly-disperse packings
Porosity	0.14–0.35

This work aims to identify the most relevant network features for predicting ETC in dry granular materials. Firstly, mono-disperse and poly-disperse sphere packings are generated using a discrete element method (DEM) and networks representing these packings are derived. Then the network features and ETC of each packing are computed with complex network theory and the finite element method, respectively. Network features are computed both for the contact network and the thermal network. Machine learning techniques are then employed to investigate the correlation of network features with the ETC. Next, the importance of individual network features to the ETC for mono-disperse and poly-disperse packings are analysed. The general performance of network features on all samples is also investigated.

2. Methods

A framework that integrates several techniques is proposed to identify the most relevant physical variables and (new) network features affecting heat transfer in granular materials using complex network theory (Fig. 1). In step 1, DEM is used to generate synthetic mono-disperse and poly-disperse sphere packings. These various packings are used both to compute the ETC via the finite element method in step 2 and to construct networks and extract network features using complex network theory in step 3. Then, the calculated features are collected in step 4 and used in several machine learning algorithms to

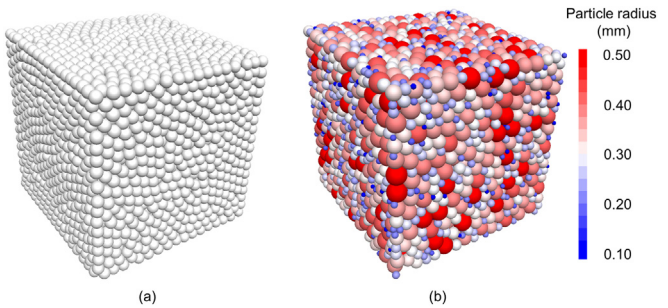

Fig. 2. Sphere packings are generated in PFC (a) mono-disperse packing, (b) poly-disperse packing. Both of the two packings have the porosity of 0.28.

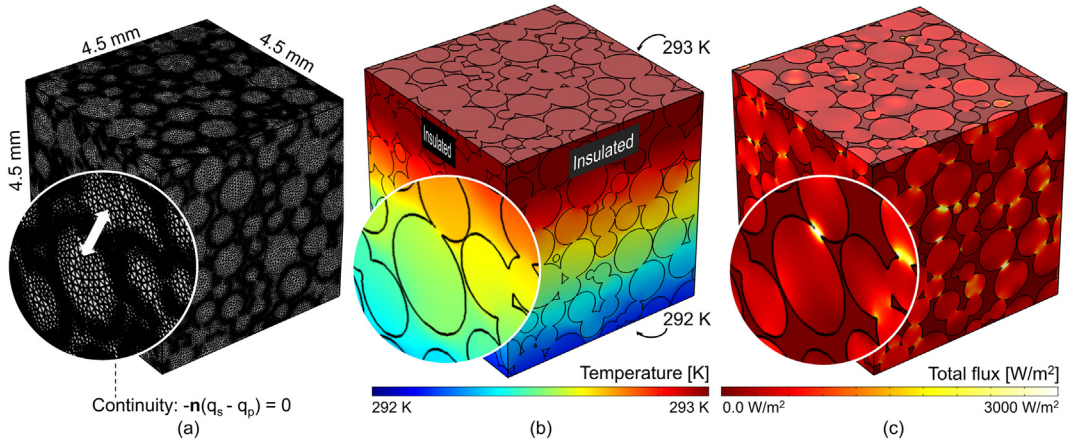

Fig. 3. Finite element mesh and heat transfer simulation results (a) mesh generated from Simpleware ScanIP, (b) temperature distribution, and (c) heat flux distribution.

select the 'best fit' model for each feature in step 5. Finally, the importance of the features is analysed and compared in step 6. The details of each component in this framework are discussed in the following subsections.

2.1. Discrete element modelling

Numerical mono-disperse and poly-disperse assemblies are constructed using the PFC software [38]. Spheres are assembled in a cubic box with dimensions of 10 × 10 × 10 *mm*. Twenty-four mono-disperse and twenty-four poly-disperse packings are generated using the parameters shown in Table 1. The porosity in PFC can be used as an input parameter to generate each assembly. The friction coefficient is selected as zero in this work to enhance the particle rearrangement. Spheres in dense mono-disperse packings may overlap to simulate changing interparticle contact area [36,39] which is important in heat transfer. Representative element volume (REV) subsamples with dimensions of 4.55 × 4.55 × 4.55 *mm* are sampled from the centre of the assemblies. The selected REV size results in a REV/D_{50} ratio of 7.6 × 7.6 × 7.6 which is larger than 5.8 × 5.8 × 3 as previously suggested in paper [39] and 7.1 × 7.1 × 3.6 used in paper [40]. The total number of particles in our model (~280) is almost three times the value recommended by Kanit et al. (2003) [41]. Examples of the assemblies of mono-disperse and poly-disperse packings are shown in Fig. 2.

2.2. Finite element simulation

The geometry of each sample constructed with PFC is imported into Simpleware ScanIP [42] to generate finite element meshes. A mesh size sensitivity analysis was conducted in previous related works by the authors [43,44] to ensure that the computed ETC convergences to an asymptotic value. In this work, the mesh comprises 9,516,529 tetahedral elements as shown in Fig. 3 (a). The number of the elements across the particle (average) diameter is approximately 28. The selection of D_{50}/(mesh size) ≈ 28 is larger than that in simulating fluid flow in heterogeneous sandstone (D_{50}/(mesh size) ≈ 10 as suggested in paper [45] and 17.6 as suggested in paper [46]) and in simulating heat transfer (D_{50}/(mesh size) ≈ 17 in paper [39]). As a result, the mesh size selected here is considered small enough for computing a reasonable accurate thermal conductivity. Once created, the finite element meshes are transferred to COMSOL Multiphysics [47] to simulate heat transfer by solving [48]:

$$\rho C \frac{\partial T}{\partial t} + \rho C u \cdot \nabla T = \nabla \cdot (\lambda \nabla T) + Q \tag{1}$$

where, for each phase involved in the simulation (solid grains, air or water in the pore space), ρ is the density [kg/m^3], C is the heat capacity [J/(kg K)], T is the temperature [K], t is the time [s], u is the velocity vector [m/s], λ is the thermal conductivity [W/(m K)]. The thermal conductivity of the solid phase is taken as 3 W/(m K) [13,36,49] and the air thermal conductivity, as 0.025 W/(m K) in this work, Q is the heat sources [W/m^3], nil in all cases analysed here, but included for completeness.

The conductive heat flux vector q can be computed using the simplest form of Fourier's law:

$$q = \lambda \nabla T \tag{2}$$

Additionally, to ensure the continuity at the particle-pore interface, a continuity equation is used to compensate the system [39]:

$$-n\left(q_s - q_p\right) = 0 \tag{3}$$

where n is the unit normal vector of the solid-pore interface, q_s and q_p are the heat fluxes in the particle and pore, respectively.

All samples are simulated using the same heat transfer model and boundary conditions. An example of the mesh and simulation results are shown in Fig. 3. The boundary temperature on the top is 293 K while the temperature on the bottom is 292 K, to generate a small temperature gradient along the vertical axis. Other boundaries are set as insulated. Given the heat fluxes at inlet and outlet planes, the ETC on these two boundaries can be computed using [39]:

$$\lambda_{eff} = \frac{\frac{1}{A}\int_A Q_z \, dA}{\frac{T_a - T_b}{L}} \tag{4}$$

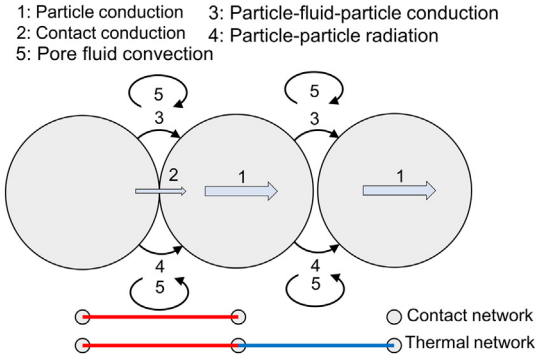

Fig. 4. Heat conducts through not only the physical contact(s) between particles (path 2) but also through the pore space (paths 3, 4 and 5). Hence, an edge is also assigned to the near-contact in a thermal network.

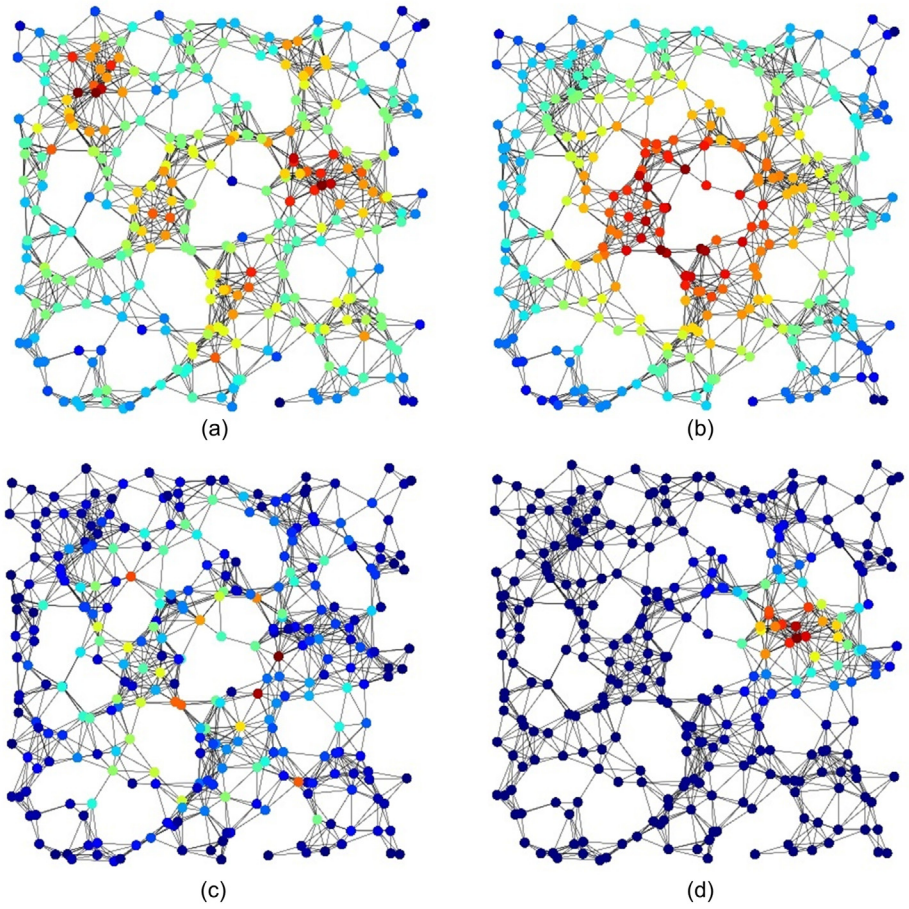

Fig. 5. Example of the same contact network and its different centrality values for nodes: (a) Degree, (b) Closeness centrality, (c) Betweenness centrality and (d) Eigenvector centrality. Each definition of centrality highlights different significances of centrality at nodes. The colour shows the value of each feature, red means high value while blue represents low value. (For interpretation of the references to colour in this figure legend, the reader is referred to the web version of this article.)

where λ_{eff} is the ETC of a sample [W/(m K)], A is the horizontal cross-section area of the sample [m^2], $T_a = 293$ K and $T_b = 294$ K at the inlet and outlet boundary temperatures, L is the height of the sample [m], Q_z is the vertical heat flux of nodes at the inlet or outlet [W/m^2].

Finally, the average value of the two thermal conductivities at the inlet and outlet is taken as the ETC of the whole sample.

2.3. Complex network features

A *contact* network is built by allocating a node at each particle centroid and an edge is created when particles are in contact (shown at the bottom of Fig. 4). In dry granular materials, heat travels not only within particles (path 1 in Fig. 4) and through the interparticle contact area (path 2 in Fig. 4) but also via particle-fluid-particle conduction (path 3 in Fig. 4), particle-particle radiation (path 4 in Fig. 4) and pore fluid convection (path 5 in Fig. 4). As radiation becomes important after the temperature is above 1000 K and convection mode is relevant when D_{50} is larger than 6 mm [13,50], heat transfer is mostly attributed to conduction [13,51] in dry granular materials. Therefore, a *thermal* network is established by assigning nodes to particle centroids and allocating edges to both the real contacts (schematically in red in Fig. 4) and near-contacts (schematically in blue in Fig. 4), similar to what is proposed in paper [36].

Once the networks are built, complex network theory is employed to extract multiscale network features. The network

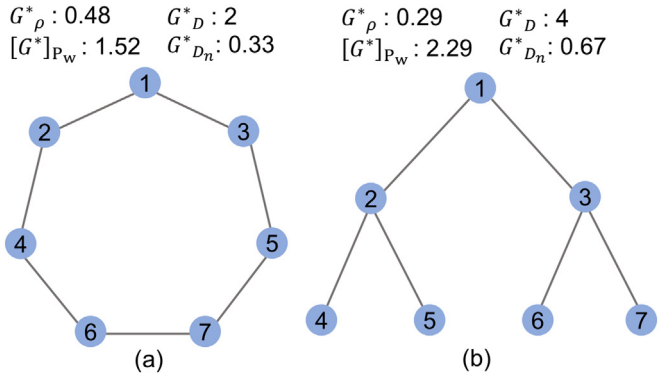

Fig. 6. Network diameter and average shortest path length can indicate the network structure: (a) a ring type network and (b) and tree like network with the same number of nodes shown as examples.

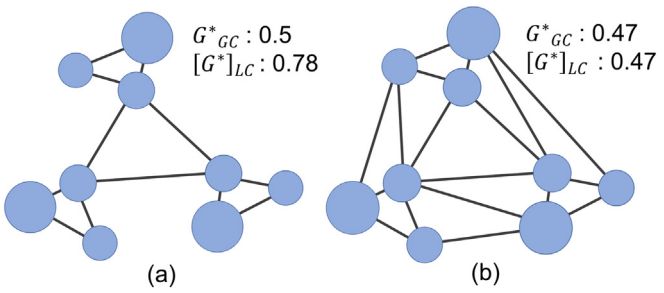

Fig. 7. Clustering features example: an integrated network (a) shows lower clustering coefficients than a fractured network (b).

features can be categorised into four types: (1) Centrality, (2) Network scale, (3) Cycle and (4) Clustering.

2.3.1. Centrality

Centrality indicates the node position and the "significance" of a node in the network, with varying types of centrality defining this significance in distinct ways. Five metrics for measuring centrality are calculated in this paper: *degree, closeness centrality, node betweenness centrality, edge betweenness centrality and eigenvector centrality*. The *degree* $\kappa(i)$ of a node is measured as the number of edges linked to a node. The *degree* calculated from the contact network is the well-known *coordination number*.

Closeness centrality is a measure of the distance of a node to all others. A node with high *closeness centrality* $[G^*]_C$ indicates it is at a 'central' position. If using V to indicate the set of vertices in networks, the *closeness centrality* of *node* $i \in V$ can be computed as [52]:

$$[G^*]_C(i) = \beta\left[\sum_{j=1}^{|V|-1} d(i,j)\right]^{-1} \tag{5}$$

where $d(i,j)$ is the shortest path between node $i, j \in V$ and β is a normalisation term. β is set as the number of reachable nodes ($|V| - 1$) and as the number of max possible edges $[|V|(|V| - 1)]/2$ in this work, respectively.

Table 2
Feature notation.

Type	No.	Notation	Attribute
Classic	1	n	Porosity
	2	γ	Contact radius ratio
	3	C_u	Coefficient of uniformity
	4	C_c	Coefficient of curvature
Centrality	5	$[G^*]_\kappa$	Degree
	6	$[G^*]_{\kappa_w}$	Weighted Degree
	7	$[G^*]_C$	Closeness centrality
	8	$[G^*]_{C_{n1}}$	Closeness centrality normalised by $\|V\| - 1$
	9	$[G^*]_{C_{n2}}$	Closeness centrality normalised by $[\|V\|(\|V\| - 1)]/2$
	10	$[G^*]_{C_w}$	Weighted closeness centrality
	11	$[G^*]_{C_{nw1}}$	Weighted closeness centrality normalised by $\|V\| - 1$
	12	$[G^*]_{C_{nw2}}$	Weighted closeness centrality normalised by $[\|V\|(\|V\| - 1)]/2$
	13	$[G^*]_{B^{node}}$	Node betweenness centrality
	14	$[G^*]_{B_n^{node}}$	Normalised node betweenness centrality
	15	$[G^*]_{B_w^{node}}$	Weighted node betweenness centrality
	16	$[G^*]_{B_{nw}^{node}}$	Normalised weighted node betweenness centrality
	17	$[G^*]_{B^{edge}}$	Edge betweenness centrality
	18	$[G^*]_{B_n^{edge}}$	Normalised edge betweenness centrality
	19	$[G^*]_{B_w^{edge}}$	Weighted edge betweenness centrality
	20	$[G^*]_{B_{nw}^{edge}}$	Normalised weighted edge betweenness centrality
	21	$[G^*]_{B_w^{edgetp}}$	Weighted top-to-bottom edge betweenness centrality average
	22	$[G^*]_{B_{nw}^{edgetp}}$	Normalised weighted top-to-bottom edge betweenness centrality average
	23	$[G^*]_E$	Eigenvector centrality
	24	$[G^*]_{E_w}$	Weighted eigenvector centrality
Network scale	25	G_ρ^*	Network density
	26	G_D^*	Network diameter
	27	$G_{D_n}{}^*$	Normalised network diameter
	28	$[G^*]_{P_w}$	Weighted shortest path (average)
	29	$[G^*]_{P_w^{tp}}$	Weighted shortest path from between nodes at inlet and outlet (average)
Clustering	30	$G^*{}_{GC}$	Global clustering coefficient
	31	$[G^*]_{LC}$	Local clustering coefficient
Cycles	32	G_{3C}^*	The number of 3-cycles
	33	$[G^*]_{3C^{node}}$	Average number of node 3-cycles
	34	$[G^*]_{3C^{edge}}$	Average number of edge 3-cycles

Note that $[G^*]$ is a unified indicator of a network feature, specifically, $[G^C]$ [55] means a feature is calculated from the contact network while $[G^T]$ means a feature is based on the thermal network. The brackets in $[G^*]$ are used to denote the average value of a parameter. Degree $[G^C]_\kappa$ computed from the contact network is equivalent to the well-known classic coordination number.

Betweenness centrality characterises the importance of a node or an edge as the bridge between other nodes or edges in a network. A node with high *node betweenness centrality* or an edge with high *edge betweenness centrality* means that it is important for heat to transfer through. *Betweenness centrality* $[G^*]_B$ of a node or an edge is computed as [53]:

$$[G^*]_{B^{node}}(i) = \beta\sum_{j,k\in V}\frac{\sigma(j,k|i)}{\sigma(j,k)} \tag{6}$$

where $\sigma(j,k)$ is the total number of shortest paths from node j to k, $\sigma(j, k|i)$ is the number of shortest paths from node j to k and overpass i. Similarly, the *edge betweenness centrality* can be calculated by computing $\sigma(j, k|e)$ as the number of shortest paths from node j to k that overpass edge e. β is a normalisation term, equal to $2/[|V - 1|(|V| - 2)]$ for *node betweenness centrality* and $2/[|V|(|V| - 1)]$ for *edge betweenness centrality*.

Eigenvector centrality considers the contribution of nodes to the connectivity of the whole network and indicates the node which has wide-reaching influence in a network. Relative scores are assigned to all nodes in a network and the score is high if a node is highly connected to other nodes who also have high score [54].

Fig. 5 illustrates the difference between different centrality features in the same network. A node has a high degree but may have low eigenvector centrality if edges hold similar low score. In a social network, a node with high betweenness centrality also may have low eigenvector centrality if it is away from the power centres in the network.

2.3.2. Network scale

Network scale is a measure indicating the average distance of one node from another in a network. This information is used to interpret how rapidly something can spread through a network. Network diameter and average shortest path length can be used to present the network scale. More nodes are reachable in a network with a smaller network diameter and smaller average shortest path length. The two different networks in Fig. 6 have the same number of nodes. However, from node 1 to the bottom of the network, four other nodes are reachable in two steps in the ring network (a) while six other nodes can be reached in two steps in the tree network (b). Furthermore, it takes two steps to reach the end in the tree network, while three steps are required to reach the end (node 7) in a ring network. In other words, a process (e.g. heat transfer) propagates faster in the tree network (b) than in the ring network (a). Network scale can be quantified by *Network diameter* G_D^*, *average shortest path length* $[G^*]_{P_w}$ and *network density* G_ρ^*. *Network diameter* G_D^* is the longest one of the shortest paths between two nodes in the network and it can be normalised by $|V|-1$ to be $G_{D_n}{}^*$. Apart from using the *average weighted shortes path* $[G^*]_{P_w}$ in this work, we also introduce the *average shortest path length between nodes at inlet and outlet* $[G^*]_{P_w^{tp}}$ because it resembles a heat transfer path.

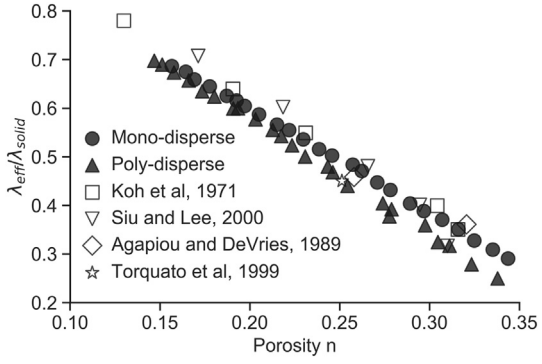

Fig. 8. Computed ETC for mono-disperse and poly-disperse packings in this work (solid symbols) show good agreement with those found in the literature (hollow symbols).

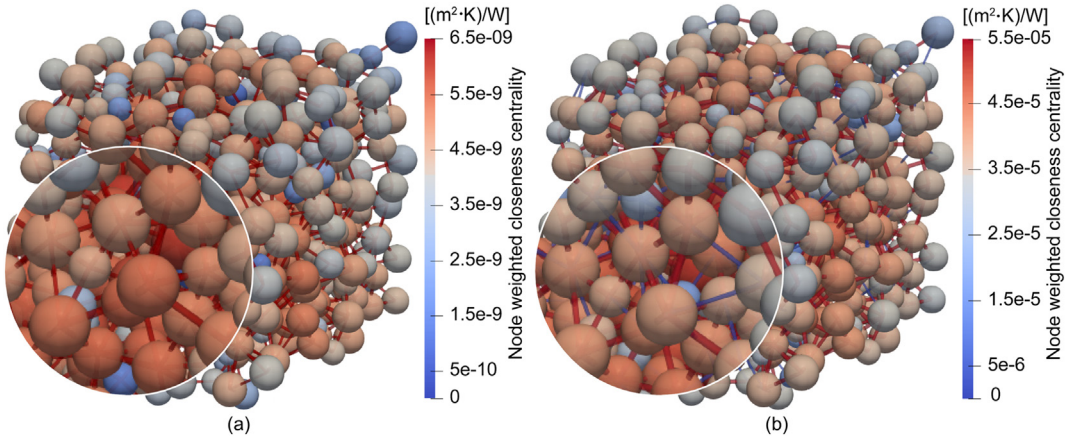

Fig. 9. Networks of the poly-disperse sample with porosity 0.246: (a) Contact network, (b) Thermal network. The colour at nodes represents the node weighted closeness centrality while the colour at edges represents the type of edge (red edges represent particle contacts while the blue edges represent near-contacts). The node size is scaled by particle radius. (For interpretation of the references to colour in this figure legend, the reader is referred to the web version of this article.)

Moreover, we employ *network density* G^*_ρ, which describes the ratio of the actual edge number to the potential edge number in a network,

$$G^*_\rho = \frac{|E|}{|V| \cdot (|V|-1)} \tag{7}$$

where E is the set of edges in a network.

2.3.3. Cycles

A cycle in a network is a loop of edges that starts and ends at the same node. An *l-cycle* is a cycle containing *l* edges. By assuming straight edges between nodes, a *3-cycle* is a triangle. Cycles in granular materials help describe the mesoscale structure of networks [55–58] which make them appealing since mesoscale features are vital to the behaviour of granular systems [59]. For instance, a triangle is an inherently rigid structure, so the number of *3-cycle* in contact network can hint the rigidity of granular materials [44,60].

2.3.4. Clustering

Clustering implies how integrated or fractured the overall network system is. *Clustering coefficients* are calculated as the *degree* of local clusters. Global clustering coefficient G^*_{GC} [34] measures the density of the triangles in a network using Eq. (8) while the local clustering coefficient $[G^*]_{LC}$ in Eq. (9) [61] quantifies the fraction of triangles through each node [44]:

$$G^*_{GC} = 3\frac{number\ of\ triangles}{number\ of\ connected\ triples} \tag{8}$$

where a triple means that three nodes can generate either three edges or two edges.

$$[G^*]_{LC}(i) = \frac{2T(i)}{\kappa(i)[\kappa(i)-1]} \tag{9}$$

where $T(i)$ is the number of triangles (or *3-cycles*) through node *i*, and $\kappa(i)$ is the degree of node *i*.

A network with a high *clustering coefficient* indicates the presence of more local clusters, i.e. the network is more fractured (Fig. 7).

2.4. Feature set

For each sample, the network features described in section 2.3 are computed for each contact network and thermal network. As higher contact area and thermal conductance are related to larger heat transfer fluxes, and higher *degree* indicates more interparticle contacts, the *degree* is weighted by interparticle contact area in the contact network and thermal conductance in the thermal network. In other words, the weighted degree $\kappa_w(i)$ of each node $i \in V$ is $\kappa(i)$ multiplied by contact area and thermal conductance. In contrast, most of the other network features are computed based on the shortest path which is calculated with the minimisation of edge weighting. Hence, edge length for calculating these network features is weighted by the reciprocal of the contact area in the contact network and the reciprocal of thermal conductance in the thermal network.

If the weighted network features have dimensions (m^2 from a weighted contact network and W/K from a weighted thermal network), the features in the contact network will be normalised by D_{50}^2 in the contact network and normalised by $(\lambda_{solid} \cdot D_{50})$ in the thermal network to make all the features dimensionless. In addition to the network features, classic physical parameters including porosity, contact radius ratio (the ratio of the radius of contact area to the radius of the neighbouring particle), coefficient of uniformity and coefficient of curvature are calculated. All the features are summarised in Table 2.

As the range of values of different features varies widely, in order to weigh them equally, feature scaling is employed by subtracting the average and dividing by the standard deviation (Eq. (10)):

$$\tilde{x_i} = \frac{x_i - \mu(X)}{\sigma(X)} \tag{10}$$

where $X = (x_1, x_2, \ldots, x_n)$ is one of the features from Table 2, μ is the average and σ is the standard deviation of the feature X.

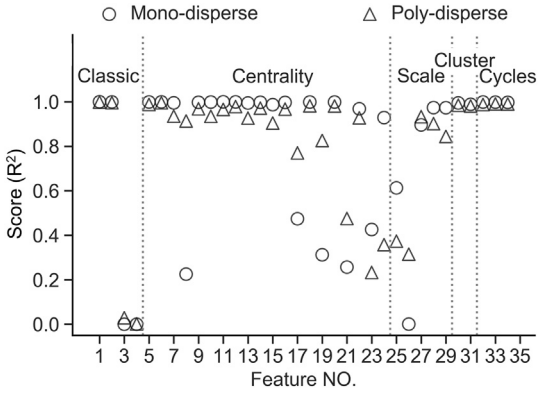

Fig. 10. Scores between contact network features and ETC (feature numbers corresponds to those in Table 2).

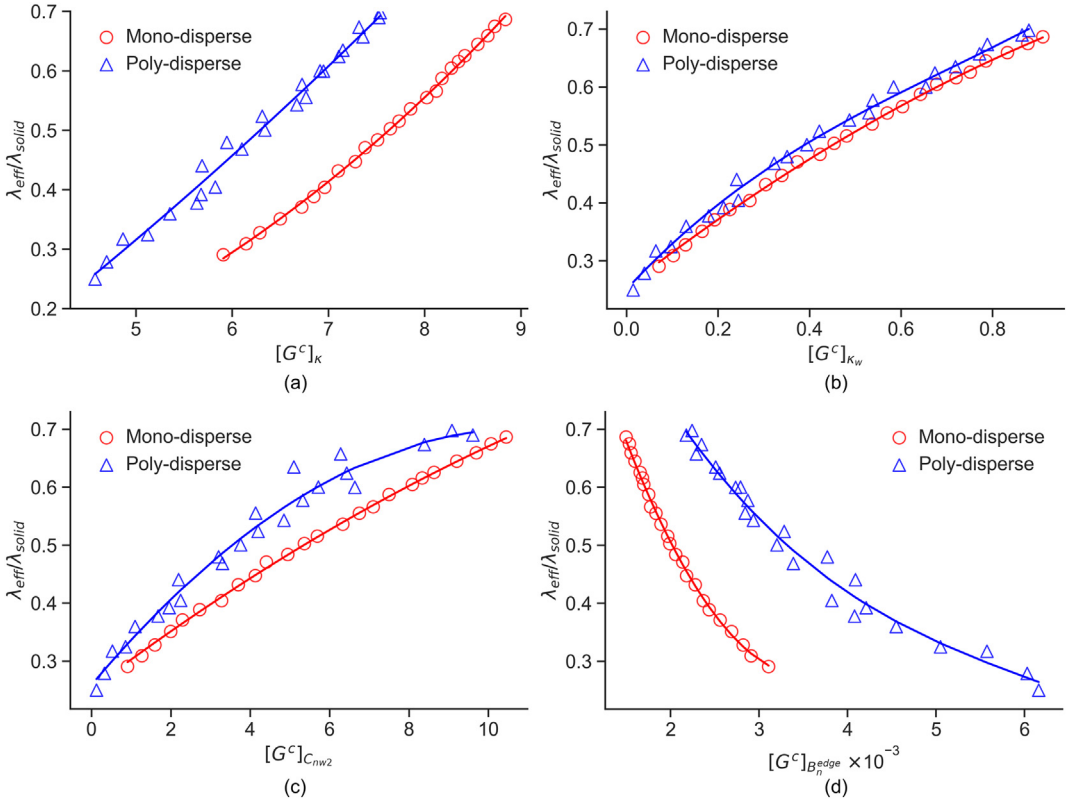

Fig. 11. The relationship between ETC and contact network centrality features: (a) Degree (= coordination number), (b) Weighted degree, (c) Weighted closeness centrality normalised by $[|V|(|V|-1)]/2$, and (d) Normalised edge betweenness centrality. Points in the figure represent the data used to train models while lines represent the predicted values from selected models.

2.5. Model selection

As a broad feature set is shown in Table 2, we aim to identify the most 'important' features in each group for predicting the ETC. To compute the importance, supervised machine learning techniques are employed to fit a model, predict the performance of the model and calculate the score of each feature. Six models are tested (linear, quadratic polynomial, cubic polynomial, exponential, logarithmic, power), generically listed in Eqs. (11)–(16), to fit the relationship between individual features (typically x) and the ETC (typically y). In order to apply the models more efficiently, nonlinear models are transformed into linear formats.

$$y = ax + b \tag{11}$$

$$y = aX_1 + bX_2 + c,\ X_1 = x^2,\ X_2 = x \tag{12}$$

$$y = aX_1 + bX_2 + cX_3 + d,\ X_1 = x^3,\ X_2 = x^2,\ X_3 = x \tag{13}$$

$$Y = A + bx,\ Y = \ln(y),\ A = \ln(a) \tag{14}$$

$$y = aX + b,\ X = \ln(x) \tag{15}$$

$$Y = bX + A,\ X = \ln(x),\ Y = \ln(y),\ A = \ln(a) \tag{16}$$

Then lasso regression [62], a modified linear regression for avoiding overfitting, is used to train models and calculate the correlation between individual features and ETC. For each feature, six models are trained and the one rendering the highest correlation is selected as the 'best fit' model. Additionally, random forest regression [52] is employed to study the effect of multi-feature (or multi-variable) correlations on ETC.

2.5.1. Regressions

1. Lasso regression

Linear regression is simple and effective. However, quadratic polynomial and cubic polynomial models are prone to overfit the training data set. One available method of mitigating the overfitting in polynomial models is to implement regularisation. The regularisation is applied by penalising the errors between trained and predicted values. Lasso regression [62] is one of the regularisation methods embedded in the python library scikit-learn [63] and has been employed in this work.

2. Random forest regression

A random forest [64,65] constructs multiple decision trees at training time and merges the output of the individual trees to obtain a more accurate prediction. Here, a decision tree [66] is a predictive

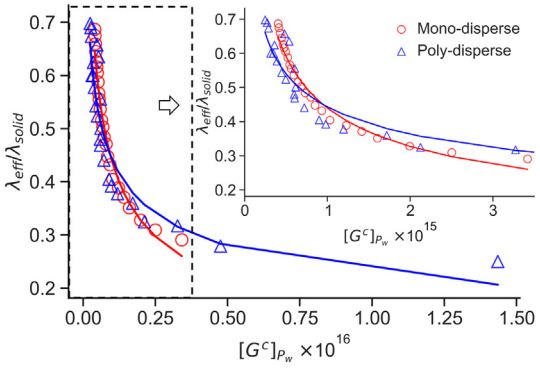

Fig. 12. ETC decreases when increasing the average weighted shortest path. Points in the figure represent the data used to train models while lines represent the predicted values from selected models.

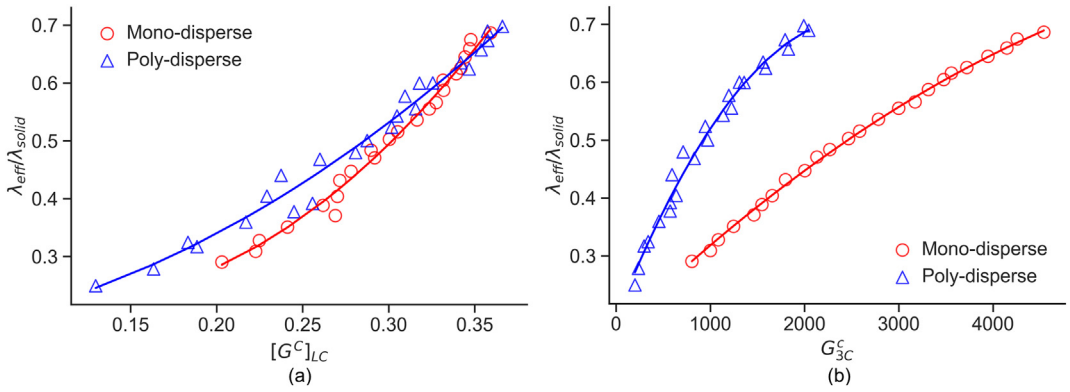

Fig. 13. The relationship between ETC and (a) Global clustering coefficient and (b) 3-cycle. Points in the figure represent the data used to train models while lines represent the predicted values from selected models.

model based on a branching series of Boolean tests. A merit of the random forest algorithm is that the relative importance of each feature can be easily measured.

2.5.2. Cross-validation

Scarce data used in machine learning may lead to insufficient data for the test set, which then may result in a poor estimation of the generalisation performance. A widely used method to mitigate this issue is K-fold cross-validation [67]. K-fold cross-validation is a resampling procedure and it contains the following steps:

1. Shuffle the data randomly.
2. Split data into K parts.
3. Use K-1 parts as a training set to fit models and the remaining part as a validation set to calculate a score (refer to section 2.6). The procedure has to repeat K times and each model will achieve K scores. The average scores of these models are compared, and then the model with the highest score is selected as the 'best fit' model.

Utilising this approach enables each data point to be used in the validation set once and in the training set K-1 times. In the present work, K is set to 4, which means eighteen samples are used to train models and six samples are used to validate the models in either mono-disperse or poly-disperse samples.

2.6. Feature importance

After selecting the 'best fit' model for each feature, the whole set of data is used as a test set to calculate the generalised performance score of the model. The score of the models under lasso regression is the coefficient of determination R^2. As each feature is adopted in lasso regression models, R^2 also indicates the correlation between the feature and the ETC. Furthermore, R^2 is used to evaluate the performance of random forest regression model. Meanwhile, the importance of each feature in a random forest regression is measured by Gini impurity [68].

3. Results and discussion

The ETC calculated by using finite element method is validated in Section 3.1. Then the importance of individual network features to ETC in mono-disperse and poly-disperse packings are investigated in Section 3.2 followed by a wider generalisation regarding the relevance of network features to ETC in all the samples in Section 3.3.

3.1. Effective thermal conductivity

The ETC computed from finite element modelling and normalised by the thermal conductivity of the solid phase of the packing is shown in Fig. 8 against the porosity n of each packing. Our results show good agreement with theoretical results [29], experimental results [69,70] and modelling results [71] available in the literature. According to Fig. 8, ETC decreases linearly with porosity for both mono-disperse packings and poly-disperse packings. However, the ETC in the two types of samples diverges with the increment of porosity, which indicates that porosity-dependent models may not be sufficient to cover a wide range of porosity, although it may be sufficiently accurate for particular engineering applications.

3.2. Importance of network features to ETC in mono-disperse and poly-disperse packings

Both contact network and thermal network are constructed for each packing. The identification of interparticle contacts and near-contacts as well as the calculation of contact area and thermal conductance follow the strategies in paper [36]. The topologies of the networks for the poly-disperse sample with porosity 0.246 is visualised in ParaView [72] as an example (Fig. 9). In Fig. 9, the contact network (a) show fewer edges than the thermal network (b), 1803 (shown in red) and 2471 (in red and blue), respectively. In other words, 668 near-contacts, shown as blue edges are considered in the thermal network. This difference in the networks may lead to highlight the different heat transfers mechanics within the packings. Network features arising from these networks can capture these differences and these will be explained in more detail in this section.

3.2.1. Importance of contact networks features

In this section, the importance of each feature in Table 2 to ETC is assessed using its score and consistency. The score R^2, ranging from 0 to 1, is computed between each feature and the ETC by applying six models with lasso regression (Section 2.5.1). Furthermore, a feature

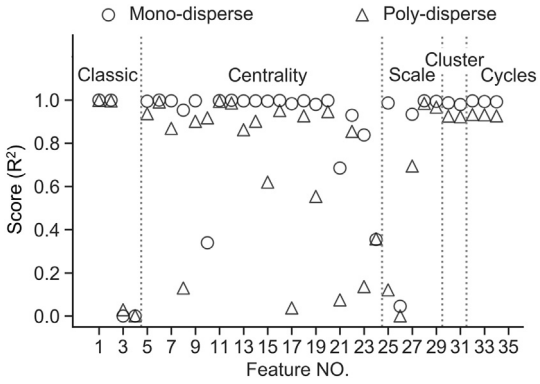

Fig. 14. Scores between thermal network features and ETC (feature numbers are corresponding to Table 2).

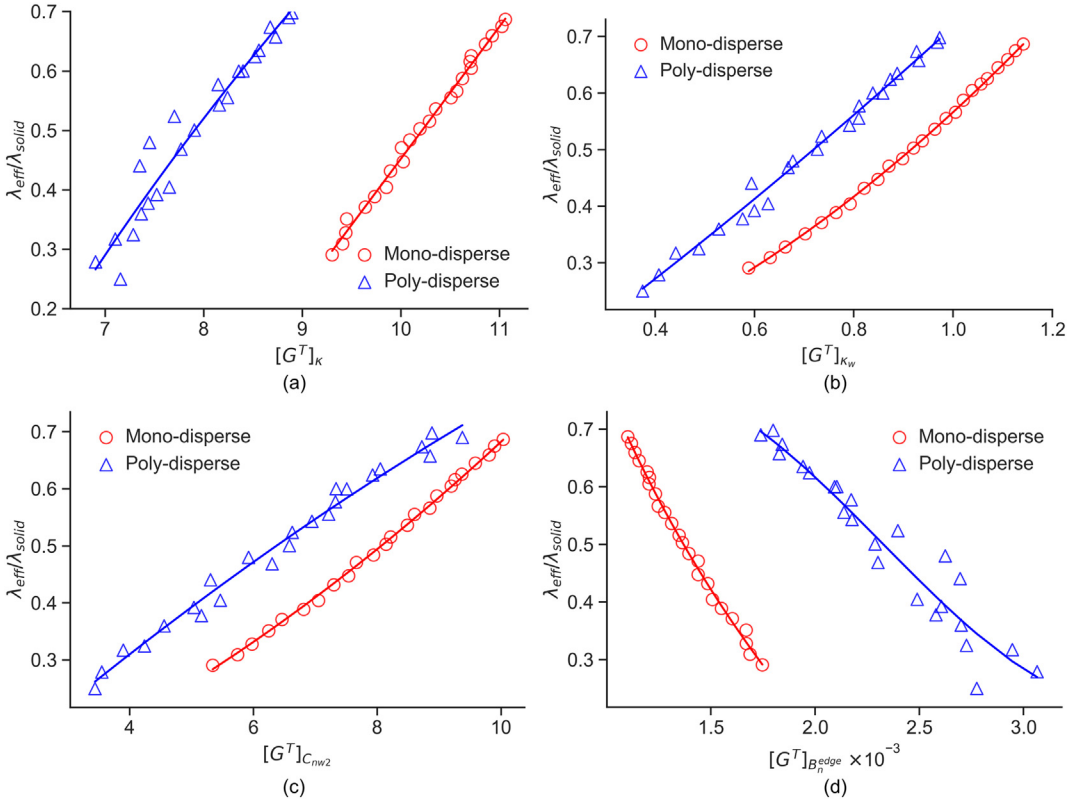

Fig. 15. The relationship between ETC and thermal network centrality features: (a) Degree, (b) Weighted degree, (c) Weighted closeness centrality normalised by $[|V|(|V|-1)]/2$, and (d) Normalised edge betweenness centrality. Points in the figure represent the data used to train models while lines represent the predicted values from selected models.

has a good consistency if its score in mono-disperse and poly-disperse packings are similar.

Fig. 10 depicts the performance of each contact feature on predicting ETC. The various models (Section 2.5) used to calculate the scores are summarised in Appendix 1. It can be observed that 25 out of 34 features have scores larger than 0.8 in mono-disperse while 27 features in poly-disperse packings, which indicates they have good correlations with ETC and the scores are consistent. These features except ${G_{D_n}}^c$ (Feature 27) render higher scores in mono-disperse packings than in poly-disperse packings. Classic features such as porosity (Feature 1), contact radius ratio (Feature 2) and coordination number (Feature 5) have scores close to 1, as expected.

As shown in Table 2, centrality-type features include degree (Feature 6), closeness centrality (Features 7–12), betweenness centrality (Features 13–22) and eigenvector centrality (Features 23–24). Fig. 10 shows that weighted degree $[G^c]_{\kappa_w}$ (Feature 6) has a high score and consistency than coordination number (Feature 5), which means considering the interparticle contact area in the coordination number (as the weighted degree does) can enhance its correlation to ETC. All the closeness centrality features except $[G^c]_{C_{n1}}$ (Feature 8) in mono-disperse packings have scores higher than 0.85. In particular, $[G^c]_{C_{n2}}$ (Feature 9) and $[G^c]_{C_{nw2}}$ (Feature 12) have both high scores and consistence. Betweenness centrality features also have high scores except for $[G^c]_{B_w^{node}}$ (Feature 15), $[G^c]_{B^{edge}}$ (Feature 17) and $[G^c]_{B_w^{edge}}$ (Feature 19) in both mono-disperse and poly-disperse packings. However, when normalised, these three features show high scores (Features 16, 18 and 20) and good consistency. In contrast, eigenvector centrality features do not show good performance, only $[G^c]_{E_w}$ (Feature 24) in mono-disperse packings have a score around 0.93.

Since $[G^c]_{\kappa}$ (Feature 5), $[G^c]_{\kappa_w}$ (Feature 6), $[G^c]_{C_{nw2}}$ (Feature 12) and $[G^c]_{B_n^{edge}}$ (Feature 18) perform well in both scores and consistency, the original data and fitted models are superimposed in Fig. 11. For a given ETC, mono-disperse packings require more particle contacts (Fig. 11 (a)) and show lower betweenness centrality (Fig. 11 (d)) than poly-disperse packings. It is also shown that $[G^c]_{\kappa_w}$ and $[G^c]_{C_{nw2}}$ tend to collapse the data arising from the two types of packings into just one group. While degree $[G^c]_{\kappa}$ (or 'classic' condonation number) only considers the particles' connectivity, the weighted degree $[G^c]_{\kappa_w}$also considers the contact quality (contact area) besides connectivity. As heat conduction depends on the thermal conductivity of solid particles [13], the structure of particle packings [73,74] and the interparticle contact conductance [13,75–79] in dry granular packings, $[G^c]_{\kappa_w}$shows a better performance in predicting ETC than the degree $[G^c]_{\kappa}$.

In terms of the scale-type features, average weighted shortest path $[G^c]_{P_w}$ (Feature 28) has a score around 0.97 in mono-disperse packings but around 0.90 in poly-disperse packings. Normalised network diameter ${G_{D_n}}^c$ (Feature 27) has a lower score than $[G^c]_{P_w}$ in mono-disperse packings but has a better consistency. Fig. 12 shows that ETC decreases with the increase of $[G^c]_{P_w}$ even though $[G^c]_{P_w}$ has a jump when $[G^c]_{P_w}$

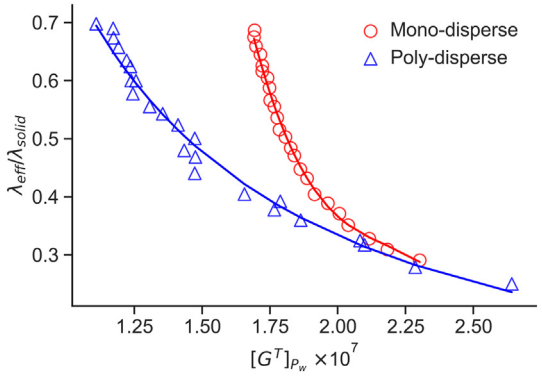

Fig. 16. ETC monotonically and smoothly decreases with the increasing average weighted shortest path GTPw calculated from a thermal network.

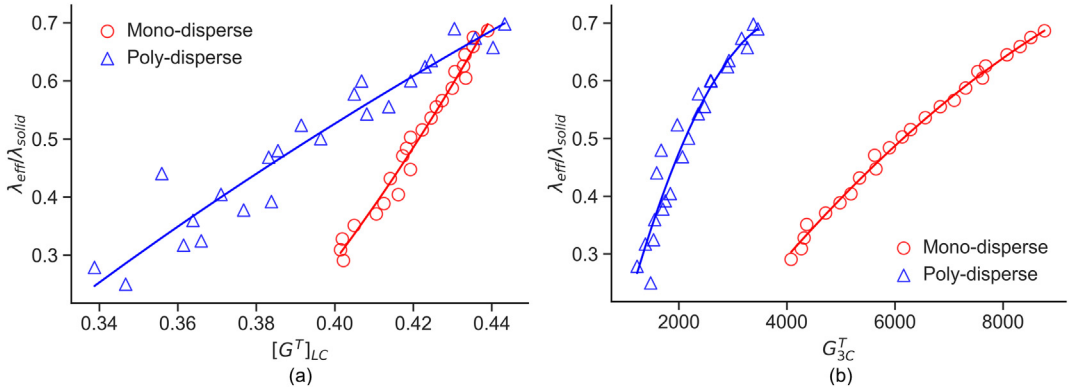

Fig. 17. The relationship between ETC and (a) Global clustering coefficient and (b) 3-cycle. Points in the figure represent the data used to train models while lines represent the predicted values from selected models.

is larger than 5×10^{15}. As $[G^c]_{P_w}$ is related to the average contact area of a sphere packing, it can quantify the interparticle contact quality which affects ETC. It also shows a similar score to contact radius ratio γ (Feature 2) when predicting the ETC of mono-disperse packings in Fig. 10. However, it achieves a lower score than γ when applying to predict the ETC of poly-disperse packings because γ considers both the contact area and particle size.

According to Fig. 10, the scores and consistency of cluster-type features and cycle-type features remain high for both mono-disperse and poly-disperse packings. Their relative importance to heat transfer is similar to that of porosity (Feature 1), contact radius ratio (Feature 2) and coordination number (Feature 5), so they can be taken as alternatives to these classical variables or features for predicting the ETC of sphere packings. Fig. 10 also shows that cluster-type features and cycle-type features are better candidates used to predict ETC than scale-type features, which indicates that particle-connectivity is more critical to heat transfer than contact quality in sphere packings.

One feature from each cluster-type features and cycle-type features are selected to show the relationship with ETC in Fig. 13. It can be seen from Fig. 13 (a) that the relationship between the local clustering coefficient (a scale-type feature) and the ETC in mono-disperse has a similar incremental ratio to that in poly-disperse packings. In contrast, Fig (b) shows that the trend between 3-cycle and ETC in mono-disperse are different from that in poly-disperse packings. Hence, the local clustering coefficient may be more consistent than 3-cycle for predicting ETC in different types of sphere packings.

In general, cluster features and cycles features computed from contact networks are shown to be highly relevant for predicting ETC, while scale features are less desirable for such correlations. In addition, all centrality features but eigenvector centrality could be used to predict ETC. In particular, the centrality features such as $[G^c]_{\kappa_w}$ and $[G^c]_{C_{nw2}}$ considering both particle connectivity and contact area are proven to be good candidates to predict ETC.

3.2.2. Importance of thermal network features

Similar to the performance of contact network features, thermal network features whose score are higher than 0.8 also perform better in mono-disperse packings than in poly-disperse packings (Fig. 14 and Appendix 2).

As for the relevance of centrality features computed from thermal networks, weighted degree $[G^T]_{\kappa W}$ (Feature 6), $[G^T]_{C_{nw1}}$ (Feature 11) and $[G^T]_{C_{nw2}}$ (Feature 12) could be the most suitable centrality features for predictability of ETC because they consider both particle connectivity and contact quality. Compared with the vital contact network centrality features in Fig. 10, Fig. 14 shows that less important thermal network centrality features are available in predicting ETC but the available thermal network features have a higher correlation with ETC in both mono-disperse and poly-disperse packings. As the thermal network is an extension of contact network by adding near-contacts as edges, network features considering heat transfer through gaps between neighbouring particles enhance the accuracy of predicting ETC. The original data of the same features in Fig. 11 together with the fitted models are presented in Fig. 15. For each feature, the data are still clustered into two groups corresponding to mono-disperse packings and poly-disperse packings. The correlation for each feature has a similar trend in different groups. However, by comparing Figs. 11 and 15, it can be observed that the difference of a feature calculated from the thermal network between two types of packings is larger than that from the contact network when aiming to achieve the same ETC. Thermal networks are different from contact networks because they consider near-contacts as edges. As degree measure the edge number, it can be known that more near contacts are required in a mono-disperse packing than in a poly-disperse packing to achieve the same ETC. Weighted degree $[G^c]_{\kappa_w}$ in the contact network measure the contact area at each interparticle contacts, so it indicates the heat transfer through interparticle contacts. In contrast, $[G^T]_{\kappa_w}$ in thermal network measure thermal conductance at both interparticle contacts and near-contacts, it implies the heat transfer through both interparticle contacts and the small gap between neighbouring particles. As the same amount of heat transfers through interparticle contacts in a mono-disperse packing as that in a

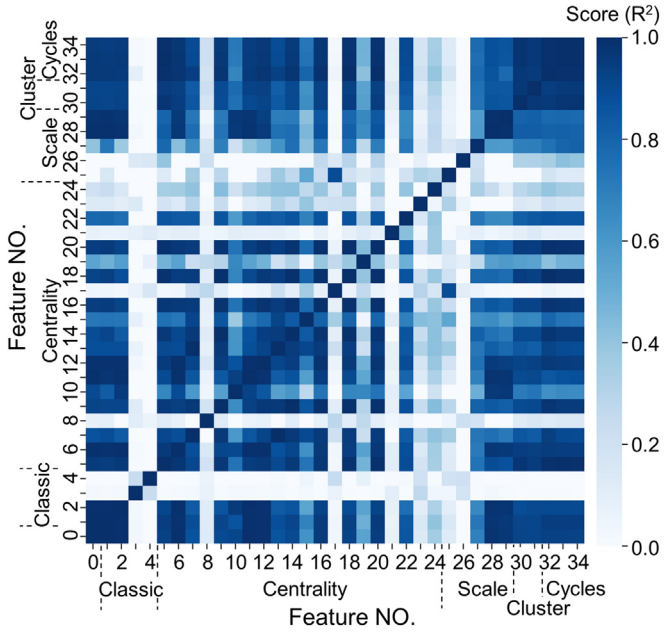

Fig. 18. A heatmap shows the score of correlation between a different pair of features in poly-disperse packings. Feature 0 is the ETC and other feature numbers refer to Table 2.

Table 3
The score of correlation between thermal network features.

	$[G^T]_{C_{nw1}}$ (Feature 11)	$[G^T]_P$ (Feature 28)	$[G^T]_{LC}$ (Feature 31)	G^T_{3C} (Feature 32)
$[G^T]_{C_{nw1}}$ (Feature 11)	1	0.9839	0.9295	0.9564
$[G^T]_P$ (Feature 28)	0.9839	1	0.8509	0.8622
$[G^T]_{LC}$ (Feature 31)	0.9295	0.8509	1	0.9654
G^T_{3C} (Feature 32)	0.9564	0.8622	0.9654	1

poly-disperse packing can achieve the similar ETC (Fig. 11 (b)), it indicates that the heat transfers in dry sphere packings is mainly attributed to the heat transfer through interparticle contacts and the contribution of near-contact to the heat transfer in dry sphere packings is minor. Additionally, more edges in the thermal network reduce the role of the nodes/edges as unique 'bridges'. Hence, the betweenness centrality becomes smaller, resulting in that the fitted two lines in Fig. 15 (d) are further away from each other compared with the distance in Fig. 11 (d)).

As for scale features, both $[G^T]_{P_w}$ (Feature 28) and $[G^T]_{P^{pp}_w}$ (Feature 29) are important and relevant given their high scores and consistency. Compared with the trend of the relationship between $[G^C]_{P_w}$ and ETC in Fig. 12, the ETC decreases smoothly with increasing $[G^T]_{P_w}$ (Fig. 16) which considers the heat transfers through near-contacts. Batchelor and O'Brien [26] reported that heat fluxes in particulate materials are influenced by the near-contacts between particles and the mean of the local curvature of neighbouring particles. Indeed, a thermal network also considers the near-contacts as edges, and $[G^T]_{P_w}$ includes thermal conductance through both interparticle contacts and near-contacts in its definition, it is then not surprising that it results in being a highly important feature for predicting the ETC of sphere packings. The different slope of the fitted lines for mono-disperse packings and poly-disperse packings may be because the local curvature of neighbouring particles is not involved at each edge.

All cluster features and cycle features have scores higher than 0.92. To achieve the same ETC, the difference of the local clustering coefficient between mono-disperse packings and poly-disperse packing becomes small with the increase of local clustering coefficient in Fig. 17 (a). In contrast, the value of 3-cycles in poly-disperse packings are always lower than mono-disperse packings as shown in Fig. 17 (b).

From Figs. 10 and 14, it is known that many network features show good correlation with ETC, which may be because a strong relationship exists between different network features. Hence, the same model selection and feature importance evaluation methods used to access the scores of the relationship between features and ETC are now applied to investigate the relationships between different network features. The score of correlation between each different pair of thermal features in poly-disperse packings is shown in a heatmap (Fig. 18). It can be seen from Fig. 18 that more than one-third of the score is larger than 0.8.

Since $[G^T]_{C_{nw1}}$ (Feature 11), $[G^T]_P$ (Feature 28), $[G^T]_{LC}$ (Feature 31) and G^T_{3C} (Feature 32) are important in each type of thermal network features, the scores of their relationship are high as shown in Table 3 for four types of network features (centrality, scale, clustering, cycles). As these essential features have close interplay relevance and have high scores when predicting ETC (Fig. 14), each of them could be used as an alternative to coordination number or porosity in an equation to predict ETC.

Overall, among different types of thermal network features, centrality features including weighted degree and closeness centrality features are essential to heat transfer. Scale features are also available to predict ETC. However, cluster and cycles features perform slightly worse compared with their peers from contact networks.

3.3. Importance of network features to ETC in combined mono-disperse and poly-disperse packings

In section 3.2, we discussed the importance of network features in mono-disperse and poly-disperse packings, respectively. In this section, we investigate the general performance of network features on combined data including both mono-disperse and poly-disperse packings, as one may think of mono-disperse being a sub-set of poly-disperse beds.

Firstly, the correlations of individual features against ETC are computed (Fig. 19). Some contact network features such as $[G^c]_{\kappa_w}$ (Feature 6), $[G^c]_{C_{nw1}}$ (Feature 11) and $[G^c]_{LC}$ (Feature 31) still show high scores (>0.9) while all of the thermal network features show lower scores (<0.8). The relationship between $[G^c]_{\kappa_w}$ and ETC is fitted into a quadratic polynomial equation (Eq. (17)) with R^2 of 0.99 as shown in Fig. 20. The high R^2 indicates the correlation between $[G^c]_{\kappa_w}$ and ETC is better than that between porosity (Feature 1) and ETC, which also can be observed by comparing Figs. 20 and 8. The contact network features having high scores means the data from mono-disperse packings are closer to the data from poly-disperse packings as shown in Figs. 11(b), (c) and 13 (a). In contrast, the low score of contact network features and thermal network features in combined packings is the result of the clustering of the data into two groups corresponding to mono-disperse packings and poly-disperse packings as shown from Figs. 11 to 13 and Figs. 15 to 17. Furthermore, clustering of the data still manifests for the difference of the same network features from thermal networks and contact networks. The reason is that near-contacts are considered in the thermal network but they seem to contribute little to heat transfer in dry

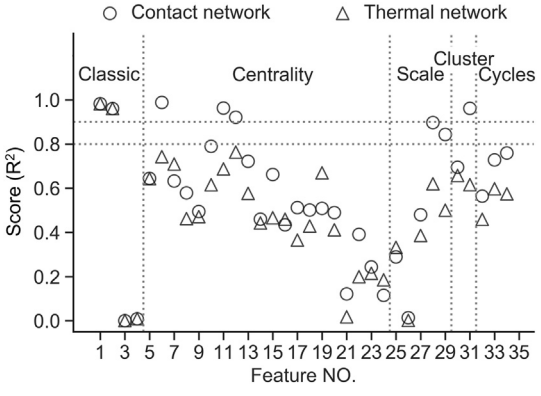

Fig. 19. Scores between network features and ETC in combined packings. The feature numbers are corresponding to Table 2.

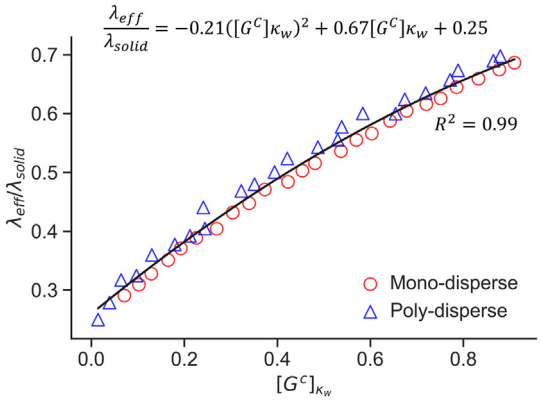

Fig. 20. The relationship between weighted degree from contact network and ETC.s.

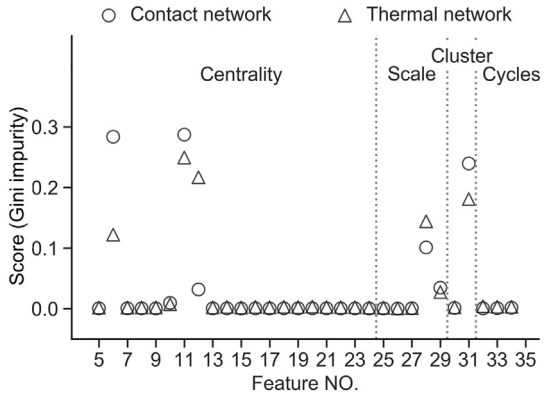

Fig. 21. Network feature importance in random forest regression models. (a) Contact network (b) Thermal network.

spheres as explained in section 3.2.2. However, the contribution of near-contacts may become important in wet sphere packings [43] or when considering radiation [80] between particles, important only at high temperatures. In order to investigate the potential applicability of thermal network features in more complex conditions, we attempt to analyse the correlation between multiple-features and ETC.

$$\frac{\lambda_{eff}}{\lambda_{solid}} = -0.21\left(\left[G^C\right]\kappa_w\right)^2 + 0.67\left[G^C\right]\kappa_w + 0.25 \tag{17}$$

Random forest scores are used to compute the score of the relationship between multi-network features and ETC as well as the relative importance of each feature. The score arising from testing thermal network features with random forest regression is around 0.94 which is higher than the score of an individual feature as shown in Fig. 19. The score of applying contact network features with random forest regression is calculated and around 0.98. The importance/relevance of each feature in a random forest regression is measured by Gini impurity [68] and shown in Fig. 21. The figure shows that weighted closeness centrality $[G^*]_{C_{nw1}}$ (Feature 11) in either contact network or thermal network contributes the most when predicting ETC. The importance of $[G^*]_{C_{nw1}}$ hints again that a feature considering both particle connectivity and contact quality is crucial to predict ETC. Weighted degree $[G^*]_{\kappa_w}$ (Feature 6) is another important feature and it also measures both particle connectivity and contact quality. As for the rest of two relative important features, average weighted shortest path $[G^*]_{P_w}$ (Feature 28) is related to contact quality

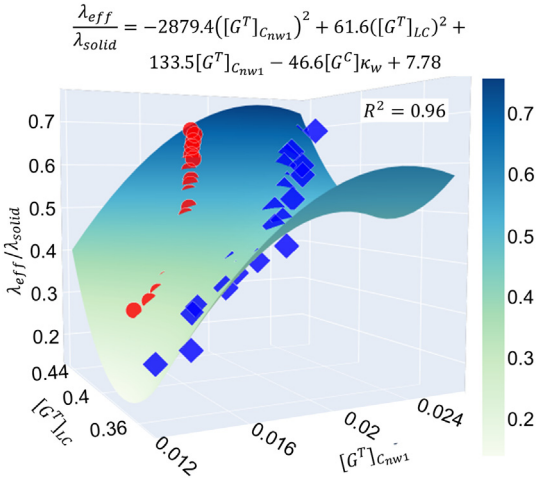

Fig. 22. The relationship between $[G^T]_{C_{nw1}}$ (weighted closeness centrality normalised by $[|V|(|V|-1)]/2$, $[G^T]_{LC}$ (local clustering coefficient) and ETC (https://wenbinfei.github.io/research_demos/5-sphere-network-features/).

while local clustering coefficient $[G^*]_{LC}$ (Feature 31) is related to particle connectivity. Therefore, it is necessary to consider both contact quality and particle connectivity in a model for predicting ETC.

Random forest regression shows the feasibility of predicting ETC using multi-network features. However, equations cannot be derived from the random forest algorithm because it is based on a branching series of Boolean tests. To clearly show the relationship between multiple thermal network features and ETC, $[G^T]_{C_{nw1}}$ (Feature 11) and $[G^*]_{LC}$ (Feature 31) are used to build a predictive Eq. (18) from different types of features that show high scores (as depicted in Fig. 21):

$$\frac{\lambda_{eff}}{\lambda_{solid}} = -2879.4\left(\left[G^T\right]_{C_{nw1}}\right)^2 + 61.6\left(\left[G^T\right]_{LC}\right)^2 + 133.5\left[G^T\right]_{C_{nw1}} - 46.6\left[G^C\right]\kappa_w + 7.78 \tag{18}$$

The resulting predictive equation has a high correlation coefficient R^2 of 0.96 as shown in Fig. 22, which indicates again the importance of particle connectivity and contact quality in heat transfer.

4. Conclusion

A framework is proposed to select essential features (or new 'variables') which can be used to predict ETC. By computing the individual feature relevance to the ETC in mono-disperse and poly-disperse packings, we found individual network features can be alternatives to other classic or traditional parameters (such as porosity) when predicting ETC for mono-disperse and poly-disperse packings respectively. Moreover, the correlations of features to ETC is higher in simpler mono-disperse packings than that in poly-disperse packings. By comparing the performance of individual contact network features and thermal network features on ETC, we found cluster and cycle features derived from the contact network to be more relevant than those arising from the thermal network. In contrast, centrality and scale features from the thermal network are more relevant than those from the contact network.

In order to analyse the general feature importance in a model that predicts the ETC in more extensive data set, the correlation of individual features with ETC was studied for combined mono-disperse and poly-disperse packings. Weighted degree $[G^c]_{\kappa_w}$, normalised weighted closeness centrality $[G^c]_{C_{nw1}}$ and local clustering coefficient $[G^c]_{LC}$ from contact networks can still be used as individual features to predict ETC. Despite an individual thermal network feature rendering a relatively lower correlation to the ETC, random forest regression model with multiple thermal network features can achieve similar accuracy as that when using either an individual or multiple contact network features. The network feature involving both particle connectivity and contact quality always performs well in both small dataset size (mono-disperse packing or poly-disperse packing) and larger dataset size (combined mono-disperse and poly-disperse packings).

As computed tomography (CT) can be used to scan real granular materials and reconstruct their geometry [44], future work can expand on extracting the network features from these real materials and investigate the correlation with ETC.

Declaration of Competing Interest

The authors declare that they have no known competing financial interests or personal relationships that could have appeared to influence the work reported in this paper.

Acknowledgements

We thank Min Zhang from the University of Nottingham Ningbo China for sharing the experience of generating multiple samples using PFC. This work is supported by the Melbourne Research Scholarship from The University of Melbourne.

Appendix 1 Contact network feature importance

Type	No.	Notation	Mono-disperse packings		Poly-disperse packings	
			Score	Model	Score	Model
Classic	1	n	0.9995	Quadratic polynomial	0.9979	Linear
	2	γ	0.9988	Exponential	0.9951	Exponential
	3	C_u	0.0000	Quadratic polynomial	0.0289	Quadratic polynomial
	4	C_c	0.0000	Quadratic polynomial	0.0012	Linear
Centrality	5	$[G^c]_{\kappa}$	0.9986	Power	0.9871	Quadratic polynomial
	6	$[G^c]_{\kappa_w}$	0.9990	Quadratic polynomial	0.9949	Cubic polynomial
	7	$[G^c]_C$	0.9945	Logarithmic	0.9345	Logarithmic
	8	$[G^c]_{C_{n1}}$	0.2251	Linear	0.9131	Logarithmic
	9	$[G^c]_{C_{n2}}$	0.9971	Linear	0.9677	Logarithmic
	10	$[G^c]_{C_w}$	0.9982	Exponential	0.9339	Linear
	11	$[G^c]_{C_{nw1}}$	0.9992	Linear	0.9652	Quadratic polynomial
	12	$[G^c]_{C_{nw2}}$	0.9989	Quadratic polynomial	0.9777	Quadratic polynomial
	13	$[G^c]_{B^{node}}$	0.9939	Logarithmic	0.9259	Logarithmic
	14	$[G^c]_{B_n^{node}}$	0.9972	Quadratic polynomial	0.9707	Quadratic polynomial
	15	$[G^c]_{B_w^{node}}$	0.9864	Quadratic polynomial	0.9039	Logarithmic
	16	$[G^c]_{B_{nw}^{node}}$	0.9965	Exponential	0.9665	Exponential
	17	$[G^c]_{B^{edge}}$	0.4738	Power	0.7695	Exponential
	18	$[G^c]_{B_n^{edge}}$	0.9983	Quadratic polynomial	0.9811	Cubic polynomial
	19	$[G^c]_{B_w^{edge}}$	0.3120	Exponential	0.8253	Exponential
	20	$[G^c]_{B_{nw}^{edge}}$	0.9983	Cubic polynomial	0.9803	Cubic polynomial
	21	$[G^c]_{B_w^{edgetp}}$	0.2567	Power	0.4748	Logarithmic
	22	$[G^c]_{B_{nw}^{edgetp}}$	0.9679	Exponential	0.9269	Quadratic polynomial
	23	$[G^c]_E$	0.4256	Exponential	0.2324	Exponential
	24	$[G^c]_{E_w}$	0.9283	Quadratic polynomial	0.3574	Power
Network scale	25	G_D^c	0.6126	Exponential	0.3729	Power
	26	$G_{\bar{D}}^c$	0.0006	Logarithmic	0.3147	Exponential
	27	$G_{D_n}{}^c$	0.8955	Logarithmic	0.9323	Power
	28	$[G^c]_{P_w}$	0.9731	Power	0.9010	Power
	29	$[G^c]_{P_w}{}^{tp}$	0.9727	Power	0.8438	Power
Clustering	30	$G^c{}_{GC}$	0.9942	Quadratic polynomial	0.9840	Exponential
	31	$[G^c]_{LC}$	0.9880	Quadratic polynomial	0.9801	Quadratic polynomial
Cycles	32	G_{3C}^c	0.9985	Quadratic polynomial	0.9869	Quadratic polynomial
	33	$[G^c]_{3C^{node}}$	0.9978	Quadratic polynomial	0.9898	Quadratic polynomial
	34	$[G^c]_{3C^{edge}}$	0.9968	Quadratic polynomial	0.9893	Linear

Appendix 2 Thermal network feature importance

Type	No.	Notation	Mono-disperse packings		Poly-disperse packings	
			Score	Model	Score	Model
Classic	1	n	0.9995	Quadratic polynomial	0.9979	Linear
	2	γ	0.9988	Exponential	0.9951	Exponential
	3	C_u	0.0000	Quadratic polynomial	0.0289	Quadratic polynomial
	4	C_c	0.0000	Quadratic polynomial	0.0009	Logarithmic
Centrality	5	$[G^T]_{\kappa}$	0.9939	Linear	0.9363	Logarithmic
	6	$[G^T]_{\kappa w}$	0.9992	Quadratic polynomial	0.9905	Quadratic polynomial
	7	$[G^T]_C$	0.9957	Logarithmic	0.8682	Logarithmic
	8	$[G^T]_{C_{n1}}$	0.9525	Logarithmic	0.1295	Quadratic polynomial
	9	$[G^T]_{C_{n2}}$	0.9958	Logarithmic	0.9010	Cubic polynomial
	10	$[G^T]_{C_w}$	0.3390	Linear	0.9169	Exponential
	11	$[G^T]_{C_{nw1}}$	0.9967	Cubic polynomial	0.9929	Exponential
	12	$[G^T]_{C_{nw2}}$	0.9984	Quadratic polynomial	0.9854	Quadratic polynomial
	13	$[G^T]_{B^{node}}$	0.9953	Logarithmic	0.8617	Logarithmic
	14	$[G^T]_{B_n^{node}}$	0.9955	Logarithmic	0.9013	Cubic polynomial
	15	$[G^T]_{B_w^{node}}$	0.9942	Logarithmic	0.6195	Linear
	16	$[G^T]_{B_{nw}^{node}}$	0.9972	Quadratic polynomial	0.9506	Cubic polynomial
	17	$[G^T]_{B^{edge}}$	0.9825	Logarithmic	0.0373	Logarithmic
	18	$[G^T]_{B_n^{edge}}$	0.9958	Logarithmic	0.9261	Cubic polynomial
	19	$[G^T]_{B_w^{edge}}$	0.9792	Logarithmic	0.5534	Exponential
	20	$[G^T]_{B_{nw}^{edge}}$	0.9970	Quadratic polynomial	0.9459	Logarithmic
	21	$[G^T]_{B_w^{edgetp}}$	0.6845	Cubic polynomial	0.0747	Exponential
	22	$[G^T]_{B_{nw}^{edgetp}}$	0.9289	Logarithmic	0.8540	Cubic polynomial
	23	$[G^T]_E$	0.8378	Logarithmic	0.1361	Linear
	24	$[G^T]_{E_w}$	0.3541	Cubic polynomial	0.3570	Logarithmic
Network scale	25	G_D^T	0.9856	Linear	0.1210	Logarithmic
	26	$G_{\bar{D}}^T$	0.0450	Logarithmic	0.0002	Logarithmic
	27	$G_{D_n}{}^T$	0.9335	Exponential	0.6939	Linear
	28	$[G^T]_{P_w}$	0.9958	Cubic polynomial	0.9839	Power
	29	$[G^T]_{P_w^{tp}}$	0.9932	Cubic polynomial	0.9665	Cubic polynomial

(*continued*)

Type	No.	Notation	Mono-disperse packings		Poly-disperse packings	
			Score	Model	Score	Model
Clustering	30	G^T_{GC}	0.9862	Quadratic polynomial	0.9248	Logarithmic
	31	$[G^T]_{LC}$	0.9785	Quadratic polynomial	0.9218	Logarithmic
Cycles	32	G^T_{3C}	0.9955	Quadratic polynomial	0.9321	Quadratic polynomial
	33	$[G^T]_{3C^{node}}$	0.9925	Quadratic polynomial	0.9309	Logarithmic
	34	$[G^T]_{3C^{edge}}$	0.9913	Linear	0.9260	Logarithmic

Appendix 3 Feature importance in combined samples

Type	No.	Notation	Contact network		Thermal network	
			Score	Model	Score	Model
Classic	1	n	0.9819	Linear	0.9819	Linear
	2	γ	0.9599	Exponential	0.9599	Exponential
	3	C_u	0.0004	Logarithmic	0.0004	Logarithmic
	4	C_c	0.0088	Quadratic polynomial	0.0088	Quadratic polynomial
Centrality	5	$[G^*]_{\kappa}$	0.6441	Logarithmic	0.6428	Cubic polynomial
	6	$[G^*]_{\kappa_w}$	0.9877	Quadratic polynomial	0.7427	Logarithmic
	7	$[G^*]_C$	0.6323	Cubic polynomial	0.7092	Cubic polynomial
	8	$[G^*]_{C_{n1}}$	0.5785	Cubic polynomial	0.4619	Cubic polynomial
	9	$[G^*]_{C_{n2}}$	0.4941	Cubic polynomial	0.4708	Cubic polynomial
	10	$[G^*]_{C_w}$	0.7895	Power	0.6152	Cubic polynomial
	11	$[G^*]_{C_{nw1}}$	0.9622	Quadratic polynomial	0.6870	Quadratic polynomial
	12	$[G^*]_{C_{nw2}}$	0.9205	Cubic polynomial	0.7631	Logarithmic
	13	$[G^*]_{B^{node}}$	0.7217	Cubic polynomial	0.5765	Cubic polynomial
	14	$[G^*]_{B^{node}_n}$	0.4594	Linear	0.4422	Cubic polynomial
	15	$[G^*]_{B^{node}_w}$	0.6619	Cubic polynomial	0.4658	Cubic polynomial
	16	$[G^*]_{B^{node}_{nw}}$	0.4339	Linear	0.4592	Linear
	17	$[G^*]_{B^{edge}}$	0.5118	Cubic polynomial	0.3646	Cubic polynomial
	18	$[G^*]_{B^{edge}_n}$	0.5009	Linear	0.4282	Cubic polynomial
	19	$[G^*]_{B^{edge}_w}$	0.5084	Cubic polynomial	0.6692	Quadratic polynomial
	20	$[G^*]_{B^{edge}_{nw}}$	0.4893	Linear	0.4113	Cubic polynomial
	21	$[G^*]_{B^{edgetp}_w}$	0.1215	Logarithmic	0.0175	Logarithmic
	22	$[G^*]_{B^{edgetp}_{nw}}$	0.3906	Linear	0.1994	Linear
	23	$[G^*]_E$	0.2434	Cubic polynomial	0.2151	Logarithmic
	24	$[G^*]_{E_w}$	0.1151	Linear	0.1851	Cubic polynomial
Network scale	25	G^*_P	0.2888	Cubic polynomial	0.3318	Cubic polynomial
	26	G^*_D	0.0138	Logarithmic	0.0016	Logarithmic
	27	$G_{D_n}{}^*$	0.4796	Linear	0.3857	Linear
	28	$[G^*]_{P_w}$	0.8965	Power	0.6198	Quadratic polynomial
	29	$[G^*]_{P^{tp}_w}$	0.8429	Power	0.5002	Cubic polynomial
Clustering	30	G^*_{GC}	0.6947	Logarithmic	0.6574	Cubic polynomial
	31	$[G^*]_{LC}$	0.9609	Quadratic polynomial	0.6156	Linear
Cycles	32	G^*_{3C}	0.5638	Logarithmic	0.4588	Cubic polynomial
	33	$[G^*]_{3C^{node}}$	0.7279	Logarithmic	0.5971	Cubic polynomial
	34	$[G^*]_{3C^{edge}}$	0.7593	Logarithmic	0.5740	Cubic polynomial

References

[1] W.M. Rohsenow, J.P. Hartnett, E.N. Ganic, Handbook of Heat Transfer Applications, McGraw-Hill Book Co, New York, 1985 973 1985. No individual items are abstracted in this volume.

[2] D.M. Scott, D.K. Das, V. Subbaihaannadurai, V.A. Kamath, A computational scheme for fluid flow and heat transfer analysis in porous media for recovery of oil and gas, Pet. Sci. Technol. 23 (2005) 843–862.

[3] W.B. Fei, Q. Li, X.C. Wei, R.R. Song, M. Jing, X.C. Li, Interaction analysis for CO2 geological storage and underground coal mining in Ordos Basin, China, Eng. Geol. 196 (2015) 194–209.

[4] A.E. Bergles, J. Collier, J.M. Delhaye, G. Hewitt, F. Mayinger, Two-Phase Flow and Heat Transfer in the Power and Process Industries, Hemisphere, New York, 1981.

[5] W.H. Somerton, Thermal Properties and Temperature-Related Behavior of Rock/Fluid Systems, Elsevier, 1992.

[6] H. Kivohashi, M. Deguchi, Derivation of a correlation formula for the effective thermal conductivity of geological porous materials by the three-phase geometric-mean model, High Temperatures. High Pressures 30 (1998) 25–35.

[7] V. Odelevskii, Calculation of the generalized conductivity of heterogeneous systems, Zh. Tekh. Fiz 21 (1951) 678–685.

[8] G. Dul'nev, Y.P. Zarichnyak, Thermal Conductivity of Mixtures and Composite Materials, Energiya, Leningrad, 1974.

[9] A. Mendel, Relation between thermal conductivity of rocks and structure of the pores, Russ J Geology Prospect 1 (1997) 112–119.

[10] R. Krupiczka, Analysis of thermal conductivity in granular materials, International Chemical Engineering 7 (1967)122−+.

[11] Z. Abdulagatova, I. Abdulagatov, V. Emirov, Effect of temperature and pressure on the thermal conductivity of sandstone, Int. J. Rock Mech. Min. Sci. 46 (2009) 1055–1071.

[12] J. Mo, H. Ban, Measurements and theoretical modeling of effective thermal conductivity of particle beds under compression in air and vacuum, Case studies in thermal engineering 10 (2017) 423–433.

[13] T.S. Yun, J.C. Santamarina, Fundamental study of thermal conduction in dry soils, Granul. Matter 10 (2008) 197.

[14] J. Sass, A.H. Lachenbruch, R.J. Munroe, Thermal conductivity of rocks from measurements on fragments and its application to heat-flow determinations, J. Geophys. Res. 76 (1971) 3391–3401.

[15] A.L. DeVera Jr., W. Strieder, Upper and lower bounds on the thermal conductivity of a random, two-phase material, J. Phys. Chem. 81 (1977) 1783–1790.

[16] A. Beck, An improved method of computing the thermal conductivity of fluid-filled sedimentary rocks, Geophysics 41 (1976) 133–144.

[17] P. Yang, Y. Yu, L. Chen, W. Mao, Experimental determination and theoretical prediction of twin orientations in magnesium alloy AZ31, Scr. Mater. 50 (2004) 1163–1168.

[18] C. Clauser, E. Huenges, Thermal conductivity of rocks and minerals, Rock physics & phase relations 3 (1995) 105–126.

[19] F. Brigaud, G. Vasseur, Mineralogy, porosity and fluid control on thermal conductivity of sedimentary rocks, Geophys. J. Int. 98 (1989) 525–542.

[20] J.C. Maxwell, A Treatise on Electricity End Magnetism, Clarendon Press, 1873.

[21] Y. Chiew, E. Glandt, The effect of structure on the conductivity of a dispersion, J. Colloid Interface Sci. 94 (1983) 90–104.
[22] E.E. Gonzo, Estimating correlations for the effective thermal conductivity of granular materials, Chem. Eng. J. 90 (2002) 299–302.
[23] J. Gan, Z. Zhou, A. Yu, Effect of particle shape and size on effective thermal conductivity of packed beds, Powder Technol. 311 (2017) 157–166.
[24] X. Huang, Q. Zhou, J. Liu, Y. Zhao, W. Zhou, D. Deng, 3D stochastic modeling, simulation and analysis of effective thermal conductivity in fibrous media, Powder Technol. 320 (2017) 397–404.
[25] G. Wei, H. Zhang, X. An, B. Xiong, S. Jiang, CFD-DEM study on heat transfer characteristics and microstructure of the blast furnace raceway with ellipsoidal particles, Powder Technol. 346 (2019) 350–362.
[26] G.K. Batchelor, R. O'brien, Thermal or electrical conduction through a granular material, Proc. R. Soc. Lond. A 355 (1977) 313–333.
[27] J. Finney, Random packings and the structure of simple liquids. I. The geometry of random close packing, Proc. R. Soc. Lond. A 319 (1970) 479–493.
[28] G. Cheng, A. Yu, P. Zulli, Evaluation of effective thermal conductivity from the structure of a packed bed, Chem. Eng. Sci. 54 (1999) 4199–4209.
[29] W. Siu, S.-K. Lee, Effective conductivity computation of a packed bed using constriction resistance and contact angle effects, Int. J. Heat Mass Transf. 43 (2000) 3917–3924.
[30] I. Fatt, The Network Model of Porous Media, 1956.
[31] J.H. van der Linden, G.A. Narsilio, A. Tordesillas, Machine learning framework for analysis of transport through complex networks in porous, granular media: a focus on permeability, Phys. Rev. E 94 (2016), 022904.
[32] X. Huang, Y. He, W. Zhou, D. Deng, Y. Zhao, Pore network modeling of fibrous porous media of uniform and gradient porosity, Powder Technol. 343 (2019) 350–361.
[33] M. Newman, Networks, Oxford university press, 2018.
[34] M.E. Newman, The structure and function of complex networks, SIAM Rev. 45 (2003) 167–256.
[35] S. Russell, D.M. Walker, A. Tordesillas, A characterization of the coupled evolution of grain fabric and pore space using complex networks: pore connectivity and optimized flows in the presence of shear bands, Journal of the Mechanics and Physics of Solids 88 (2016) 227–251.
[36] T.S. Yun, T.M. Evans, Three-dimensional random network model for thermal conductivity in particulate materials, Comput. Geotech. 37 (2010) 991–998.
[37] G. Cheng, J. Gan, D. Xu, A. Yu, Evaluation of effective thermal conductivity in random packed bed: heat transfer through fluid voids and effect of packing structure, Powder Technol. (2019)(In press, Corrected Proof).
[38] P.D. Itasca, Particle flow code in 3 dimensions, User's Guide, 2008.
[39] G.A. Narsilio, J. Kress, T.S. Yun, Characterisation of conduction phenomena in soils at the particle-scale: finite element analyses in conjunction with synthetic 3D imaging, Comput. Geotech. 37 (2010) 828–836.
[40] P. Azadi, R. Farnood, N. Yan, FEM–DEM modeling of thermal conductivity of porous pigmented coatings, Comput. Mater. Sci. 49 (2010) 392–399.
[41] T. Kanit, S. Forest, I. Galliet, V. Mounoury, D. Jeulin, Determination of the size of the representative volume element for random composites: statistical and numerical approach, Int. J. Solids Struct. 40 (2003) 3647–3679.
[42] S. Ltd, Simpleware ScanIP, http://www.simpleware.com/software/scanip , Date of access, 15 2015 12.
[43] W. Fei, G.A. Narsilio, M.M. Disfani, Impact of three-dimensional sphericity and roundness on heat transfer in granular materials, Powder Technol. 355 (2019) 770–781.
[44] W. Fei, G.A. Narsilio, J.H. van der Linden, M.M. Disfani, Quantifying the impact of rigid interparticle structures on heat transfer in granular materials using networks, Int. J. Heat Mass Transf. 143 (2019), 118514.
[45] W.J. Bosl, J. Dvorkin, A. Nur, A study of porosity and permeability using a lattice Boltzmann simulation, Geophys. Res. Lett. 25 (1998) 1475–1478.
[46] X. Garcia, L.T. Akanji, M.J. Blunt, S.K. Matthai, J.P. Latham, Numerical study of the effects of particle shape and polydispersity on permeability, Phys. Rev. E 80 (2009), 021304.
[47] C. AB, COMSOL multiphysics v5.0, http://www.comsol.com 2015.
[48] H. Carslaw, J. Jaeger, Conduction of Heat in Solids, Oxford Science Publications, Oxford, England, 1959.
[49] J. Sundberg, P.-E. Back, L.O. Ericsson, J. Wrafter, Estimation of thermal conductivity and its spatial variability in igneous rocks from in situ density logging, Int. J. Rock Mech. Min. Sci. 46 (2009) 1023–1028.
[50] R.E. Thalmann, Thermal Conductivity of Dry Soils, University of Kansas, Mechanical Engineering, 1950.
[51] C. Argento, D. Bouvard, Thermal conductivity of granular media, Powders & Grains (1993) 129–134.
[52] L.C. Freeman, Centrality in social networks conceptual clarification, Soc. Networks 1 (1978) 215–239.
[53] L.C. Freeman, A set of measures of centrality based on betweenness, Sociometry (1977) 35–41.
[54] A.N. Langville, C.D. Meyer, A survey of eigenvector methods for web information retrieval, SIAM Rev. 47 (2005) 135–161.
[55] D.M. Walker, A. Tordesillas, Topological evolution in dense granular materials: a complex networks perspective, Int. J. Solids Struct. 47 (2010) 624–639.
[56] R. Arévalo, I. Zuriguel, D. Maza, Topology of the force network in the jamming transition of an isotropically compressed granular packing, Phys. Rev. E 81 (2010), 041302.
[57] A. Tordesillas, D.M. Walker, Q. Lin, Force cycles and force chains, Phys. Rev. E 81 (2010), 011302.
[58] R. Arevalo, I. Zuriguel, D. Maza, Topological properties of the contact network of granular materials, International Journal of Bifurcation and Chaos 19 (2009) 695–702.
[59] D.S. Bassett, E.T. Owens, K.E. Daniels, M.A. Porter, Influence of network topology on sound propagation in granular materials, Phys. Rev. E 86 (2012), 041306.
[60] A. Tordesillas, Q. Lin, J. Zhang, R. Behringer, J. Shi, Structural stability and jamming of self-organized cluster conformations in dense granular materials, Journal of the Mechanics and Physics of Solids 59 (2011) 265–296.
[61] D.J. Watts, S.H. Strogatz, Collective dynamics of 'small-world'networks, nature 393 (1998) 440.
[62] F. Santosa, W.W. Symes, Linear inversion of band-limited reflection seismograms, SIAM J. Sci. Stat. Comput. 7 (1986) 1307–1330.
[63] F. Pedregosa, G. Varoquaux, A. Gramfort, V. Michel, B. Thirion, O. Grisel, M. Blondel, P. Prettenhofer, R. Weiss, V. Dubourg, Scikit-learn: machine learning in python, J. Mach. Learn. Res. 12 (2011) 2825–2830.
[64] T.K. Ho, Random decision forests, document analysis and recognition, 1995, Proceedings of the Third International Conference on, IEEE 1995, pp. 278–282.
[65] I. Barandiaran, The random subspace method for constructing decision forests, IEEE Trans. Pattern Anal. Mach. Intell. 20 (1998).
[66] B. Kamiński, M. Jakubczyk, P. Szufel, A framework for sensitivity analysis of decision trees, CEJOR 26 (2018) 135–159.
[67] M. Stone, Cross-validatory choice and assessment of statistical predictions, J. R. Stat. Soc. Ser. B Methodol. (1974) 111–147.
[68] P. Breheny, Classification and Regression Trees, 1984.
[69] J. Koh, A. Fortini, Thermal Conductivity and Electrical Resistivity of Porous Material, 1971.
[70] J. Agapiou, M. DeVries, An experimental determination of the thermal conductivity of a 304L stainless steel powder metallurgy material, J. Heat Transf. 111 (1989) 281–286.
[71] S. Torquato, I.C. Kim, D. Cule, Effective conductivity, dielectric constant, and diffusion coefficient of digitized composite media via first-passage-time equations, J. Appl. Phys. 85 (1999) 1560–1571.
[72] U. Ayachit, The Paraview Guide: A Parallel Visualization Application, Kitware, Inc., 2015
[73] U. El Shamy, O. De Leon, R. Wells, Discrete element method study on effect of shear-induced anisotropy on thermal conductivity of granular soils, International Journal of Geomechanics 13 (2013) 57–64.
[74] Y. Hu, J. Wang, J. Yang, I. Mudawar, Q. Wang, Experimental study of forced convective heat transfer in grille-particle composite packed beds, Int. J. Heat Mass Transf. 129 (2019) 103–112.
[75] R. Askari, S.H. Hejazi, M. Sahimi, Thermal conduction in deforming isotropic and anisotropic granular porous media with rough grain surface, Transp. Porous Media 124 (2018) 221–236.
[76] B. Aduda, Effective thermal conductivity of loose particulate systems, J. Mater. Sci. 31 (1996) 6441–6448.
[77] M. Gangadhara Rao, D. Singh, A generalized relationship to estimate thermal resistivity of soils, Can. Geotech. J. 36 (1999) 767–773.
[78] J. Côté, J.-M. Konrad, Thermal conductivity of base-course materials, Can. Geotech. J. 42 (2005) 61–78.
[79] L. Fletcher, Recent developments in contact conductance heat transfer, J. Heat Transf. 110 (1988) 1059–1070.
[80] Y. Asakuma, M. Asada, Y. Kanazawa, T. Yamamoto, Thermal analysis with contact resistance of packed bed by a homogenization method, Powder Technol. 291 (2016) 46–51.

5.3 NETWORK ANALYSIS OF HEAT TRANSFER IN SANDS

Type of paper: full length article - revision (*Computers and Geotechnics*)
Date text written: May 2020
Number of words in main text = 6442
Number of figures = 14
Number of tables = 2

NETWORK ANALYSIS OF HEAT TRANSFER IN SANDS

Author 1
Wenbin Fei, PhD student, ME, BE
Department of Infrastructure Engineering, The University of Melbourne, Parkville, Australia
ORCID: 0000-0002-9275-8403

Author 2
Guillermo A. Narsilio, PhD, MSc (Math), MSc (CE), CEng
Department of Infrastructure Engineering, The University of Melbourne, Parkville, Australia
ORCID: 0000-0003-1219-5661

Full contact details of corresponding author
Guillermo A. Narsilio, Associate Professor
Engineering Block B 208, Department of Infrastructure Engineering, The University of Melbourne, Parkville, VIC 3010, Australia
Email: narsilio@unimelb.edu.au, Phone: +61 (3) 8344 4659, Fax: +61 (3) 8344 4616

Abstract

Differences in the effective thermal conductivity (ETC) between measurements and models may be attributed to the limited ability to capture microstructural information of geomaterials. Today, computed tomography (CT) technology offers unprecedented access to such information, particularly for sands. Since a sand can be represented as a contact network made of nodes (particles) connected by edges (contacts), features (or variables) arising from the contact network can characterise particle connectivity. However, existing contact network features neglect the contribution of contact quality and of small gaps between neighbouring particles to heat transfer. To redress these issues, this paper introduces new weighted *contact* network features by considering contact area at each edge in the *contact* network. Additionally, *thermal* network features are proposed by considering small gaps as edges with/without being weighted by thermal conductance. All network features are calculated based on CT images of five real sands. The relationships between each feature and ETC are investigated. The results show that some network features that account for both the particle connectivity and contact quality can be used to predict ETC accurately. Advantages and limitations of this approach are also identified.

Keywords: fabric/structure of soils; particle-scale behaviour; sands; finite-element modelling; complex network theory;

1. Introduction

Heat transfer processes in soils are important in a variety of engineering applications. Take shallow geothermal energy projects as an example. Here heat is exchanged between the ground and fluid circulating in pipes embedded directly in the soil [1] (or rock) in purposely built boreholes or trenches, or incorporated in geostructures (e.g., energy piles, energy walls) [2]. With the help of a heat pump, the heat is upgraded to efficiently provide space heating and cooling to buildings. The effective thermal conductivity (ETC) of the ground is a key parameter in geothermal design [3]. ETC presents the ease of heat transfer in the ground, and thus largely determines the efficiency of the geothermal system [4, 5]. .

Predicting ETC accurately is difficult due to the complex microstructure of the soils [6]. Since heat is transferred via particles [7], and porosity indicates the fraction of particles in a soil mass, the porosity is widely used to predict ETC, as it is readily obtainable. However, porosity-dependent models neglect the effects of the microstructure such as particle connectivity and contact quality on heat transfer [8-10], given that porosity is a macro-scale parameter. As a result, porosity-dependent models are rarely valid for wide porosity ranges [10], especially for materials with a large ratio of solid to fluid thermal conductivity [11].

Packing structure models offer alternatives to porosity-dependent models by using structural characteristics instead of porosity as the key controlling variable [12]. The lack of accountability of structural data may result in the difference of ETC between models and experimental methods [6]. Some scholars have proposed microstructural characteristics such as: i) the minimum gap between particles and the mean local curvature [13, 14], ii) connectivity represented by Voronoi tessellation [15, 16], iii) an order characteristic by measuring rotational symmetry of particles [14], iv) the ratio

between the radius of contact area and particle radius [17], v) particle size distribution [18], and vi) some results for typical regular structures [19] (simple cubic, body-centred cubic and face-centred cubic). However, these works focus on sphere packings rather than the irregular sand size particles prevalent in nature. Even though a number of microstructural descriptors are available in the literature [20], the characterisations of particle connectivity in real sands are still scarce.

Recently, the wider availability of X-ray computed tomography (CT) has shed light on the microstructure of irregular granular materials [21-23]. Using imaging techniques, the structures of granular materials can be simplified into networks [24, 25]. A network is a web consisting of nodes and edges, which are defined depending on the type of network. For instance, in a *contact* network, each node represents a particle in a sand, and an edge is created when two particles touch. Based on the network, a number of network features (or variables such as degree, walks, paths, cycles, centralities and clustering coefficients in the literature [26]) can be calculated using complex network theory, and be employed to characterise the microstructure of granular materials. Russel et al. [27] advocated that a *contact* network could be used to understand mechanical stability, and a *pore* network could offer knowledge about the flow pathway in deforming granular materials. Fei et al. [28] found the local clustering coefficient (a contact network feature presenting particle connectivity) together with particle shape descriptor [29] have good correlations with ETC of sands under loadings. However, their work only applied a few *contact* network features to quantify the particle connectivity without evaluating the interparticle contact quality. Furthermore, the *contact* network features could not characterise the contribution of small gaps (near-contacts) between neighbouring particles to ETC. Since particle connectivity variables are still scarce, a question raised is whether more particle

connectivity parameters can be discovered and whether a single variable can cover both particle connectivity and contact quality. Fei et al. [30] constructed *contact* networks and also extended them to *thermal* networks by considering the small gaps between neighbouring particles as new edges. Analytical ("exact") expressions can be used to compute the interparticle contact area and construct networks for sphere packings; however, different image processing techniques and mathematical approach are required when dealing with real sands.

In the present paper, five irregular sands were used to quantify the correlations between network features and ETC. Both *contact* network features and *thermal* network features were extracted from each irregular sand. They are not only used to characterise the particle connectivity but also contact quality by considering the contact area in *contact* networks or thermal conductance in *thermal* networks, resulting in comprehensive microstructural parameters. Then, machine learning techniques were employed to evaluate the importance of the microstructural parameters in predicting ETC.

2. Materials

Five sands with different particle shapes were selected, as shown in Fig. 1. The glass beads are round and made of silica, enabling studying almost perfectly regular packings, a strategy and material often adopted by many geotechnical researchers [31-33]. The particles of the Ottawa 20-30 sand [34] also contain quartz [35] and are rounded over time by hydromechanical weathering (e.g., in a river). Angular sand is also mainly composed of quartz, but its particles are more irregular than those of Ottawa sand. The particles in crushed Schist A are more irregular still, and are mostly made of chlorites. Finally, Schist B is collected from the Delamarian Fold Belt in western Victoria, Australia, and consists of quartz and biotite; its particles are the most

irregular of the group under study, with half of them being elongated and platy [36]. The measured particle sizes of the five sands are summarised in Table 1.

<Fig. 1 around here>

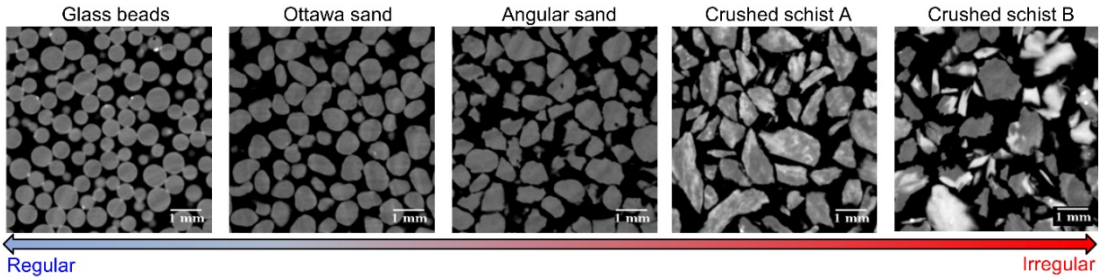

Fig. 1. Five types of natural sand scanned with computed tomography.

<Table 1 around here>

Table 1 Particle size for the selected sands

Sand	D_{50} (mm)	Min particle diam. (mm)	Max particle diam. (mm)
Glass beads	0.60	0.50	0.70
Ottawa sand	0.73	0.60	0.85
Angular sand	0.89	0.60	1.18
Crushed schist rock A	0.84	0.50	1.18
Crushed schist rock B	0.84	0.50	1.18

3. Methods

Fig. 2 shows a proposed framework which includes six blocks. In block 1, image stacks with a certain interval (resolution) were created by air-pluviating the sand in a PVC cylinder with a diameter of 25 mm and a height of 25 mm, and then scanning it with X-ray CT. The image stacks were cropped to the representative element volume and then used for three purposes: (i) calculating classic geotechnical microstructural parameters such as the average particle diameter and contact area ; (ii) constructing networks and computing network features (block 2); (iii) simulating heat transfer and calculating ETC using finite element method (FEM) (block 3); and For each feature, its correlation coefficient against ETC was presented using six mathematical models

(block 5). The model with the highest correlation coefficient was recognised as the 'best fit' model, and the correlation coefficient was used to assess the importance of the feature in predicting ETC (block 6).

<Fig. 2 around here>

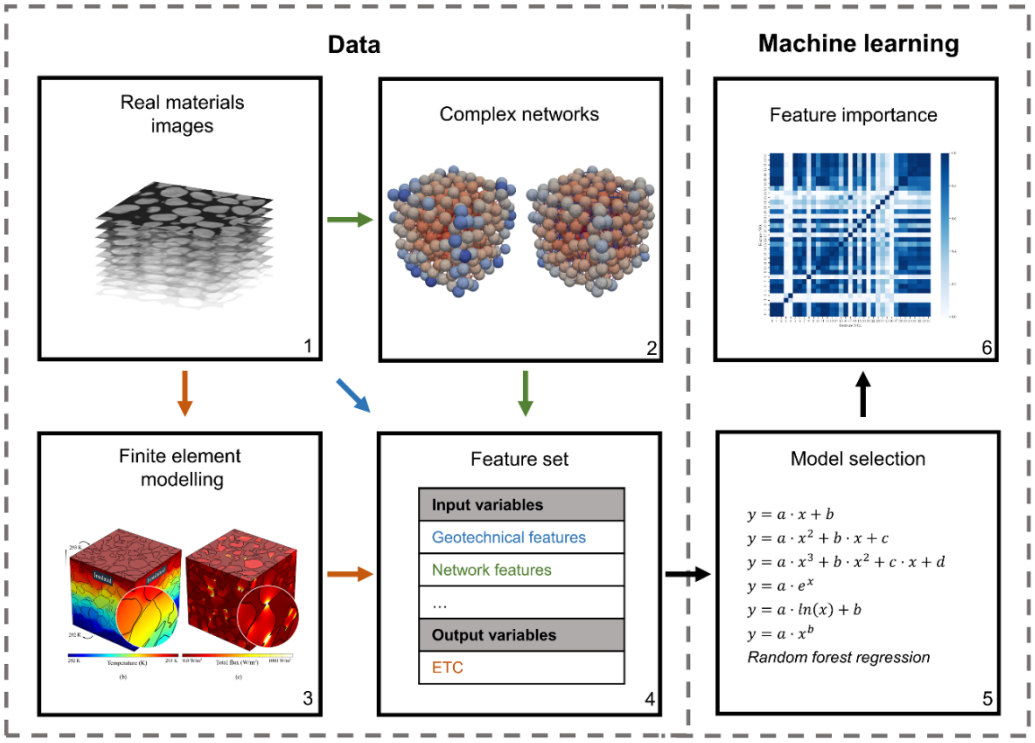

Fig. 2 Framework used to calculate the microstructural parameters and analyse their impact on the effective thermal conductivity of granular materials.

3.1 Numerical simulation and experiment

Since this paper focuses on the impact of microstructure on ETC, the variance in ETC induced by mineral components was assumed to be mitigated by assigning the same thermal conductivity to the solids in the finite element models. The numerical results were also validated using the experimental results.

3.1.1 Finite element simulation

For each sand, four representative element volumes (REVs) of dimensions 4.55 × 4.55 × 4.55 mm (320 grains in Ottawa sand as an example) were randomly selected

from the CT images. These dimensions are consistent or exceeding previously reported REVs of similar materials [37-40]. As shown in Fig. 3, the geometry of each subsample was reconstructed based on these CT images. The solid and pore phases were then split using the widely accepted Otsu threshold segmentation [41-44]. The thermal conductivity of the solid used in this paper was 3 $\mathrm{W/(m\ K)}$ [45-47], while that of air in the pore spaces was taken as 0.025 $\mathrm{W/(m\ K)}$ [48]. Reconstruction and segmentation were completed using Simpleware ScanIP [49] with a further meshing step. The mesh was then imported to a FEM software application called COMSOL Multiphysics [50] to simulate heat transfer [29, 51].

In COMSOL Multiphysics, the boundary temperature at the top T_a was prescribed as 293 K, while that on the bottom T_b was 292 K to create a thermal gradient to drive heat flux (a different thermal gradient would render similar results), and the other boundary surfaces were insulated (i.e., nil heat flux). Next, the temperature distribution was computed by solving the governing energy balance equations [52]. Since dry sands were tested using a thermal needle, the simulation model only considered heat conduction. Fourier's law was used to calculate the conductive heat flux, and a continuity equation was applied to ensure flux continuity at the particle-pore interface [51]. An example of the temperature and flux distribution is shown in Fig. 3. Based on the solutions for the heat flux at the top (inlet) and bottom (outlet) boundaries, the ETC at the two surfaces was calculated using Equation 1. The mean ETC at the two boundaries was regarded as the ETC of the whole sample:

$$\lambda_{eff} = \frac{\frac{1}{A}\int_A Q_z \, dA}{\frac{T_a - T_b}{L}} \tag{1}$$

where λ_{eff} (W/mK) is the ETC of the sample, A (m^2) is a typical cross-sectional area, L (m) is the height of the packing, T_a = 293 K and T_b = 292 K are boundary

temperatures at the top and bottom of the sample respectively, and Q_z (W/m^2) is the vertical heat flux at a typical cross-section.

<Fig. 3 around here>

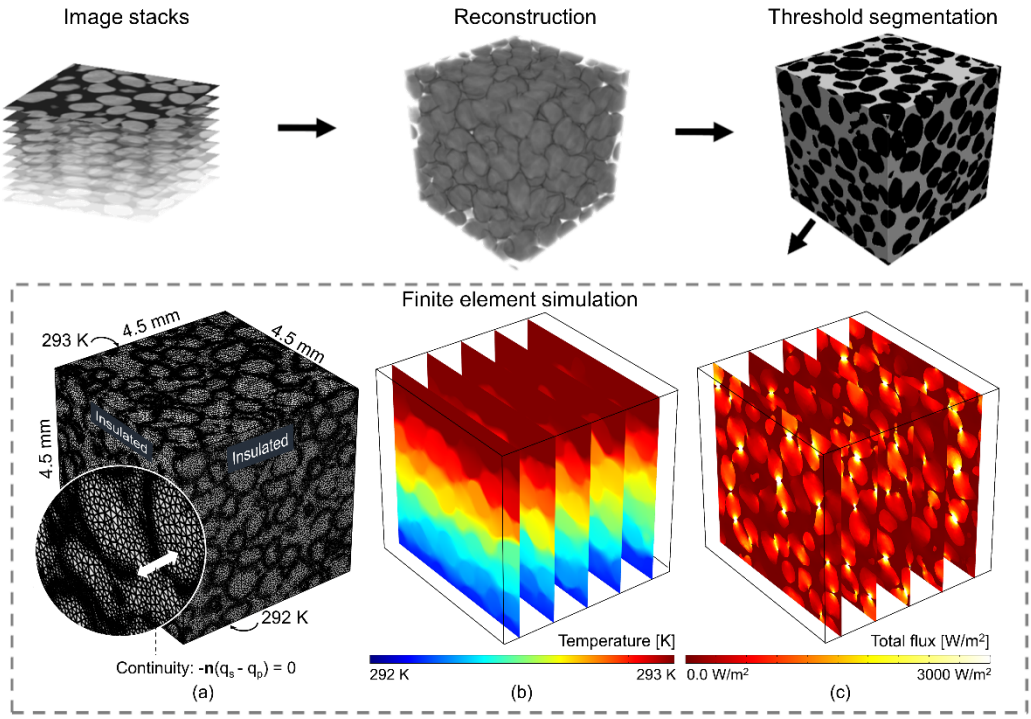

Fig. 3 The process of heat transfer simulation based on CT scanned images.

3.1.2 Laboratory experiment

In order to validate the ETC from numerical simulation, thermal needle testings were conducted to measure the ETC. The sands were rained into a PVC cylinder of diameter 50 mm and height 120 mm using the same air-pluviation method to prepare a homogeneous specimen. A 100-mm long thermal needle probe of diameter 2.4 mm was used to measure the ETC at room temperature, following ASTM standard D5334-14 [53]. The diameter of the selected needle was larger than the particle diameter (Table 1) to ensure more contacts between the probe and particles. A KD2 Pro thermal properties analyser with a manufacturer reported accuracy of $\pm 10\%$ for 0.2-4 W/mK materials was used [54]. This is consistent with standard requirements.

3.2 Complex networks

3.2.1 Network construction

A *contact* network can be constructed by assigning a node to the centroid of each particle and generating an edge between two nodes if the corresponding particles touch (Fig. 4). The particles in the CT images (Fig. 1) were connected, and watershed segmentation was required to split the connected particles into individual ones using an add-in called 'MorphoLibj' [55] in Fiji [56]. To avoid over-segmentation of the contact area, which is important for heat transfer [7], a six-voxel neighbourhood [57] was used in the watershed algorithm. However, the contact network only considered interparticle heat transfer and neglected heat conducts via the air in the small gap between particles [46]. To address this, the *contact* network was extended to a *thermal* network by considering the small gaps as 'near-contacts' and allocating edges to them, as shown in Fig. 4.

<Fig. 4 around here>

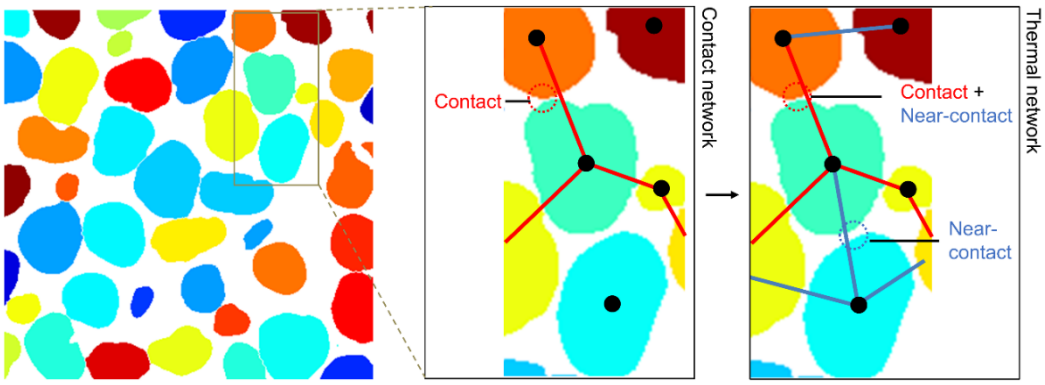

Fig. 4 The heat transfer path includes both interparticle contact and the small gaps between particles. Only interparticle contact is considered in the *contact* network, while both paths are involved in the *thermal* network.

In a sphere packing (Fig. 5 (a)), any two adjacent particles are connected by either a circular contact of radius r_c or a gap of distance h_{ij}. Hence, the network edges related

to interparticle contacts and near-contacts can be easily determined using analytical expressions. In contrast, the irregular particle shape of natural sands obtained through micro-CT (Fig. 5 (b)) posts a significant challenge to build networks representing them. In this work, the boundary voxels of each particle were first identified in the watershed-segmented CT images using an edge detection algorithm and used to determine the interparticle contacts and near-contacts as follows: Boundary voxels shared between two particles made up an interparticle *contact*. For those voxels that are not in contact, if the distance between two voxels at the boundaries of two neighbouring particles are less than a certain threshold distance, they were labelled as in a *near-contact*. By following the work of van der Linden et al. [58] and Fei et al. [28], half the average particle radius was selected as this threshold distance by calibrating our thermal network model with network models for sphere packings [46] which was developed based on theoretical equations. There is another important difference when dealing with sphere packings vs real sands. To compute the thermal conductance at interparticle contacts and near-contacts, the analytical solutions are available for sphere packings [46]. In contrast, the thermal conductance at the interparticle contact in real sands is computed in this work using the number of shared boundary voxels (Fig. 5 (b)), and the thermal conductance at near-contacts is calculated using the distance between voxels and computing conductance in parallel of a series of cylinders filling the near-contact gap between particles [28].

<Fig. 5 around here>

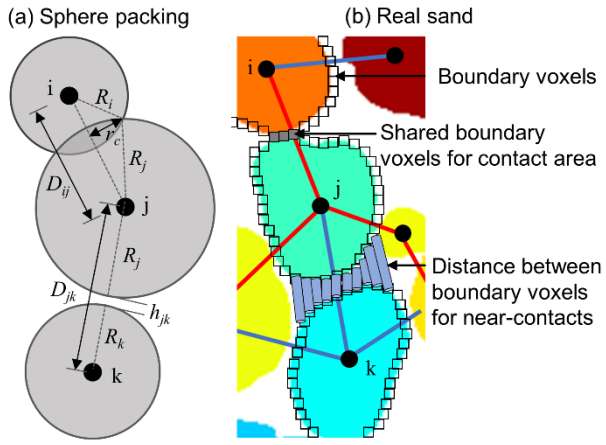

Fig. 5 Identification of the interparticle contact and the near-contact in (a) a sphere packing and (b) a real sand from voxelated images.

3.2.2 Network features

After constructing the networks, network features can be extracted by using complex network theory. Four types of features were used here: (i) *centrality*; (ii) *network scale*; (iii) *cycles*; and (iv) *clustering*.

Centrality quantifies the 'significance' of a node, edge or structure in a network [59]. As shown in Fig. 6 (a), five metrics of centrality are used in this work. They highlight the significance of the nodes in different ways. The *degree* $\kappa(i)$ of a node i, also known as the *coordination number*, is the number of edges linked to this node. *Closeness centrality* quantifies the closeness of a node to others in a network, and high *closeness centrality* means a node is in a 'central' position. *Betweenness centrality* qualifies the importance of a node or edge that acts as a 'bridge' between other nodes or edges. A high *betweenness centrality* indicates that the node or edge plays a vital role in the heat transfer path. *Eigenvector centrality* measures the wide-reaching influence of a node in a network by assigning a relative score to each node. A node with high *eigenvector centrality* indicates that it has good connections to other nodes with high scores. *Top-to-bottom edge betweenness centrality* is used to only consider the corresponding heat transfer paths when heat travels predominantly in one

dimension (say, top to bottom) in response to the thermal gradient prescribed in this direction. Let us summarise next the formal definitions of key network features.

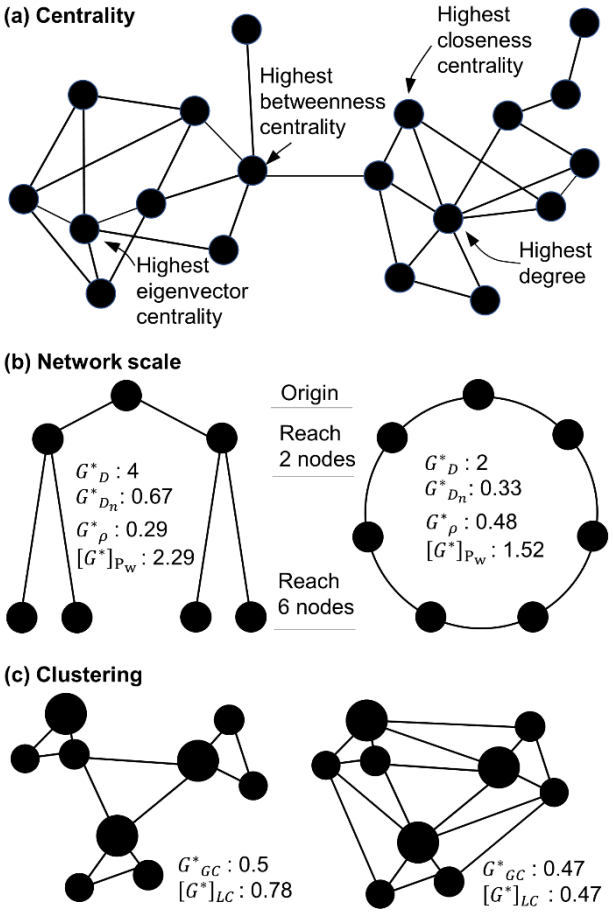

Fig. 6 Network features: (a) Identifying the nodes with the highest values of the different types of centrality features in a given network, (b) network scale features and (c) clustering coefficients for different networks with the same number of nodes [30].

For a node i in a node-set V, its closeness centrality is defined as the reciprocal of the sum over the shortest path $d(i,j)$ from the node i to all other nodes j (Equation 2) [60].

$$[G^*]_C(i) = \beta \left[\sum_{j=1}^{|V|-1} d(i,j) \right]^{-1} \tag{2}$$

where β is a normalisation term set to be the number of reachable nodes $|V|-1$ and the number of maximum possible edges $(|V|(|V|-1))/2$ in this study (both normalisations are trialled), here $|V|$ is the number of nodes in the network.

As shown in Equation 3, the *node betweenness centrality* of node *i* can be calculated as the sum of the ratio of $\sigma(j,k|i)$ (the number of shortest paths from any other two nodes *j* and *k* and pass *i*) to $\sigma(j,k)$ (the number of shortest paths from any other two nodes *j* and *k*). Similarly, the *edge betweenness centrality* of edge *e* is computed as the ratio of $\sigma(j,k|e)$ (the number of shortest paths from any other two edges *j* and *k* and pass *e*) to $\sigma(j,k)$ (the number of shortest paths from any other two edges *j* and *k*). The *betweenness centrality* can be further normalised with β, which is *2/(|V-1|(|V|-2))* for *node betweenness centrality* and *2/[|V|(|V|-1)]* for *edge betweenness centrality* [61].

$$[G^*]_{B^{node}}(i) = \beta \sum_{j,k \epsilon V} \frac{\sigma(j,k|i)}{\sigma(j,k)} \tag{3}$$

Network scale indicates the average distance from one node to others in a network. It helps in understanding the speed of heat transfer through networks with different topologies. As shown inFig. 6 (b), , heat transfers faster in a 'tree' network, since only two steps are required to reach six nodes compared with the three steps required in a 'ring' network. The *network diameter* G_D^*, *average shortest path length* $[G^*]_{P_w}$ and *network density* G_ρ^* are used here to quantify the network scale. *Network diameter* is the length of the longest of the shortest paths in a network, and the *normalised network diameter* $G_{D_n}^*$ can be achieved by dividing G_D^* by *|V|-1*. As heat is transferred from the top surface (inlet) to the bottom surface (outlet) in the FEM models, as shown in Fig. 3, the *average shortest path length between the inlet and outlet nodes* is related to the heat transfer path and is used as another network feature. *Network density* G_ρ^* is the

ratio between the real edge number and the potential edge number, and represents the different particle connectivity in networks. The values of network-scale-type features in ring and tree networks are shown in Fig. 6 (b).

A *cycle* is a loop that begins and ends at the same node. A *L-cycle* indicates that a loop has *l* edge, meaning that a *3-cycle* is a triangle. As triangles are isostatic [62-64], a *3-cycle* resists deformation, and the number of *3-cycles* represents the rigidity of the microstructure of a sample [28, 65]. In this work, the number of *3-cycles* and the normalised value based on edge and node numbers were calculated.

Clustering measures the integrity of a network. left figure of Fig. 6 (c) shows a fractured network with three clusters, where only one edge connects each of the clusters. In contrast, the right figure of Fig. 6 (c) shows a relatively integrated network, where the three clusters are well connected. The global [66] and local cluster coefficients [67] can be used to quantify the clustering of networks, as defined in Equations 4 and 5, respectively. It can be seen from Fig. 6 (c) that a fractured network has a higher clustering coefficient than an integrated network.

$$G^*{}_{GC} = 3\,\frac{number\ of\ triangles}{number\ of\ connected\ triples} \tag{4}$$

$$[G^*]_{LC}\,(\mathrm{i}) = \frac{2T(i)}{\kappa(i)[\kappa(i)-1]} \tag{5}$$

where *T(i)* is the number of triangles pass node *i* and $\kappa(i)$ is the degree of node i.

Network features were determined from the contact and thermal networks for each sample. An edge represents an interparticle contact in a contact network (Fig. 4) and the contact area can be calculated using the shared boundary voxels. As a larger contact area leads to greater heat transfer via interparticle contact [68, 69] and a larger *degree* indicates more interparticle contacts, the length of each edge for degree was weighted by the contact area in the contact network which only considered interparticle contact.

Hence, the physical meaning of $G^C_{\kappa_w}(i)$ of node i is the total contact area between node i and its neighbours, $[G^C]_{\kappa_w}$ is the average of $G^C_{\kappa_w}$ of all nodes in a network. As other network features with higher value such as closeness centrality in Equation 2 could be achieved by minimising the length of the shortest path, the length of each edge for other contact network features was weighted by the reciprocal of the contact area. Similarly, since thermal conductance can be calculated at interparticle contacts and near-contacts at thermal network edges, the length of each edge for *degree* was weighted by sum of thermal conductance through interparticle contact and near-contact between two neighbouring particles. Consequently, the physical meaning of $G^T_{\kappa_w}(i)$ of node i is the total thermal conductance between node i and its neighbours, $[G^T]_{\kappa_w}$ is the average of $G^T_{\kappa_w}$ of all nodes in a network. The length of each edge for other thermal network features can be weighted by the reciprocal of thermal conductance.

Classic geotechnical parameters including porosity and contact radius ratio (the radius of the contact area divided by that of the particle) were also calculated for each sample. Finally, all features were collected as a feature set (Table 2). The features were scaled (normalisation terminology in machine learning) [30]. since they had distinct ranges.

<Table 2 around here>

Table 2 Summary of features used in this work

Type	No.	Notation	Attribute
Geotechnics	1	n	Porosity
	2	γ	Contact radius ratio
	3	D_{50}	Average particle diameter
	4	C_u	Coefficient of uniformity
	5	C_c	Coefficient of curvature
Centrality	6	$[G^*]_\kappa$	Degree ('coordination number' in a contact network)
	7	$[G^*]_{\kappa_w}$	Weighted degree
	8	$[\mathrm{G}^*]_\mathrm{C}$	Closeness centrality
	9	$[\mathrm{G}^*]_{\mathrm{C_{n1}}}$	Closeness centrality normalised by $\lvert\mathrm{V}\rvert - 1$
	10	$[G^*]_{C_{n2}}$	Closeness centrality normalised by $[\lvert\mathrm{V}\rvert(\lvert\mathrm{V}\rvert - 1)]/2$

Type	No.	Notation	Attribute
	11	$[G^*]_{C_w}$	Weighted closeness centrality
	12	$[G^*]_{C_{nw1}}$	Weighted closeness centrality normalised by $\|V\| - 1$
	13	$[G^*]_{C_{nw2}}$	Weighted closeness centrality normalised by $[\|V\|(\|V\| - 1)]/2$
	14	$[G^*]_{B^{node}}$	Node betweenness centrality
	15	$[G^*]_{B_n^{node}}$	Normalised node betweenness centrality
	16	$[G^*]_{B_w^{node}}$	Weighted node betweenness centrality
	17	$[G^*]_{B_{nw}^{node}}$	Normalised weighted node betweenness centrality
	18	$[G^*]_{B^{edge}}$	Edge betweenness centrality
	19	$[G^*]_{B_n^{edge}}$	Normalised edge betweenness centrality
	20	$[G^*]_{B_w^{edge}}$	Weighted edge betweenness centrality
	21	$[G^*]_{B_{nw}^{edge}}$	Normalised weighted edge betweenness centrality
	22	$[G^*]_{B_w^{edge^{tp}}}$	Weighted top-to-bottom edge betweenness centrality average
	23	$[G^*]_{B_{nw}^{edge^{tp}}}$	Normalised weighted top-to-bottom edge betweenness centrality average
	24	$[G^*]_E$	Eigenvector centrality
	25	$[G^*]_{E_w}$	Weighted eigenvector centrality
Network scale	26	G_ρ^*	Network density
	27	G_D^*	Network diameter
	28	$G_{D_n}^*$	Normalised network diameter
	29	$[G^*]_{P_w}$	Weighted shortest path (average)
	30	$[G^*]_{P_w^{tp}}$	Average weighted shortest path between inlet and outlet nodes
Clustering	31	$G^*{}_{GC}$	Global clustering coefficient
	32	$[G^*]_{LC}$	Local clustering coefficient
Cycles	33	G_{3C}^*	Number of 3-cycles
	34	$[G^*]_{3C^{node}}$	Average number of node 3-cycles
	35	$[G^*]_{3C^{\text{edge}}}$	Average number of edge 3-cycles

[G]* is a unified characteristic, and *[G^C]* refers to *contact* network features, while *[G^T]* refers to *thermal* networks. The brackets in *[G*]* indicate an average value of the parameter. *|V|* is the total number of nodes in the network.

3.3 Model selection and feature importance

3.3.1 Model selection

We aimed to identify the essential features for ETC from the 35 features shown in Table 2. For each pair of a feature and ETC, six common mathematical models (linear, quadratic polynomial, cubic polynomial, exponential, logarithmic and power) were used to compute their correlation coefficient R^2. These six models were linearized for higher computational efficiency. Among the six models, the one with the highest R^2 was selected as the 'best fit' model. The challenge when using different orders of

polynomials was to avoid over-fitting. To address this concern, LASSO regression and cross-validation were used in this study [70].

LASSO (least absolute shrinkage and selection operator) regression [71] is an extension of regression analysis that considers regularisation in generalised linear models. It penalises the non-zero coefficient of the variables in linear models, meaning that many coefficients will be zeroed. The process of zeroing covariates is also a variable selection which benefits the interpretability of the models and the accuracy of prediction. We adopted the LASSO regression, embedded in a Python library called scikit-learn [72].

In a prediction problem, one part of the dataset (training dataset) is used to train the model, while another part (validation or testing dataset) is used to test its performance. However, if the dataset is small, there may be insufficient unknown data for testing. K-fold cross validation [73] can resolve this issue by partitioning the dataset randomly into K subsets, each of which is used in turn as a validation dataset, while the other K−1 subsets are combined as the training dataset, generating a total of K scores for R^2. The average K score is then used to evaluate the fitting accuracy of the model. As six models were involved in this work, the model with the highest average score was selected as the 'best fit' model. K was set to four in this work.

3.3.2 Feature relevance

The average score can only be used to evaluate the model, rather than to assess the importance of a feature, since the type of model is a new feature that is not considered in training. In order to evaluate the importance of each score to the ETC, a new general correlation coefficient R^2 was calculated, based on all of the data.

4. Results and Discussion

4.1 Effective thermal conductivity

Four subsamples were selected from each sand, and ETC values were computed using FEM, as shown in Fig. 7. The simulated results were also validated using the experimental results and data reported by Narsilio et al. [51] and Yun and Santamarina [7]. The simulated ETC decreases as porosity increases from 0.35 to 0.50. Increasing porosity indicates a lower percentage of solid particles in the sand, resulting in a potential decrease in interparticle contact number, which forms the primary heat transfer path in dry granular materials [45]. However, when the porosity increases beyond 0.50, the variation in the ETC becomes minimal. This demonstrates that the porosity is not directly related to ETC in geomaterials such as frozen ground where void space is largely occupied by ice or ice lenses, and a large porosity of more than 0.5 is common.

The experimental results show a similar trend, although their absolute values are lower. This difference arises from several aspects: (i) the error in needle probe testing; (ii) since the CT images are voxelated and the interface between the solid and void phases has a sawtooth pattern, the contact area may be overestimated when threshold segmentation is used [28, 44]; (iii) the image resolution and finite element meshing techniques cannot capture the particle surface roughness [51]. CT images with higher resolution can improve the calculation of the contact area. However, the selection of the image resolution is a trade-off between sample size and resolution: a larger sample (more grains) with lower resolution while smaller sample (fewer grains) boosting higher resolution. Estimating ETC accurately and directly from large size and high-resolution CT images using finite element methods is not currently practical.

<Fig. 7 around here>

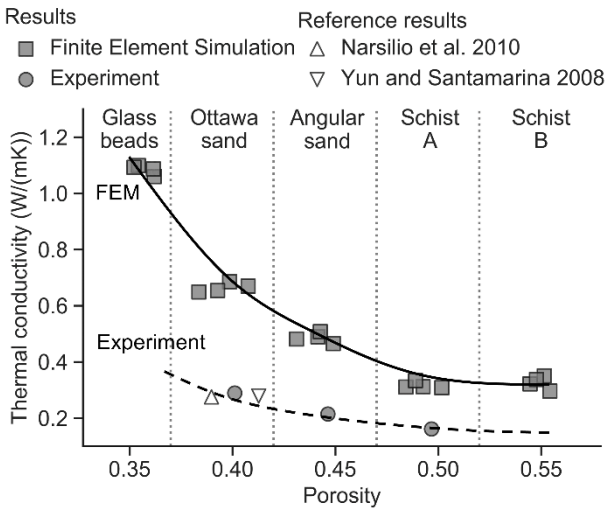

Fig. 7. The ETC of five types of sand are computed using the finite element method and validated using experimental results.

4.2 Effects of network features on ETC

Contact and thermal networks were constructed to compute the network feature set in Table 2. Fig. 8 shows examples of these networks for the same sample. The thermal network has more edges than the contact network does since it considers not only interparticle contacts but also near-contacts. The different number of edges changes the values of the network features. As 'near-contact' edges in the thermal network reduce the shortest path between nodes, the node closeness centrality calculated from the thermal network is larger than that for the contact network, according to Equation 2.

<Fig. 8 around here>

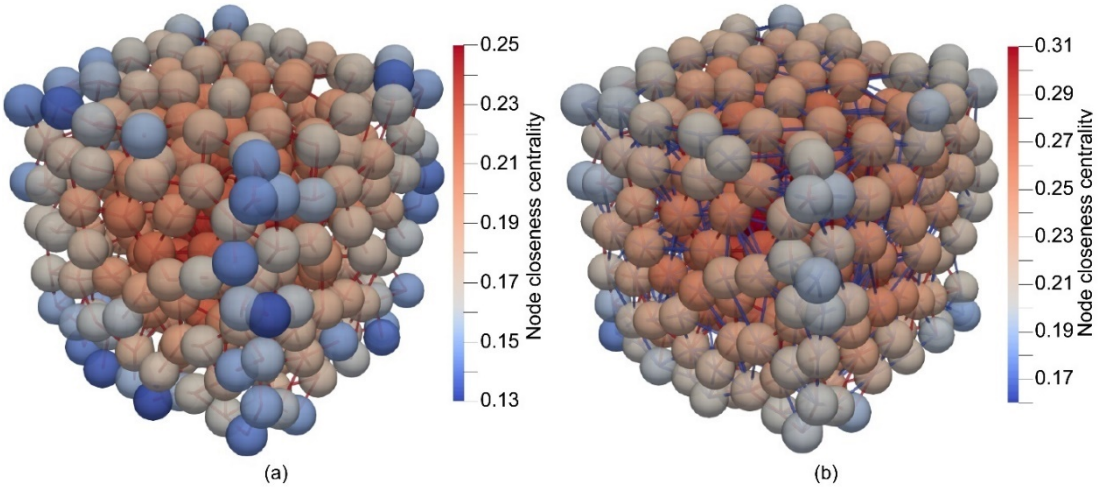

Fig. 8. Contact and thermal networks: (a) Only real contacts (red edges) are considered in a contact network, while (b) both real contacts and 'near-contacts' (blue edges) are considered in a thermal network for the same sample. Sand grains were presented by spheres with equivalent particle diameters.

Using the model selection and feature importance evaluation methods, the correlations between each pair of features and simulated ETC is calculated, and the scores are shown in Fig. 9. The 'best fit' model for each feature and the exact values of the scores are summarised in Appendix 1. Fig. 9 shows that porosity (Feature 1) as a classic geotechnical feature that has a high score of 0.93. The degree $[G^C]_\kappa$ (Feature 6) of the contact network, also known as the coordination number in geotechnics, has a high score of 0.96. Fig. 10(a) shows that ETC increases with $[G^C]_\kappa$, indicating that more interparticle contacts result in a larger ETC. Although the values of $[G^C]_\kappa$ for crushed Schist A and B are similar as shown in Fig. 10(a), the values of the four subsamples in a given sand disperses. Samples of Ottawa and angular sand may have the same $[G^C]_\kappa$ but quite different values of ETC. In contrast, the weighted degree $[G^C]_{\kappa_w}$ (Feature 7) considers the interparticle contact area at each network edge based on $[G^C]_\kappa$ (coordination number) which characterises only the particle connectivity. In

other words, the physical meaning of $G^C_{\kappa_w}(i)$ of node *i* is the total contact area between node *i* and its neighbours, $[G^C]_{\kappa_w}$ is the average of $G^C_{\kappa_w}$ of all nodes in a network. Fig. 10(b) shows that $[G^C]_{\kappa_w}$ classifies the five materials into different groups, indicating a feature including both particle connectivity and contact quality (interparticle contact area) could have a better correlation with ETC. It also can be seen from Fig. 10(b) that the data for crushed Schist B do not fall on the fitted line, due to its larger contact ratio (Fig. 10(c)) than crushed Schist A, even though they have similar coordination numbers (Fig. 10(a)). The larger interparticle contact area may be because half of the particles in crushed Schist B are elongated and platy (Fig. 1) [29]. Although the score of $[G^C]_{\kappa_w}$ is slightly lower than $[G^C]_{\kappa}$ due to data deviation in crushed Schist B, weighted degree $[G^C]_{\kappa_w}$ is still a good candidate for predicting ETC, since it has a high correlation with ETC and it involves information on both particle connectivity and contact quality. Instead of quantifying the contact quality using the interparticle contact area, thermal conductance can measure both the interparticle contact quality and near-contact (Fig. 4) quality. The weighted degree $[G^T]_{\kappa_w}$ derived from the thermal network (as opposed to from the contact network, note the T superscript) was calculated by adding the thermal conductance at each thermal network edge. The physical meaning of $G^T_{\kappa_w}(i)$ of node *i* is the total thermal conductance between node *i* and its neighbours, $[G^T]_{\kappa_w}$ is the average of $G^T_{\kappa_w}$ of all nodes in a network. A curve presented by Equation 6 describes the correlation between $[G^T]_{\kappa_w}$ and ETC as shown in Fig. 10(d). The data for crushed Schist B now is on the fitted curve rather than off the fitted curve as shown in Fig. 10(b). Compared with the differences in porosity between crushed Schist A and B for the same ETC (Fig. 7), the values of $[G^T]_{\kappa_w}$ are similar, the plateau in Fig. 7 indicates that heat transfer more directly relies on the particle connectivity than the solid/pore fraction.

<Fig. 9 around here>

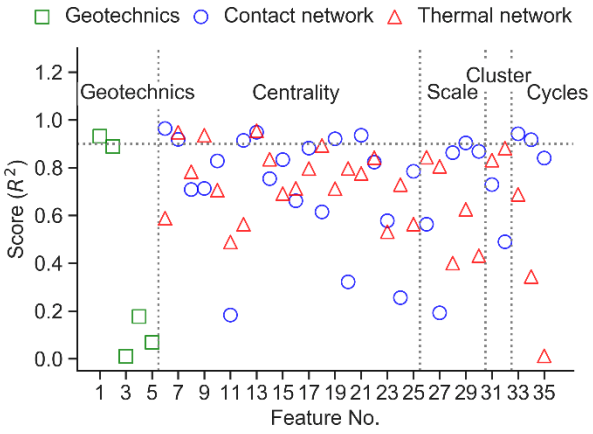

Fig. 9. The importance of each feature to ETC (feature number refers to the listing in Table 2).

<Fig. 10 around here>

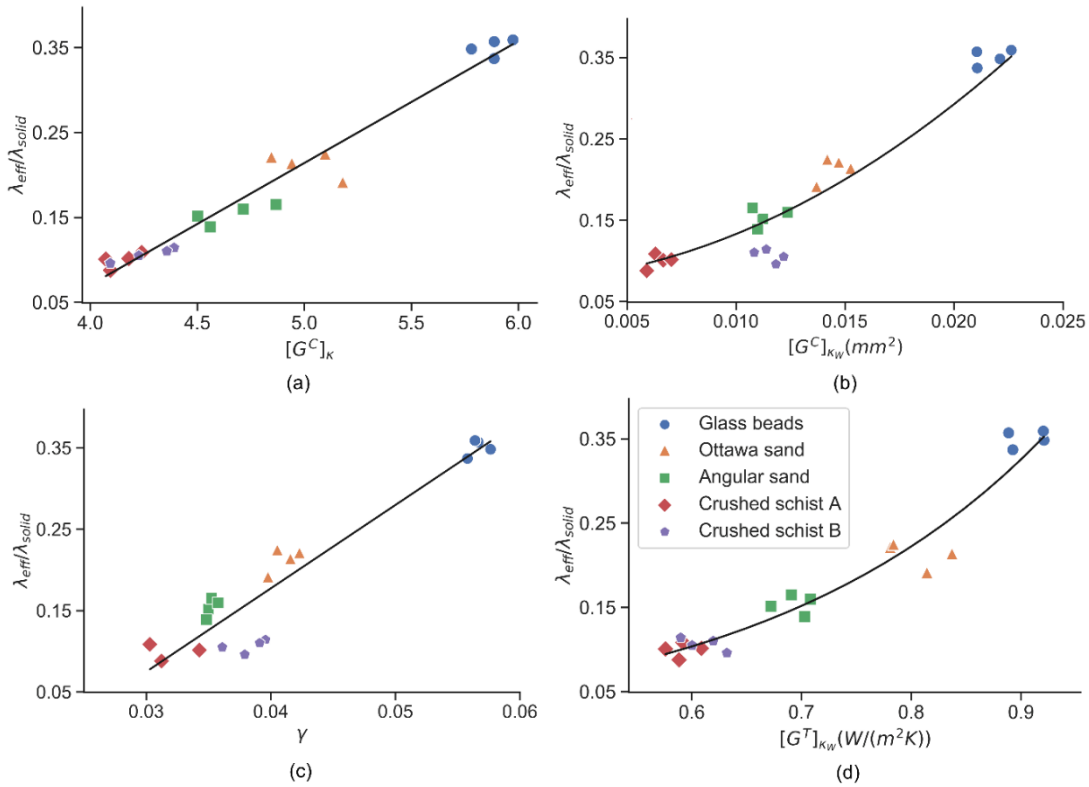

Fig. 10. Relationship between ETC and (a) contact network feature *degree* $[G^C]_\kappa$ (coordination number); (b) contact network feature *weighted degree* $[G^C]_{\kappa_w}$; (c) : *contact radius ratio* γ; and (d) thermal network feature *weighted degree* $[G^T]_{\kappa_w}$.

$$\frac{\lambda_{eff}}{\lambda_{solid}} = 1.71\left([G^T]_{\kappa_w}\right)^2 - 1.81[G^T]_{\kappa_w} + 0.58 \quad (6)$$

For *closeness centrality* type of features (Features 8–13 in Fig. 9) which indicate the distance between nodes in a network, $[G^T]_{C_{n1}}$ (Feature 9) has the highest score of 0.94. Fig. 11(a) shows that ETC decreases with increasing $[G^T]_{C_{n1}}$; the trend is different from the relationship between ETC and other unweighted particle connectivity variables such as $[G^C]_{\kappa}$ for the contact network. The decreasing trend of ETC with $[G^T]_{C_{n1}}$ is because near-contacts in the thermal network reduce the shortest path *d(i,j)* used in Equation 2. The high percentage of near-contact edges in a thermal network constructed from irregular particles such as crushed Schist results in a high $[G^T]_{C_{n1}}$ [28]. As heat transfer is lower through near-contacts than that in interparticle contacts, thermal conductance was added as weight at thermal network edges to obtain $[G^T]_{C_{nw2}}$(Feature 13). A near-contact acting as the shortest path in the unweighted thermal network may not be the shortest path in the weighted thermal network since thermal conductance is low at near-contacts. Fig. 11(b) shows the increase in $[G^C]_{C_{nw1}}$ with ETC, which is similar to the effect of $[G^C]_{\kappa_w}$ on ETC, as shown in Fig. 10(b). Since Fig. 9 shows $[G^*]_{C_{nw2}}$ (Feature 13) from both contact network and thermal network have high linear correlation (R^2 around 0.95) with ETC, the relationships are plotted in Fig. 11(c) for $[G^C]_{C_{nw2}}$ and Fig. 11(d) for $[G^T]_{C_{nw2}}$, respectively. The relationship between $[G^T]_{C_{nw2}}$and ETC is described by Equation 7, this simple linear equation results in a similar R^2 as the Quadratic polynomial Equation 6 which considers $[G^T]_{\kappa_w}$ as a single variable. However, the values of $[G^T]_{C_{nw2}}$ for different sands are not distribute as evenly as the values of $[G^T]_{\kappa_w}$.

<Fig. 11 around here>

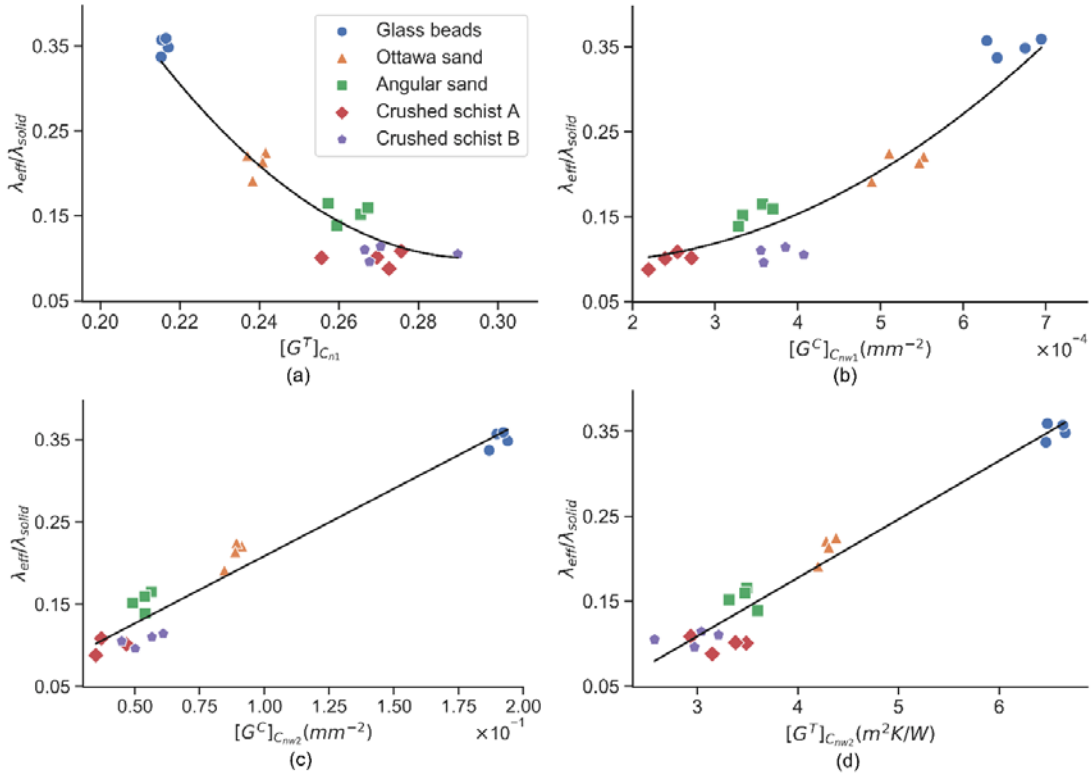

Fig. 11. The relationship between ETC and contact network feature (a) $[G^T]_{C_{n1}}$ (*closeness centrality normalised by |V|-1)* and (b) $[G^T]_{C_{nw1}}$ (*weighted closeness centrality normalised by |V|-1)*.

$$\frac{\lambda_{eff}}{\lambda_{solid}} = 0.069[G^T]_{C_{nw1}} - 0.098 \quad (7)$$

Betweenness centrality is another type of centrality to quantify the importance of a node or edge as a 'bridge'. Fig. 9 shows that contact network features $[G^C]_{B_n^{edge}}$ (Feature 19) and $[G^C]_{B_{nw}^{edge}}$ (Feature 21) have scores larger than 0.9, and their relationships with ETC are shown in Fig. 12. Higher $[G^C]_{B_n^{edge}}$ means that the different parts of the sample are more separated, and ETC is lower in a sample with a larger $[G^C]_{B_n^{edge}}$, as shown in Fig. 12. Since the *betweenness centrality* calculates a percentage (Equation 3) of the shortest path via a node or edge, adding weight keeps the value of the *betweenness centrality* (percentage) within a similar range, even

though the shortest paths are changed. The *weighted edge betweenness centrality* $[G^C]_{B_{nw}^{edge}}$ also enables data from the a given material to be closer by comparing the data for the angular sand in Fig. 12(a) and Fig. 12Fig. 12(b). In contrast to the *weighted edge betweenness centrality* for the contact network $[G^C]_{B_{nw}^{edge}}$, the *weighted edge betweenness centrality* $[G^T]_{B_{nw}^{edge}}$ for the thermal network has a lower score of 0.78 (Fig. 9). The lower score of $[G^T]_{B_{nw}^{edge}}$ indicates that heat transfer via near-contacts reduces the correlation between *edge betweenness centrality* and ETC, it is possibly because the directions of heat transfer at near-contact edges are not considered when calculating the shortest path. The shortest path with highest local thermal conductance without considering the heat transfer orientation may not be the optimal heat transfer path, resulting in the *average weighted shortest path* $[G^T]_{P_w}$ (Feature 29) in the thermal network having a lower correlation with ETC than $[G^C]_{P_w}$. In contrast, $[G^T]_{B_w^{edge^{tp}}}$ (Feature 22), which only measures the *edge betweenness centrality* in the main heat transfer direction (between the top and bottom sample surfaces) for the thermal network, has a similar score to $[G^C]_{B_w^{edge^{tp}}}$ for the contact network.

<Fig. 12 around here>

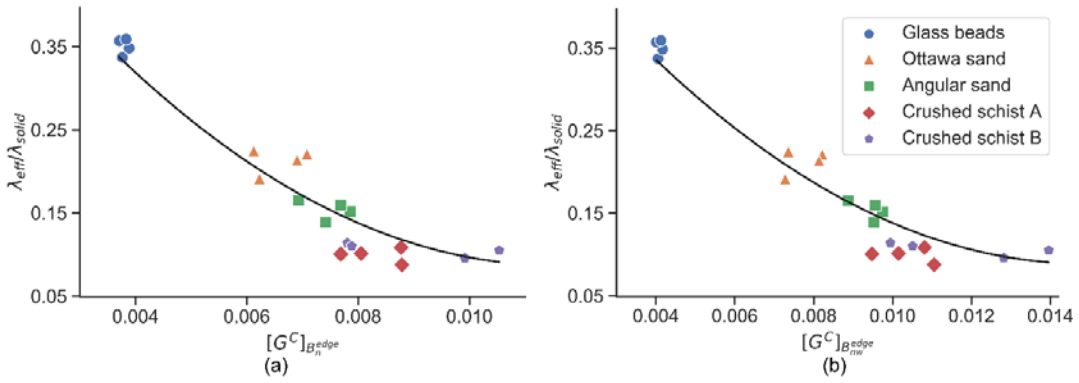

Fig. 12. Contact network features: (a) $[G^C]_{B_n^{edge}}$ (*normalised edge betweenness centrality*) and (b) $[G^C]_{B_{nw}^{edge}}$ (*normalised weighted edge betweenness centrality*) has a high correlation with ETC.

From the definitions of cluster-type and cycle-type features, they are related only to the particle connectivity, without quantifying the contact quality. However, the *local clustering coefficient* $[G^T]_{LC}$ (Feature 32) for the thermal network and the number of *3-cycles* G_{3C}^C (Feature 33) for the contact network show good correlation with ETC. Since $[G^T]_{LC}$ measures the density of triangles in the thermal network, ETC decreases with increasing $[G^T]_{LC}$ (Fig. 13(a)) due to the large percentage of near-contacts in irregular particle packings. In contrast, ETC increases with the number of *3-cycles* in regular particle packings, as shown in Fig. 13(b).

<Fig. 13 around here>

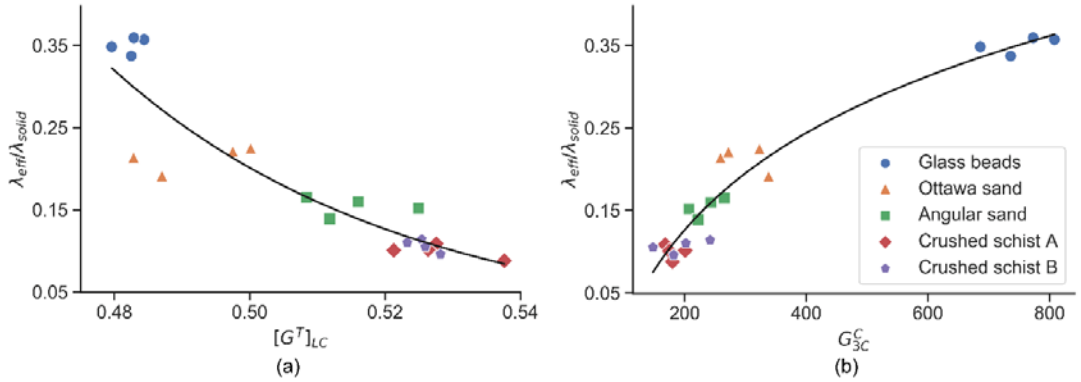

Fig. 13. (a) Thermal network feature $[G^T]_{LC}$ (*local clustering coefficient)* and (b) contact network feature G_{3C}^C (*number of 3-cycles*) show good correlation with ETC.

4.3 Relationships between features

Several network features affect ETC and all of these are mesoscale features used to indicate the connectivity of particles, and some consider contact quality. Hence, strong relationships may exist between them. Fig. 9 shows that thermal network features present lower correlations with ETC than contact network features, indicating that

correlation between the former is weaker than for the latter. The correlations between each pair of the variables in Table 2 were therefore calculated (network features computed from thermal networks). The same procedures for model selection and feature importance were used to study the relationship between each feature and ETC. Fig. 14 shows that the correlation between centrality features (Features 6–25) is high, and the correlation coefficient between $[G^T]_{\kappa_w}$ (Featrue 7) and $[G^T]_{C_{nw2}}$ (Featrue 13) is 0.94. Fig. 15(a) shows they have a positive relationship since they both measure the weighted particle connectivity. $[G^T]_{B_w^{edge^{tp}}}$ (Feature 22) and $[G^T]_{LC}$ (Feature 32) are both percentages according to their definitions and have a correlation coefficient of 0.80. Fig. 15(b) shows they have a negative relationship, since higher $[G^T]_{B_w^{edge^{tp}}}$ means that a network is more fractured (the sample is looser), while higher $[G^T]_{LC}$ indicates more integration (the sample is denser).

<Fig. 14 around here>

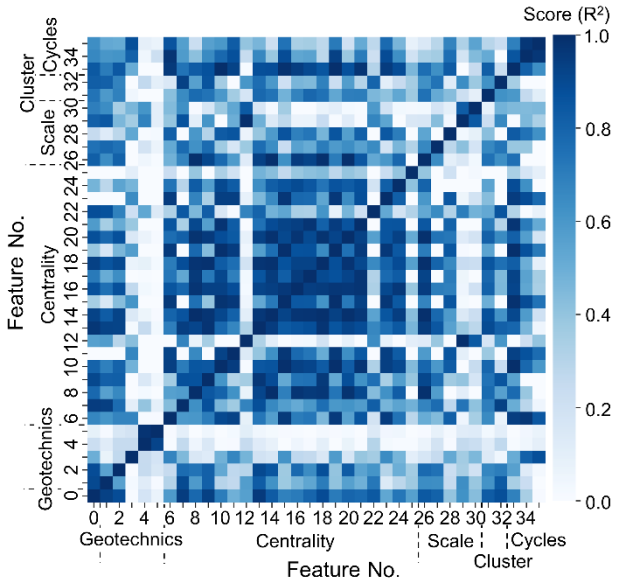

Fig. 14. The score between each two features. Feature 0 is the dimensionless ETC and other features refer to Table 2.

<Fig. 15 around here>

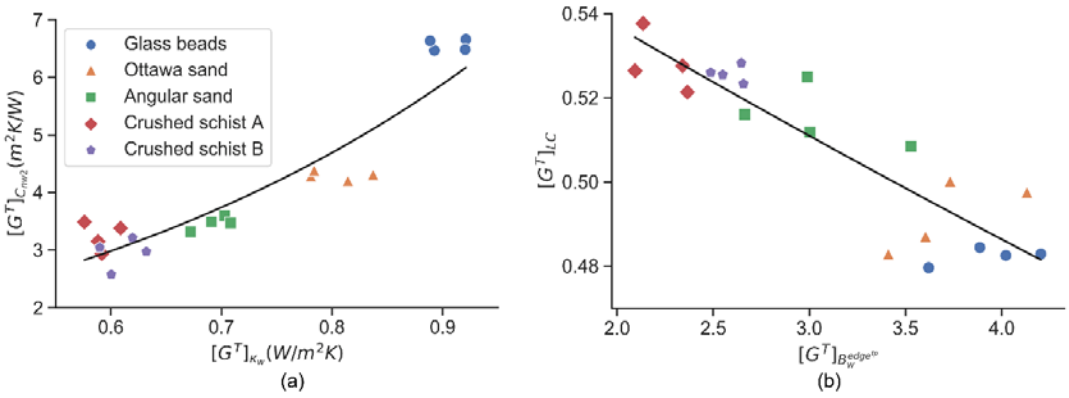

Fig. 15. Relationships between thermal network features: (a) relationship between $[G^T]_{\kappa_W}$ (*weighted degree*) and $[G^T]_{C_{n1}}$ (*closeness centrality normalised by |V|-1*); (b) relationship between $[G^T]_{B_w^{edge^{tp}}}$ (*average weighted top-to-bottom edge betweenness centrality*) and $[G^T]_{LC}$ (*local clustering coefficient*).

5. Conclusion

In order to find microstructural features to predict ETC, five sands were selected, and multiple network features for both contact and thermal networks were calculated. After analysing the relationships between each feature and the ETC, network features such as *weighted degree* and *weighted closeness centrality* are good predictors of ETC not only for sphere packings [30] but also for real sands. Their merit is because they can capture more information (both the particle connectivity and contact quality) than traditional parameters such as porosity. The importance of network features to ETC also relieve the concern that the lack of structural data may result in the difference of ETC between models and methods [6]. We also note that estimating ETC accurately using finite element methods may be practically feasible only when enough computational power and higher CT image resolutions are available.

Both contact and thermal network features have certain benefits and limitations. The thin wedge of interstitial gas between two particles [74], moisture content around the interparticle spaces and thermal radiation may enable more indirect heat transfers

via ‘near-contacts’, therefore enhance the importance of thermal network features. Some network features may have close correlations with each other, and it may be sufficient to use just one of these in the model.

The acquirement of network features for real sands needs image processing techniques and network construction and feature extractions (i.e. additional mathematic calculations). However, with the affordability of CT and a well-developed framework that the authors are working on, numerous parameters/features can be achieved more efficiently and cost-effectively. For example, twenty-four hours saturation is required to measure the porosity of a sample while it takes thirty minutes CT scanning and five minutes to achieve not only porosity but particle size, shape, connectivity with this framework. Moreover, the work also shows the potential capability of extracting macroscopic quantities related to mechanical response, fluid flow, heat transfer and electrical conduction based on the CT images.

Declaration of Competing Interest

The authors declare that they have no known competing financial interests or personal relationships that could have appeared to influence the work reported in this paper.

Acknowledgements

The authors would like to thank Yu Zhou for photographing the sands, and Dr Anton Maksimenko and the other academics at Australian Synchrotron, Victoria, Australia for supporting us in obtaining images via CT imaging and medical beamline (IMBL). The first author would like to thank the University of Melbourne for support via a Melbourne Research Scholarship and Dr Joost van der Linden and Dr Mahdi Miri Disfani for fruitful discussions.

References

[1] Johnston IW, Narsilio GA, Colls S. Emerging geothermal energy technologies. KSCE Journal of Civil Engineering. 2011;15(4):643-53.
[2] Loveridge F, Holmes G, Powrie W, Roberts T. Thermal response testing through the Chalk aquifer in London, UK. ICE Themes Geothermal Energy, Heat Exchange Systems and Energy Piles2018. p. 157-77.
[3] Xinbao Y, Nan Z, Asheesh P, J. PA. Thermal conductivity of sand–kaolin clay mixtures. Environmental Geotechnics. 2016;3(4):190-202.
[4] Rotta Loria AF, Laloui L. The equivalent pier method for energy pile groups. Géotechnique. 2017;67(8):691-702.
[5] Bidarmaghz A, Choudhary R, Soga K, Kessler H, Terrington RL, Thorpe S. Influence of geology and hydrogeology on heat rejection from residential basements in urban areas. Tunnelling and Underground Space Technology. 2019;92(103068.
[6] Yüksel N. The review of some commonly used methods and techniques to measure the thermal conductivity of insulation materials. Insulation Materials in Context of Sustainability: IntechOpen, 2016.
[7] Yun TS, Santamarina JC. Fundamental study of thermal conduction in dry soils. Granular matter. 2008;10(3):197-207.
[8] Dong Y, McCartney JS, Lu N. Critical Review of Thermal Conductivity Models for Unsaturated Soils. Geotechnical and Geological Engineering. 2015;33(2):207-21.
[9] Zhang N, Wang Z. Review of soil thermal conductivity and predictive models. International Journal of Thermal Sciences. 2017;117(172-83.
[10] Chu Z, Zhou G, Wang Y, Zhao X, Mo P-Q. A supplementary analytical model for the stagnant effective thermal conductivity of low porosity granular geomaterials. International Journal of Heat and Mass Transfer. 2019;133(994-1007.
[11] Abdulagatova Z, Abdulagatov I, Emirov V. Effect of temperature and pressure on the thermal conductivity of sandstone. International Journal of Rock Mechanics and Mining Sciences. 2009;46(6):1055-71.
[12] Mo J, Ban H. Measurements and theoretical modeling of effective thermal conductivity of particle beds under compression in air and vacuum. Case studies in thermal engineering. 2017;10(423-33.
[13] Batchelor GK, O'brien R. Thermal or electrical conduction through a granular material. Proc R Soc Lond A. 1977;355(1682):313-33.
[14] Dai W, Hanaor D, Gan Y. The effects of packing structure on the effective thermal conductivity of granular media: A grain scale investigation. International Journal of Thermal Sciences. 2019;142(266-79.
[15] Finney J. Random packings and the structure of simple liquids. I. The geometry of random close packing. Proc R Soc Lond A. 1970;319(1539):479-93.
[16] Cheng G, Yu A, Zulli P. Evaluation of effective thermal conductivity from the structure of a packed bed. Chemical Engineering Science. 1999;54(19):4199-209.
[17] Bahrami M, Culham J, Yovanovich M. Modeling thermal contact resistance: a scale analysis approach. Journal of heat transfer. 2004;126(6):896-905.
[18] Liang Y. Expression for effective thermal conductivity of randomly packed granular material. International Journal of Heat and Mass Transfer. 2015;90(1105-8.
[19] Siu W, Lee S-K. Effective conductivity computation of a packed bed using constriction resistance and contact angle effects. International journal of heat and mass transfer. 2000;43(21):3917-24.
[20] Torquato S, Haslach Jr H. Random heterogeneous materials: microstructure and macroscopic properties. Appl Mech Rev. 2002;55(4):B62-B3.
[21] Nadimi S, Fonseca J, Andò E, Viggiani G. A micro finite-element model for soil behaviour: experimental evaluation for sand under triaxial compression. Géotechnique. 2019;0(0):1-6.

[22] Reimann J, Vicente J, Brun E, Ferrero C, Gan Y, Rack A. X-ray tomography investigations of mono-sized sphere packing structures in cylindrical containers. Powder technology. 2017;318(471-83.
[23] Druckrey A, Alshibli K, Al-Raoush R. Discrete particle translation gradient concept to expose strain localisation in sheared granular materials using 3D experimental kinematic measurements. Géotechnique. 2017;68(2):162-70.
[24] Tordesillas A, Tobin ST, Cil M, Alshibli K, Behringer RP. Network flow model of force transmission in unbonded and bonded granular media. Physical Review E. 2015;91(6):062204.
[25] Sufian A, Russell AR, Whittle AJ. Anisotropy of contact networks in granular media and its influence on mobilised internal friction. Géotechnique. 2017;67(12):1067-80.
[26] Papadopoulos L, Porter MA, Daniels KE, Bassett DS. Network analysis of particles and grains. Journal of Complex Networks. 2018;6(4):485-565.
[27] Russell S, Walker DM, Tordesillas A. A characterization of the coupled evolution of grain fabric and pore space using complex networks: Pore connectivity and optimized flows in the presence of shear bands. Journal of the Mechanics and Physics of Solids. 2016;88(227-51.
[28] Fei W, Narsilio GA, van der Linden JH, Disfani MM. Quantifying the impact of rigid interparticle structures on heat transfer in granular materials using networks. International Journal of Heat and Mass Transfer. 2019;143(118514.
[29] Fei W, Narsilio GA, Disfani MM. Impact of three-dimensional sphericity and roundness on heat transfer in granular materials. Powder Technology. 2019;355(770-81.
[30] Fei W, Narsilio GA, van der Linden JH, Disfani MM. Network analysis of heat transfer in sphere packings. Powder Technology. 2020;362(790-804.
[31] Alramahi B, Alshibli KA, Fratta D. Effect of Fine Particle Migration on the Small-Strain Stiffness of Unsaturated Soils. Journal of Geotechnical and Geoenvironmental Engineering. 2010;136(4):620-8.
[32] Roshankhah S, Santamarina JC. Engineered granular materials for heat conduction and load transfer in energy geotechnology. Géotechnique Letters. 2014;4(2):145-50.
[33] Yang J, Gu XQ. Shear stiffness of granular material at small strains: does it depend on grain size? Géotechnique. 2013;63(2):165-79.
[34] ASTM. C778-17 standard specification for standard sand. ASTM International, West Conshohocken, PA. 2017.
[35] Zhang N, Yu X, Pradhan A, Puppala AJ. Thermal conductivity of quartz sands by thermo-time domain reflectometry probe and model prediction. Journal of Materials in Civil Engineering. 2015;27(12):04015059.
[36] Neuendorf KK, Mehl Jr JP, Jackson JA. Glossary of Geology: American Geological Institute. Alexandria, Virginia. 2005.
[37] Narsilio GA, Buzzi O, Fityus S, Yun TS, Smith DW. Upscaling of Navier–Stokes equations in porous media: Theoretical, numerical and experimental approach. Computers and Geotechnics. 2009;36(7):1200-6.
[38] Azadi P, Farnood R, Yan N. FEM–DEM modeling of thermal conductivity of porous pigmented coatings. Computational Materials Science. 2010;49(2):392-9.
[39] Łydżba D, Różański A. Microstructure measures and the minimum size of a representative volume element: 2D numerical study. Acta Geophysica. 2014;62(5):1060-86.
[40] Fei W, Narsilio GA. Impact of three-dimensional sphericity and roundness on coordination number. Journal of Geotechnical and Geoenvironmental Engineering. 2020:(Accepted).
[41] Otsu N. A threshold selection method from gray-level histograms. IEEE transactions on systems, man, and cybernetics. 1979;9(1):62-6.
[42] Schlüter S, Sheppard A, Brown K, Wildenschild D. Image processing of multiphase images obtained via X-ray microtomography: a review. Water Resources Research. 2014;50(4):3615-39.
[43] Karatza Z, Andò E, Papanicolopulos S, Ooi J, Viggiani G. Evolution of deformation and breakage in sand studied using X-ray tomography. Géotechnique. 2018;1(1-11.

[44] Wiebicke M, Andò E, Herle I, Viggiani G. On the metrology of interparticle contacts in sand from x-ray tomography images. Measurement Science and Technology. 2017;28(12):124007.
[45] Yun TS, Santamarina JC. Fundamental study of thermal conduction in dry soils. Granular matter. 2008;10(3):197.
[46] Yun TS, Evans TM. Three-dimensional random network model for thermal conductivity in particulate materials. Computers and Geotechnics. 2010;37(7):991-8.
[47] Sundberg J, Back P-E, Ericsson LO, Wrafter J. Estimation of thermal conductivity and its spatial variability in igneous rocks from in situ density logging. International Journal of Rock Mechanics and Mining Sciences. 2009;46(6):1023-8.
[48] Haigh SK. Thermal conductivity of sands. Géotechnique. 2012;62(7):617-25.
[49] Simpleware Ltd. Simpleware ScanIP, http://www.simpleware.com/software/scanip. Date of access. 2015;15(12.
[50] AB C. COMSOL multiphysics v5.0, http://www.comsol.com. 2015.
[51] Narsilio GA, Kress J, Yun TS. Characterisation of conduction phenomena in soils at the particle-scale: Finite element analyses in conjunction with synthetic 3D imaging. Computers and Geotechnics. 2010;37(7):828-36.
[52] Carslaw H, Jaeger J. Conduction of heat in solids: Oxford Science Publications: Oxford, England, 1959.
[53] ASTM D5334-14. Standard Test Method for Determination of Thermal Conductivity of Soil and Soft Rock by Thermal Needle Probe Procedure. West Conshohocken, PA: ASTM International, 2014.
[54] Brandon T, Mitchell J. Factors influencing thermal resistivity of sands. Journal of Geotechnical Engineering. 1990;115(12):1683-98.
[55] Legland D, Arganda-Carreras I, Andrey P. MorphoLibJ: integrated library and plugins for mathematical morphology with ImageJ. Bioinformatics. 2016;32(22):3532-4.
[56] Schindelin J, Arganda-Carreras I, Frise E, Kaynig V, Longair M, Pietzsch T, et al. Fiji: an open-source platform for biological-image analysis. Nature methods. 2012;9(7):676.
[57] Fonseca J, O'Sullivan C, Coop MR, Lee P. Non-invasive characterization of particle morphology of natural sands. Soils and Foundations. 2012;52(4):712-22.
[58] van der Linden JH, Narsillio GA, Antoinette T. Thermal conductance network model for computerised tomography images of real geomaterials (Conditionally accepted). Computers and Geotechnics. 2019.
[59] Newman MEJ. Networks : an introduction: Oxford ; New York : Oxford University Press, 2010., 2010.
[60] Freeman LC. Centrality in social networks conceptual clarification. Social networks. 1978;1(3):215-39.
[61] Freeman LC. A set of measures of centrality based on betweenness. Sociometry. 1977:35-41.
[62] Laman G. On graphs and rigidity of plane skeletal structures. Journal of Engineering mathematics. 1970;4(4):331-40.
[63] Asimow L, Roth B. The rigidity of graphs. Transactions of the American Mathematical Society. 1978;245(279-89.
[64] Crapo H. Structural rigidity. Structural topology, 1979, núm 1. 1979.
[65] Tordesillas A, Lin Q, Zhang J, Behringer R, Shi J. Structural stability and jamming of self-organized cluster conformations in dense granular materials. Journal of the Mechanics and Physics of Solids. 2011;59(2):265-96.
[66] Newman ME. The structure and function of complex networks. SIAM review. 2003;45(2):167-256.
[67] Watts DJ, Strogatz SH. Collective dynamics of 'small-world'networks. nature. 1998;393(6684):440.
[68] Abyzov AM, Goryunov AV, Shakhov FM. Effective thermal conductivity of disperse materials. I. Compliance of common models with experimental data. International Journal of Heat and Mass Transfer. 2013;67(752-67.

[69] Liu F, Cai Y, Wang L, Zhao J. Effects of nanoparticle shapes on laminar forced convective heat transfer in curved ducts using two-phase model. International Journal of Heat and Mass Transfer. 2018;116(292-305.
[70] van der Linden JH, Narsilio GA, Tordesillas A. Machine learning framework for analysis of transport through complex networks in porous, granular media: a focus on permeability. Physical Review E. 2016;94(2):022904.
[71] Santosa F, Symes WW. Linear inversion of band-limited reflection seismograms. SIAM Journal on Scientific and Statistical Computing. 1986;7(4):1307-30.
[72] Pedregosa F, Varoquaux G, Gramfort A, Michel V, Thirion B, Grisel O, et al. Scikit-learn: Machine learning in Python. Journal of machine learning research. 2011;12(Oct):2825-30.
[73] Stone M. Cross-validatory choice and assessment of statistical predictions. Journal of the royal statistical society Series B (Methodological). 1974:111-47.
[74] Morris AB, Pannala S, Ma Z, Hrenya CM. A conductive heat transfer model for particle flows over immersed surfaces. International Journal of Heat and Mass Transfer. 2015;89(1277-89.

Appendix

Appendix 1 The score and model used to evaluate the importance of each feature to ETC.

Type	NO.	Notation	Contact network features		Thermal network features	
			Score	Model	Score	Model
Geotechnics	1	n	0.9317	Quadratic polynomial	0.9317	Quadratic polynomial
	2	γ	0.8889	Linear	0.8889	Linear
	3	D_{50}	0.0106	Cubic Polynomial	0.0106	Cubic Polynomial
	4	C_u	0.1772	Logarithmic	0.1772	Logarithmic
	5	C_c	0.0694	Logarithmic	0.0694	Logarithmic
Centrality	6	$[G^*]_{\kappa}$	0.9638	Linear	0.5883	Cubic Polynomial
	7	$[G^*]_{\kappa_w}$	0.9184	Quadratic polynomial	0.9515	Quadratic polynomial
	8	$[\mathrm{G}^*]_{\mathrm{C}}$	0.7084	Logarithmic	0.783	Logarithmic
	9	$[\mathrm{G}^*]_{\mathrm{C_{n1}}}$	0.7129	Cubic Polynomial	0.9354	Quadratic polynomial
	10	$[G^*]_{C_{n2}}$	0.8281	Linear	0.7055	Cubic Polynomial
	11	$[G^*]_{C_w}$	0.1831	Quadratic polynomial	0.4884	Cubic Polynomial
	12	$[G^*]_{C_{nw1}}$	0.914	Quadratic polynomial	0.5629	Power
	13	$[G^*]_{C_{nw2}}$	0.9481	Linear	0.9545	Linear
	14	$[G^*]_{B^{node}}$	0.7539	Linear	0.8352	Linear
	15	$[G^*]_{B_n^{node}}$	0.8336	Quadratic polynomial	0.691	Cubic Polynomial
	16	$[G^*]_{B_w^{node}}$	0.6613	Linear	0.7129	Linear
	17	$[G^*]_{B_{nw}^{node}}$	0.8818	Quadratic polynomial	0.7961	Cubic Polynomial
	18	$[G^*]_{B^{edge}}$	0.6148	Cubic Polynomial	0.8924	Linear
	19	$[G^*]_{B_n^{edge}}$	0.9207	Quadratic polynomial	0.7119	Cubic Polynomial
	20	$[G^*]_{B_w^{edge}}$	0.3219	Cubic Polynomial	0.7963	Linear
	21	$[G^*]_{B_{nw}^{edge}}$	0.9356	Quadratic polynomial	0.7754	Cubic Polynomial
	22	$[G^*]_{B_w^{edge^{tp}}}$	0.8232	Quadratic polynomial	0.8416	Exponential
	23	$[G^*]_{B_{nw}^{edge^{tp}}}$	0.5777	Logarithmic	0.5318	Cubic Polynomial
	24	$[G^*]_E$	0.2557	Logarithmic	0.7287	Cubic Polynomial
	25	$[G^*]_{E_w}$	0.7846	Quadratic polynomial	0.5632	Quadratic polynomial
Network scale	26	G_{ρ}^*	0.5631	Cubic Polynomial	0.8434	Quadratic polynomial
	27	G_D^*	0.1922	Linear	0.8051	Quadratic polynomial
	28	$G_{D_n}^*$	0.8627	Quadratic polynomial	0.4004	Cubic Polynomial
	29	$[G^*]_{P_w}$	0.9036	Cubic Polynomial	0.625	Exponential
	30	$[G^*]_{P_w^{tp}}$	0.868	Cubic Polynomial	0.4311	Exponential
Clustering	31	$G^*{}_{GC}$	0.7292	Quadratic polynomial	0.8314	Quadratic polynomial
	32	$[G^*]_{LC}$	0.4897	Linear	0.8812	Exponential
Cycles	33	G_{3C}^*	0.9418	Logarithmic	0.688	Quadratic polynomial
	34	$[G^*]_{3C^{node}}$	0.9169	Linear	0.344	Cubic Polynomial
	35	$[G^*]_{3C^{\mathrm{edge}}}$	0.8401	Quadratic polynomial	0.0121	Logarithmic

[G]* is a unified characteristic, and *[G^C]* refers to *contact* network features, while *[G^T]* refers to *thermal* networks. The brackets in *[G*]* indicate an average value of the parameter.

5.4 CONCLUSIONS

Analytical expressions and image techniques are implemented to construct contact and thermal networks for sphere packings and real sands, respectively. Network features are extracted from the various networks of the different samples to enrich the microstructural parameters available to potentially characterise heat transfer, especially for the quantification of particle connectivity. Compared with the traditionally used coordination number, some single network features can capture more information including both contacts, contact areas, are and particle connectivity, making these network feature very good predictors of effective thermal conductivity. After investigating the correlation between each network features and the effective thermal conductivity, *weighted degree* and *weighted closeness centrality* are found to be the best predictors of effective thermal conductivity for both sphere packings and real sands. Additionally, the benefits and limitations of contact and thermal network features are identified. For example, in sphere packings, cluster and cycle features derived from the contact network to be more relevant than those arising from the thermal network. In contrast, centrality and scale features from the thermal network are more relevant than those from the contact network.

Chapter 6: Predicting effective thermal conductivity of sands by artificial neural network with multiscale microstructural parameters

6.1 OVERVIEW AND STRUCTURE

Multiple microstructure parameters (e.g., traditional geotechnical parameters and network features) and boundary conditions (e.g., loading stress and conduction pathway changes due to diagenesis) affect the λ_{eff} of granular materials. Traditional methods used to analyse the effects of multi-variables on λ_{eff} may be time-consuming and expensive. Machine learning techniques are able to identify relevant non-redundant important parameters and to generate a robust predictive model with uncertainties and errors rigorously addressed. In this chapter, additional sands varying in size, shape and under different loadings are scanned using micro-CT. Based on the CT images, traditional parameters such as porosity along with new network features (from networks representing the assembly of particles) are extracted. These variables can be used as input features in machine learning techniques to build a model for predicting effective thermal conductivity which is computed using a thermal conductance network model (Chapter 5). This chapter has a different focus but may use some of the samples and methods summarised in previous ones.

This chapter is summarised in a manuscript entitled "Predicting effective thermal conductivity of sands by artificial neural network with multiscale microstructural parameters" to be submitted to the ASCE's *Journal of Geotechnical and Geoenvironmental Engineering.* An advanced draft is included here.

Type of paper: full-length article (Journal Name – **Journal of Geotechnical and Geoenvironmental Engineering**)
Date text written: February 2020
Number of words in the main text and tables = 6248
Number of figures = 13
Number of tables = 2

6.2 PREDICTING EFFECTIVE THERMAL CONDUCTIVITY OF SANDS BY ARTIFICIAL NEURAL NETWORK WITH MULTISCALE MICROSTRUCTURAL PARAMETERS

Author 1
Wenbin Fei, PhD student
Department of Infrastructure Engineering, The University of Melbourne, Parkville, Australia
ORCID: 0000-0002-9275-8403

Author 2
Guillermo A. Narsilio, PhD, MSc (Math), MSc (CE), CEng
Department of Infrastructure Engineering, The University of Melbourne, Parkville, Australia
ORCID: 0000-0003-1219-5661

Author 3
Mahdi M. Disfani, PhD, MSc, BSc
Department of Infrastructure Engineering, The University of Melbourne, Parkville, Australia
ORCID: 0000-0002-9231-8598

Full contact details of the corresponding author
Guillermo A. Narsilio, Associate Professor
Engineering Block B 208, Department of Infrastructure Engineering, The University of Melbourne, Parkville, VIC 3010, Australia
Email: narsilio@unimelb.edu.au, Phone: +61 (3) 8344 4659, Fax: +61 (3) 8344 4616

ABSTRACT

Sands are complex granular materials composed by particles varying in size, shape, connectivity and mineral compositions. The variation of these microstructural features and the boundary conditions of the sands make it challenging to predict their effective thermal conductivities accurately and efficiently. Artificial neural network (ANN) has been attempted to predict the effective thermal conductivity. However, existing works use sphere packings or artificially generated irregular particle packings (e.g., via discrete element method). Although the structural arrangement is required to analyse heat transfer, the existing machine learning models have not taken the particle connectivity variables as input parameters nor have dealt with actual granular materials. Since a sand can be represented as a network of nodes (grains) and edges (interparticle contacts or/and small gaps between neighbouring particles), network features that account for interparticle connectivity can be extracted and used in ANN models. *Weighted coordination number* (WCN) is used in the models. WCN is a network feature that captures both particle connectivity and contact area, which are essential to heat transfer. Here we show the need to use WCN alongside roundness, sphericity, solid thermal conductivity and porosity as input parameters in ANN models. The network is also extended to build a thermal conductance network model (TCNM) to estimate the effective thermal conductivity. Results show that WCN is a good predictor of ECT. The selected input parameters can quantify the microstructure of sands at multiple scales and the application to the ANN model can predict well the effective thermal conductivities of sands.

KEYWORDS: Machine learning; Heat transfer; Thermal network model; Microstructure; Micro-CT.

INTRODUCTION

Granular materials are dealt with in a wide range of applications in geothermal engineering (Yang et al. 2019), petroleum and gas extraction (Scott et al. 2005), carbon dioxide geological storage (Fei et al. 2015) and pebble bed reactors (Moscardini et al. 2018). In these projects, heat transfer is one of the processes that are key in designing the projects and determining their capital costs. As effective thermal conductivity is a critical parameter that indicates the ease of heat transfer, predicting its value accurately and efficiently is essential.

The difficulty of accurately predicting the effective thermal conductivities (λ_{eff}) of granular materials arises from their complex microstructure and boundary conditions (Singh and Devid 2000). The microstructure can be characterized at different scales, considering attributes such as particle size, shape, gradation and minerality at the microscale (particle scale); particle connectivity at the mesoscale and porosity at the macroscale. Work by van Antwerpen et al. (2010), Abdulagatova et al. (2009) and Abyzov et al. (2013) compared the results from a number of λ_{eff} models against experimental data and found existing λ_{eff} models have limited applicability. Some models simplify granular materials as packings of spheres, ellipsoids or parallel cylinders (regular geometrical forms), providing insights, but hindering wide applicability. Despite knowing that bulk porosity alone cannot characterise the packing structure for analysing heat transfer (van Antwerpen et al. 2010), and that microstructural parameter about grain-grain resistance (Abdulagatova et al. 2009) and contact area (Abyzov et al. 2013; Askari et al. 2017) in λ_{eff} models are important (Yüksel 2016), they have not been directly involved or combined in the λ_{eff} models. In addition, particle connectivity, i.e., microstructural contact topology related to thermo-mechanical response (Desu et al. 2019), has seldomly been quantified except using coordination number.

Recently, (Fei et al. 2020) abstracted granular materials as contact networks and thermal networks by creating nodes for particles and edges for interparticle contacts (contact networks), and with the addition of near-contacts, the small gap between two neighbouring particles (thermal networks). Then based on complex network theory (Papadopoulos et al. 2018), contact area or thermal conductance can be added as a weight to each edge in the network to eventually identify a single mesoscale network feature which can characterise both the particle connectivity and contact quality. One

such feature from the contact network is *weighted degree*, which represents an upgraded coordination number that accounts for the contact area for each interparticle contact. Hence, while coordination number only counts the number of neighbouring particles in contact surround the target particle, the weighted coordination number (WCN) quantifies both the contact number (particle connectivity) and contact area (contact quality). The physical meaning of WCN is the total contact area of a target particle to its neighbours.

Numerical simulation methods such as finite element methods (FEM) (Narsilio et al. 2010), discrete element methods (DEM) (Gan et al. 2017) and lattice Boltzmann methods (LBM) (Fang et al. 2017) can be used to estimate λ_{eff} and to involve in more detailed complex microstructure in the process. However, these approaches require to solve a system of partial differential equations and the computations are generally time-consuming (Desu et al. 2019; Wei et al. 2018). On the other hand, physical experiments are commonly undertaken to measure λ_{eff} (ASTM D5334-14 2014), but one of the drawbacks is the need for relatively large samples and often times large undisturbed samples which may be difficult to obtain. In contrast, the utilisation of small undisturbed samples can reduce the sampling cost significantly. The aim of the present paper is to develop a model that can predict λ_{eff} accurately and computationally efficiently, even from very small undisturbed samples, e.g., inexpensive spoil from drilling.c

Machine learning techniques have enabled substantial asdvances in data-driven approaches throughout academia and industry. In the materials' science, materials informatics combine machine learning, Bayesian optimization and Carlo tree search in an attempt to address the challenge of finding optimal materials fast (Ju and Shiomi 2019). Machine learning has also been used in a limited number of studies to predict λ_{eff} on sphere packings (Desu et al. 2019; Kautz et al. 2019) and virtual irregular materials (Wei et al. 2018). The input parameters for the machine learning models in these works include porosity, particle size, the thermal conductivity of solid and interstitial gas, temperature and loadings. Although these parameters are measurable in a laboratory, bypassing the detailed understanding of structural arrangement and the physical mechanism may be the cause for the differences observed between calculation and measurement (van Antwerpen et al. 2010; Yüksel 2016). Hence, it is necessary to include particle connectivity parameters for instance, in machine learning models.

This work intends to predict λ_{eff} accurately and efficiently by employing an ANN model involving WCN which quantifies the topological structure in sands. Here we justify the selection of WCN and other microstructural variables including particle diameter, three-dimensional sphericity and roundness as input parameters in the ANN model. Computed tomography (CT) scanned images of four dry sands varying in shape and size and subjected to different loads are used to calculate these parameters. The λ_{eff} acting as the output parameter in the ANN model was computed using a recently in-house developed thermal conductance network model (TCNM) (Fei et al. 2019; van der Linden et al. 2019) alongside selected experimental measurements. TCNM has the merit of mitigating overestimation of λ_{eff} possibly induced by the particle volume effect (Wiebicke et al. 2017) from threshold segmentation, and the estimation of variations of λ_{eff} for different particle arrangements without additional disturbance of samples upon insertion of thermal probes.

ARTIFICIAL NEURAL NETWORK MODEL

Artificial neural network (ANN) is the core of deep Machine Learning (ML) technique and has gained great success and high accuracy in image classification (e.g., Google Images), voice recognition (e.g., Apple's Siri) and learning to be a *Go* champion (e.g., AlphaGo). The ANN was inspired by the architecture of the human brain and its architecture composites of an input layer, one or more hidden layers and an output layer. Each layer has one or more neurons (units/nodes), the neurons in different layers are connected by edges. As this work attempts to find an accurate and efficient model to predict λ_{eff}, the neurons in the input layer could be microstructural variables while the neuron in the output layer is λ_{eff}. The neuron in the latter layer is computed by non-linear functions (activation functions) with weights corresponding to the neurons in the previous layer. The present paper employs ReLU activation function in the hidden layers due to its high efficiency and general applicability (Géron 2019). Apart from choosing a proper activation function, an appropriate optimizer can adjust the weights and learning rate. Adam optimization was selected in this work because it is an adaptive learning rate algorithm and owns several advantages of other optimization algorithms such as Momentum optimization and RMSProp (Géron 2019).

Input parameters determination

Even though ANN performs well in solving complex problems, feeding input features without discretion is not recommended. In this section, the heat transfer mechanisms and λ_{eff} models were reviewed to justify the input features selected in this work.

Heat transfers in gas-stagnant granular materials occurs via four pathways: (1) heat conduction within solid particles; (2) heat conduction via interparticle contacts; (3) heat conduction via particle-gas-particle; (4) heat radiation across the solid surface and it is neglectable when the temperature is below 600° (Abdulagatova et al. 2009). Since the thermal conductivity of the solid is two orders of magnitude larger than that of air and this work focus on the samples at room temperature, heat travels via the first two mechanisms is known to be the case for dry soils (Yun and Santamarina 2008). Therefore, parameters related to the particle and interparticle contacts are to be involved in the ANN model. Particle diameter should be an input parameter since it is related to the distance that heat transfers within the particles as well as the solid thermal conductivity controlling the ease of heat transfer in the particle. In terms of a parameter that can capture interparticle contact, WCN was identified as a good candidate (Fei et al. 2020) due to its capacity to capture both the existence of a interparticle contacts but also the area (or intensity) of contact as opposed to coordination number which only takes the existence (or lack) of contacts into consideration.

Parameters used in existing λ_{eff} models were also critically analysed for selecting the input parameters for the ANN model. Porosity and the thermal conductivity of different phases are most widely used in various λ_{eff} models (Abdulagatova et al. 2009; Abyzov et al. 2013; van Antwerpen et al. 2010). Some complex semi-empirical λ_{eff} models also consider particle/pore shape and are summarised in Table 1. Eq. (1) introduces a parameter B to adjust the particle shape while Eq. (2) and Eq. (3) employ aspect ratio to characterise the shape of the particle and/or pore. However, they are only applicable to particles with regular shape.

Table 1 Summary of effective thermal conductivity models considering particle/pore shape

Reference		
Zehner and Schlunder (1970)	$\frac{\lambda_{eff}}{\lambda_f} = 1 - \sqrt{1-\phi} + \frac{2\sqrt{1-\phi}}{1-\xi B}\left[\frac{(1-\xi)B}{(1-\xi B)^2}\ln\left(\frac{1}{\xi B}\right) - \frac{B+1}{2} - \frac{B-1}{1-\xi B}\right]$, $\xi = \frac{\lambda_f}{\lambda_s}$, $r^2 + \frac{z^2}{[B-(B-1)z]^2} = 1$. r and z are the radii of the particle in two principal axes. B is the shape factor. The particle becomes the z-axis with no solid volume when $B \to 0$, a sphere when $B \to 1$ and a cylinder when $B \to \infty$.	(1)
Fricke (1924)	$\frac{\lambda_{eff}}{\lambda_s} = \frac{(1-\phi)(1-\xi)+\xi\beta\phi}{(1-\phi)(1-\xi)+\beta\phi}$, $\xi = \frac{\lambda_f}{\lambda_s}$, β is related to ξ and aspect ratio.	(2)
Keller et al. (2001)	$\lambda_{eff} = \lambda_s\left[1 + \frac{\alpha_p}{\alpha_s}\left(\frac{b}{a}\right)^2\left(2 - \frac{b/a}{(1-b/a)^2}\right)\right]^{-1}$, $\phi = \frac{\alpha_p}{\alpha_s}\left(\frac{b}{a}\right)^2\left(2 - \frac{b}{a}\right)$, α_p is the aspect ratio of the pore α_s is the aspect ratio of solid (grain) b is the pore radius while a is the grain radius.	(3)

λ_s is the thermal conductivity of solid and λ_f is the thermal conductivity of gas/fluid in the void space, ϕ is porosity.

Since aspect ratio cannot adequately cover the shape of all irregular particle/pores (Fei et al. 2019), three-dimensional (3D) sphericity (S in Eq. (4)) and roundness (R in Eq. (5)) were used in this work to describe the particle shape, details of computational steps can be found in (Fei et al. 2019):

$$S = \frac{36\pi V^2}{\mathrm{SA}^3} \tag{4}$$

$$R = \frac{\sum r_i/N}{r_{max-in}} \tag{5}$$

where V is particle volume, SA is particle surface area, r_i is the radius of each corner (Fei et al. 2019), N is the total number of corners and $r_{max\text{-}in}$ is the radius of the maximum sphere in the particle.

Based on the above analysis, particle size, the thermal conductivity of solid and fluid/gas, WCN, 3D sphericity and roundness, and porosity are selected as sensible candidates for input parameters in the ANN model.

Performance indicator

Data is used for ANN modelling and is usually divided into three sets: a training set, a validation set and a test set when embarking in supervised ML. The training set is firstly used to train ML models which are evaluated to select the one that has the best performance on the validation set. The performance of the final model is again evaluated on the test set.

The evaluations can be quantified using mean square error (MSE) or correlation coefficient (R^2). MSE measures the *standard deviation* of the errors that a model makes in its prediction. MSE is generally the preferred choice (Géron 2019) for regression problems. In contrast, R^2 is usually used to quantify the linear correlation between the predicted value and actual value. It has a range from 0 to 1, 0 means no relationship while 1 means perfect fit. Accordingly, MSE was employed in this study to monitor the performance of the ANN model when tuning hyperparameters (e.g., the number of nodes in each layer) to select models while R^2 is used to present the general performance of the ANN model.

Materials

Four sands varying in particle shape were selected and sent to Australian Synchrotron, Imaging and Medical BeamLine (IMBL) for CT scanning at a pixel size of 13 μm. A selection of the acquired images is shown in Fig. 1. Glass beads have the roundest particles. The particles in Ottawa sand are more irregular than that of glass beads but still have round corners. Compared to the particles in Ottawa sand, it is clear to see that particles in the angular sand are even more irregular and have sharp corners. Lastly, particles made from crushing schist have the most irregular shape, half of them are considered platy and elongated.

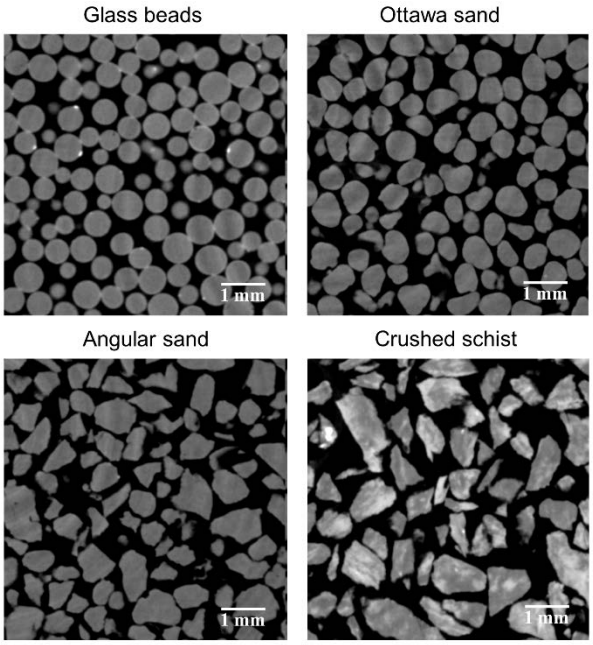

Fig. 1. Four selected sand varying in particle shape.

In order to achieve a more universal applicable ANN model, different particle sizes were chosen and axial loads were applied to each sand shown in Fig. 1 in a rigid wall cell to vary porosity and particle arrangement further (Table 2). The equivalent particle size was calculated based on CT images, consistent with results in (Fei et al. 2019) and sieve analysis. The samples shown in Fig. 1 correspond to GB-L, OS, AS-L and CS-M without a load in Table 2 and they have similar equivalent D_{50}.

Table 2 Particle size and loads applied to each sample

Sand	Sample name	Particle size (mm)[a]	Particle size (mm)[b]	Equivalent D_{50} (mm)[b]	Loads (MPa)
Glass beads	GB-S	0.20-0.30	0.12-0.37	0.24	0, 2.0, 6.1, 10.2
	GB-N	0.50	0.33-0.68	0.54	0, 2.0, 6.1, 10.2
	GB-L	**0.50-0.70**	**0.40-0.80**	**0.60**	0, 2.0, 6.1, 10.2, 20.4, 40.7
Ottawa sand	**OS**	**0.60-0.85**	**0.58-0.94**	**0.76**	0, 2.0, 6.1, 10.2, 20.4, 40.7
Angular sand	AS-P	0.15-0.30	0.12-0.41	0.24	0
	AS-M	0.43-0.60	0.32-0.64	0.48	0, 2.0, 6.1, 10.2, 20.4, 40.7
	AS-L	**0.60-1.18**	**0.39-0.99**	**0.68**	0, 2.0, 6.1, 10.2, 20.4, 40.7
Crushed schist	CS-S	0.30-0.50	0.17-0.61	0.39	0, 2.0, 6.1, 10.2
	CS-M	**0.50-1.18**	**0.23-0.95**	**0.58**	0

[a] Particle size from sieve analysis

[b] Particle size calculated based on CT reconstructed sample.

Microstructural variables

This section briefly introduces how to obtain the aforementioned particle size, WCN, 3D sphericity, 3D roundness and porosity.

Image processing

After CT scanning, sequential slices of images with a pixel size of 13 μm were acquired. In each image stack, four regions of interest (ROI) with a dimension of 4.55 × 4.55 × 4.55 *mm* were selected to eliminate the effect of potential heterogeneity. Fig. 2 (a) shows a cross-section of the ROI after denoising by applying a 3D median filter. Then a commonly used Otsu threshold segmentation algorithm (Otsu 1979) was employed to distinguish the solid phase (in black) and air phase (in white) as shown in Fig. 2 (b). The adjacent particles in Fig. 2 (b) are still connected and required to be 'split' to achieve the properties (i.e., particle size, shape and WCN) of each particle. This expectation was completed by executing watershed segmentation. Meanwhile, each particle was assigned a unique identifier (ID) and rendered by random colour as shown in Fig. 2 (c). The Taubin smooth algorithm was chosen to smooth each particle

surface out. Based on the smoothed particle, particle volume, particle surface area, 3D sphericity and roundness were computed following the steps in (Fei et al. 2019). Having the particle volume, equivalent particle size can be calculated. Porosity can also be computed using the volumes of all the particles and the known dimension of the ROI.

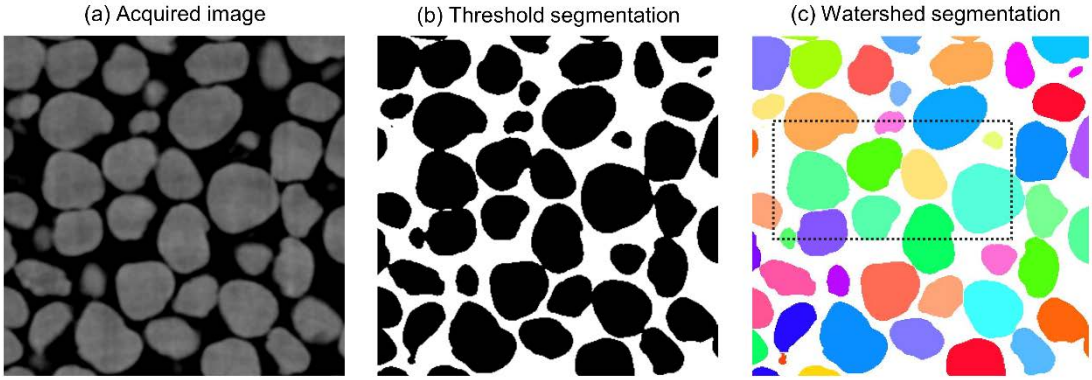

Fig. 2. Overview of key steps in image processing to identify individual particles

Weighted coordination number (WCN)

Complex network theory was used to compute the network feature called *degree* (Papadopoulos et al. 2018), for which a network needs to be built first. The weighted *degree* is basically a weighted coordination number (WCN). For each sample, a contact network was constructed by creating a node at the centroid of each particle and an edge for each interparticle contact between adjacent particles, as shown in Fig. 3. To identify the interparticle contacts, boundary voxels were recognized first if the voxels in a particle are adjacent to anything else that was not in the same particle. The average coordinate of the boundary voxels can help to find the location of the centroid of each particle. Furthermore, if boundary voxels bordered on another particle, they were identified as interparticle contact voxels which were further used to estimate interparticle contact area.

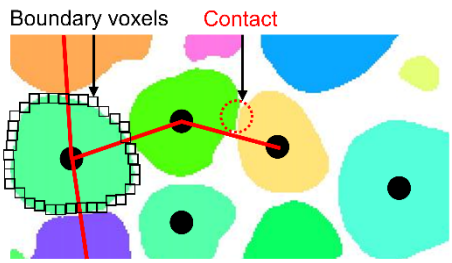

Fig. 3. Contact network construction for a sample (detailed from the dashed rectangle in Fig. 2 (c))

A simple way to calculate the interparticle contact area is directly counting the number of interparticle contact voxels but may result in an overestimation after threshold segmentation due to partial volume effect (Wiebicke et al. 2017). As shown in Fig. 4 (a), each pixel in the CT image has its own grayscale. Black and white voxels indicate solid and void, respectively; whereas other voxels are "grey". Some of these grey voxels at the 1-pixel gap between the two particles (Fig. 4 (a)) are incorrectly identified as contact, which will lead to the overestimation of contact area and λ_{eff}.

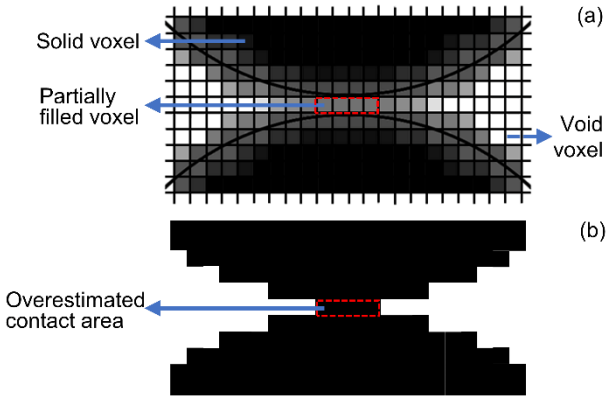

Fig. 4. Some partially filled voxels in (a) CT image are incorrectly identified as contact area after (b) threshold segmentation.

To correct the interparticle contact area, a penalty factor that takes into account the grayscale of these partially filled voxels was introduced. The corrected interparticle contact area A^C was computed as the sum of $A^v_{(i,j,k)}$ which was weighed by the ratio of grayscale values of individual interparticle voxels $g_{(i,j,k)}$ to the maximum grayscale value among them (Eq. (6)). A power penalty factor τ further ponders this ratio. The penalty factor τ was set as 10 after calibrating the λ_{eff} of sphere packings with the result from a theoretical thermal network model (van der Linden et al. 2019; Yun and Evans 2010):

$$A^C = \sum_{i,j,k} A^v_{i,j,k} = \sum_{i,j,k} \left[\left(\frac{g_{(i,j,k)}}{\max[g_{(i,j,k)}]} \right)^{\tau} L_v^2 \right] \tag{6}$$

where L_v is the length of a voxel, which is 13 μm in this work.

Once the contact network was constructed and interparticle contact area was calculated, a computational efficiently Python library named *graph-tool* (Peixoto

2014) was implemented to calculate WCN (i.e., *degree* in the terminology of complex network theory with adding interparticle contact area to each corresponding edge). The degree of a node is the total number of edges that are attached to it, whereas weighted degree of a node is equal to the sum of weights at the attached edges (Papadopoulos et al. 2018).

Effective thermal conductivity estimation

Effective thermal conductivity from thermal conductance network model (TCNM)

In order to calculate λ_{eff}, the contact network in Fig. 3 can be extended to a thermal network by considering the small gap as near-contact (e.g., blue edges in Fig. 5) which correspond to the heat conduction pathway of particle-gas-particle. A near-contact was identified if the distance between boundary voxels of two adjacent particles was shorter than the average particle radius (Fei et al. 2019; van der Linden et al. 2019). Then a TCNM model was generated by calculating the thermal conductance at three main heat transfer paths (i.e., through the particles, interparticle contacts and near-contacts), which is valid for dry granular materials at room temperature.

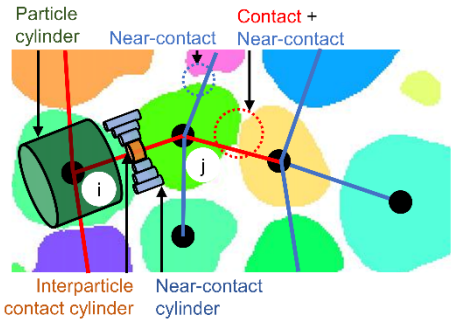

Fig. 5. Thermal network construction. Red edges represent interparticle contacts while blue edges indicate near-contacts. An equivalent particle cylinder (dark green), an interparticle contact cylinder (orange) and a series of near-contact cylinders (light blue) are used to calculate thermal conductance through the particle, interparticle contact and near-contact, respectively. The process is repeated for all particles in the granular material.

As shown in Fig. 5, three types of equivalent material cylinders corresponding to the three heat transfer mechanisms were used to calculate the thermal conductance. The thermal conductance C_{cy} of a cylinder with a thermal conductivity λ_{cy}, cross-section area A^{cy} and length L^{cy} is computed as $C_{cy} = \lambda_{cy} A^{cy}/L^{cy}$. Hence, the thermal conductance C^P through an equivalent particle cylinder (dark green cylinder in Fig. 5)

was calculated using the solid thermal conductivity λ_s and its cross-section area A^P and length L^P as following:

$$C^p = \lambda_s \frac{A^p}{L^p} = \lambda_s \frac{V^P/L^P/CN}{L^P} \tag{7}$$

where V^P is the particle volume, L^P is the distance from the particle centroid to the corresponding contact and CN is the coordination number of the target particle.

Similarly, Eq. (8) was used to calculate the thermal conductance $C^{contact}$ via an interparticle contact cylinder (orange cylinder in Fig. 5) with the corrected interparticle contact area A^C from Eq. (6). The length of the contact cylinder was defined as $3L^v$ (L^v *is the pixel size or voxel length*) as suggested by (Shapiro et al. 2004) which was a validation of (Bauer and Schlunder 1978). A coefficient κ was also introduced in Eq. (8) to indicate the particle surface roughness since interparticle contact is a combination of point-to-point contacts in real but are not presented in CT images in Fig. 1 due to the physical limitation of the CT facility. κ was set as 0.75 since Askari et al. (2015) concluded that the overestimation of may be 25% if neglecting the effect of roughness.

$$C^{contact} = \lambda_s \frac{\kappa A^C}{3L^v} \tag{8}$$

The thermal conductance C^{gap} through the near-contacts is the sum of the thermal conductance C^g (Eq. (9)) via each near-contact cylinder (light blue in Fig. 5). The cross-section area of the cylinder is the area of a pixel ($(L^v)^2$) and the length of the cylinder was computed during the process of its identification.

$$\mathrm{C}^{gap} = \sum_l C_l^g = \lambda_v (L^v)^2 \sum_l \frac{1}{L_l^g} \tag{9}$$

The three conductance were then combined to calculate the equivalent capacitance C_{ij} between the centroid of particle i and j using Eq. (10). The $C^{contact}$ is zero when two adjacent particles that only have near contacts.

$$C_{ij} = \left[\frac{1}{C_i^p} + \frac{1}{(C^{contact} + C^{gap})} + \frac{1}{C_j^p} \right]^{-1} \tag{10}$$

The C_{ij} calculated using Eq. (10) was imported to the Fourier's law (Eq. (11)) to calculate heat flux Q_{ij} using an open-source Python library OpenPNM (Gostick 2017) as a function of the temperature T in nodes i and j:

$$\sum_{i \to j} Q_{ij} = \sum_{i \to j} C_{ij}(T_i - T_j) \tag{11}$$

The temperatures on the opposite sides of the sample (inlet and outlet) were prescribed as T_{in} = 293 K and T_{out} = 292 K to create a small thermal gradient, whereas other boundaries were simulated as in thermally isolated conditions (or symmetrical, Q_{ij} = nil on these boundaries). The $Q_{ij,}$ integrated on a across-section perpendicular to the dominant heat transfer direction was selected to calculate the λ_{eff} of the sample as:

$$ETC = \frac{\frac{1}{A}\sum Q_{ij}}{(T_{in} - T_{out})/L} \quad (12)$$

where A is the area of a selected cross-section, L is the length of the simulated sample.

Since the penalized interparticle contact area from Eq. (6) and a coefficient related to particle surface roughness were used in Eq. (8) to calculate the thermal conductance at interparticle contacts, TCNM has the merit of mitigating the overestimation of λ_{eff} caused by the partial volume effect and particle surface roughness.

Effective thermal conductivity from physical testing

The selected sand samples were also poured into PVC containers with a height of 120 mm and a diameter of 50 mm using the same air-pluviation method to ensure consistency with the samples for CT scanning. A thermal needle probe with a length of 100 mm and a diameter of 2.4 mm was used to measure the λ_{eff} of each specimen following the ASTM standard D5334-14 (ASTM D5334-14 2014). The probe with the relatively large diameter probe improves contacts with the sand particles for more accurate measurements. The PVC containers were also scanned to check density consistency with the smaller axially loaded micro-CT scanned samples.

RESULTS AND DISCUSSION

Effective thermal conductivity results and TCNM validation

From the CT images of each sand under no load, four cubic ROIs with an edge length of 4.55 *mm* were imported to our TCNM for λ_{eff} calculations and comparisons with physical testing. Although the different grayscales in the CT images in Fig. 1 indicates minerals with different densities and thermal conductivities in the sands, a fixed thermal conductivity (3 W/(mK)) previously used in (Sundberg et al. 2009; Yun and Evans 2010) was assigned to solids to eliminate the effect of mineral composition, and isolate the effects of microstructure such as particle shape, connectivity and porosity. The thermal conductivity of air was set as 0.025 W/(mK). As shown in Fig. 6, the λ_{eff} from TCNM have a similar decreasing trend to that of the experimental

results. The λ_{eff} using the two methods are close for Ottawa sand (OS) while the λ_{eff} from TCNM is larger than that from measurements for angular sand (AS-L) and crushed schist (CS-M). The main reason is that the thermal conductivity of the solid phase in all samples are same in TCNM simulation but different in reality.

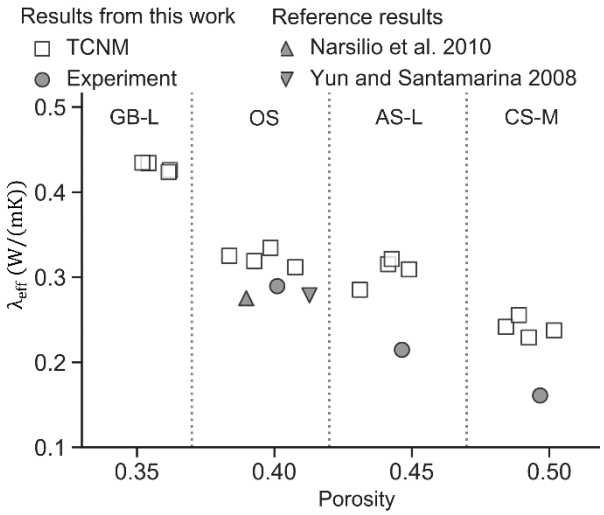

Fig. 6. The effective thermal conductivity computed from TCNM were validated by the experimental results of glass beads (GB-L), Ottawa sand (OS), angular sand (AS-L) and crushed schist sand (CS-M) (refer to Table 2)

Effect of WCN on effective thermal conductivity

For granular materials under loads, their thermo-mechanical behaviour is not only related to the bulk properties such as porosity but also microstructural contact variables (Desu et al. 2019) such as WCN. Therefore, the effect of WCN on λ_{eff} should be investigated. For GB-L, OS and AS-L under stress levels of 0, 2, 6.1 and 10.2 MPa, the average λ_{eff} of the four subsamples in each sand were calculated. Fig. 7 (a) shows that their average λ_{eff} has a directly proportional relationship with WCN, in contrast with the inverse proportionality with porosity (Fig. 7 (b)). In Fig. 7 (a), the data from GB-L and OS align along an overall trendline while the data in Fig. 7 (b) are clustered in three groups. Since particles in the three sands have distinct shapes, Fig. 7 (a) and Fig. 7 (b) were extended to include an additional dimension, by considering the average of sphericity and roundness in the third axis. In the 3D graphs shown in Fig. 7, planes were also fit to the data and R^2 were calculated. Fig. 7 (c) shows the R^2 is high at 0.98, which means the microscale geometrical parameter together with mesoscale topographic and contact quality variable can predict λ_{eff} well. If the mesoscale WCN is replaced by macroscale porosity as shown in Fig. 7 (d), the R^2 is

decreased to 0.88, indicating porosity alone cannot characterize the microstructure and the importance of mesoscale connectivity parameters in the study of the thermo-mechanics response of sands.

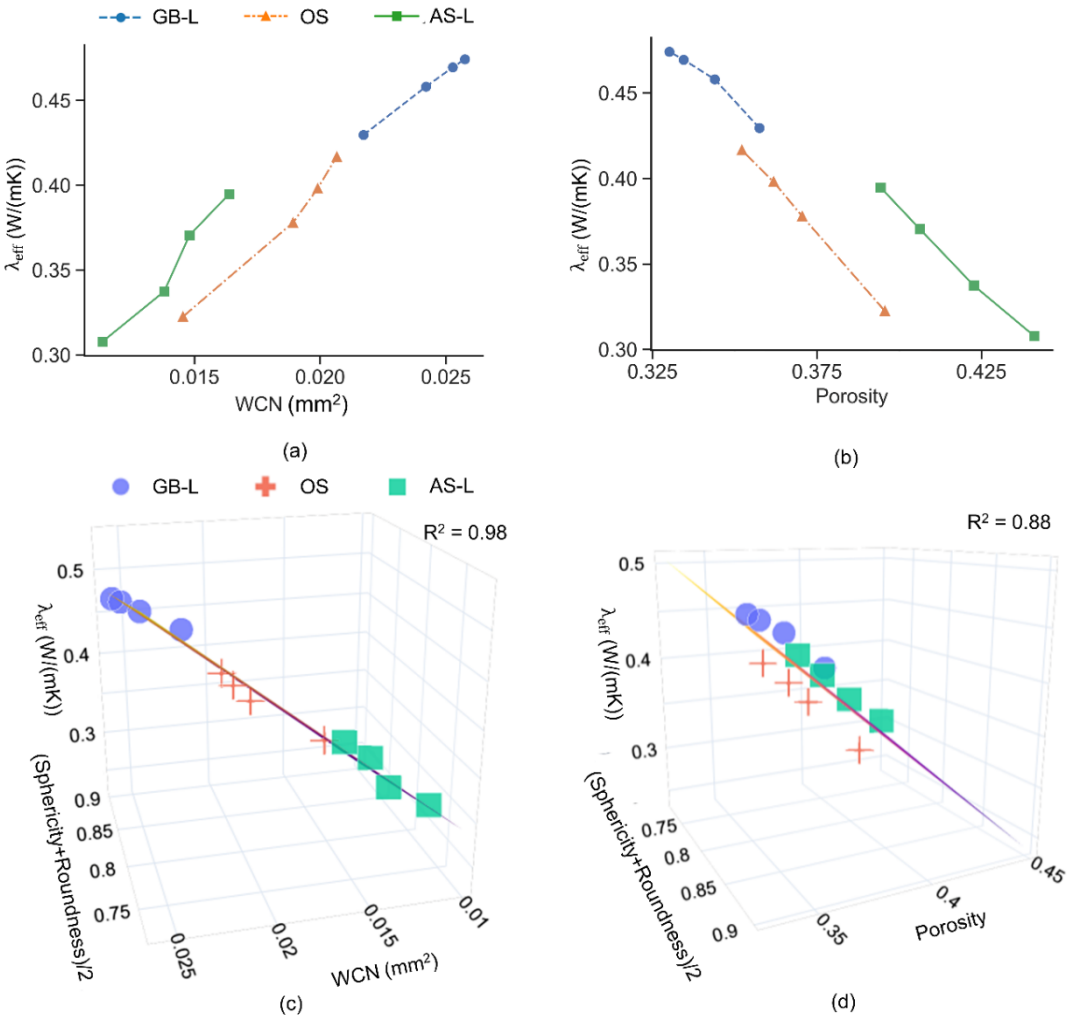

Fig. 7. The relationship between effective thermal conductivity and (a) WCN, (b) porosity, (c) WCN and particle shape, and (d) porosity and particle shape. (Click here to access the interactive graphs).

Relationships between WCN and traditional parameters

An analysis of why WCN can be an λ_{eff} predictor will be presented in this section. From the perspective of complex network theory, the WCN unifies the coordination number (connectivity) and contact area (as a weight in each edge of the network) as a single parameter. While the axial stress under zero lateral strain on samples is *under 2 MPa*, Fig. 8 shows that the slopes of the correlation between axial stress and λ_{eff} (Fig. 8 (a)) are similar to the slopes of the relationship between axial stress and contact area for three soils (Fig. 8 (c)). WCN also has similar corresponding increasing slopes (Fig.

8 (b)), however, while the coordination number versus axial stress trends are also increasing, the gradients for OS and AS-L (for axial stress ≤ 2MPa) are similar to each other but different from the corresponding gradients observed in effective thermal conductivity versus axial stress. As the axial stress increases beyond 2 MPa, contact area shows a stagnant increase (Fig. 8 (c)) which is not same as the gradients observed in the λ_{eff} plots (Fig. 8 (a)) any more. However, coordination number and WCN can capture the increase of λ_{eff} when axial stress is larger than 2 MPa. In other words, WCN can closely follow the increase of λ_{eff} over the whole range of axial stress since it captures the advantages of both contact area and coordination number at different stages of axial stress. Fig. 8 (b) also shows that the WCN has a good relationship with axial stress for each sand and the value in spherical GB-L is always the highest, which indicates that stress may be redundant and may not be necessary for the ANN model to predict λ_{eff} if WCN is used.

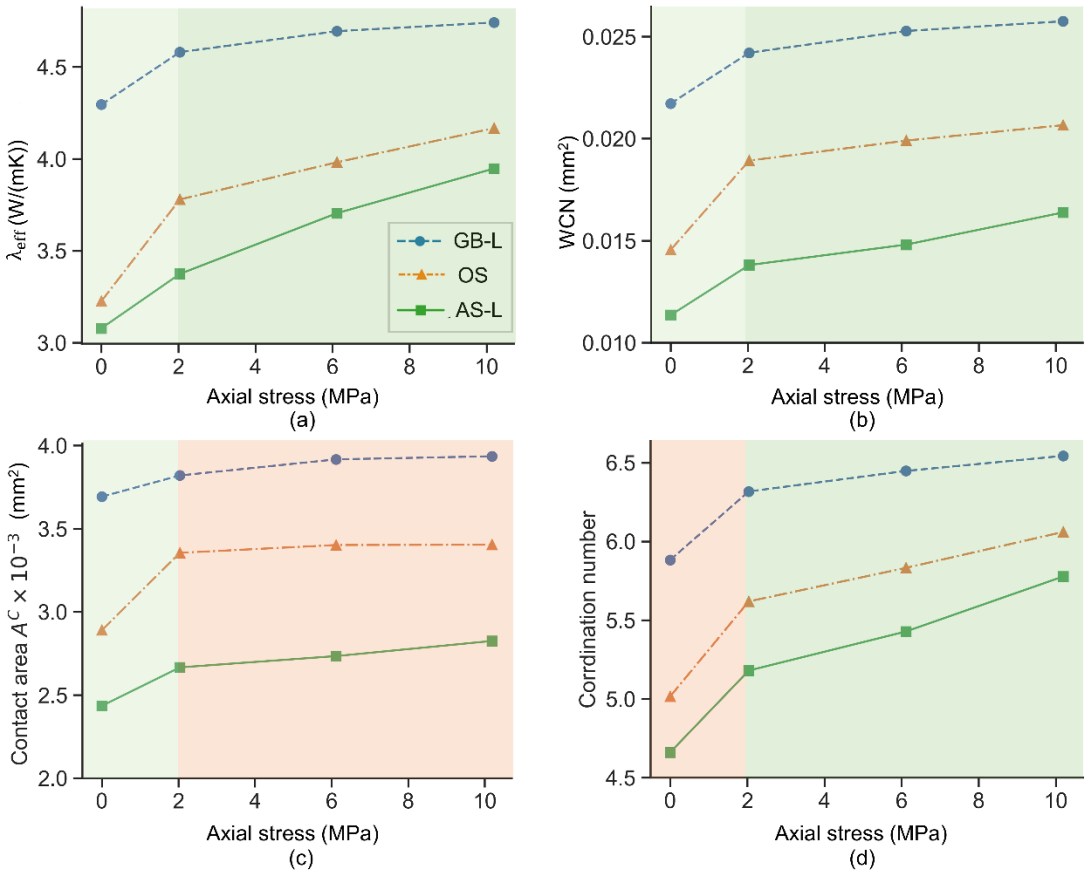

Fig. 8. Variation of (a) effective thermal conductivity, (b)WCN, (c) average intercontact area and (d) average coordination number with axial stress (and zero lateral strain).

As one of the main heat transfer processes is through particles in dry granular materials, the particle diameter affects the heat transfer distance in the particle and the impact on WCN should be explored. For each particle in the four ROIs of each sand, its equivalent particle diameter and WCN were computed and shown in Fig. 9. A clear directly proportional relationship between particle equivalent diameter and WCN can be seen in Fig. 9 (a) for spherical GB-L, which is reasonable since a large particle has a higher opportunity to touch more particles and have a larger total contact area once touching. The positive trend also exists in Fig. 9 (b) and Fig. 9 (c) for more irregular OS and AS-L sands. Therefore, the equivalent particle diameter is unnecessary to be involved in the ANN model on top of WCN for λ_{eff} prediction, WCN would suffice. In Fig. 9 (c), particles with larger equivalent diameter have lower WCN (Point A) than that of some particles with a smaller equivalent diameter (Point B). Particles with smaller equivalent diameter are irregular and elongated in AS-L and may exhibit a larger size in sieve analysis and a larger coordination number compared with regular particles in the same packing (Gan et al. 2017). In an ANN model, the offset could be compensated by choosing 3D sphericity and roundness as input parameters.

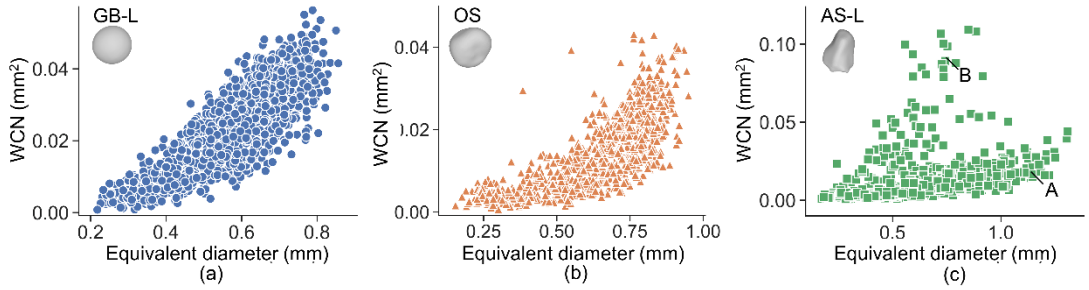

Fig. 9. The dependence of WCN on equivalent particle diameter

Effect of WCN on heat flux

Since heat flux was used in Eq. (11) to compute λ_{eff}, the particles at inlet and outlet of a subsample in each sand were used to study the relationship between WCN and heat flux. The heat flux from the centroid of a particle to the centroid of all its adjacent particles was calculated in TCNM and it has a positive correlation with WCN as shown in Fig. 10. The clear relationship is because WCN considers contact area which was used to calculate thermal conductance (Eq. (8)) and further served the computation of heat flux using the Fourier's law. Similar to Fig. 9, the correlation is clearest in spherical GB-L and become weaker in more irregular sands.

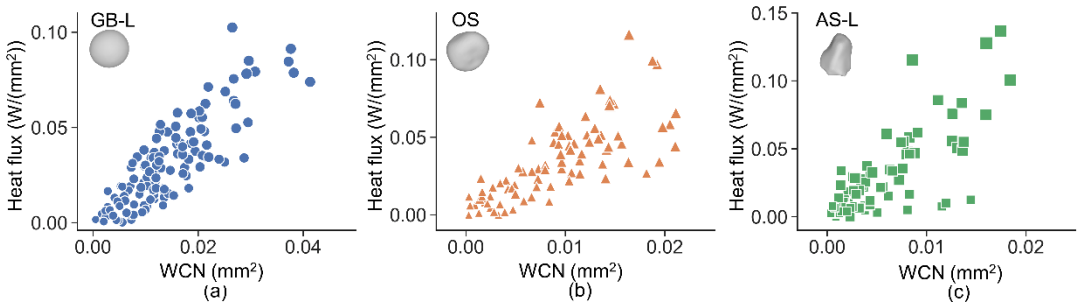

Fig. 10. The relationship between the total heat flux through a particle and WCN

ANN model construction

Only a small part of the samples shown in Table 2 has been used for the above analysis and data from more samples are required to build a database for ANN model construction. For the samples that have not been used, four subsamples (ROIs) were also selected and their 3D sphericity, 3D roundness, WCN, porosity and λ_{eff} under a larger range of loads (up to 40.7 MPa) were calculated. In addition to setting the thermal conductivity of the solid phase as 3 W/(mK), 5 and 7 W/(mK) were also used for enriching the database. Although dimensionless $\lambda_{eff}/\lambda_{solid}$ instead of λ_{eff} was used as the output of the ANN model, the data in Fig. 11 (a) whose markers were rendered by λ_{solid} still shows three distinct cluster groups corresponding to different λ_{solid} Therefore, λ_{solid} is also required to be an input parameter to the ANN model. In Fig. 11 (a), the different markers represent different sands and the size of the markers indicates the equivalent average particle diameter of the subsample. Fig. 11 (b) is the same as Fig. 11 (a) except for the meaning of markers which show the loadings applied to the subsamples. The data were randomly split into a training set (80%), a validation set (10%) and a testing set (10%).

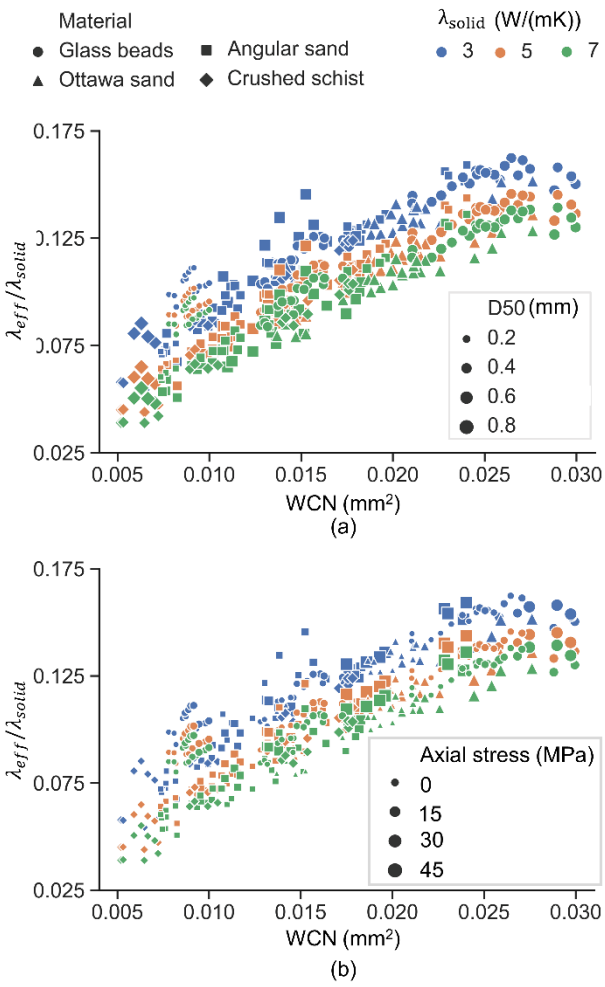

Fig. 11. The database used for ANN model construction.

ANN model I: λ_{solid}, sphericity, roundness and WCN as input parameters

Since WCN can quantify the structure of granular materials and *packing structure models* (Mo and Ban 2017) is a type of models to predict λ_{eff}, ANN model I used λ_{solid}, sphericity, roundness and WCN (but not porosity) as input parameters and $\lambda_{eff}/\lambda_{solid}$ as the output to imitate the *packing structure models* (Mo and Ban 2017) which also involve particle connectivity measured using Voronoi tessellation (Finney 1970) or typical lattice structure (Siu and Lee 2000). Fig. 12 shows that the R^2 between each pair of the parameters. Sphericity and roundness show a good correlation to each other with R^2 of 0.96 for the four tested sands. Still, both of them are required to cover the wide range of irregular particle shapes, as shown in (Fei et al. 2019). The R^2 of the correlation between the particle shape descriptors, WCN and λ_{solid} in Fig. 12 are not high, which implies these parameters are not redundant for ANN model I. The R^2 of the relationship between WCN and $\lambda_{eff}/\lambda_{solid}$ is 0.87, indicating that interparticle

connectivity and contact quality play crucial role in heat transfer in dry granular materials.

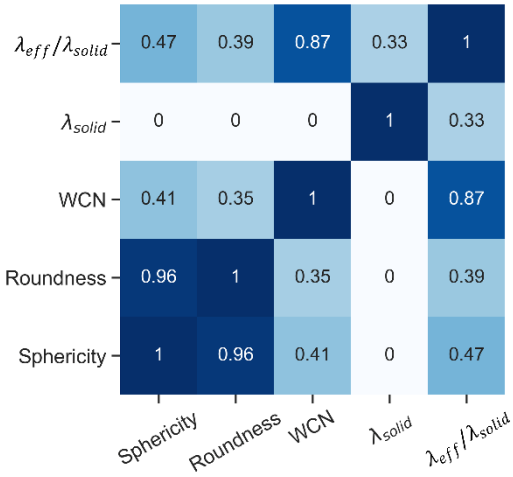

Fig. 12. A heatmap presents the R^2 between each pair of features used in the ANN model I

ANN is suitable for numerous complex problems due to its flexibility which is also one of its main drawbacks (Géron 2019). Values of model and algorithm parameters (i.e., hyperparameters) should be decided since any imaginable network topologies can be used. This study tuned the learning rate η, the neuron number in the hidden layer, and the structure indicating how neurons are interconnected to find the desirable ANN model. MSE was used to monitor the error during the training processes which were completed when the *epoch* reached 2,000. An epoch is one cycle that the model learns through the full training dataset.

The effect of learning rate η and neuron number on the performance of the ANN model I was first studied using ANN model I with one hidden layer. The ANN model with different learning rates $\eta = 0.1, 0.01, 0.001, 0.0001$ and constant 30 neurons in the single hidden layer was trained. As shown in Fig. 13 (a), large learning rates such as $\eta = 0.1, 0.01$ boosted the ANN model, showing low MSE even at the very beginning of training. However, the MSE kept the same level until the end of the training. In contrast, $\eta = 0.001$ can reach a low MSE which is similar to the MSE when $\eta = 0.0001$, and converge at an earlier stage. Therefore, $\eta = 0.001$ was selected as the learning rate for the ANN model I and it is also a commonly used value (Géron 2019). Next, the neuron number was tuned in the single hidden ANN model with the learning rate $\eta = 0.001$. Fig. 13 (b) shows that the ANN model with more

neurons requires a longer training time. Here we choose 30 neurons in a hidden layer to balance efficiency and accuracy. In the next study, five structures [50], [50,30], [50, 30, 10], [100, 50, 30], [100, 50, 30, 10] with $\eta = 0.001$ were implemented to analyse the effect of interconnection of neurons on the performance of ANN model. A structure indicates the number of hidden layers and the number of neurons in each hidden layer. For example, the second structure [50, 30] means that an ANN model has two hidden layers, the first hidden layer has 50 neurons while the second hidden layer has 30 neurons. It can be observed from Fig. 13 (c) that the second structure is appropriate for ANN model I since it is relatively simple and its MSE converges at a medium rate. The converged MSE in Fig. 13 (c) is smaller than that in Fig. 13 (a) and Fig. 13 (b) by two orders of magnitude, which hints the importance of a proper structure to an ANN model. Since the converged MSE in Fig. 13 (c) is also much smaller than the $\lambda_{eff}/\lambda_{solid}$ as shown in Fig. 11, the tuned hyperparameters were believed to be a proper combination for ANN model I. Finally, the testing dataset was used to predict $\lambda_{eff}/\lambda_{solid}$ which was compared with the 'true' values as shown in Fig. 13 (d). The predicted values have a high correlation (R^2=0.97) with the actual values, indicating that WCN and particle shape characteristics can be used as variables in *packing structure models* to predict $\lambda_{eff}/\lambda_{solid}$ quite well.

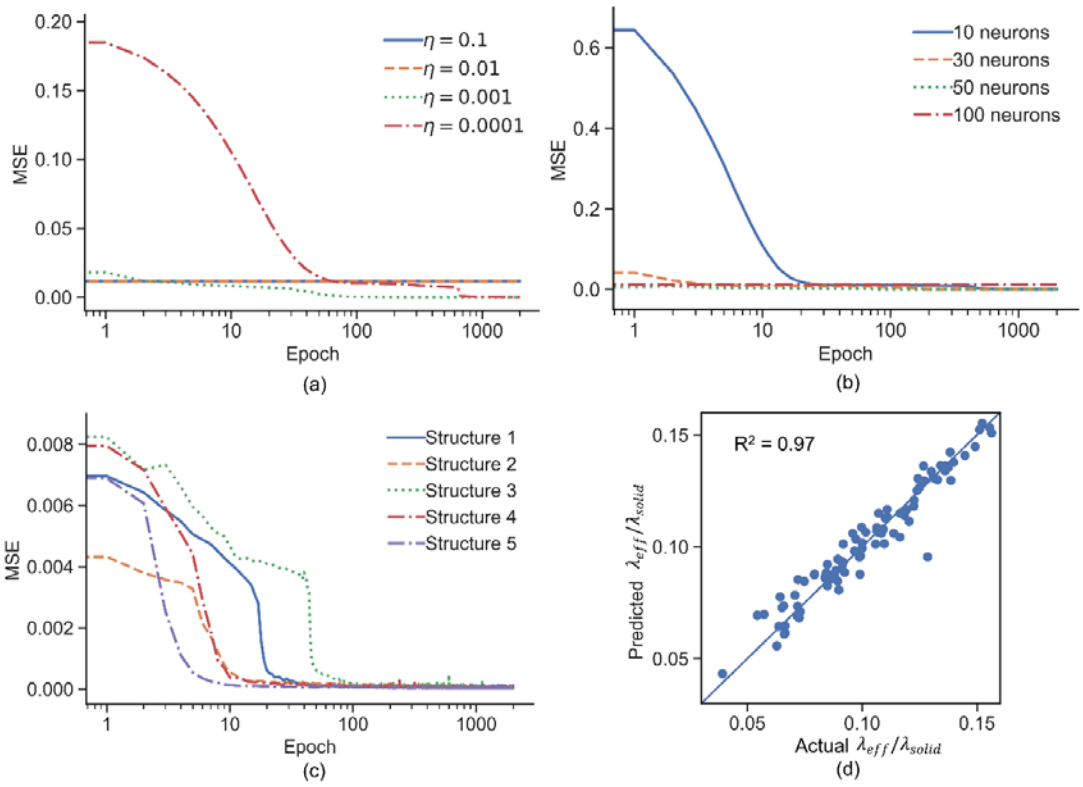

Fig. 13. Tuning learning rate η (a), neuron number in the hidden layer (b) and (c) on the for ANN model I. The correlation between the actual effective thermal conductivity and predicted effective thermal conductivity using tuned ANN model I on the testing set is show in (d)

ANN model II: $\lambda_{solid,}$ sphericity, roundness, WCN and porosity as input parameters

In this section, combined input parameters across scales were used in a new ANN model II. In the ANN model I, sphericity and roundness are among the input parameters to describe the geometry of a particle, so they capture information of the granular materials at the scale of a single particle (microscale). WCN quantifies the particle connectivity and contact quality (mesoscale) but it does not reach the whole sample as the bulk properties do. Porosity, a bulk property, is used in ANN model II to include a variable at the sample scale (macroscale). After using the similar tuning processes for hyperparameters as shown in Fig. 14 (a)-(c), the same structure No.2 [50,30] with learning rate $\eta = 0.001$ were also selected for ANN model II. Fig. 14 (d) presents that the R^2 of the relationship between the predicted and actual $\lambda_{eff}/\lambda_{solid}$ is 0.99 which is higher than that from ANN model I. The porosity, as a new input parameter in ANN model II, quantifies the void fraction and loosely indicates the number of particles in a sample. Higher particle count means more potential heat transfer pathways in granular assemblies. As explained in previous sections, other parameters are also related to heat transfer mechanisms capturing diverse aspects: (1) λ_{solid} determines the heat transfer efficiency within particle; (2) sphericity and roundness indicate interparticle contact quality and (3) WCN measures particle connectivity and interparticle contact quality, and also related to particle diameter (the heat transfer pathway within particles) and thermal conductance. Capturing abundant microstructural information that influence heat transfer certainly results in an accurate λ_{eff} prediction. Consequently, it is concluded that by considering parameters that characterise granular materials at different scales in λ_{eff} models can result in an accurate λ_{eff} prediction.

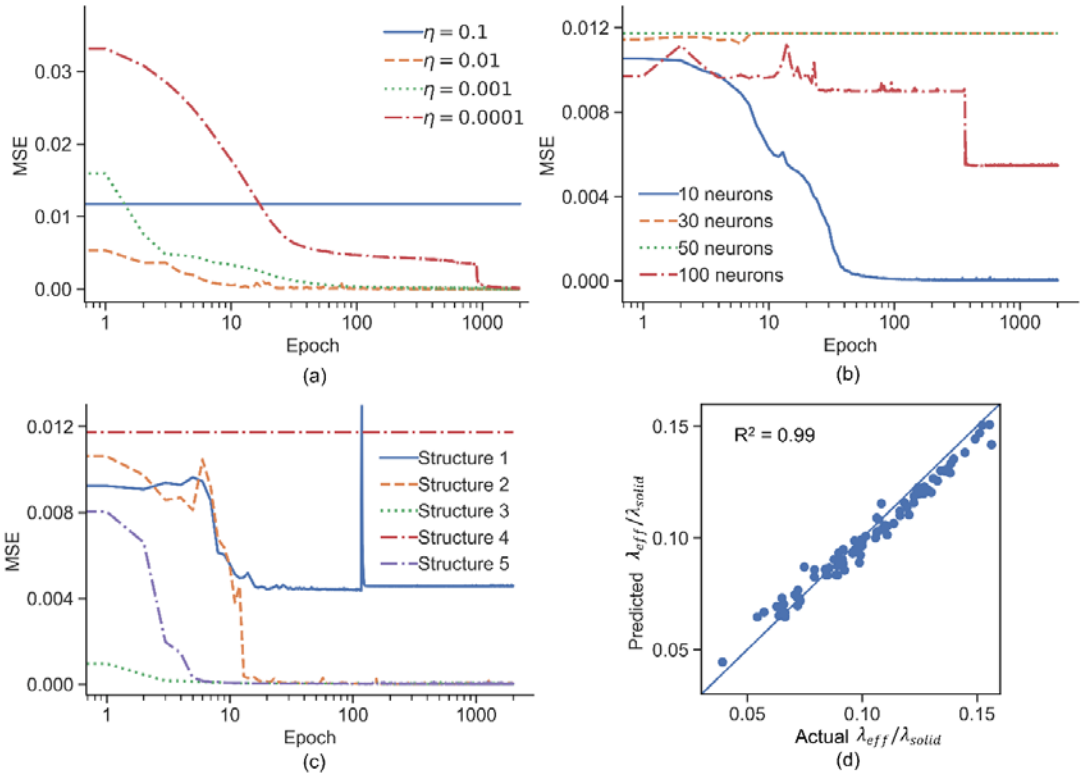

Fig. 14. Tuning learning rate η (a), neuron number in the hidden layer (b) and (c) on the for ANN model II. The correlation between the actual effective thermal conductivity and predicted effective thermal conductivity using tuned ANN model II

CONCLUSIONS

In granular materials, microstructure and boundary conditions (e.g., axial loading) control the effective thermal conductivity (λ_{eff}) but parameters indicative of microstructure are seldomly used in the existing λ_{eff} models, perhaps with the exception of (global) porosity and aspect ratio. The advancement of new techniques such as CT, complex network theory, and new numerical simulation methods enable the access to the microstructure of natural sands and promote a need of data-driven approaches, for example with advancement of machine learning techniques, to predict λ_{eff} accurately and efficiently.

Four sand assemblies varying in particle size, shape and under different stress levels were CT scanned to achieve image stacks. By applying image processing methods to the image stacks, microstructural parameters such as particle size, 3D sphericity and roundedness and porosity were obtained. In addition, the contact network was constructed and WCN was calculated according to complex network theory. The applicability of these parameters to the ANN model was justified by the analysis of heat transfer mechanism, review of λ_{eff} models and their interplay. The utilisation of

microstructural parameters provides ANN model with some physically-based preconditioning, rather than utilizing an ANN model merely as a black-box with somehow random input parameters. Finally, the results indicate that the ANN model that considers multiple-scale microstructural parameters can predict λ_{eff} well, with best predictions using parameters that characterise granular materials across scales: λ_{solid}, *sphericity, roundness* (at the particle scale), *WCN* (at the mesoscale) and *porosity* (at the macroscale)

This work proves the feasibility of applying ANN to material science, predicting λ_{eff} in particular. The physics-based data-driven approach allows the acceleration of material design in a more autonomous and objective process. This paper uses WCN from a contact network since it is easier to estimate than other mesoscale network features listed in (Fei et al. 2020). However, WCN from the contact network only considers the interparticle contacts but not near-contacts which can be involved in thermal network features (Fei et al. 2020). The authors are striving to merge the several aforementioned techniques into a platform which can enable the academic community to achieve microstructural parameters including thermal network features easily and conveniently. Future work includes to continue increasing the current database of granular materials of different shapes and to explore ANN models built with thermal network features.

CONFLICT OF INTEREST

The authors declared that there is no conflict of interest.

ACKNOWLEDGEMENTS

This research was undertaken in the Imaging and Medical Beam Line (IMBL) at the Australian Synchrotron, Victoria, Australia. The authors would like to acknowledge Dr Anton Maksimenko and the other beam scientists at Australian Synchrotron for their support during our experiments. The authors also thank Dr Tabassom Afshar, Dr Joost van der Linden and Dr Xiuxiu Miao for their support in collecting the CT images. The first author thanks The University of Melbourne for offering the Melbourne Research Scholarship.

REFERENCES

Abdulagatova, Z., Abdulagatov, I. & Emirov, V. (2009) Effect of temperature and pressure on the thermal conductivity of sandstone. *International Journal of Rock Mechanics and Mining Sciences* **46(6)**:1055-1071.

Abyzov, A. M., Goryunov, A. V. & Shakhov, F. M. (2013) Effective thermal conductivity of disperse materials. I. Compliance of common models with experimental data. *International Journal of Heat and Mass Transfer* **67**:752-767.

Askari, R., Hejazi, S. H. & Sahimi, M. (2017) Effect of deformation on the thermal conductivity of granular porous media with rough grain surface. *Geophysical Research Letters* **44(16)**:8285-8293.

Astm D5334-14 (2014)Standard Test Method for Determination of Thermal Conductivity of Soil and Soft Rock by Thermal Needle Probe Procedure. West Conshohocken, PA, ASTM International.

Desu, R. K., Peeketi, A. R. & Annabattula, R. K. (2019) Artificial neural network-based prediction of effective thermal conductivity of a granular bed in a gaseous environment. *Computational Particle Mechanics* **6(3)**:503-514.

Fang, W.-Z., Zhang, H., Chen, L. & Tao, W.-Q. (2017) Numerical predictions of thermal conductivities for the silica aerogel and its composites. *Applied Thermal Engineering* **115**:1277-1286.

Fei, W., Narsilio, G. A. & Disfani, M. M. (2019a) Impact of three-dimensional sphericity and roundness on heat transfer in granular materials. *Powder Technology* **355**:770-781.

Fei, W., Narsilio, G. A., Van Der Linden, J. H. & Disfani, M. M. (2019b) Quantifying the impact of rigid interparticle structures on heat transfer in granular materials using networks. *International Journal of Heat and Mass Transfer* **143**:118514.

Fei, W., Narsilio, G. A., Van Der Linden, J. H. & Disfani, M. M. (2020) Network analysis of heat transfer in sphere packings. *Powder Technology* **362**:790-804.

Fei, W. B., Li, Q., Wei, X. C., Song, R. R., Jing, M. & Li, X. C. (2015) Interaction analysis for CO2 geological storage and underground coal mining in Ordos Basin, China. *Engineering geology* **196**:194-209.

Fricke, H. (1924) A mathematical treatment of the electric conductivity and capacity of disperse systems I. The electric conductivity of a suspension of homogeneous spheroids. *Physical Review* **24(5)**:575.

Gan, J., Zhou, Z. & Yu, A. (2017) Effect of particle shape and size on effective thermal conductivity of packed beds. *Powder Technology* **311**:157-166.

Géron, A. (2019) *Hands-On Machine Learning with Scikit-Learn, Keras, and TensorFlow: Concepts, Tools, and Techniques to Build Intelligent Systems.* O'Reilly Media.

Gostick, J. T. (2017) Versatile and efficient pore network extraction method using marker-based watershed segmentation. *Physical Review E* **96(2)**:023307.

Ju, S. & Shiomi, J. (2019) Materials Informatics for Heat Transfer: Recent Progresses and Perspectives. *Nanoscale and Microscale Thermophysical Engineering* **23(2)**:157-172.

Kautz, E. J., Hagen, A. R., Johns, J. M. & Burkes, D. E. (2019) A machine learning approach to thermal conductivity modeling: A case study on irradiated uranium-molybdenum nuclear fuels. *Computational Materials Science* **161**:107-118.

Keller, T., Motschmann, U. & Engelhard, L. (2001) Modelling the poroelasticity of rocks and ice. *Geophysical prospecting* **47(4)**:509-526.

Mo, J. & Ban, H. (2017) Measurements and theoretical modeling of effective thermal conductivity of particle beds under compression in air and vacuum. *Case studies in thermal engineering* **10**:423-433.

Moscardini, M., Gan, Y., Pupeschi, S. & Kamlah, M. (2018) Discrete element method for effective thermal conductivity of packed pebbles accounting for the Smoluchowski effect. *Fusion Engineering and Design* **127**:192-201.

Narsilio, G. A., Kress, J. & Yun, T. S. (2010) Characterisation of conduction phenomena in soils at the particle-scale: Finite element analyses in conjunction with synthetic 3D imaging. *Computers and Geotechnics* **37(7)**:828-836.
Otsu, N. (1979) A threshold selection method from gray-level histograms. *IEEE transactions on systems, man, and cybernetics* **9(1)**:62-66.
P., Z. & Schlunder, E. U. (1970) Thermal Conductivity of Granular Materials at Moderate Temperatures. *Chemie. Ingr-Tech.* **42**:933-941.
Papadopoulos, L., Porter, M. A., Daniels, K. E. & Bassett, D. S. (2018) Network analysis of particles and grains. *Journal of Complex Networks* **6(4)**:485-565.
Peixoto, T. P. (2014) The graph-tool python library. *figshare*.
Scott, D. M., Das, D. K., Subbaihaannadurai, V. & Kamath, V. A. (2005) A computational scheme for fluid flow and heat transfer analysis in porous media for recovery of oil and gas. *Petroleum science and technology* **23(7-8)**:843-862.
Singh, D. N. & Devid, K. (2000) Generalized relationships for estimating soil thermal resistivity. *Experimental Thermal and Fluid Science* **22(3)**:133-143.
Sundberg, J., Back, P.-E., Ericsson, L. O. & Wrafter, J. (2009) Estimation of thermal conductivity and its spatial variability in igneous rocks from in situ density logging. *International Journal of Rock Mechanics and Mining Sciences* **46(6)**:1023-1028.
Van Antwerpen, W. D., Du Toit, C. & Rousseau, P. (2010) A review of correlations to model the packing structure and effective thermal conductivity in packed beds of mono-sized spherical particles. *Nuclear Engineering and design* **240(7)**:1803-1818.
Van Der Linden, J. H., Narsillio, G. A. & Antoinette, T. (2019) Thermal conductance network model for computerised tomography images of real geomaterials (Conditionally accepted). *Computers and Geotechnics*.
Wei, H., Zhao, S., Rong, Q. & Bao, H. (2018) Predicting the effective thermal conductivities of composite materials and porous media by machine learning methods. *International Journal of Heat and Mass Transfer* **127**:908-916.
Yang, H., Zhang, L., Liu, R., Wen, X., Yang, Y., Zhang, L., Zhang, K. & Askari, R. (2019) Thermal Conduction Simulation Based on Reconstructed Digital Rocks with Respect to Fractures. *Energies* **12(14)**:2768.
Yu, W., Xie, H., Xin, S., Yin, J., Jiang, Y. & Wang, M. (2015) Thermal properties of polymethyl methacrylate composite containing copper nanoparticles. *Journal of nanoscience and nanotechnology* **15(4)**:3121-3125.
Yüksel, N. (2016) The review of some commonly used methods and techniques to measure the thermal conductivity of insulation materials. In *Insulation materials in context of sustainability*.) IntechOpen.
Yun, T. S. & Evans, T. M. (2010) Three-dimensional random network model for thermal conductivity in particulate materials. *Computers and Geotechnics* **37(7-8)**:991-998.
Yun, T. S. & Santamarina, J. C. (2008) Fundamental study of thermal conduction in dry soils. *Granular matter* **10(3)**:197.

Chapter 7: Conclusions

Since λ_{eff} plays a crucial role in the design, performance and maintenance of various engineering projects, there is a long history of λ_{eff} models that have been developed over the years, with incremental improvement over time. However, the developments were limited by the unavailability of characterising the microstructure at multiple length scales, especially for real granular geomaterials which are generally composed by irregular particles. Based on artificial sphere packings generated using DEM and digital sands reconstructed from CT scanned images, a series of studies in this thesis enrich the collection of multiscale microstructural variables by developing in-house codes to compute 3D sphericity and roundness in Chapter 3, by applying rigidity theory for deforming materials in Chapter 4, by implementing complex network theory in Chapter 5. In order to select the most essential microstructural parameters to λ_{eff}, a number of machine learning techniques were used in Chapter 5. Then, a more advanced deep learning machine method − artificially neural network – with selected input parameters was used to train an λ_{eff} model rendering high accuracy and computational efficiency.

The techniques and tools involved in this thesis may be assembled in a platform (Figure 1.1) that provides an avenue to promote a thorough understanding of transport properties. The CT techniques, image processing algorithms and complex network theory overcome the obstacle of accessing the microstructure in the past, enabling the mining of multiscale parameters. Mesoscale parameters such as *local clustering coefficient* in Chapter 4 and *weighted degree* in Chapter 5 shows a better correlation with λ_{eff} than porosity, which is in line with the suggestions that 'heat transfer in a packed bed is considered as the effect of the packing structure which cannot be characterized by the porosity alone' by (Van Antwerpen et al. 2010) and 'The difference of thermal conductivity values between models and methods can be considered due to the lack of structural data' by (Yüksel 2016). With the large number of microstructural characteristics that are now readily accessible using the platform developed in this thesis, data-driven studies on transport phenomena based on high-resolution images are enabled.

7.1 SUMMARY OF FINDINGS

Given the lack of proper particle shape descriptors in the existing λ_{eff} models, Chapter 3 develops a framework to calculate 3D sphericity and roundness of each particle in the sands. A critical assessment of the literature allowed the selection of these descriptors among others and choosing the most appropriate definitions (equations) for them. By applying the framework to glass beads, Ottawa sand, angular sand and two types of crushed schist, it is found that (1) Irregular particles have a smaller value of sphericity and roundness but wider distribution than round particles; (2) Higher average sphericity or roundness tend to render higher λ_{eff}. Additionally, the impacts of 3D sphericity and roundness on contact radius ratio and coordination number are investigated. For particles in a given sample, the coordination number shows a subtle increase when decreasing sphericity and roundness. However, it is found by comparing different samples that the average coordination in a sample may be smaller if it has lower average sphericity and roundness due to particle orientational alignment, particle interlocking and surface roughness.

Heat transfer in geomaterials under loading is a common situation in, for example, shallow geothermal energy projects involving energy piles. Hence Chapter 4 employs the number of triangles formed by touching particles (called triples or 3-cycles) and clustering coefficient to study the variation of rigid structure in sands. Results show that *local clustering coefficient* has the ability to quantify the rigidity of granular materials. The *local clustering coefficient* only characterises the particle connectivity, so 3D sphericity and roundness are calculated to incorporate the involvement of interparticle contact area as shown in Chapter 3. The combination of *local clustering coefficient* and *particle shape* has a better correlation with λ_{eff} than the combination of porosity and particle shape. In other words, a mesoscale rigidity variable together with microscale particle shape descriptors better captures the variation of microstructure for predicting λ_{eff}.

Inspired by the lack of mesoscale parameters and the good performance of the involvement of mesoscale parameters for predicting λ_{eff} in Chapter 4, Chapter 5 aims to identify more mesoscale parameters that are important to λ_{eff}. Since particle connectivity and contact quality are essential to heat transfer, this chapter also explores individual variables related to both of the two properties. Both contact networks and thermal networks are built for granular materials so that different types of network

features can be computed using complex network theory. After calculating the relationship between each network feature and λ_{eff}, it is found that network features can be alternative to traditional geotechnical parameters (e.g. porosity) to predict λ_{eff} for granular geomaterials. Especially the network features weighted by the interparticle contact area in a contact network or thermal conductance in a thermal network capture both the information of particle connectivity and contact quality, showing high correlation with λ_{eff} for a range of different granular materials.

With the abundant new microstructural parameters available as introduced in the previous chapters, new λ_{eff} models considering them can be developed. This goal is achieved in Chapter 6 by using ANN which is an advanced machine learning technique and to date has limited application in predicting λ_{eff} for granular geomaterials. Among the numerous available parameters, the input parameters for ANN are strictly selected according to the heat transfer mechanics, existing λ_{eff} models and its interplay with other parameters. The utilisation of these microstructural parameters provides ANN model with some physically-based preconditioning, rather than utilising an ANN model merely as a black-box with somehow random inputs. Results show that the ANN model that considers multiple-scale microstructural parameters can predict λ_{eff} well for complex granular geomaterials encompassing a wide range of particle size, particle shape and loading conditions.

7.2 RECOMMENDATIONS FOR FUTURE RESEARCH

The capability of using mesoscale network features being predictors of λ_{eff} for dry granular geomaterials has been proved. The process of heat transfer through small gaps is considered in thermal network features since they include additional edges in the network compared with edges assigned only to actual contacts in a contact network. This consideration will become more important in wet granular geomaterials since the thermal conductivity of water is larger than that of air. Therefore, the effect of network features on λ_{eff} under this unsaturated condition can be further investigated.

Both FEM and TCNM are used in this thesis for computing λ_{eff} but pore fluid convection and radiation have not been considered, this becomes more relevant for larger size particles or high temperatures (e.g., in nuclear waste disposal projects). Additionally, the system properties such as gas pressure and temperature in dry granular materials also affect the λ_{eff} because the thermal conductivity of gas reduces

with the decrease in pressure (known as Smoluchowski effect (Moscardini et al. 2018)). FEM and TCNM models involving these effects could thus be further developed.

A real sand particle surface is not smooth, so an interparticle contact is not a surface-to-surface contact but a series of point-to-point contacts. Hence particle surface roughness affects the interparticle contact area and is required to be quantified for real sand particles. According to the results in Chapter 3, particle orientation influences the coordination number and thus affects λ_{eff} (Kain et al. 2016). Quantifying the orientation of regular particles such as ellipsoids is possible using the direction of the principal axis. This direct information may be used to improve the predictability of models and physical understanding.

The development of the key ingredients of the overall platform developed in this PhD project include CT, image processing algorithms, complex network theory, different numerical simulation methods and machine learning techniques. These new advanced techniques could potentially be used to study various transport phenomena, so studying the effect of microstructure on coupled thermo-mechanical-hydraulic response can be future work to benefit material design. An example could be producing materials with high thermal conductivity but low permeability by controlling its microstructure.

Bibliography

AB, C. (2015). "COMSOL multiphysics v5.0, http://www.comsol.com."

Abdulagatova, Z., Abdulagatov, I., and Emirov, V. (2009). "Effect of temperature and pressure on the thermal conductivity of sandstone." *International Journal of Rock Mechanics and Mining Sciences*, 46(6), 1055-1071.

Aboufoul, M., Chiarelli, A., Triguero, I., and Garcia, A. (2019). "Virtual porous materials to predict the air void topology and hydraulic conductivity of asphalt roads." *Powder Technology*, 352, 294-304.

Abyzov, A. M., Goryunov, A. V., and Shakhov, F. M. (2013). "Effective thermal conductivity of disperse materials. I. Compliance of common models with experimental data." *International Journal of Heat and Mass Transfer*, 67, 752-767.

Aduda, B. (1996). "Effective thermal conductivity of loose particulate systems." *Journal of materials science*, 31(24), 6441-6448.

Afshar, T., Disfani, M., Narsilio, G., and Arulrajah, A. "Changes to Grain Properties due to Breakage in a Sand Assembly using Synchrotron Tomography." *Proc., EPJ Web of Conferences*, EDP Sciences, 07004.

Afshar, T., Disfani, M. M., Arulrajah, A., Narsilio, G. A., and Emam, S. (2017). "Impact of particle shape on breakage of recycled construction and demolition aggregates." *Powder technology*, 308, 1-12.

Agapiou, J., and DeVries, M. (1989). "An experimental determination of the thermal conductivity of a 304L stainless steel powder metallurgy material." *Journal of Heat Transfer*, 111(2), 281-286.

Ahmed, Z., and Lebedev, M. (2019). "Elastic properties of sands, Part 1: Micro computed tomography image analysis of grain shapes and their relationship with microstructure." *Geophysical Prospecting*, 67(4), 723-744.

Alramahi, B., Alshibli, K. A., and Fratta, D. (2010). "Effect of Fine Particle Migration on the Small-Strain Stiffness of Unsaturated Soils." *Journal of Geotechnical and Geoenvironmental Engineering*, 136(4), 620-628.

Anthony, J. W., Bideaux, R. A., Bladh, K. W., and Nichols, M. C. (1990). *Handbook of mineralogy*, Mineral Data Publ. Tucson.

Arevalo, R., Zuriguel, I., and Maza, D. (2009). "Topological properties of the contact network of granular materials." *International Journal of Bifurcation and Chaos*, 19(02), 695-702.

Arévalo, R., Zuriguel, I., and Maza, D. (2010). "Topology of the force network in the jamming transition of an isotropically compressed granular packing." *Physical Review E*, 81(4), 041302.

Arganda-Carreras, I., Kaynig, V., Rueden, C., Eliceiri, K. W., Schindelin, J., Cardona, A., and Sebastian Seung, H. (2017). "Trainable Weka Segmentation: a machine learning tool for microscopy pixel classification." *Bioinformatics*, 33(15), 2424-2426.

Argento, C., and Bouvard, D. (1993). "Thermal conductivity of granular media." *Powders & grains*, 129-134.

Asakuma, Y., Asada, M., Kanazawa, Y., and Yamamoto, T. (2016). "Thermal analysis with contact resistance of packed bed by a homogenization method." *Powder technology*, 291, 46-51.

Asimow, L., and Roth, B. (1978). "The rigidity of graphs." *Transactions of the American Mathematical Society*, 245, 279-289.
Askari, R., Hejazi, S. H., and Sahimi, M. (2017). "Effect of deformation on the thermal conductivity of granular porous media with rough grain surface." *Geophysical Research Letters*, 44(16), 8285-8293.
Askari, R., Hejazi, S. H., and Sahimi, M. (2018). "Thermal Conduction in Deforming Isotropic and Anisotropic Granular Porous Media with Rough Grain Surface." *Transport in Porous Media*, 124, 221-236.
Askari, R., Taheri, S., and Hejazi, S. H. (2015). "Thermal conductivity of granular porous media: A pore scale modeling approach." *AIP Advances*, 5(9).
ASTM (2017). "C778-17 standard specification for standard sand." *ASTM International, West Conshohocken, PA*.
ASTM D5334-14 (2014). "Standard Test Method for Determination of Thermal Conductivity of Soil and Soft Rock by Thermal Needle Probe Procedure." ASTM International, West Conshohocken, PA.
Ayachit, U. (2015). *The paraview guide: a parallel visualization application*, Kitware, Inc.
Azadi, P., Farnood, R., and Yan, N. (2010). "FEM–DEM modeling of thermal conductivity of porous pigmented coatings." *Computational Materials Science*, 49(2), 392-399.
Bagheri, G., and Bonadonna, C. (2016). "On the drag of freely falling non-spherical particles." *Powder Technology*, 301, 526-544.
Bahrami, M., Culham, J., and Yovanovich, M. (2004). "Modeling thermal contact resistance: a scale analysis approach." *Journal of heat transfer*, 126(6), 896-905.
Banala, A., Ma, H., and Kumar, A. (2019). "Influence of particulate geometry on permeability of porous materials." *Powder Technology*.
Baram, R. M., Herrmann, H., and Rivier, N. (2004). "Space-filling bearings in three dimensions." *Physical review letters*, 92(4), 044301.
Barandiaran, I. (1998). "The random subspace method for constructing decision forests." *IEEE transactions on pattern analysis and machine intelligence*, 20(8).
Bassett, D. S., Owens, E. T., Daniels, K. E., and Porter, M. A. (2012). "Influence of network topology on sound propagation in granular materials." *Physical Review E*, 86(4), 041306.
Batchelor, G. K., and O'brien, R. (1977). "Thermal or electrical conduction through a granular material." *Proc. R. Soc. Lond. A*, 355(1682), 313-333.
Bauer, R., and Schlunder, E. (1978). "Effective radial thermal-conductivity of packings in gas flow, part -ii: Thermal conductivity of packing fraction without gas flow." *International Chemical Engineering*, 18(2), 189-204.
Beck, A. (1976). "An improved method of computing the thermal conductivity of fluid-filled sedimentary rocks." *Geophysics*, 41(1), 133-144.
Belyaev, A. G., Ohtake, Y., and Abe, K. "Detection of ridges and ravines on range images and triangular meshes." *Proc., Vision Geometry IX*, International Society for Optics and Photonics, 146-155.
Belyaev, Y., and Seidel, H. "Mesh smoothing by adaptive and anisotropic Gaussian filter applied to mesh normals." *Proc., Vision, modeling, and visualization*, 203-210.

Bergles, A. E., Collier, J., Delhaye, J. M., Hewitt, G., and Mayinger, F. (1981). *Two-phase flow and heat transfer in the power and process industries*, Hemisphere New York.

Bidarmaghz, A., Choudhary, R., Soga, K., Kessler, H., Terrington, R. L., and Thorpe, S. (2019). "Influence of geology and hydrogeology on heat rejection from residential basements in urban areas." *Tunnelling and Underground Space Technology*, 92, 103068.

Birkholz, O., Gan, Y., and Kamlah, M. (2019). "Modeling the effective conductivity of the solid and the pore phase in granular materials using resistor networks." *Powder Technology*, 351, 54-65.

Boas, F. E., and Fleischmann, D. (2012). "CT artifacts: causes and reduction techniques." *Imaging in medicine*, 4(2), 229-240.

Bosl, W. J., Dvorkin, J., and Nur, A. (1998). "A study of porosity and permeability using a lattice Boltzmann simulation." *Geophysical Research Letters*, 25(9), 1475-1478.

Brandon, T., and Mitchell, J. (1990). "Factors influencing thermal resistivity of sands." *Journal of Geotechnical Engineering*, 115(12), 1683-1698.

Breheny, P. (1984). "Classification and regression trees."

Brigaud, F., and Vasseur, G. (1989). "Mineralogy, porosity and fluid control on thermal conductivity of sedimentary rocks." *Geophysical Journal International*, 98(3), 525-542.

Brown, R., and Richards, J. (1970). "Principles of powder mechanics." Pergamon Press, London.

Buades, A., Coll, B., and Morel, J.-M. "A non-local algorithm for image denoising." *Proc., 2005 IEEE Computer Society Conference on Computer Vision and Pattern Recognition (CVPR'05)*, IEEE, 60-65.

Carmo, M. d. (1993). "Differential geometry of curves and surfaces. 1976." *Prentice-Hall, Englewood Cliffs, New Jersey). Rehsteiner, F. and Rewker, HJ Collision free five axis milling of twisted ruled surface. Ann. CIRP*, 42(1), 457-461.

Carslaw, H., and Jaeger, J. (1959). *Conduction of heat in solids: Oxford Science Publications*, Oxford, England.

Cavarretta, I., Coop, M., and O'Sullivan, C. (2010). "The influence of particle characteristics on the behaviour of coarse grained soils."

Cernuschi, F., Rothleitner, C., Clausen, S., Neuschaefer-Rube, U., Illemann, J., Lorenzoni, L., Guardamagna, C., and Larsen, H. E. (2017). "Accurate particle speed prediction by improved particle speed measurement and 3-dimensional particle size and shape characterization technique." *Powder technology*, 318, 95-109.

Chen, Y. F., Wang, M., Zhou, S., Hu, R., and Zhou, C. B. (2015). "An effective thermal conductivity model for unsaturated compacted bentonites with consideration of bimodal shape of pore size distribution." *Sci. China Technol. Sci.*, 58(2), 369-380.

Cheng, G., Gan, J., Xu, D., and Yu, A. (2019). "Evaluation of effective thermal conductivity in random packed bed: Heat transfer through fluid voids and effect of packing structure." *Powder Technology*.

Cheng, G., Yu, A., and Zulli, P. (1999). "Evaluation of effective thermal conductivity from the structure of a packed bed." *Chemical Engineering Science*, 54(19), 4199-4209.

Cherkasova, A. S., and Shan, J. W. (2008). "Particle aspect-ratio effects on the thermal conductivity of micro-and nanoparticle suspensions." *Journal of Heat Transfer*, 130(8), 082406.

Chiew, Y., and Glandt, E. (1983). "The effect of structure on the conductivity of a dispersion." *Journal of Colloid and Interface Science*, 94(1), 90-104.

Cho, G.-C., Dodds, J., and Santamarina, J. C. (2006). "Particle shape effects on packing density, stiffness, and strength: natural and crushed sands." *Journal of geotechnical and geoenvironmental engineering*, 132(5), 591-602.

Choo, J., Kim, Y. J., Lee, J. H., Yun, T. S., Lee, J., and Kim, Y. S. (2013). "Stress-induced evolution of anisotropic thermal conductivity of dry granular materials." *Acta Geotechnica*, 8(1), 91-106.

Chu, Z., Zhou, G., Wang, Y., Zhao, X., and Mo, P.-Q. (2019). "A supplementary analytical model for the stagnant effective thermal conductivity of low porosity granular geomaterials." *International Journal of Heat and Mass Transfer*, 133, 994-1007.

Cignoni, P., Callieri, M., Corsini, M., Dellepiane, M., Ganovelli, F., and Ranzuglia, G. "Meshlab: an open-source mesh processing tool." *Proc., Eurographics Italian chapter conference*, 129-136.

Clauser, C., and Huenges, E. (1995). "Thermal conductivity of rocks and minerals." *Rock physics & phase relations*, 3, 105-126.

Cnudde, V., Masschaele, B., Dierick, M., Vlassenbroeck, J., Van Hoorebeke, L., and Jacobs, P. (2006). "Recent progress in X-ray CT as a geosciences tool." *Applied Geochemistry*, 21(5), 826-832.

Côté, J., and Konrad, J.-M. (2005). "Thermal conductivity of base-course materials." *Canadian Geotechnical Journal*, 42(1), 61-78.

Cox, M. R., and Budhu, M. (2008). "A practical approach to grain shape quantification." *Engineering Geology*, 96(1-2), 1-16.

Crapo, H. (1979). "Structural rigidity." *Structural topology, 1979, núm. 1*.

Dai, W., Hanaor, D., and Gan, Y. (2019). "The effects of packing structure on the effective thermal conductivity of granular media: A grain scale investigation." *International Journal of Thermal Sciences*, 142, 266-279.

Dai, W., Pupeschi, S., Hanaor, D., and Gan, Y. (2017). "Influence of gas pressure on the effective thermal conductivity of ceramic breeder pebble beds." *Fusion Engineering and Design*, 118, 45-51.

Delaney, G. W., and Cleary, P. W. (2010). "The packing properties of superellipsoids." *EPL (Europhysics Letters)*, 89(3), 34002.

Desu, R. K., Peeketi, A. R., and Annabattula, R. K. (2019). "Artificial neural network-based prediction of effective thermal conductivity of a granular bed in a gaseous environment." *Computational Particle Mechanics*, 6(3), 503-514.

DeVera Jr, A. L., and Strieder, W. (1977). "Upper and lower bounds on the thermal conductivity of a random, two-phase material." *The Journal of Physical Chemistry*, 81(18), 1783-1790.

Donev, A., Cisse, I., Sachs, D., Variano, E. A., Stillinger, F. H., Connelly, R., Torquato, S., and Chaikin, P. M. (2004). "Improving the density of jammed disordered packings using ellipsoids." *Science*, 303(5660), 990-993.

Dong, Y., McCartney, J. S., and Lu, N. (2015). "Critical Review of Thermal Conductivity Models for Unsaturated Soils." *Geotechnical and Geological Engineering*, 33(2), 207-221.

Druckrey, A., Alshibli, K., and Al-Raoush, R. (2017). "Discrete particle translation gradient concept to expose strain localisation in sheared granular materials

using 3D experimental kinematic measurements." *Géotechnique*, 68(2), 162-170.
Dul'nev, G., and Zarichnyak, Y. P. (1974). "Thermal conductivity of mixtures and composite materials." *Energiya, Leningrad*.
El Shamy, U., De Leon, O., and Wells, R. (2013). "Discrete element method study on effect of shear-induced anisotropy on thermal conductivity of granular soils." *International Journal of Geomechanics*, 13(1), 57-64.
Fang, W.-Z., Zhang, H., Chen, L., and Tao, W.-Q. (2017). "Numerical predictions of thermal conductivities for the silica aerogel and its composites." *Applied Thermal Engineering*, 115, 1277-1286.
Fatt, I. (1956). "The network model of porous media."
Fei, W., and Narsilio, G. A. (2020). "Impact of three-dimensional sphericity and roundness on coordination number." *Journal of Geotechnical and Geoenvironmental Engineering*, (Accepted).
Fei, W., Narsilio, G. A., and Disfani, M. M. (2019). "Impact of three-dimensional sphericity and roundness on heat transfer in granular materials." *Powder Technology*, 355, 770-781.
Fei, W., Narsilio, G. A., van der Linden, J. H., and Disfani, M. M. (2019). "Quantifying the impact of rigid interparticle structures on heat transfer in granular materials using networks." *International Journal of Heat and Mass Transfer*, 143, 118514.
Fei, W., Narsilio, G. A., van der Linden, J. H., and Disfani, M. M. (2020). "Network analysis of heat transfer in sphere packings." *Powder Technology*, 362, 790-804.
Fei, W. B., Li, Q., Wei, X. C., Song, R. R., Jing, M., and Li, X. C. (2015). "Interaction analysis for CO2 geological storage and underground coal mining in Ordos Basin, China." *Engineering geology*, 196, 194-209.
Finney, J. (1970). "Random packings and the structure of simple liquids. I. The geometry of random close packing." *Proc. R. Soc. Lond. A*, 319(1539), 479-493.
Fletcher, L. (1988). "Recent developments in contact conductance heat transfer." *Journal of Heat Transfer*, 110(4b), 1059-1070.
Fonseca, J., O'Sullivan, C., Coop, M. R., and Lee, P. (2013). "Quantifying the evolution of soil fabric during shearing using directional parameters." *Géotechnique*, 63(6), 487-499.
Fonseca, J., O'Sullivan, C., Coop, M. R., and Lee, P. (2012). "Non-invasive characterization of particle morphology of natural sands." *Soils and Foundations*, 52(4), 712-722.
Fonseca, J., Sim, W., Shire, T., and O'sullivan, C. (2014). "Microstructural analysis of sands with varying degrees of internal stability." *Géotechnique*, 64(5), 405-411.
Freeman, L. C. (1977). "A set of measures of centrality based on betweenness." *Sociometry*, 35-41.
Freeman, L. C. (1978). "Centrality in social networks conceptual clarification." *Social networks*, 1(3), 215-239.
Fricke, H. (1924). "A mathematical treatment of the electric conductivity and capacity of disperse systems I. The electric conductivity of a suspension of homogeneous spheroids." *Physical Review*, 24(5), 575.

Fu, G., Wilkinson, S., and Dawson, R. J. (2016). "A spatial network model for civil infrastructure system development." *Computer-Aided Civil and Infrastructure Engineering*, 31(9), 661-680.
Gan, J., Zhou, Z., and Yu, A. (2017). "Effect of particle shape and size on effective thermal conductivity of packed beds." *Powder Technology*, 311, 157-166.
Gangadhara Rao, M., and Singh, D. (1999). "A generalized relationship to estimate thermal resistivity of soils." *Canadian Geotechnical Journal*, 36(4), 767-773.
Garcia, X., Akanji, L. T., Blunt, M. J., Matthai, S. K., and Latham, J. P. (2009). "Numerical study of the effects of particle shape and polydispersity on permeability." *Physical Review E*, 80(2), 021304.
Gerhardter, H., Prieler, R., Schluckner, C., Knoll, M., Hochenauer, C., Mühlböck, M., Tomazic, P., and Schroettner, H. (2019). "Modelling convective heat transfer to non-spherical particles." *Powder Technology*, 343, 245-254.
Géron, A. (2019). *Hands-On Machine Learning with Scikit-Learn, Keras, and TensorFlow: Concepts, Tools, and Techniques to Build Intelligent Systems*, O'Reilly Media.
Göktepe, A. B., and Sezer, A. (2010). "Effect of particle shape on density and permeability of sands." *Proceedings of the Institution of Civil Engineers-Geotechnical Engineering*, 163(6), 307-320.
Gonzo, E. E. (2002). "Estimating correlations for the effective thermal conductivity of granular materials." *Chemical Engineering Journal*, 90(3), 299-302.
Gostick, J. T. (2017). "Versatile and efficient pore network extraction method using marker-based watershed segmentation." *Physical Review E*, 96(2), 023307.
Haigh, S. K. (2012). "Thermal conductivity of sands." *Géotechnique*, 62(7), 617-625.
Hamilton, R. L., and Crosser, O. (1962). "Thermal conductivity of heterogeneous two-component systems." *Industrial & Engineering chemistry fundamentals*, 1(3), 187-191.
Ho, T. K. "Random decision forests." *Proc., Document analysis and recognition, 1995., proceedings of the third international conference on*, IEEE, 278-282.
Hryciw, R. D., Zheng, J., and Shetler, K. (2016). "Particle roundness and sphericity from images of assemblies by chart estimates and computer methods." *Journal of Geotechnical and Geoenvironmental Engineering*, 142(9), 04016038.
Huang, X., He, Y., Zhou, W., Deng, D., and Zhao, Y. (2019). "Pore network modeling of fibrous porous media of uniform and gradient porosity." *Powder technology*, 343, 350-361.
Huang, X., Zhou, Q., Liu, J., Zhao, Y., Zhou, W., and Deng, D. (2017). "3D stochastic modeling, simulation and analysis of effective thermal conductivity in fibrous media." *Powder technology*, 320, 397-404.
Hughey, J. (2020). "Ridler-Calvard image thresholding " *MATLAB Central File Exchange*, MATLAB Central File Exchange.
Iassonov, P., Gebrenegus, T., and Tuller, M. (2009). "Segmentation of X-ray computed tomography images of porous materials: A crucial step for characterization and quantitative analysis of pore structures." *Water Resources Research*, 45(9).
Itasca, P. D. (2008). "Particle Flow Code in 3 Dimensions, User's Guide."
Johnston, I. W., Narsilio, G. A., and Colls, S. (2011). "Emerging geothermal energy technologies." *KSCE Journal of Civil Engineering*, 15(4), 643-653.
Ju, S., and Shiomi, J. (2019). "Materials Informatics for Heat Transfer: Recent Progresses and Perspectives." *Nanoscale and Microscale Thermophysical Engineering*, 23(2), 157-172.

Kain, G., Lienbacher, B., Barbu, M.-C., Plank, B., Richter, K., and Petutschnigg, A. (2016). "Evaluation of relationships between particle orientation and thermal conductivity in bark insulation board by means of CT and discrete modeling." *Case studies in nondestructive testing and evaluation*, 6, 21-29.

Kamiński, B., Jakubczyk, M., and Szufel, P. (2018). "A framework for sensitivity analysis of decision trees." *Central European journal of operations research*, 26(1), 135-159.

Kanit, T., Forest, S., Galliet, I., Mounoury, V., and Jeulin, D. (2003). "Determination of the size of the representative volume element for random composites: statistical and numerical approach." *International Journal of solids and structures*, 40(13-14), 3647-3679.

Karatza, Z., Andò, E., Papanicolopulos, S., Ooi, J., and Viggiani, G. (2018). "Evolution of deformation and breakage in sand studied using X-ray tomography." *Géotechnique*, 1, 1-11.

Kautz, E. J., Hagen, A. R., Johns, J. M., and Burkes, D. E. (2019). "A machine learning approach to thermal conductivity modeling: A case study on irradiated uranium-molybdenum nuclear fuels." *Computational Materials Science*, 161, 107-118.

Keller, T., Motschmann, U., and Engelhard, L. (2001). "Modelling the poroelasticity of rocks and ice." *Geophysical prospecting*, 47(4), 509-526.

Kerckhofs, G., Pyka, G., Moesen, M., Schrooten, J., and Wevers, M. "High-resolution micro-CT as a tool for 3D surface roughness measurement of 3D additive manufactured porous structures." *Proc., iCT Conf*, 77-83.

Kim, H., Haas, C. T., Rauch, A. F., and Browne, C. (2003). "3D image segmentation of aggregates from laser profiling." *Computer-Aided Civil and Infrastructure Engineering*, 18(4), 254-263.

KIVOHASHI, H., and Deguchi, M. (1998). "Derivation of a correlation formula for the effective thermal conductivity of geological porous materials by the three-phase geometric-mean model." *High Temperatures. High Pressures*, 30(1), 25-35.

Koh, J., and Fortini, A. (1971). "Thermal conductivity and electrical resistivity of porous material."

Krumbein, W. C., and Sloss, L. L. (1963). "Stratigraphy and sedimentation."

Krupiczka, R. (1967). "Analysis of thermal conductivity in granular materials." *International Chemical Engineering*, 7(1), 122-+.

Lai, Z., and Chen, Q. (2019). "Reconstructing granular particles from X-ray computed tomography using the TWS machine learning tool and the level set method." *Acta Geotechnica*, 14(1), 1-18.

Laman, G. (1970). "On graphs and rigidity of plane skeletal structures." *Journal of Engineering mathematics*, 4(4), 331-340.

Landini, G. "Advanced shape analysis with ImageJ." *Proc., Proceedings of the Second ImageJ user and developer Conference, Luxembourg*, 6-7.

Langville, A. N., and Meyer, C. D. (2005). "A survey of eigenvector methods for web information retrieval." *SIAM review*, 47(1), 135-161.

Lee, C., Suh, H. S., Yoon, B., and Yun, T. S. (2017). "Particle shape effect on thermal conductivity and shear wave velocity in sands." *Acta Geotechnica*, 12(3), 615-625.

Legland, D., Arganda-Carreras, I., and Andrey, P. (2016). "MorphoLibJ: integrated library and plugins for mathematical morphology with ImageJ." *Bioinformatics*, 32(22), 3532-3534.

Liang, Y. (2015). "Expression for effective thermal conductivity of randomly packed granular material." *International Journal of Heat and Mass Transfer*, 90, 1105-1108.

Liu, A. J., Nagel, S. R., Van Saarloos, W., and Wyart, M. (2011). "The jamming scenario-an introduction and outlook." *Dynamical heterogeneities in glasses, colloids, and granular media*, Oxford University Press.

Liu, F., Cai, Y., Wang, L., and Zhao, J. (2018). "Effects of nanoparticle shapes on laminar forced convective heat transfer in curved ducts using two-phase model." *International Journal of Heat and Mass Transfer*, 116, 292-305.

Loveridge, F., Holmes, G., Powrie, W., and Roberts, T. (2018). "Thermal response testing through the Chalk aquifer in London, UK." *ICE Themes Geothermal Energy, Heat Exchange Systems and Energy Piles*, 157-177.

Ltd., S. (2015). "Simpleware ScanIP, http://www.simpleware.com/software/scanip." *Date of access*, 15, 12.

Lu, Y., Xiao, S., Ge, Z., Zhou, Z., Ling, Y., and Wang, L. (2019). "Experimental study on rock-breaking performance of water jets generated by self-rotatory bit and rock failure mechanism." *Powder Technology*, 346, 203-216.

Łydżba, D., and Różański, A. (2014). "Microstructure measures and the minimum size of a representative volume element: 2D numerical study." *Acta Geophysica*, 62(5), 1060-1086.

Maxwell, J. C. (1873). "A treatise on electricity end magnetism." Clarendon Press.

Mendel, A. (1997). "Relation between thermal conductivity of rocks and structure of the pores." *Russ J Geology Prospect*, 1, 112-119.

Miettinen, L., Kekäläinen, P., Turpeinen, T., Hyväluoma, J., Merikoski, J., and Timonen, J. (2012). "Dependence of thermal conductivity on structural parameters in porous samples." *AIP Advances*, 2(1), 012101.

Minh, N., and Cheng, Y. (2013). "A DEM investigation of the effect of particle-size distribution on one-dimensional compression." *Géotechnique*, 63(1), 44.

Mo, J., and Ban, H. (2017). "Measurements and theoretical modeling of effective thermal conductivity of particle beds under compression in air and vacuum." *Case studies in thermal engineering*, 10, 423-433.

Morris, A. B., Pannala, S., Ma, Z., and Hrenya, C. M. (2015). "A conductive heat transfer model for particle flows over immersed surfaces." *International Journal of Heat and Mass Transfer*, 89, 1277-1289.

Moscardini, M., Gan, Y., Pupeschi, S., and Kamlah, M. (2018). "Discrete element method for effective thermal conductivity of packed pebbles accounting for the Smoluchowski effect." *Fusion Engineering and Design*, 127, 192-201.

Münch, B., Trtik, P., Marone, F., and Stampanoni, M. (2009). "Stripe and ring artifact removal with combined wavelet—Fourier filtering." *Optics express*, 17(10), 8567-8591.

Nadimi, S., Fonseca, J., Andò, E., and Viggiani, G. (2019). "A micro finite-element model for soil behaviour: experimental evaluation for sand under triaxial compression." *Géotechnique*, 0(0), 1-6.

Narsilio, G. A., Buzzi, O., Fityus, S., Yun, T. S., and Smith, D. W. (2009). "Upscaling of Navier–Stokes equations in porous media: Theoretical, numerical and experimental approach." *Computers and Geotechnics*, 36(7), 1200-1206.

Narsilio, G. A., Kress, J., and Yun, T. S. (2010). "Characterisation of conduction phenomena in soils at the particle-scale: Finite element analyses in conjunction with synthetic 3D imaging." *Computers and Geotechnics*, 37(7), 828-836.

Neuendorf, K. K., Mehl Jr, J. P., and Jackson, J. A. (2005). "Glossary of Geology: American Geological Institute." *Alexandria, Virginia*.

Neumann, J., Simon, J.-W., and Reese, S. (2018). "Digital sieving of irregular 3D particles—A study using XRCT and statistically similar synthetic data." *Powder Technology*, 338, 1001-1015.

Newman, M. (2018). *Networks*, Oxford university press.

Newman, M. E. (2003). "The structure and function of complex networks." *SIAM review*, 45(2), 167-256.

Newman, M. E. J. (2010). *Networks : an introduction*, Oxford ; New York : Oxford University Press, 2010.

Odelevskii, V. (1951). "Calculation of the generalized conductivity of heterogeneous systems." *Zh. Tekh. Fiz*, 21(6), 678-685.

Ohtake, Y., Belyaev, A., and Bogaevski, I. (2001). "Mesh regularization and adaptive smoothing." *Computer-Aided Design*, 33(11), 789-800.

Otsu, N. (1979). "A threshold selection method from gray-level histograms." *IEEE transactions on systems, man, and cybernetics*, 9(1), 62-66.

Papadopoulos, L., Porter, M. A., Daniels, K. E., and Bassett, D. S. (2018). "Network analysis of particles and grains." *Journal of Complex Networks*, 6(4), 485-565.

Pedregosa, F., Varoquaux, G., Gramfort, A., Michel, V., Thirion, B., Grisel, O., Blondel, M., Prettenhofer, P., Weiss, R., and Dubourg, V. (2011). "Scikit-learn: Machine learning in Python." *Journal of machine learning research*, 12(Oct), 2825-2830.

Peixoto, T. P. (2014). "The graph-tool python library." *figshare*.

Persson, B., Albohr, O., Tartaglino, U., Volokitin, A., and Tosatti, E. (2004). "On the nature of surface roughness with application to contact mechanics, sealing, rubber friction and adhesion." *Journal of physics: Condensed matter*, 17(1), R1.

Reimann, J., Vicente, J., Brun, E., Ferrero, C., Gan, Y., and Rack, A. (2017). "X-ray tomography investigations of mono-sized sphere packing structures in cylindrical containers." *Powder technology*, 318, 471-483.

Richard, P., Nicodemi, M., Delannay, R., Ribiere, P., and Bideau, D. (2005). "Slow relaxation and compaction of granular systems." *Nature materials*, 4(2), 121-128.

Rivier, N. (2006). "Extended constraints, arches and soft modes in granular materials." *Journal of non-crystalline solids*, 352(42-49), 4505-4508.

Rohsenow, W. M., Hartnett, J. P., and Ganic, E. N. (1985). "Handbook of heat transfer applications." *New York, McGraw-Hill Book Co., 1985, 973 p. No individual items are abstracted in this volume.*

Rorato, R., Arroyo, M., Andò, E., and Gens, A. (2019). "Sphericity measures of sand grains." *Engineering Geology*, 254, 43-53.

Roshankhah, S., and Santamarina, J. C. (2014). "Engineered granular materials for heat conduction and load transfer in energy geotechnology." *Géotechnique Letters*, 4(2), 145-150.

Rotta Loria, A. F., and Laloui, L. (2017). "The equivalent pier method for energy pile groups." *Géotechnique*, 67(8), 691-702.

Russell, S., Walker, D. M., and Tordesillas, A. (2016). "A characterization of the coupled evolution of grain fabric and pore space using complex networks: Pore connectivity and optimized flows in the presence of shear bands." *Journal of the Mechanics and Physics of Solids*, 88, 227-251.

Samuel, A. L. (1959). "Some studies in machine learning using the game of checkers." *IBM Journal of research and development*, 3(3), 210-229.

Santamarina, J., and Cho, G.-C. "Soil behaviour: The role of particle shape." *Proc., Advances in geotechnical engineering: The skempton conference*, Citeseer, 604-617.

Santosa, F., and Symes, W. W. (1986). "Linear inversion of band-limited reflection seismograms." *SIAM Journal on Scientific and Statistical Computing*, 7(4), 1307-1330.

Sass, J., Lachenbruch, A. H., and Munroe, R. J. (1971). "Thermal conductivity of rocks from measurements on fragments and its application to heat-flow determinations." *Journal of geophysical research*, 76(14), 3391-3401.

Schindelin, J., Arganda-Carreras, I., Frise, E., Kaynig, V., Longair, M., Pietzsch, T., Preibisch, S., Rueden, C., Saalfeld, S., and Schmid, B. (2012). "Fiji: an open-source platform for biological-image analysis." *Nature methods*, 9(7), 676.

Schlüter, S., Sheppard, A., Brown, K., and Wildenschild, D. (2014). "Image processing of multiphase images obtained via X-ray microtomography: a review." *Water Resources Research*, 50(4), 3615-3639.

Scott, D. M., Das, D. K., Subbaihaannadurai, V., and Kamath, V. A. (2005). "A computational scheme for fluid flow and heat transfer analysis in porous media for recovery of oil and gas." *Petroleum science and technology*, 23(7-8), 843-862.

Scott, J. (1988). "Social network analysis." *Sociology*, 22(1), 109-127.

Sezgin, M., and Sankur, B. (2004). "Survey over image thresholding techniques and quantitative performance evaluation." *Journal of Electronic imaging*, 13(1), 146-166.

Shapiro, M., Dudko, V., Royzen, V., Krichevets, Y., Lekhtmakher, S., Grozubinsky, V., Shapira, M., and Brill, M. (2004). "Characterization of Powder Beds by Thermal Conductivity: Effect of Gas Pressure on the Thermal Resistance of Particle Contact Points." *Particle & Particle Systems Characterization*, 21(4), 268-275.

Shin, H., and Santamarina, J. (2012). "Role of particle angularity on the mechanical behavior of granular mixtures." *Journal of Geotechnical and Geoenvironmental Engineering*, 139(2), 353-355.

Shire, T., and O'Sullivan, C. (2013). "Micromechanical assessment of an internal stability criterion." *Acta Geotechnica*, 8(1), 81-90.

Simpleware Ltd. (2015). "Simpleware ScanIP, http://www.simpleware.com/software/scanip." *Date of access*, 15, 12.

Singh, D. N., and Devid, K. (2000). "Generalized relationships for estimating soil thermal resistivity." *Experimental Thermal and Fluid Science*, 22(3), 133-143.

Siu, W., and Lee, S.-K. (2000). "Effective conductivity computation of a packed bed using constriction resistance and contact angle effects." *International journal of heat and mass transfer*, 43(21), 3917-3924.

Smailovic, V., Podobnik, V., and Lovrek, I. (2018). "A methodology for evaluating algorithms that calculate social influence in complex social networks." *Complexity*, 2018.

Smart, A. G., and Ottino, J. M. (2008). "Evolving loop structure in gradually tilted two-dimensional granular packings." *Physical Review E*, 77(4), 041307.

Sneed, E. D., and Folk, R. L. (1958). "Pebbles in the lower Colorado River, Texas a study in particle morphogenesis." *The Journal of Geology*, 66(2), 114-150.

Soille, P., and Vincent, L. M. "Determining watersheds in digital pictures via flooding simulations." *Proc., Visual Communications and Image Processing'90: Fifth in a Series*, International Society for Optics and Photonics, 240-250.

Somerton, W. H. (1992). *Thermal properties and temperature-related behavior of rock/fluid systems*, Elsevier.

Stone, M. (1974). "Cross-validatory choice and assessment of statistical predictions." *Journal of the royal statistical society. Series B (Methodological)*, 111-147.

Sufian, A., Russell, A. R., and Whittle, A. J. (2017). "Anisotropy of contact networks in granular media and its influence on mobilised internal friction." *Géotechnique*, 67(12), 1067-1080.

Sundberg, J., Back, P.-E., Ericsson, L. O., and Wrafter, J. (2009). "Estimation of thermal conductivity and its spatial variability in igneous rocks from in situ density logging." *International Journal of Rock Mechanics and Mining Sciences*, 46(6), 1023-1028.

Tarnawski, V., Momose, T., and Leong, W. (2009). "Assessing the impact of quartz content on the prediction of soil thermal conductivity." *Geotechnique*, 59(4), 331-338.

Taubin, G. "Curve and surface smoothing without shrinkage." *Proc., Computer Vision, 1995. Proceedings., Fifth International Conference on*, IEEE, 852-857.

Taylor, H., O'Sullivan, C., and Sim, W. (2015). "A new method to identify void constrictions in micro-CT images of sand." *Computers and Geotechnics*, 69, 279-290.

TEACHERS (2012). "Mica." <https://www.teachersource.com/product/mica-by-the-pound/earth-rocks>.

Thalmann, R. E. (1950). "Thermal conductivity of dry soils." University of Kansas, Mechanical Engineering.

Thibault, J. B., Sauer, K. D., Bouman, C. A., and Hsieh, J. (2007). "A three-dimensional statistical approach to improved image quality for multislice helical CT." *Medical physics*, 34(11), 4526-4544.

Tordesillas, A., Lin, Q., Zhang, J., Behringer, R., and Shi, J. (2011). "Structural stability and jamming of self-organized cluster conformations in dense granular materials." *Journal of the Mechanics and Physics of Solids*, 59(2), 265-296.

Tordesillas, A., Tobin, S. T., Cil, M., Alshibli, K., and Behringer, R. P. (2015). "Network flow model of force transmission in unbonded and bonded granular media." *Physical Review E*, 91(6), 062204.

Tordesillas, A., Walker, D. M., and Lin, Q. (2010). "Force cycles and force chains." *Physical Review E*, 81(1), 011302.

Torquato, S., and Haslach Jr, H. (2002). "Random heterogeneous materials: microstructure and macroscopic properties." *Appl. Mech. Rev.*, 55(4), B62-B63.

Torquato, S., Kim, I. C., and Cule, D. (1999). "Effective conductivity, dielectric constant, and diffusion coefficient of digitized composite media via first-passage-time equations." *Journal of Applied Physics*, 85(3), 1560-1571.

Van Antwerpen, W., Du Toit, C., and Rousseau, P. (2010). "A review of correlations to model the packing structure and effective thermal conductivity in packed beds of mono-sized spherical particles." *Nuclear Engineering and design*, 240(7), 1803-1818.

van der Linden, J. H., Narsilio, G. A., and Tordesillas, A. (2016). "Machine learning framework for analysis of transport through complex networks in porous, granular media: a focus on permeability." *Physical Review E*, 94(2), 022904.
van der Linden, J. H., Narsillio, G. A., and Antoinette, T. (2019). "Thermal conductance network model for computerised tomography images of real geomaterials (Conditionally accepted)." *Computers and Geotechnics*.
VandenBerg, A. (2000). *The Tasman Fold Belt system in Victoria: geology and mineralisation of Proterozoic to Carboniferous rocks*, Geological Survey of Victoria.
Verma, L., Shrotriya, A., Singh, R., and Chaudhary, D. (1991). "Thermal conduction in two-phase materials with spherical and non-spherical inclusions." *Journal of Physics D: Applied Physics*, 24(10), 1729.
Vincent, L., and Soille, P. (1991). "Watersheds in digital spaces: an efficient algorithm based on immersion simulations." *IEEE Transactions on Pattern Analysis & Machine Intelligence*(6), 583-598.
Wadell, H. (1932). "Volume, shape, and roundness of rock particles." *The Journal of Geology*, 40(5), 443-451.
Walker, D. M., and Tordesillas, A. (2010). "Topological evolution in dense granular materials: a complex networks perspective." *International Journal of Solids and Structures*, 47(5), 624-639.
Wang, J., Wu, S., Zhao, L., Wang, W., Wei, J., and Sun, J. (2019). "An effective method for shear-wave velocity prediction in sandstones." *Marine Geophysical Research*, 40(4), 655-664.
Watts, D. J., and Strogatz, S. H. (1998). "Collective dynamics of 'small-world'networks." *nature*, 393(6684), 440.
Wei, D., Zhao, B., Dias-da-Costa, D., and Gan, Y. (2019). "An FDEM study of particle breakage under rotational point loading." *Engineering Fracture Mechanics*.
Wei, G., Zhang, H., An, X., Xiong, B., and Jiang, S. (2019). "CFD-DEM study on heat transfer characteristics and microstructure of the blast furnace raceway with ellipsoidal particles." *Powder technology*, 346, 350-362.
Wei, H., Zhao, S., Rong, Q., and Bao, H. (2018). "Predicting the effective thermal conductivities of composite materials and porous media by machine learning methods." *International Journal of Heat and Mass Transfer*, 127, 908-916.
Wiebicke, M., Andò, E., Herle, I., and Viggiani, G. (2017). "On the metrology of interparticle contacts in sand from x-ray tomography images." *Measurement Science and Technology*, 28(12), 124007.
Woodside, W., and Messmer, J. (1961). "Thermal conductivity of porous media. I. Unconsolidated sands." *Journal of applied physics*, 32(9), 1688-1699.
Xinbao, Y., Nan, Z., Asheesh, P., and J., P. A. (2016). "Thermal conductivity of sand–kaolin clay mixtures." *Environmental Geotechnics*, 3(4), 190-202.
Yang, H., Zhang, L., Liu, R., Wen, X., Yang, Y., Zhang, L., Zhang, K., and Askari, R. (2019). "Thermal Conduction Simulation Based on Reconstructed Digital Rocks with Respect to Fractures." *Energies*, 12(14), 2768.
Yang, J., and Gu, X. Q. (2013). "Shear stiffness of granular material at small strains: does it depend on grain size?" *Géotechnique*, 63(2), 165-179.
Yang, P., Yu, Y., Chen, L., and Mao, W. (2004). "Experimental determination and theoretical prediction of twin orientations in magnesium alloy AZ31." *Scripta Materialia*, 50(8), 1163-1168.
Young, H. D., Freedman, R. A., Sandin, T., and Ford, A. L. (1996). *University physics*, Addison-Wesley Reading, MA.

Yüksel, N. (2016). "The review of some commonly used methods and techniques to measure the thermal conductivity of insulation materials." *Insulation materials in context of sustainability*, IntechOpen.

Yun, T. S., and Evans, T. M. (2010). "Three-dimensional random network model for thermal conductivity in particulate materials." *Computers and Geotechnics*, 37(7), 991-998.

Yun, T. S., and Santamarina, J. C. (2008). "Fundamental study of thermal conduction in dry soils." *Granular matter*, 10(3), 197-207.

Zehner, P., and Schlunder, E. U. (1970). "Thermal Conductivity of Granular Materials at Moderate Temperatures." *Chemie. Ingr-Tech.*, 42, 933-941.

Zhang, N., and Wang, Z. (2017). "Review of soil thermal conductivity and predictive models." *International Journal of Thermal Sciences*, 117, 172-183.

Zhang, N., Yu, X., Pradhan, A., and Puppala, A. J. (2015). "Thermal conductivity of quartz sands by thermo-time domain reflectometry probe and model prediction." *Journal of Materials in Civil Engineering*, 27(12), 04015059.

Zhao, B., Wang, J., Coop, M., Viggiani, G., and Jiang, M. (2015). "An investigation of single sand particle fracture using X-ray micro-tomography." *Géotechnique*, 65(8), 625-641.

Zhao, S., Zhang, N., Zhou, X., and Zhang, L. (2017). "Particle shape effects on fabric of granular random packing." *Powder technology*, 310, 175-186.

Zhou, B., Wang, J., and Wang, H. (2017). "Three-dimensional sphericity, roundness and fractal dimension of sand particles." *Géotechnique*, 68(1), 18-30.

Zhou, Z.-Y., Zou, R.-P., Pinson, D., and Yu, A.-B. (2011). "Dynamic simulation of the packing of ellipsoidal particles." Industrial & Engineering Chemistry Research, 50(16), 9787-9798.